

EXAFS STUDIES ON NANOSTRUCTURE SYSTEMS AND THIN FILM MULTILAYERS

By

NIDHI TIWARI

PHYS01201504012

Bhabha Atomic Research Centre

*A thesis submitted to the
Board of Studies in Physical Sciences
In partial fulfilment of requirements
for the Degree of*

DOCTOR OF PHILOSOPHY

of

HOMI BHABHA NATIONAL INSTITUTE



February, 2019

HOMI BHABHA NATIONAL INSTITUTE

Recommendations of the Viva Voce Committee


As members of the Viva Voce Committee, we certify that we have read the dissertation prepared by Ms. Nidhi Tiwari entitled "EXAFS studies on nanostructure systems and thin film multilayers" and recommend that it may be accepted as fulfilling the thesis requirement for the award of Degree of Doctor of Philosophy.

Sr.No.	Name	Designation	Signature	Date
1.	Dr. N.K. Sahoo	Chairman		4/2/2019
2.	Prof. Subodh Kumar De	External examiner		04.02.19
3.	Dr. D.K. Aswal	Member		4/2/19
4.	Dr. T. Ganguli	Member		04/02/2019
5.	Dr. D. Bhattacharyya	Guide & Convener		04/02/2019

Final approval and acceptance of this thesis is contingent upon the candidate's submission of the final copies of the thesis to HBNI.

I hereby certify that I have read this thesis prepared under my direction and recommend that it may be accepted as fulfilling the thesis requirement.

Date: 04/02/2019
Place: Mumbai


Dr. Dibyendu Bhattacharyya
(Guide)

STATEMENT BY AUTHOR

This dissertation has been submitted in partial fulfilment of requirements for an advanced degree at Homi Bhabha National Institute (HBNI) and is deposited in the Library to be made available to borrowers under rules of the HBNI.

Brief quotations from this dissertation are allowable without special permission, provided that accurate acknowledgement of source is made. Requests for permission for extended quotation from or reproduction of this manuscript in whole or in part may be granted by the Competent Authority of HBNI when in his or her judgment the proposed use of the material is in the interests of scholarship. In all other instances, however, permission must be obtained from the author.



NIDHI TIWARI

DECLARATION

I, hereby declare that the investigation presented in the thesis has been carried out by me. The work is original and has not been submitted earlier as a whole or in part for a degree / diploma at this or any other Institution / University.



NIDHI TIWARI

List of Publications arising from the thesis

Journals:

1. "Insight into the origin of ferromagnetism in Fe-doped ZnO dilute magnetic semiconductor nanocrystals: an EXAFS study of local structure", Shiv Kumar, Nidhi Tiwari, S. N. Jha, S. Chatterjee, D. Bhattacharyya, N.K.Sahoo, RSC Adv., **5** (2015) 94658-69.
2. "Structural and optical properties of sol-gel derived Cr-doped ZnO diluted magnetic semiconductor nanocrystals: an EXAFS study to relate the local structure," Shiv Kumar, Nidhi Tiwari, S. N. Jha, S. Chatterjee, D. Bhattacharyya and Anup K. Ghosh, RSC Adv., **6** (2016) 107816.
3. "Local structure investigation of (Co, Cu) co-doped ZnO nanocrystals and its correlation with magnetic properties," Nidhi Tiwari, S. Doke A. Lohar, Shailaja Mahamuni, C. Kamal, Aparna Chakrabarti, R. J.Choudhary, P.Mondal, S.N. Jha and D. Bhattacharyya, J. Phys. and Chem. Sol. **90** (2016) 110-130.
4. "Structural and magnetic studies on (Fe, Cu) co-doped ZnO nanocrystals," Nidhi Tiwari, A. Lohar, C. Kamal, Aparna Chakrabarti, C.L. Prajapat, P.K. Mishra, P. Mondal B.Karnar, N.L. Misra, S.N. Jha, D. Bhattacharyya, J. Phys. and Chem. Sol., **104** (2017) 198–206.
5. "Structural investigations of (Mn, Dy) co-doped ZnO using X-ray absorption studies," Nidhi Tiwari, S. Kumar, A.K. Ghosh, S. Chatterjee, S. N. Jha and D. Bhattacharyya, RSC advances, RSC Adv., **7** (2017) 56662-56675.
6. "Structural investigations of (Cu, Ni) co-doped ZnO nanocrystals by X-ray Absorption spectroscopy," Nidhi Tiwari, S. Kumar, C. Kamal, Aparna Chakrabarti, C. L. Prajapat, P.K. Mishra, P. Mondal, S.N. Jha and D. Bhattacharyya, Chem. Select, **3** (2018) 5644-5651.

Conference paper (related to PhD work):

1. "Synthesis and characterisation of (Fe,Cu) co-doped ZnO nanoparticles," Nidhi Tiwari, A. Lohar, Shailaja Mahamuni, B. Karnar, N.L. Misra, S.N.Jha and D. Bhattacharyya, Presented in 61th DAE-Solid State Physics Symposium, December 26-30, 2016, KIIT University, Bhubaneswar, Odisha, India.
2. "Local structural investigation of (Fe, Cu) co-doped ZnO nanocrystals by X-ray absorption spectroscopy measurements", Nidhi Tiwari, A. Lohar, Shailaja Mahamuni, C. L. Prajapat, P.K. Mishra, P. Mondal, B. Karnar, N.L.Misra, S.N.Jha, D. Bhattacharyya

and N.K. Sahoo, Presented in Italian Society of Synchrotron Meeting (SILS-2016), 21-23 September, 2016, Bari, Italy.

3. “Grazing Incidence XAS measurement of Ni/Ti thin film multilayer at Indus-2 SRS”, Nidhi Tiwari, P. Rajput, P. Sarkar, Rajnarayan De, K.D. Rao, A. Biswas, D.Bhattacharyya, S.N. Jha and N.K. Sahoo. Presented in 62nd DAE-Solid State Physics Symposium, December 26-30, 2017, Bhabha Atomic Research Centre, Mumbai.
4. “Depth dependent structural probing of magnetic multilayers by Grazing Incidence XAFS study at Indus-2 SRS”, Nidhi Tiwari, P. Rajput, D.Bhattacharyya, S.N. Jha and N.K. Sahoo, 17th International Conference on X-ray Absorption Fine Structure (XAFS2018), July 22-27, 2018, Krakow, Poland.

Nidhi Tiwari

NIDHI TIWARI

Dedicated
To
My Parents

ACKNOWLEDGEMENTS

I would like to express my sincere gratitude to my supervisor Dr. Dibyendu Bhattacharyya, Head Synchrotron Science & Multilayer Physics Section, Atomic & Molecular Physics Division, BARC, for his guidance, motivation, enthusiasm and patience during my doctoral studies. His guidance helped me in all the time of research and writing of this thesis. I am also thankful to Dr. Shambhu Nath Jha, who has been very supportive and encouraging during the course of my research work. I would like to thank all of the members of my XAFS research group, Shri Ashok Kumar Yadav, Ms. Chandrani Nayak, Shri Ankur Agrawal, Shri Ashutosh Dwivedi, Dr. Arup Biswas, Dr. Parasmani Rajput, Shri Ashwini Poswal and other colleagues who have helped me in every possible way. A special mention for Shri Ashok Kumar Yadav and Mr. Chandrani Nayak, who made my long working hours worthwhile and for the stimulating discussions on XAFS. I take the opportunity to thank my friend Shri Chilukoti Ashok, Ms. Channprit Kaur and Shri Anil Bohra, who directly or indirectly have helped me in achieving my goals.

I am grateful to Dr. N. K. Sahoo, Head, A&MPD, BARC for his guidance and support in every way possible. Besides my advisor, I would like to thank members of my doctoral committee for their input and valuable discussions. I am also thankful to my principal collaborators, Dr. Shiv Kumar, Dr. (Smt.) A. Chakrabarti, and Prof. (Smt.) S. M. Mahamuni Dr. C.L. Prajapat and Dr. P.K. Mishra

Last but not the least, I would like to thank my family: my parents and to my brother and sister for supporting me spiritually throughout writing this thesis and my life in general.

CONTENTS

Synopsis	01
List of Figures	12
List of Tables	21
 Chapter 1: INTRODUCTION	 24
1.1 Model for Magnetism in DMS:	29
1.1.1 Carrier mediated exchange interactions:	29
1.1.2 The bound magnetic polaron model:	30
1.2 X-ray standing wave generation in multilayer structure:	32
1.2.1 Theoretical formulation:	33
1.3 Motivation of the thesis work:	34
1.4 Outline of the thesis:	36
 Chapter 2: EXPERIMENTATION AND DATA ANALYSIS	 38
2.1 Sample preparation:	38
2.1.1 Sol-gel method:	38
2.1.2 Wet chemical route method	39
2.1.3 Magnetron sputtering:	39
2.2 XAS measurements and data analysis:	41
2.2.1 Theoretical Description of XAFS:	41
2.2.2 Theoretical formulation of EXAFS equation:	45
2.2.3 XAFS measurements:	50
2.2.4 XANES interpretation	56
2.2.5 EXAS data analysis:	58
2.2.6 Data reduction using Athena:	59
2.2.7 Data fitting using Artemis:	61
2.3 Other characterisation techniques:	65
2.3.1 X-ray Diffraction:	65
2.3.2 Transmission Electron Microscopy:	67
2.3.3 FTIR Spectroscopy:	68
2.3.4 Raman spectroscopy:	69
2.3.5 Photoluminescence	70
2.3.6 Magnetic measurements:	71
2.3.7 Theoretical calculations:	72
 Chapter 3: Fe & Cr doped ZnO Nanocrystals (NCs)	 74

3.1 Fe Doped ZnO::	74
3.1.1 Experimental Details:	75
3.1.2 Results and discussion:	76
3.2 Cr doped ZnO NCs	97
3.2.1 Experimental details:	98
3.2.2 Results and discussions:	99
 Chapter 4: (Co,Cu) co-doped ZnO NCs	 119
4.1 Introduction	119
4.2 Experimental details:	119
4.3 Results and discussion:	121
4.3.1 X-ray diffraction:	121
4.3.2 Transmission Electron Microscopy:	123
4.3.3 FTIR Spectroscopy:	124
4.3.4 Raman Spectroscopy:	126
4.3.5 Optical Absorption studies:	128
4.3.6 EPR Spectroscopy:	129
4.3.7 Theoretical calculations:	131
4.3.8 Magnetic Measurements:	133
4.3.9 EXAFS Spectroscopy:	135
4.3.9.1 Zn K-edge data:	135
4.3.9.2 Co K-edge data:	138
4.3.9.3 Cu K-edge data:	141
 Chapter 5: (Fe, Cu) co-doped ZnO NCs COMPOSITE THIN FILMS	 148
5.1 Introduction	147
5.2 Experimental details:	148
5.2.1 Preparation of samples::	148
5.2.2 Characterisation of samples:	149
5.3 Results and discussion	150
 Chapter 6: (Ni, Cu) co-doped ZnO NCs	 164
6.1 Introduction:	164
6.2 Experimental Details:	164
6.3 Results and discussion:	166
 Chapter 7: (Dy, Mn) co-doped ZnO Nanocrystals (NCs)	 181

7.2.1 Preparation of samples:	182
7.2.2 Characterisation of samples:	182
7.3 Results and discussion:	183
7.3.1 X-ray diffraction:	183
7.3.2 Transmission Electron Microscopy:	186
7.3.3 FTIR Spectroscopy:	186
7.3.4 Photo luminescence Measurement:	187
7.3.5 Magnetic Measurements:	188
7.3.6 EXAFS measurement:	190
 Chapter 8: GIXAFS measurement on thin film multilayer structures	 206
8.1 Introduction:	206
8.2 Experimental details:	207
8.3 Results and discussion:	208
 Chapter 9: SUMMARY, CONCLUSION	 213
References	222

Homi Bhabha National Institute

SYNOPSIS OF Ph.D. THESIS

- | | |
|--|---|
| 1. Name of the Student: | Nidhi Tiwari |
| 2. Name of the Constituent Institution: | Bhabha Atomic Research Center |
| 3. Enrolment No. : | PHYS01201504012 |
| 4. Title of the Thesis: | EXAFS studies on nanostructures and thin film multilayers |
| 5. Board of Studies: | Physical Sciences |

SYNOPSIS

EXAFS studies on nanostructure systems and thin film multilayers

X-ray Absorption (XAS) spectroscopy is an important tool to investigate the local structure around selected elements that are contained within a material. X-ray Absorption Spectroscopy (XAS), which comprises of both X-ray Near Edge Structure (XANES) and Extended X-ray Absorption Fine Structure (EXAFS) techniques, is an element specific technique which can be applied not only to crystals, but also to materials that possess little or no long-range translational order: amorphous systems, glasses, disordered films, membranes, solutions, liquids, metalloproteins and also for nanostructured materials and thin films. This versatility allows it to be used in a wide variety of disciplines: physics, chemistry, biology,

biophysics, medicine, engineering, environmental science, materials science, and geology. However, X-ray absorption measurements require an intense and energy-tuneable X-ray source like a synchrotron accelerator. The specifications of synchrotron sources, beamline optics and experimental station define the energy ranges, beam sizes, and intensities available, and dictate the practical experimental limits on the XAS measurements that can be performed.

EXAFS is not really a surface sensitive technique; however, by careful preparation of the samples and careful selection of the grazing angle of incidence of the incident synchrotron beam we can probe different depth of a thin film multilayer structure. By simulating the electric field pattern of the standing wave generated inside a multilayer structure, when electromagnetic X-ray radiation is made incident on it, we can calculate the grazing angles of incidence to probe the different depths of the multilayer.

The present thesis work is divided in to two parts: in first part we have explored the ZnO based dilute magnetic semiconductor system by using synchrotron based XAS techniques along with the other experimental techniques, subsequently the work carried out in second part accounts for the development of grazing angle incidence EXAFS (GIEXAFS) set up at energy scanning EXAFS beamline BI-09, Indus-2, RRCAT Indore to probe the local structures at different depths of a thin film multilayer structure.

Chapter 1 gives a brief introduction to the dilute magnetic semiconductor systems, and its potential application in the spintronic devices. The main challenge for practical applications of the DMS materials is the achievement of ferromagnetism (FM) above room temperature (RT). ZnO-based DMSs are appealing since they were predicted to have Curie temperature (T_C) above room temperature [1]. It is also theoretically predicted that simultaneous presence of two kinds of dopants/defects, can tailor the position and occupancy

of the Fermi energy of the materials and its magnetic behavior [2, 3]. Thus, co-doping of ZnO simultaneously with two TM ions, or with rare earth ions, might be a promising route to achieve and enhance RT ferromagnetism (FM). Various models have been explained which elucidate the origin of ferromagnetism in the DMS system such as (i) the mean-field Zener Model, (ii) the double exchange (direct interaction) mechanism or super exchange mechanism (indirect interaction through defects) between the magnetic cations and (iii) carrier (free electron)-mediated Ruderman–Kittel–Kasuya–Yosida (RKKY)-type interactions. Though a large volume of work also exists in the literature on room temperature ferromagnetism (RTFM) of doped ZnO systems, however, there are wide variations in the reported papers regarding the origin of RTFM observed in the samples which has been attributed to a variety of intrinsic and extrinsic reasons by various authors [4,5,6]. Thus origin of RTFM in doped and co-doped ZnO systems is still a fairly unresolved question and further experimental and theoretical studies are required particularly to explore the local environment around the host and the dopant cations carefully to obtain unambiguous results on the above subject. EXAFS is a short range order technique and it is element specific so it is a perfect tool to investigate the position and environment of dopants and defects in a host matrix and can yield important information regarding the presence or absence of FM in a material. Photocatalytic activity, however activity of ZnO is limited to irradiation wavelengths in the UV region because ZnO semiconductor has a wide band-gap of about 3.3 eV and can only absorb UV light. Doping of TM in ZnO nanoparticles transition metals reduces the electron–hole recombination it has been found that , Cr doped ZnO nanoparticles are observed to be efficient photo catalyst [7,8, 9].

Magnetic multilayer structures having variety of interesting properties and wide applications including as supermirror polarisers in neutron optics have also been introduced

at the end of this chapter. It is well known that interfaces play an important role in the performance of a magnetic multilayer device [10,11]. A variety of approaches can be used to determine the internal structure of multilayer's including interface roughness and inter-diffusion and compound formation at the interfaces. EXAFS is an important technique which can be used in grazing incidence configuration on a multilayer structure to probe the local structure as a function of depth. In this chapter the mechanism of electric field distribution with node and antinode positions in a magnetic multilayer, when an electromagnetic radiation is made incident on it and standing waves are generated, is described. This information is used to find out the grazing angle of incidence to probe the different region of the multilayer structure by EXAFS technique. Thus the details provide in this chapter gives both motivation and the basis for the work discussed in the succeeding chapters.

Chapter-2 of the thesis describes the various experimental techniques and data analysis formalism used in this thesis work. This chapter begins with short descriptions of the various sample preparation techniques followed in this work. Subsequently, the basics of XAS technique which comprises both XANES and EXAFS has been described. Both XAS and GIEXAFS measurement for samples described in this thesis have been performed at Energy Scanning EXAFS beamline, BI-09, Indus-2 Synchrotron radiation sources at Raja Ramanna Centre for Advanced Technology, Indore, India [12, 13] which has been briefly described here. Finally the data reduction and data analysis procedure of EXAFS is described elaborately which involves extensive use of the IFEFFIT software package including ATHENA and ARTEMIS subroutines [14]. A brief description of other characterization techniques used in this thesis work, viz., X-ray diffraction (XRD), transmission electron microscopy (TEM), photoluminescence (PL), magnetic measurements etc. are also discussed briefly in this chapter.

In subsequent chapters, the main experimental results of this thesis work have been described. In Chapter-3 we explored transition metal (TM) doped ZnO based dilute magnetic semiconductor. This chapter is divided in to two subsections. The first system which we have studied is Fe doped ZnO nanocrystals (NCs) with different doping concentration of Fe. The X-ray diffraction data with Rietveld refinement, High resolution TEM (HRTEM), and micro-Raman analysis show that Fe-doped ZnO nanoparticles have wurtzite structure as that of pure ZnO. Crystallite structure, morphology, and size have been estimated by XRD and HRTEM. XANES study clearly rules out the presence of metallic Fe clusters, FeO and Fe₂O₃ phases in the samples. However it indicates that Fe gets incorporated in the ZnO lattice as Fe³⁺ causing creation of oxygen vacancies to establish the charge balance. EXAFS results show that the reduction in oxygen coordination has taken place which manifests generation of oxygen vacancies in the samples due to Fe doping. Room temperature (weak) ferromagnetism (RTFM) is observed in the samples from M–H measurements and it is also observed that magnetization increases with increasing Fe-concentration. Thus it is believed that oxygen vacancy assisted bound magnetic polarons (BMPs) and the extrinsic grain boundary are responsible for the room temperature FM in this system.

Second system which has been described in this chapter is Cr doped ZnO NCs. Structural, local structural and optical properties of sol–gel derived Cr doped ZnO nanoparticles have been thoroughly studied by several complementary techniques. The crystallite structure, size, and lattice strain have been estimated by XRD with Rietveld refinement and HRTEM. No significant change in lattice parameters a and c has been observed upon Cr doping, though crystallite size and tensile strain in the crystals change. EXAFS measurements show that Cr doping creates oxygen vacancies without causing any significant change in the host lattice structure while XANES measurements rule out the

presence of metallic Cr clusters in the samples. XANES measurements show that Cr is present in the samples in Cr^{3+} oxidation state while pre-edge peaks in XANES spectra and FTIR results show that local structure around Cr is increasingly becoming octahedral with increase in Cr doping concentration. EXAFS and PL measurements show that Cr incorporation in ZnO lattice is accompanied by creation of more and more oxygen vacancies.

A series of studies on simultaneous doping of ZnO by two cations have also been reported after it had been predicted theoretically that co-doping of group-I elements along with TM ions in ZnO stabilizes its ferromagnetic ordering and increases the Curie temperature due to an increase in carrier concentration [15,16]. Chapters (4-6) of the thesis work deals with the study of (Fe,Cu), (Co,Cu) and (Ni,Cu) co-doped ZnO NCs.

The effect of Cu doping in Co doped ZnO nanocrystals, prepared by wet chemical route at room temperature is presented in Chapter-4. X-ray diffraction, FTIR, Raman, optical absorption and EPR spectroscopy and the results were corroborated with DFT based electronic structure calculations. Magnetic measurement reveals that (Co, Cu) co-doped sample shows weak FM behaviour and its magnetisation is less than that of the only Co doped sample. Further investigations by EXAFS measurements at Co and Cu-K-edges reveal that while Co goes into the tetrahedral lattice of ZnO, local environment of Cu resembles with that of cubic CuO than tetrahedral ZnO, manifesting the presence of CuO phase in the sample. The presence of CuO is detrimental to the magnetic properties of the sample which causes the reduction in the magnetization of the (Co, Cu) co-doped sample compared to the Co doped sample.

Chapter-5 is devoted to correlation of local structure and magnetic properties of (Fe, Cu) co-doped ZnO NCs, prepared through wet chemical route using acetate-based precursors over a wide concentration range. The samples have been characterized by X-ray fluorescence

(XRF) measurements to find out the concentration of dopants while phase purity of the samples has been investigated by XRD and TEM measurements. To have further micro structural insight, the samples have subsequently been subjected to XAS measurement. XANES measurements show the presence of Cu in the samples in Cu⁺² and Fe in Fe⁺³ oxidation states. EXAFS results manifest that Cu atoms in the (Fe, Cu) co-doped ZnO samples go to Zn sites at ZnO lattice and do not form any other metallic or oxide phase. The results of the above measurements have been used to explain the magnetic properties of the samples which have further been corroborated by density functional theory (DFT) based electronic structure calculations. It has been observed that inclusion of Cu dopants in the samples in addition to Fe increases anti-ferromagnetic (AFM) correlation among the transition metal ions and thus decreases the ferromagnetic susceptibility of the samples.

Chapter-6 deals with the structural and magnetic properties of (Ni, Cu) co-doped ZnO nanocrystals prepared through wet chemical route method. XRD measurements show that though phase purity of the ZnO samples is retained by Ni doping at 2%, Cu doping beyond 3% creates a separate CuO phase in the samples. It has also been observed that (Ni,Cu) co-doping does not introduce much deformation in the lattice though there is a shift in lower d values due to Cu inclusion followed by a decrease in crystallite size. EXAFS measurements at Zn K-edge also supports that the ZnO lattice is not too much deformed due to inclusion of Cu and Ni. XANES measurement at Ni K-edge confirms that Ni is present in the ZnO lattice is Ni⁺² oxidation states and it does not form any separate NiO phase. Cu K-edge XANES measurements however show that there is a shift in the XANES pattern from substitution Cu phase to a separate CuO phase as Cu doping concentration is increased from 1% to 5%. This manifests in the decrease in magnetization in the samples due to increase in Cu doping upto 3% observed from magnetic hysteresis measurements. Magnetic susceptibility measurement

as a function of temperature indicates an enhancement of AFM interaction in the samples with increase in Cu doping concentration upto 3%, possibly due to appearance of the CuO phase. However, it has been observed that magnetization in the sample again increases as the Cu doping concentration increases upto 5%. Thus magnetization of (Ni,Cu) co-doped ZnO system is found to be governed by two competing processes viz., decrease in magnetization due to presence of CuO phase and increase in magnetization due to interaction between the TM ions mediated by Cu doping induced free charge carriers.

Compared with 3d TMs, 4f rare earth (RE) elements have larger magnetic moments and likely to enhance the ferromagnetism (FM) in doped semiconductors [17,18]. In chapter-7 we describe the structural investigations of (Mn, Dy) co-doped ZnO nanocrystals using X-ray absorption studies, which gives useful insight into the origin of RTFM in these samples. Preliminary structural characterisations of the samples have been carried out using XRD, TEM and- (FTIR) spectroscopy. Changes in the luminescence characteristics of the samples due to rare earth doping have been investigated by PL measurement and its effect on the magnetic properties of the samples has also been studied. The local structure at the host (Zn) and dopant (Mn &Dy) sites of the samples have been thoroughly investigated by XANES and EXAFS measurements. Though TEM measurements and FTIR study show that upon rare earth doping ZnO lattice is not distorted significantly, PL measurements indicate creation of oxygen vacancies on Dy doping. Magnetic measurement shows that as doping concentration of Dy are increased, magnetic behaviour changes from weak ferromagnetic/super paramagnetic to ferromagnetic nature. EXAFS data analysis at Zn K-edge shows that the results are similar for both Mn doped and (Mn, Dy) co-doped samples corroborating the above results that Dy doping has not caused any additional changes around Zn sites. However, EXAFS results at Mn K-edge on the Mn doped and (Mn, Dy) co-doped samples

show two striking dissimilarities, viz, in case of co-doped samples, the second shell Mn-Mn peak is significantly reduced due to the disorder introduced by doping of Dy atoms and in only Mn doped samples Mn is going to the ZnO lattice is Mn^{+2} oxidation state while in case of (Mn,Dy) co-doped samples, Mn is going into the lattice in Mn^{+3} oxidation state. Dy L_3 -edge results also show that Dy is going to the ZnO lattice as Dy^{+3} and significant oxygen vacancies are created near Dy sites to compensate for the charge neutrality at Zn^{+2} sites, a result also corroborated by PL measurements. Thus, the FM observed in the Dy doped samples can be attributed to the oxygen vacancy mediated exchange interaction between the Dy^{+3} ions or in other words due to formation of bound magnetic polarons or BMP's.

Chapter-8 is dedicated to describe the development of grazing incidence EXAFS (GIXAFS) measurement facility at the Energy Scanning EXAFS beamline at Indus-2 SRS, RRCAT, Indore and the XAS measurements carried out using this facility. In this GIXAFS experimental setup, a 2-Circle goniometer with a 5-axis sample stage was used to orient the sample, where the sample was kept at the centre of the goniometer and two detectors have been used for simultaneous fluorescence and reflectance measurements on the samples. This chapter also describes the experimental work carried out by using the above facility in characterisation of Co/Ti and Ni/Ti magnetic multilayers. By theoretically simulating the behavior of the electromagnetic X-ray radiation inside the multilayer samples, three grazing angles of incidences have been found out to probe the local structure of Ni atoms at three different regions inside a 5bi-layer Ni (60\AA)/Ti(60\AA) multilayer structure, viz., within Ti layer, at Ni/Ti interface and within Ni layer . While the depth dependent XANES measurements show the metallic character of Ni in all the three regions of Ni/Ti multilayer, EXAFS results elucidate how the local coordination of Ni atoms changes as we move from Ti bulk layer, Ni/Ti interface and Ni bulk layer. Similar results have been obtained for Co/Ti

multilayers also. Thus it has been demonstrated that depth dependent XAS studies of thin films and multilayers can be carried out successfully in the above set up.

Finally in Chapter-9 the conclusions obtained from each study performed under this thesis work are summarized and future directions of the works have been mentioned.

References:

1. T. Dietl, H. Ohno, F. Matsukura, J. Cibert, D. Ferrand, *Science* 287, (2000) 1019.
2. N. Lathiotakis et al, *Phys. Rev. B* 78, (2008) 193311.
3. J. Coey et al, *J. Phys. D: Appl. Phys.* 41, (2008) 134012.
4. D. Wang, Z. Q. Chen, D. D. Wang, J. Gong, C. Y. Cao, Z. Tang, L. R. Huang, *Journal of Magnetism and Magnetic Materials* 322, (2010) 3642-3647.
5. X. Z. Li, J. Zhang, D. J. Sellmyer, *Solid State Communications* 141 (2007) 398-401.
6. W. Yan, Z. Sun, Q. Liu, Z. Li, Z. Pan, J. Wang, S. Weia, D. Wang, Y. Zhou, X. Zhang, *Appl. Phys. Lett.* 91 (2007) 062113.
7. Ansari S A, *Curr Nanosci* 8 (2012) 581.
8. Safa S, J. *Adv. Mater Process* 2 (2014) 19.
9. Wu C, Shen L, Zhang Y C, and Huan Q, *Mater Lett* 65 (2011) 179.
10. A. Biswas, A. Porwal, Debarati Bhattacharya, C.L. Prajapat, Arnab Ghosh, Mangla Nand, C. Nayak, S. Rai, S.N. Jha, M.R. Singh, D. Bhattacharyya, S. Basu, N.K. Sahoo. *Applied Surface Science* 416 (2017) 168–177.
11. Maidul Haque, A. Biswas, Debarati Bhattacharyya, R.B. Tokas, D. Bhattacharyya and N.K. Shao, *J. Appl. Phys.* 114 (2013) 103508.
12. S Basu, C Nayak, A K Yadav, A Agrawal, A K Poswal, D Bhattacharyya, S N Jha and N K Sahoo, *Journal of Physics: Conference Series* **493** (2014) 012032.

13. D. Bhattacharyya, A.K. Poswal, S.N. Jha, Sangeeta and S.C. Sabharwal, Nuclear Instruments Method. in Phys. Res. **A 609** (2009) 286.
14. M. Newville, B.Ravel, D. Haskel, J.J. Rehr, E.A. Stern and Y. Yacoby, Physica **B 154** (1995) 208.
15. L. Petit, T.C. Schulthess, A. Svane, Z. Szotek, W.M. Temmemman, A. Janotti, Phys. Rev. B **73** (2006) 045107.
16. G.Q. Pei, C.T. Xia, B. Wu, T. Wang, L.L. Zhang, Y.J. Dongand, J. Xu, Comp. Mater. Sci. **43** (2008) 489.
17. G. Vijayaprasath, R. Murugan, T. Mahalingam, Y. Hayakawa, G. Ravi, Ceram. Int. **41** (2015) 10607.
18. G. Vijayaprasath, R. Murugan, T. Mahalingam, Y. Hayakawa, G. Ravi, J. Alloy. Compd. **649** (2015) 275.

List of Figures

	Page No.
Figure 1.1: Schematic of the bound magnetic polaron model.	31
Figure 2.1: Schematic of R.F. Magnetron sputtering system.	40
Figure 2.2: Variation of X-ray absorption cross section with incident photon energy.	42
Figure 2.3: A typical X-ray absorption spectrum.	44
Figure 2.4: Typical characteristic of photoelectron mean free path vs. wave number.	49
Figure 2.5: Schematic layout of the Indus synchrotron complex (left panel) and photograph of a part of Indus-2 Synchrotron Source (2.5 GeV, 200 mA) at Raja Ramanna Centre for Advanced Technology (RRCAT), Indore, India.	51
Figure 2.6: Schematic layout of Scanning EXAFS Beamline BL-09.	53
Figure 2.7: Photograph of (a) optics hutch and (b) experimental station of the Energy Scanning EXAFS Beamline BL-09.	53
Figure 2.8: Experimental set-up for fluorescence mode of XAFS measurement.	54
Figure 2.9: Schematic layout of the GIXAFS set up at the Energy Scanning EXAFS Beamline (BL-09).	55
Figure 2.10: Photograph of the GIXAFS set up at the Energy Scanning EXAFS Beamline BL-09.	55
Figure 2.11: Screenshot of the ATHENA software code.	60
Figure 2.12: Screenshot of the ARTEMIS software code.	62
Figure 2.13: Photograph of X-ray diffractometer (Model: Miniflex-II, Rigaku, Japan)	66
Figure 2.14: Photograph of the Transmission Electron Microscope (Technai G2 S-Twin (FEI, Netherlands) used in this thesis work.	68
Figure 2.15: Photograph of Fourier transform infrared (FTIR) spectrometer (NICOLET 6700) used in this thesis work.	69
Figure 2.16: Photograph of Edinburgh spectroscopic Photoluminescence instrument.	71
Figure 2.17: Photograph of SQUID-vibrating sample magnetometer.	72

Figure 3.1:	Rietveld refinement profiles of X-ray diffraction data of the $\text{Zn}_{1-x}\text{Fe}_x\text{O}$ ($0 \leq x \leq 0.06$) samples. The circle represents the observed data (Obs) while solid line through the circles is the calculated profile (Calc), vertical ticks below curves represent allowed Bragg-reflections for the wurtzite phase. The difference pattern of the observed data and calculated profile (Obs–Calc) is given below the vertical ticks.	77
Figure 3.2:	Variation of lattice parameter ('a' and 'c') with Fe-concentration (x) calculated from Rietveld refinement. The inset (i) shows the variation of the unit cell volume and inset (ii) shows the variation of the degree of distortion (R).	78
Figure 3.3a:	Variation of average basal bond angles ($\text{O}_b\text{-Zn-O}_b$) and average base-apex angles ($\text{O}_b\text{-Zn-O}_a$) with Fe-concentration (x).	79
Figure 3.3b:	Variation of bond length Zn-O_a and Zn-O_b with Fe-concentration (x). Inset of (b) shows the variations of inter planer spacing.	79
Figure 3.4:	$(d_{hkl}\beta\cos\theta/\lambda)^2$ vs. $(d_{hkl}^2\beta\cos\theta/\lambda^2)$ plot of the ZnO:Fe samples to estimate crystallite size (D) and average strain (ϵ).	82
Figure 3.5:	Variation of average crystallite size with Fe-concentration (x) estimated from size-strain plot. The inset figure shows the variation of strain estimated from size-strain plot.	83
Figure 3.6:	Low magnification TEM (a), HRTEM (b), and SAED (c) images of ZnO nanocrystals and low magnification TEM (d), HRTEM (e), and SAED (f) images of $\text{Zn}_{0.99}\text{Fe}_{0.02}\text{O}$ nanocrystals.	85
Figure 3.7:	Normalized experimental EXAFS ($\mu(E)$ vs E) for undoped and Fe doped ZnO nanocrystals at Zn K-edge.	86
Figure 3.8:	Fourier transformed EXAFS($\chi(R)$ vs. R) for undoped and Fe doped ZnO nanocrystals at ZnK-edge.	87
Figure 3.9:	Variation of bond lengths of Zn-O shells and Zn-Zn shells with change in doping concentration.	88
Figure 3.10:	Variation of total coordination number of Zn-O shells and Zn-Zn shells with change in doping concentration.	88
Figure 3.11:	Variation of Debye-Waller factor of Zn-O shells and Zn-Zn shells with change in doping concentration.	89

Figure 3.12:	XANES spectrum of 6% Fe doped ZnO nanocrystal along with that of Fe metal foil and standard Fe ₂ O ₃ and FeO samples.	89
Figure 3.13:	Room-temperature Raman spectra of Zn _{1-x} Fe _x O (0 ≤ x ≤ 0.06) nanoparticles. Inset of figure shows the variation of the (E ₂ H) peak with Fe-concentration (x) with respect to its pure ZnO value (curve-I) and the variation of the 2(E ₂ H–E ₂ L) peak value with x with respect to its corresponding (E ₂ H–E ₂ L) peak value (curve-II).	90
Figure 3.14:	Room temperature M-H curves of the Fe doped ZnO samples. Inset shows the enlarged view of Fe ₀ (ZnO) and Fe ₂ sample.	94
Figure 3.15:	Rietveld refinement profiles of X-ray diffraction data of the Zn _{1-x} Cr _x O (0 ≤ x ≤ 0.06) samples. The circle represents the observed data (Obs) while solid line through the circles is the calculated profile (Calc), vertical ticks below curves represent allowed Bragg-reflections for the wurtzite phase. The difference pattern of the observed data and calculated profile (Obs–Calc) is given below the vertical ticks.	99
Figure 3.16:	Variation of lattice parameter ('a' and 'c') with Cr-concentration (x) calculated from Rietveld refinement. The inset plot shows the variation of the unit cell volume.	101
Figure 3.17:	$dhkl\beta\cos\theta/\lambda)^2$ vs. $(dhkl^2\beta\cos\theta/\lambda^2)$ plot of the samples to estimate crystallite size(D) and average strain (ε).	102
Figure 3.18:	Variation of average crystallite size with Cr-concentration (x) estimated from size–strain plot and Scherrer's equation.	102
Figure 3.19:	Low magnification TEM (a) SAED (b) and HRTEM (c,d), images of Zn _{0.99} Cr _{0.01} O nanocrystals.	103
Figure 3.20:	Normalized experimental EXAFS ($\mu(E)$ vs E) for undoped and Cr doped ZnO nanocrystals at Zn K-edge.	105
Figure 3.21:	Normalized experimental EXAFS ($\mu(E)$ vs E) for undoped and Cr doped ZnO nanocrystals at Cr K-edge	105
Figure 3.22:	The experimental $\chi(R)$ versus R plots and the theoretical fits of undoped and Cr -doped ZnO samples measured at Zn K-edge.	105
Figure 3.23a:	The experimental $\chi(R)$ versus R plots and the theoretical fits of Cr doped ZnO samples measured at Cr K-edge where the fitting is done assuming ZnO structure with Cr at Zn sites.	107

Figure 3.23b:	The experimental $\chi(R)$ versus R plots and the theoretical fits of Cr doped ZnO samples measured at Cr K-edge where fitting has been done assuming Cr_2O_3 structure.	107
Figure 3.24:	XANES spectrum of Cr-doped ZnO nanocrystals measured at Cr K-edge.	110
Figure 3.25:	Room-temperature Raman spectra of $\text{Zn}_{1-x}\text{Cr}_x\text{O}$ ($0 \leq x \leq 0.06$) respectively.	113
Figure 3.26:	FTIR spectra of $\text{Zn}_{1-x}\text{Cr}_x\text{O}$ ($0 \leq x \leq 0.06$) samples showing different modes.	115
Figure 3.27:	Absorption spectra of $\text{Zn}_{1-x}\text{Cr}_x\text{O}$ samples. Inset shows variation of the optical band gap (E_g) with the Cr-concentration (x).	116
Figure 3.28:	Room temperature PL spectra of the $\text{Zn}_{1-x}\text{Cr}_x\text{O}$ ($0 \leq x \leq 0.06$) samples	118
Figure 4.1:	X-ray diffraction pattern with Rietveld refinement of (a) Co doped ZnO NC's (i) as-prepared ZnO, (ii) doped with 1% Co, (iii) doped with 2% Co (iv) doped with 3% Co and (v) doped with 5% Co. (b) (Co,Cu) co-doped ZnO NCs (i) as-prepared ZnO, (ii) co-doped with (1%Co, 1%Cu), (iii) co-doped with (1.5% Co, 1.5% Cu) and (iv) co-doped with (2.5% Co, 2.5% Cu).	121
Figure 4.2:	(a) TEM micrograph, (b) histograms and (c) diffraction pattern of 2.5% Co doped ZnO NCs. (d) TEM micrograph, (e) histograms and (f) diffraction pattern of (2.5% Co, 2.5% Cu) co-doped ZnO NCs.	125
Figure 4.3:	FTIR spectra of (a) Co doped ZnO NCs and (b) (Co, Cu) co-doped ZnO NCs.	126
Figure 4.4:	Raman spectra of Co doped, Cu doped and (Co, Cu) co-doped ZnO NCs.	128
Figure 4.5:	Optical absorption spectra of (a) Co doped ZnO NCs and (b) (Co, Cu) co-doped NCs.	130
Figure 4.6:	EPR spectra of (Co,Cu) co-doped ZnO NCs.	130
Figure 4.7:	Plot of formation energy vs. the on-site Coulomb interaction (U) for both Co doped and (Co, Cu) co-doped ZnO systems.	131
Figure 4.8:	(a) M vs. H curve for a 2.5% Co doped, 2.5% Cu doped and (2.5%Co; 2.5%Cu) co-doped ZnO NCs. (b) Temperature dependence of magnetic susceptibilities χ and inverse susceptibilities χ^{-1} (inset) measured in a dc field $H=100\text{Oe}$ for the above samples.	134

Figure 4.9:	(a) Normalized experimental EXAFS ($\mu(E)$ versus E) for 2.5% Co doped, 5% Co doped, 2.5% Cu doped and (2.5% Co; 2.5% Cu) co-doped ZnO NCs measured at Zn K-edge (b) k -weighed $\chi(k)$ function of the Zn K-edge for the undoped and doped samples (c) The experimental $\chi(R)$ versus R spectra and the theoretical fits of undoped and doped ZnO samples at Zn K-edge.	136
Figure 4.10:	(a) Normalized experimental EXAFS ($\mu(E)$ vs. E) for 2.5%Co, 5% Co doped and (2.5%Co;2.5%Cu) co-doped ZnO NCs measured at Co K-edge.(b) k -weighed $\chi(k)$ function of the Co K-edge for 2.5% Co, 5% Co doped and (2.5% Co; 2.5% Cu) co-doped ZnO NCs measured at Co K-edge. (c) The experimental $\chi(R)$ vs. R spectra and the theoretical fits for the Co doped and (Co,Cu) co-doped ZnO NCs at CoK-edge where the fitting has been carried out with CoO structure. (d) The experimental $\chi(R)$ vs. R spectra and the theoretical fits for the Co doped and (Co,Cu) co-doped ZnO NCs at Co K-edge where the fitting has been carried out with ZnO structure with Zn atoms replaced by Co atoms.	140
Figure 4.11:	(a) Normalized experimental EXAFS ($\mu(E)$ vs. E) for 2.5% Cu doped and (2.5%Co;2.5%Cu) co-doped ZnO NCs measured at Cu K-edge.(b) k -weighed $\chi(k)$ function of the Cu K-edge for the 2.5% Cu and (2.5% Co; 2.5% Cu) co-doped ZnO NCs. (c) The experimental $\chi(R)$ vs. R spectra for the 2.5%Cu and (2.5%Co;2.5%Cu) co-doped ZnO NCs at Cu K-edge where the fitting has been carried out with CuO structure.(d)The experimental $\chi(R)$ vs. R spectra for the 2.5%Cu doped ZnO NCs at Cu-K-edge where the fitting has been carried out with ZnO structure with Zn atoms replaced by Cu atoms.	143
Figure 5.1	TXRF spectrum of a representative (Fe, Cu) co-doped ZnO sample. Inset shows relative concentration of the dopants in few samples	150
Figure 5.2	X-ray diffraction pattern of few representatives (Fe, Cu) co-doped ZnO samples.	151
Figure 5.3:	(a) Dark field image (b) Diffraction pattern and (c) Particle size histogram of undoped ZnO nanoparticles.	152

Figure 5.4:	(a) Bright field image and (b) Particle size histogram of 2.5% Fe doped ZnO nanoparticles.	153
Figure 5.5:	(a) Bright field image and (b) Particle size histogram of (2.5%Fe, 3%Cu) co-doped ZnO nanoparticles.	153
Figure 5.6:	Normalized XANES spectra of few representative (Fe,Cu) co-doped ZnO samples measured at (a) Fe K-edge (inset shows the pre-edge portions in expanded scale) and (b) Cu K-edge along with standards.	154
Figure 5.7:	(a) M vs H curve for a 5% Fe doped, (5% Fe, 2% Cu) co-doped and (5% Fe; 5% Cu) co-doped ZnO NCs measured at 300 K, (b) measured at 5 K (c) Temperature dependence of magnetic susceptibilities χ and inverse susceptibilities χ^{-1} (inset) for few Fe doped and (Fe, Cu) co-doped samples measured at 100 Oe.	157
Figure 5.8:	Normalized experimental EXAFS ($\mu(E)$ versus E) spectra of undoped, Fe doped and few (Fe,Cu) co-doped ZnO samples measured at (a) Zn K-edge, (b) Fe K-edge and (c) Cu K-edge	158
Figure 5.9:	(a) Experimental $\chi^{(R)}$ versus R plots alongwith best fit theoretical plots for undoped, Fe doped and few representative (Fe,Cu) co-doped ZnO samples measured at Zn K-edge. (b) Experimental $\chi^{(R)}$ versus R plots of few representative (Fe, Cu) co-doped ZnO samples measured at Cu K-edge alongwith that of CuO standard measured at Cu K-edge, undoped ZnO sample measured at Zn K edge and (10%Fe, 3%Cu) co-doped sample measured at Fe K-edge.	160
Figure 5.10:	Plot of formation energy versus the on-site Coulomb interaction (U) for both Fe doped and (Fe, Cu) co-doped ZnO systems in various configurations.	161
Figure 6.1:	X-ray diffraction pattern of (Ni, Cu)	165
Figure 6.2:	(a) TEM micrograph and (b) SAED pattern of (2% Ni, 1%Cu) co-doped ZnO nanocrystals.	167
Figure 6.3a:	M-H plots for (Ni,Cu) co-doped ZnO nanocrystals.	168
Figure 6.3b:	M-T plots for (Ni, Cu) co-doped ZnO nanocrystals.	168
Figure 6.4, 6.5, 6.6:	Normalized experimental EXAFS ($\mu(E)$ versus E) for (Ni, Cu) co-doped ZnO nanocrystals measured at Zn, Ni and Cu K-edges.	171

Figure 6.7:	Experimental $\chi(R)$ versus R data (scatter points) and best fit theoretical plots (solid line) of 2% Ni doped, (2% Ni, 1% Cu), (2% Ni, 2% Cu), (2% Ni, 3% Cu) & (2% Ni, 5% Cu) co-doped ZnO nanocrystals at Zn K-edge	172
Figure 6.8:	XANES plots for Ni doped and (Ni, Cu) co-doped ZnO samples at Ni K-edge.	173
Figure 6.9:	Experimental $\chi(R)$ versus R data (scatter points) and best fit theoretical plots (solid line) of (2%Ni, 1%Cu), (2%Ni, 2%Cu), (2%Ni, 3%Cu) and (2%Ni, 5%Cu) co-doped ZnO nanocrystals at Ni K-edge where fitting has been carried out assuming wurtzite ZnO structure with Zn atoms appropriately replaced by Ni atoms.	174
Figure 6.10:	Experimental $\chi(R)$ versus R data and best fit theoretical plots of (2% Ni, 2% Cu) co-doped ZnO nanocrystals at Ni-K-edge where fitting has been carried out by assuming NiO structures at Ni-sites	175
Figure 6.11:	XANES plots for (Ni, Cu) co-doped ZnO samples at Cu K-edge along with that of standard CuO and Cu metal foil.	177
Figure 6.12:	Plot of formation energy versus the on-site Coulomb interaction (U) for Ni doped and (Ni, Cu) co-doped ZnO systems in various configurations.	179
Figure 7.1:	X-ray diffraction pattern of (Mn, Dy) co-doped ZnO	184
Figure 7.2:	Low magnification TEM (a), SAED (b), and HRTEM (c) images of ZnO nanocrystals and low magnification TEM (d), SAED (e), and HRTEM (f) images of (2% Mn, 2% Dy) co-doped ZnO nanocrystals	185
Figure 7.3:	FTIR spectra of (Mn,Dy) co-doped ZnO nanocrystals.	187
Figure 7.4:	Photoluminescence spectra of (Mn,Dy) co-doped ZnO nanocrystals.	188
Figure 7.5:	M-H plots for (Mn, Dy) co-doped ZnO nanocrystals.	189
Figure 7.6:	(a) Normalized experimental EXAFS ($\mu(E)$ versus E) for (Mn, Dy) co-doped ZnO nanocrystals measured at Zn K-edge. (b) k^2 -weighed $\chi(k)$ function of the Zn K-edge for the (Mn,Dy) co-doped ZnO nanocrystals measured at Zn K-edge. (c) Experimental $\chi(R)$ versus R data (scatter points) and best fit theoretical plots (solid line) of undoped, (2% Mn, 2% Dy), (2% Mn, 4% Dy) & (2% Mn, 6% Dy) co-doped ZnO	191

nanocrystals at Zn K-edge. (d) Experimental $\chi(R)$ versus R data (scatter points) and best fit theoretical plots (solid line) of Mn doped ZnO samples at Zn K-edge.

- Figure 7.7 (a): Normalized experimental EXAFS ($\mu(E)$ versus E) for (Mn, Dy) co-doped ZnO nanocrystals measured at Mn K-edge. (b) k^2 -weighed $\chi(k)$ function of the Mn K-edge for the (Mn, Dy) co-doped ZnO nanocrystals. (c) Experimental $\chi(R)$ versus R data (scatter points) and best fit theoretical plots (solid line) of (2% Mn, 2% Dy), (2% Mn, 4% Dy) & (2% Mn, 6% Dy) co-doped ZnO samples at Mn K-edge (fitting have been carried out assuming Mn at Zn sites in wurtzite ZnO structure). (d) Experimental $\chi(R)$ versus R data (scatter points) and best fit theoretical plots (solid line) of (2% Mn, 2% Dy), (2% Mn, 4% Dy) & (2% Mn, 6% Dy) co-doped ZnO samples at Mn K-edge (fitting has been carried out by assuming Mn₂O₃ structure around Mn sites). 195
- Figure 7.8 (a) Experimental $c(R)$ versus R data (scatter points) and best fit theoretical plots (solid line) of Mn doped ZnO samples at Mn K-edge (fitting has been done assuming Mn at Zn sites in wurtzite ZnO structure). (b) Experimental $c(R)$ versus R data (scatter points) and best fit theoretical plots (solid line) of Mn doped ZnO samples at Mn K-edge (fitting has been carried out by assuming Mn₂O₃ structure around Mn sites). 198
- Figure 7.9 XANES plots for (Mn,Dy) co-doped ZnO samples at Mn K-edge alongwith that of standard MnO₂, Mn₂O₃ powders and Mn foil. 200
- Figure 7.10 (a) Normalized experimental EXAFS ($\mu(E)$ versus E) for (2% Mn, 2% Dy), (2% Mn, 4%Dy) & (2% Mn, 6% Dy) co-doped ZnO samples measured at Dy L3-edge. (b) k^2 -weighed $\chi(k)$ function of (2% Mn, 2% Dy), (2% Mn, 4% Dy) & (2% Mn, 6% Dy) co-doped ZnO samples measured at the Dy L3-edge. (c) Experimental $\chi(R)$ versus R data (scatter points) and best fit theoretical plots (solid line) of (2% Mn, 4% Dy) co-doped ZnO samples measured at Dy L3-edge (fitting has been carried out by assuming Dy at Zn sites in wurtzite ZnO structure). (d) Experimental $\chi(R)$ versus R data (scatter points) and best fit theoretical 201

plots (solid line) of (2% Mn, 2% Dy), (2% Mn, 4% Dy) & (2% Mn, 6% Dy) co-doped ZnO samples measured at Dy L₃-edge (fitting has been carried out by assuming Dy₂O₃ structure around Dy sites).

Figure 7.11	XANES plots for (Mn,Dy) co-doped ZnO samples at Dy L ₃ edge alongwith that of standard Dy ₂ O ₃ powder.	203
Figure 8.1	Variation of electric field intensity inside multilayer structure with grazing angle of incidences	209
Figure 8.2	(a) Normalised XANES spectra of Ni-Ti multilayer at 0.44, 0.48 and 0.57° grazing angles of incidence along with that of pure Ni foil measured at Ni K edge. (b) Fourier transformed GIEXAFS spectra (scatter points) of Ni/Ti multilayer at the three different grazing angles of incidence along with the Ni-foil at Ni K-edge and corresponding theoretical fits (solid lines).	210

List of Tables

		Page No
Table 3.1	Values of lattice parameters, bond lengths and bond angles.	80
Table 3.2	Crystallite size and average strain estimated from Williamson–Hall and Size Strain plot.	83
Table 3.3	Observed Raman peaks of Zn _{1-x} Fe _x O (0 ≤ x ≤ 0.06) nanoparticles and their symmetry assignments.	93
Table 3.4	Values of lattice parameters, bond lengths and bond angles calculated following ref. 35.	102
Table 3.5	Best fit results of the EXAFS measurements on Cr doped ZnO samples at Zn K edge.	106
Table 3.6	Fit parameters by assuming wurtzite ZnO structure with Cr at Zn sites. (Typical uncertainty for CN ~±10%; R ~±0.02 Å ; σ ² ~±0.001 Å ²).	108
Table 3.7	Fit parameters by assuming Cr ₂ O ₃ structure. (Typical uncertainty for CN ~±10%; R ~±0.02 Å ; σ ² ~±0.001 Å ²).	108
Table 4.1	Rietveld refined XRD cell parameters of NCs.	124
Table 4.2	Particle size and micro-strains obtained from Rietveld refined XRD of the NCs.	124
Table 4.3	Results of fitting of Fourier transformed EXAFS data at Zn K-edge.	138
Table 4.4	EXAFS fitted with CoO structure at Co K-edge.	145
Table 4.5	EXAFS data fitted with ZnO structure at Co K-edge.	146
Table 4.6	XAFS fitted with CuO structure at Cu K-edge.	147
Table 6.1	Particle sizes of the (Ni, Cu) co-doped ZnO nanocrystals determined from XRD patterns.	167
Table 6.2	Best-fit parameters of Zn K-edge EXAFS data for (Ni, Cu) co-doped ZnO samples where fitting has been carried out assuming wurtzite ZnO structure.	173
Table 6.3	Best-fit parameters of Ni K-edge EXAFS data for (Ni, Cu) co-doped ZnO samples where fitting has been carried out assuming wurtzite	176

	ZnO structure with Zn atoms appropriately replaced by Ni atoms.	
Table 6.4	Best-fit parameters of Ni K-edge EXAFS data for (Ni,Cu) co-doped ZnO samples where fitting has been carried out assuming NiO structure around Ni sites.	177
Table 7.1	Values of particle size, lattice parameters and interplanar spacing for different plans of the (Mn,Dy) co-doped samples:	185
Table 7.2	Fit parameters at Zn K-edge by assuming wurtzite ZnO structure for (Mn,Dy) co-doped ZnO samples:	193
Table 7.3	Fit parameters at Zn K-edge by assuming wurtzite ZnO structure for Mn doped ZnO samples:	194
Table 7.4	Fit parameters at Mn K-edge by assuming Mn at Zn sites in wurtzite ZnO structure for (Mn,Dy) co-doped ZnO samples	197
Table 7.5	Fit parameters at Mn K-edge by assuming Mn ₂ O ₃ structure at Mn site for (Mn, Dy) co-doped ZnO samples.	198
Table 7.6	Fit parameters for Mn K-edge data assuming Mn ₂ O ₃ structure at Mn site	201
Table 7.7	Fit parameters for Mn K-edge data assuming Mn ₂ O ₃ structure at Mn site.	201
Table 7.8	Fit parameters for Dy L3-edge data by assuming Dy ₂ O ₃ structure at Dy site for (Mn, Dy) co-doped ZnO samples	204
Table 8.1	Grazing angles of incidences used for probing different portions of the 10 bi-layer Ni (60Å)/Ti(60Å) multilayer.	211
Table 8.2	Best fit parameters obtained by fitting the FT- EXAFS	213

Chapter-1

Introduction

X-ray absorption fine structure (XAFS) deals with study of the oscillations that appear in the X-ray absorption spectrum (XAS) of an atom at energies near and above its core-level binding energies which directly gives information of the chemical and physical state of that particular atomic species in a material. The X-ray absorption spectrum is typically divided into two regimes: X-ray absorption near-edge structure (XANES) which gives information about the external perturbations in the valence states to which electrons make transitions from core levels upon absorption of X-ray photon energy and the second part is extended X-ray absorption fine-structure (EXAFS) which is characterized by the presence of fine structure oscillations arising due to back scattering of outgoing photo-electron by neighboring atoms and can give precise information regarding the short-range order and local structure around the particular atomic species in the material. Though the two have the same physical origin, this distinction is convenient for the interpretation. XANES is strongly sensitive to formal oxidation state and coordination chemistry (e.g., octahedral, tetrahedral coordination) of the absorbing atom, while EXAFS is used to determine the distances, coordination number, and species of the neighbors of the absorbing atom. XANES and EXAFS techniques, are element specific techniques which can be applied not only to crystals, but also to materials that possess little or no long-range translational order: amorphous systems, glasses, disordered films, membranes, solutions, liquids, metalloproteins and also for nanostructured materials and thin films. Thus X-ray absorption fine structure (XAFS) spectroscopy is a unique tool for studying, at the atomic and molecular scale, the local structure around selected elements that are contained within a material. For this reason, XAFS is a very

important probe of materials, since knowledge of local atomic structure, i.e., the species of atoms present and their locations, is essential to progress in many scientific fields: physics, chemistry, biology, biophysics, medicine, engineering, environmental science, materials science, and geology. However, X-ray absorption measurements require an intense and energy-tuneable X-ray source. X-rays generated from the conventional lab sources offers a very weak tuneable X-ray continuum and this had been a serious limitation in obtaining EXAFS spectrum of reasonable quality till a long time. The availability of modern bright Synchrotron radiation sources since 1970's, has removed this experimental difficulty and since then EXAFS has emerged out to be one of the most powerful tools for local structure determination. The specifications of synchrotron sources, beamline optics and experimental station define the energy ranges, beam sizes, and intensities available, and dictate the practical experimental limits on the XAS measurements that can be performed.

XAFS is not really a surface sensitive technique since X-rays can penetrate and also come out of the material from reasonable depth; however, by careful preparation of the samples and careful selection of the grazing angle of incidence of the incident synchrotron beam we can probe different depth of a thin film multilayer structure. By simulating the electric field pattern of the standing wave generated inside a multilayer structure, when electromagnetic X-ray radiation is made incident on it, we can estimate the grazing angles of incidence required to probe a particular depth in a multilayer structure.

Thus, to explore the versatility of XAFS technique the present thesis is divided in to two parts: the first and major part is dedicated to the local structure investigation of transition metal (TM) doped dilute magnetic semiconductors particularly ZnO nanocrystals (NCs), while the relatively shorter second part deals with Grazing incidence EXAFS (GIXAFS) study of thin film magnetic multilayers.

Nowadays, most widely used technologies are led by integrated circuits (ICs) and data storage devices. Integrated circuits utilize the charge of electrons and holes in order to perform their specific functionalities and ignore the spin of electrons. However, their memory elements are volatile which means that when the power is switched-off the stored information is lost. In the case of magnetic data storage technology, the spin of electron is the key parameter and magnetic data storage devices are non-volatile because of the natural remanence characteristic of ferromagnetic materials. Now the idea is to make a device which utilizes both the charge and spin of the electrons, which makes the device smaller as well as faster. Spintronics which is the short name for spin based electronics is a new field of research exploiting the influence of electron spin on the electrical conduction (or current is spin dependent). The basic idea is to combine the characteristics of existing magnetic devices with semiconductor devices in order to realize a new generation of devices that are much smaller, more energy efficient, non-volatile, and much faster than presently available [1-9]. Concept of spintronics is derived from the independent discovery of giant magnetic resonance (GMR) by Albert Fert [10] and Peter Grunberg [11] and the first generation of spintronic devices were developed by the discovery of giant magnetoresistance in $(\text{Fe/Cr})^n$ multilayers. Next generation was later boosted by creation and manipulation of spin-polarized electrons from a ferromagnetic metal (FM) in a host metal/semiconductor [1-3,12-14].. However, it has been shown that it is difficult to preserve the electron spin across the interface of these types of heterostructures mainly due to large mismatch in electrical conductivity between the two materials [15]. Since late 1980s, it has been noticed that in many semiconductor crystals, substitution of a transition metal element for a host element adds local magnetic moment to the system's low-energy degrees of freedom [16,17]. After this the concept of dilute magnetic semiconductor or DMS emerged which refers to the fact that some fraction of atoms in a non-magnetic semiconductor is replaced by magnetic ions.

Various semiconductor host materials have been proposed by different research groups to test their magnetic properties where the most attention has been paid to (Ga, Mn) As [18-41] and (In, Mn) As [42-48] systems. However, due to their reported highest Curie temperatures which are around 170 K for (Ga, Mn) As [49-51] and 35 K for (In, Mn) As [51, 52], they could not be considered for most of the practical applications. The main challenge for practical applications of DMSs is to achieve Curie temperature above room temperature [4]. Dietl et. al. [53] proposed by theoretical calculations that Mn-doped ZnO would exhibit ferromagnetism above room temperature. Sato *et al.* have subsequently also investigated ferromagnetism of ZnO-based DMS by *ab initio* electronic structure calculations based on the local spin density approximation and they have also reported ferromagnetic ordering of other 3d transition metal (TM) ions in ZnO [54,55]. These theoretical predictions initiated a number of experimental studies of TM-doped ZnO in various forms such as bulk, nanoparticles, thin films etc. [1-3, 56-67]. Extensive studies have been carried out in this area in last one decade or so and room temperature ferromagnetism has been observed in several types of TM (Fe, Co, Ni, Cu) doped ZnO nanoparticles [68-73]. However, few authors have reported paramagnetic behaviour of TM doped ZnO nanoparticles with antiferromagnetic coupling also [74-76]. Besides ZnO, TM doping has been done in other oxide materials viz., TiO₂, CdO, In₂O₃, SnO₂ etc. however, most of them do not show any ferromagnetic behavior [53,77-79]. Several studies have also been performed with simultaneous or co-doping of ZnO nanoparticles by two TM ions. For example, Jefferson et. al. [80] have found that co-doping of (Fe,Ni) into ZnO nanoparticles exhibit higher magnetization than that of Fe doped ZnO and Ni doped ZnO nanoparticles. They have suggested that the observed ferromagnetism in (Fe, Ni) co-doped ZnO nanoparticles could be the result of exchange interaction between conductive electron with local spin polarized electron on Ni⁺² or Fe⁺² ions [81]. It has been theoretically predicted that co-doping of group-

I elements along with TM ions in ZnO stabilizes its ferromagnetic ordering and increases the Curie temperature due to an increase in carrier concentration [82-83]. Liu et.al. [84] have prepared (Co,Al) co-doped ZnO nanoparticles by sol-gel techniques and have found ferromagnetism around 360 K. Zhang et. al. [85] reported that, doping of Cu in Fe doped ZnO nanoparticles enhances the saturation magnetization. Cu plays an important role as p-type dopant in Fe doped ZnO nanoparticles which causes a systematic increase in saturation magnetization, reported by Han et. al. [86]. On the other hand Sim et. al. [87] reported that in (Fe,Cu) co-doped ZnO sample, secondary phase of ZnFe_2O_4 is the reason behind the ferromagnetic ordering at room temperature.

Recently, rare earth (RE)-doped DMS materials together with TM dopants have also been actively investigated to get benefit of higher magnetic moment of RE ions as well as stronger exchange interaction of the TM ions [88,89]. Co-doping of TM and rare earth (RE) ions simultaneously in ZnO has also been explored by several authors including one by our group also [90,91]. In TMs, the magnetization arises from partially filled 3d shells and most of the cases since total orbital magnetic moment is zero, the magnetic moment is only due to the spin component and hence total magnetic moment per atom is less. Thus, ferromagnetism observed in TM doped ZnO samples so far has never been very significant. In rare earth (RE) elements, on the other hand, magnetisation appears due to unfilled 4f orbitals leading to higher magnetic moment per atom, though since 4f electrons only interact through 5d or 6s electrons, they offer weak exchange interaction with other RE ions in contrast to TM elements where 3d electrons directly interact [92-94]. In pure form, RE elements exhibit magnetism only at low temperatures and the advantage of rare earth compounds over other magnets is that, these materials are easy to magnetise in one direction and resist magnetisation in the other direction. Recent results for Gd in GaN, indicating high magnetic

moments [95], have instigated investigations on ZnO nanocrystals doped with RE metal ions also.

1.1 Model for Magnetism in DMS:

Though a large volume of work also exists in the literature on room temperature ferromagnetism (RTFM) of TM and rare earth doped ZnO systems, however, there are wide variations in the reported papers regarding the origin of RTFM observed in the samples which has been attributed to a variety of intrinsic and extrinsic reasons by various authors and the exact mechanism is still controversial. The theoretical models that have been most commonly used to explain ferromagnetism in TM metal doped ZnO NCS based diluted magnetic semiconductors are carrier exchange interactions and Bound magnetic polarons, which are described below.

1.1 Carrier mediated exchange interactions:

Dietl et. al. [53] proposed a model called free carrier mediated exchange model and this model was based on the original model of Zener and the Ruderman-Kittel-Kasuya-Yoshida (RKKY) interaction [96, 97]. Several author have been reported the origin of RTFM from carrier mediated exchange interactions in TM doped ZnO systems [53,98]. This model explained the ferromagnetism by exchange interaction between carriers and localized spins. In case of RKKY interaction, conduction electrons close to the magnetic ion get magnetized and act as an effective field to influence the polarization of neighbouring magnetic ions, with the oscillatory polarization decaying with distance from the magnetic ion and causing indirect super exchange interaction (RKKY) between two magnetic ions on nearest or next nearest magnetic neighbours. This coupling results in a parallel (ferromagnetic) or an anti-parallel (antiferromagnetic) setting of moments dependent on separation of the interacting atoms. Thus, it is clear that this model is not suitable for low carrier concentrations and this is valid

only for materials having high electron/hole concentrations or in other words for materials with high doping concentrations.

1.1.1 The bound magnetic polaron model:

In earlier days carrier exchange interactions were used to explain RTFM in TM doped ZnO NCs [99-101]. Later on bound magnetic polaron model (BMP) has been introduced to investigate the ferromagnetic ordering of TM metal ions in DMS materials [102-105]. A bound magnetic polaron (BMP) is a collection of electrons (or holes) bound to impurity atoms through exchange interactions within an orbit. In this model, the formation of bound magnetic polaron is explained by the exchange interaction between many localized TM ion spins via much lower number of weakly localized charge carriers. Ferromagnetic exchange can be mediated by shallow donor electrons that form bound magnetic polarons (BMPs) which overlap to create a spin split impurity band. The electrons associated with particular defects remain localized in terms of hydrogenic orbits, until a critical donor concentration is reached, at which point the impurity band becomes delocalized. The donors tend to form BMPs, coupling the 3d magnetic moments of the TM dopants within their orbits. Depending upon the system, the interaction can make carrier parallel or anti parallel to the magnetic impurity. These two configurations differ in energy, and this results in a non-zero spin flip energy that is a characteristic of BMPs. The interaction of ions with carriers is same, the net energy of the system can be lowered if the ions are aligned parallel to each other. If there is sufficiently large orbital radius, overlap between hydrogenic electron and the cation within its orbit leads to FM super coupling between them, as shown in figure 1.1. Interaction between the hydrogenic electron and the cation is represented by a Heisenberg exchange Hamiltonian [106]

$$\hat{H}_{ij} = \sum_{ij} J_{ij} \hat{S}_i \hat{S}_j \quad (1.1)$$

where, S is the spin of dopant cation and s is the donor electron spin.

The Hamiltonian of a two-polaron subsystem is given by Eq. (1.1), where the donor electron spin index j takes only two values, j_1 and j_2 , corresponding to the two polarons under consideration. The hydrogenic orbital tends to spread out sufficiently to overlap with a large number of BMPs, but some isolated polarons cannot be covered and thus cannot achieve macro-FM ordering. Thus, the overlap of neighboring magnetic polarons leads to a long-range ferromagnetic state and the ferromagnetic transition occurs when the polaron size is equal to the sample size.

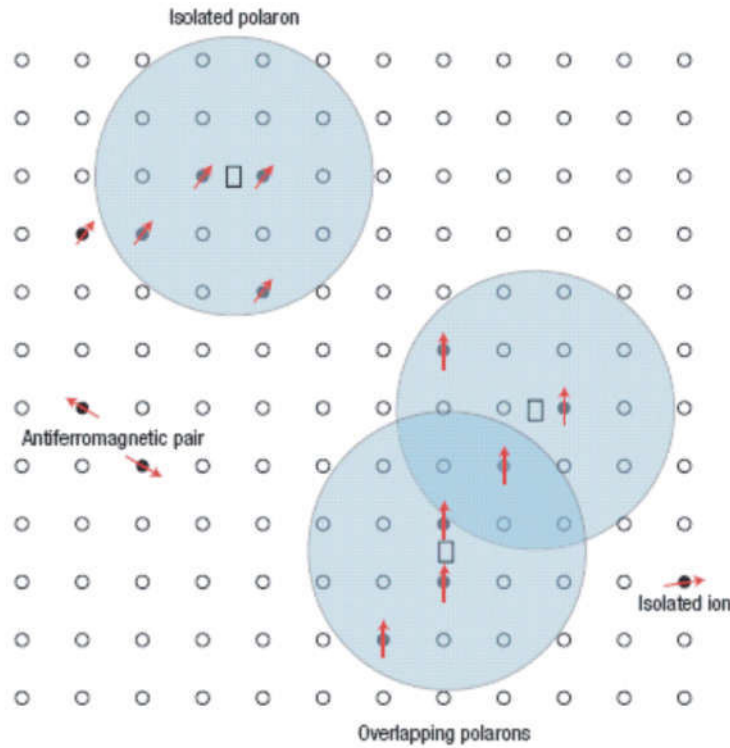


Figure 1.1: Schematic of the bound magnetic polaron model [107]

Apart from the above there are also many reports which attribute the observed ferromagnetism in dilute magnetic semiconductors to extrinsic causes viz., due to the

presence of a separate metallic cluster just a few atoms in dimension [108-110], presence of magnetic contamination [114] or secondary phases [112-117].

1.2 X-ray standing wave generation in multilayer structure:

X-ray standing wave spectroscopy has been demonstrated to be a versatile method to characterize multilayer thin films and elemental distributions in the multilayer. According to the dynamical theory of X-ray diffraction [118,119] when X-rays are Bragg reflected by a crystal a standing wave field is generated within the crystal as a result of superposition of the incident and the diffracted waves. At an angle of incidence corresponding to the rising edge of the diffraction peak the antinodal planes of the standing wave field lie between the diffracting planes. As the angle of incidence increases the antinodal planes move continuously inward onto the diffracting planes at the falling edge of the diffraction peak. X-ray fluorescence and electron emissions can be strongly modified in the angular region of Bragg reflection [120-123] Thus by measuring the angular dependence of the intensity of the emitted fluorescence and comparing with the computed angular dependence, the standing wave field has been used as a structural probe [120-128]. Various applications of the X-ray standing wave (XSW) technique to problems relating to single crystal surfaces and interfaces may be found in recent reviews [129,130]. The standing wave phenomenon was also observed in multilayer mirrors [131-133] and Langmuir Blodgett multilayer films [134] which actually work as artificial Bragg crystals. This standing wave field was also used in different ways for analyzing the local structure of multilayers [135-136], density evaluation of deposited films on multilayers [137] and selective extended X-ray absorption fine structure analysis [138].

1.2.1 Theoretical formulation:

When an electromagnetic wave is incident on a multilayer structure it gets reflected from each interface due difference in the refractive index of the two layers, and interference between the incident electromagnetic wave and the reflected wave forms a standing wave pattern inside the multilayer. Dev et. al. [139] has theoretically explained the formation of X-ray standing wave inside a multilayer structure, using the recursion method of Parratt [140] and has obtained an expression for the electric field intensity of the standing wave at a certain point inside a multilayer structure. Following the above formalism, the electric fields of the transmitted (E_j^t) and reflected (E_j^r) waves at a certain point \mathbf{r} inside the jth layer of a multilayer structure are given by:

$$E_j^t(\mathbf{r}) = E_j^t(0) \exp(-ik_{j,z}z) \exp[i(\omega t - k_{j,x}x)], \quad (1.2)$$

and

$$E_j^r(\mathbf{r}) = E_j^r(0) \exp(+ik_{j,z}z) \exp[i(\omega t - k_{j,x}x)] \quad (1.3)$$

where, $E_j^t(0)$ and $E_j^r(0)$ are the respective fields at the top of the jth layer.

Hence, the total electric field at a point \mathbf{r} in the j-th layer is given by:

$$E_j^T(\mathbf{r}) = E_j^t(\mathbf{r}) + E_j^r(\mathbf{r}) \quad (1.4)$$

and the field intensity $I(\theta, z) = |E_j^T(r)|^2$ is given by

$$I(\theta, z) = |E_j^t(0)|^2 \left[1 + \left| \frac{E_j^r(0)}{E_j^t(0)} \right|^2 + 2 \left| \frac{E_j^r(0)}{E_j^t(0)} \right| \cos\{\nu(\theta) + 2k_{j,z}'z\} \right] \quad (1.5)$$

where, θ is grazing angle of incidence of the electromagnetic wave on the multilayer and $\nu(\theta)$ is the phase of the electric field ratio at the top of the jth layer. It is clear that eqn.(1.5)

that the intensity expression represents a standing wave pattern whose peak positions depend on the grazing angle of incidence θ [141,142].

1.3 Motivation of the thesis work:

It is clear from the above discussion that different groups have reported different reasons for the origin of ferromagnetism in a same DMS system and contradictory reports are available in the literature towards this. Thus, the origin of ferromagnetism in TM doped and co-doped ZnO is still fairly unresolved and thus further investigations are required on these samples through both experimental and theoretical approach. A systematic investigation of the local environment around the host and the dopant cations can yield unambiguous results regarding the origin of FM in these systems and synchrotron based X-ray Absorption Spectroscopy (XAS), which comprises of both X-ray Near Edge Structure (XANES) and Extended X-ray Absorption Fine Structure (EXAFS) techniques, is a perfect tool to study this.

XAS is an element specific tool and thus can yield local structural results separately surrounding both the host and dopant species present in a material. Moreover, DMS materials being discussed here are generally nanocrystalline with very small amount of the dopant materials and hence, X-ray diffraction, which acts on the principle of long range order, might not give the correct phase information and for such systems since single-phase domains are not sufficiently large in these materials. EXAFS on the other hand probes the local order and does not depend on the long range order and thus can yield better result so far microscopic behaviour of the samples is concerned [142-145].

Thus keeping the above challenges in mind, and considering the fact that there are theoretical predictions of observing higher FM in co-doped DMS materials, in this thesis work we have prepared a range of transition metal (Fe and Cr) doped, transition metal and Cu

co-doped (Fe-Cu, Co-Cu and Ni-Cu) and transition metal and rare earth (Dy,Mn) co-doped ZnO nanocrystals. The samples have been prepared by sol-gel and wet chemical routes and these DMS samples have primarily been characterised by EXAFS and XANES measurements. The results have also been complemented with other measurements viz., Transmission Electron Microscopy (TEM), X-ray diffraction (XRD), X-ray fluorescence (XRF), UV-Vis, RAMAN and FTIR spectroscopy and Photoluminescence (PL) measurements also whenever was required. In most of the cases the results have also been compared with theoretically simulated results obtained from ab-initio first principle density functional theory calculations. These results have subsequently been used to explain the observed magnetic properties of the samples.

As has been mentioned earlier, in this thesis work we have also performed the depth dependent EXAFS study on Ni/Ti and Co/Ti thin film magnetic multilayers. As we all know that magnetic multilayer structures having variety of interesting properties and wide applications spanning from storage devices to supermirror polarisers in neutron optics. It is well known that interfaces play an important role in the performance of a magnetic multilayer device [146-147]. A variety of approaches can be used to probe the interfaces of a multilayer structure including specular and diffused X-ray reflectivity, neutron reflectivity and X-ray photoelectron spectroscopy (XPS) or secondary ion mass spectrometry (SIMS) with destructive ion etching. However, these techniques primarily yield information regarding the interface roughness and inter-diffusion and compound formation at the interfaces and not much structural information can be obtained by these techniques. X-ray absorption spectroscopy (XAS) on the other hand is an important technique to investigate element specific local structure in a system. Though it is not really a surface sensitive technique, however as has been discussed above, by carefully preparing the sample and choosing proper grazing angle of incidence, and thereby controlling the nodes and anti-nodes of the X-ray

standing waves generated inside the multilayer, we can carry out depth selective XAS measurements in a multilayer structure.

1.4 Outline of the thesis:

Apart from the first chapter which gives the introduction and motivation of the thesis work, the rest thesis is divided into eight more chapters.

Chapter-2 of the thesis describes the various experimental techniques and data analysis formalism used in this thesis work. This chapter begins with short descriptions of the various sample preparation techniques followed in this work. Subsequently, the basics of XAS technique which comprises both XANES and EXAFS has been described. Both XAS and GIEXAFS measurement for samples described in this thesis have been performed at Energy Scanning EXAFS beamline, BI-09, Indus-2 Synchrotron radiation sources at Raja Ramanna Centre for Advanced Technology, Indore, India [148-149] which has been briefly described here. Finally the data reduction and data analysis procedure of EXAFS is described elaborately which involves extensive use of the IFEFFIT software package including ATHENA and ARTEMIS subroutines [150]. A brief description of other characterization techniques used in this thesis work, viz., X-ray diffraction (XRD), transmission electron microscopy (TEM), photoluminescence (PL), magnetic measurements etc. have also been discussed briefly in this chapter.

In subsequent chapters, the main experimental results of this thesis work has been described. In Chapter-3 we explored transition metal (TM) doped ZnO based dilute magnetic semiconductor. This chapter is divided in to two subsections. The first section describes the results on Fe doped ZnO nanocrystals (NCs) with different doping concentration of Fe, while the second section comprises of the results Cr doped ZnO NCs. In next few chapters a series of studies on simultaneous doping of ZnO by two cations have also been reported. Chapters

(4-6) of the thesis work deals with the study of (Fe,Cu), (Co,Cu) and (Ni,Cu) co-doped ZnO NCs while in Chapter-7 we describe the structural investigations of (Mn, Dy) co-doped ZnO nanocrystals. Chapter-8 is dedicated to describe the development of grazing incidence EXAFS (GIXAFS) measurement facility at the Energy Scanning EXAFS beamline at Indus-2 SRS, RRCAT, Indore and the subsequently, the experimental work carried out by using the above facility in characterisation of Co/Ti and Ni/Ti magnetic multilayers. Finally in Chapter-9 the conclusions obtained from each study performed under this thesis work are summarized and future directions of the works have been mentioned.

Chapter- 2

Experimentation and data analysis

In the first section of this chapter we describe the different synthesis processes which have been used to prepare the ZnO based DMS systems and magnetic multilayer devices. For the present thesis to synthesis TM doped and Co-doped ZnO NCs sol-gel and wet chemical synthesis methods have been used, while the Ni/Ti and Co/Ti thin film multilayer samples used for GIXAFS measurement were prepared by sputtering technique. The second section of this chapter contains the brief introduction of several characterization techniques used to analyze all the samples focusing mainly on X-ray Absorption Spectroscopy technique, which is the main

2.1 Sample preparation:

2.1.1 Sol-gel method:

The sol-gel method is a wet-chemical synthesis technique widely used for the preparation of oxide gels, glasses, thin films and ceramic materials at low temperature. The sol-gel process, as the name implies, involves transition from a liquid ‘sol’ (colloidal solution) into a ‘gel’ phase [151]. A sol is a dispersion of the solid particles of size $\sim 0.1 - 1 \mu\text{m}$ in a liquid where there is only the Brownian motions of suspended particles. A gel is a state where the solid network contains liquid components. Usually inorganic metal salts or metal alkoxides are used as precursors for producing metal oxide thin films. The sol-gel process can be described by the hydrolysis, alcohol and water condensation and

polymerization. Ceramic oxide films can be formed by spin, dip or spray coating techniques using sol-gel method.

2.1.2 Wet chemical route method:

This is a common name for a group of methods used for producing nano- and ultra-dispersed inorganic powders from aqueous and non-aqueous solutions. The term "wet chemical methods" emerged in contrast to conventional solid-state synthesis methods of compounds and materials. Today the term refers to a group of methods of powder and material production (liquid phase sol-gel process, hydrothermal synthesis, Pechini method, spray drying, aerosol spray pyrolysis, cryochemical synthesis, etc.) using liquid phase at one of the process stages. The main differences between wet chemistry products and similar products of solid-phase synthesis are much smaller grains (crystallites) and, usually, lower temperature and shorter duration of phase formation. [152]

2.1.3 Magnetron sputtering:

The thin film magnetic multilayer samples used in this thesis work for GIXAFS studies have been prepared by d.c. magnetron sputtering technique which is briefly described here. Sputtering is a physical vapour deposition (PVD) process in which a plasma is created between two electrodes in an inert gas atmosphere (generally argon) using an electric field. The momentum transfer theory can be used to understand the physics of sputtering, where kinetic momentum of incident ions are transferred to the atoms at the target surface upon collision and a collision cascade takes place within the top few layers in the material which results ejection of the target surface species. The efficiency of sputtering is quantified by sputtering yield which is defined as the average number of ejected target atoms/molecules per single ion hitting the target. The yield of sputtering depends upon ion/target atomic mass, ion energy, target crystallinity and angle of incidence. Sputtering technique had different variants.

The simplest variant of sputtering deposition is dc sputtering. In case of dc sputtering, positively charged ions (Ar^+) from the plasma are accelerated towards the negatively charged electrode where the material to be deposited or the “target” is kept. The positive ions are accelerated by potentials ranging from a few hundred to a few thousand electron volts and strike the negative electrode with sufficient force to dislodge and eject atoms from the target. These atoms (cluster of atoms or ad-atoms) condense on substrate surface that is placed in proximity to the sputtering cathode and is generally kept grounded. In DC sputtering, there is a low concentration of secondary electrons. So, there will be fewer collisions in the plasma and thus large voltage and higher chamber ambient pressure are required to sustain the plasma.

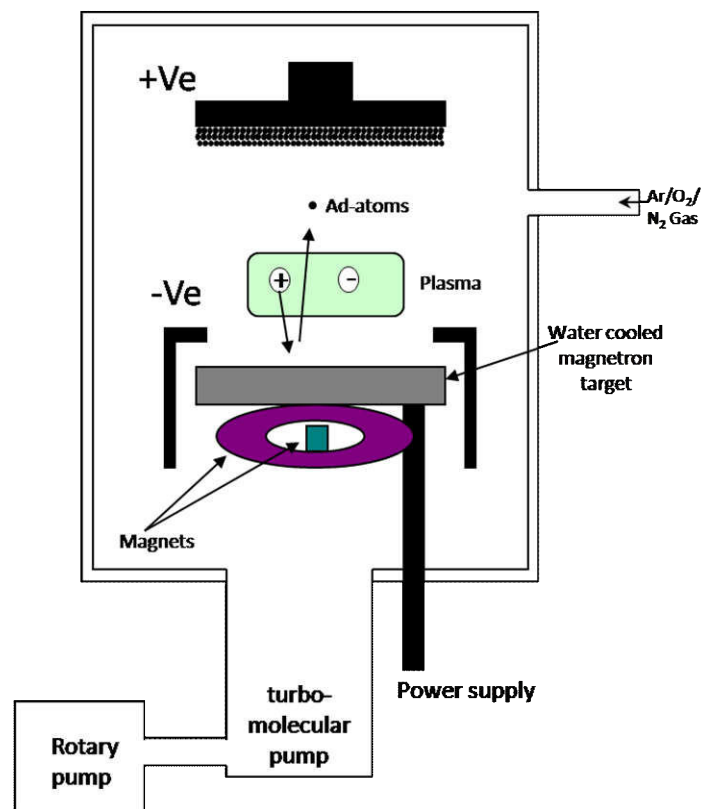


Figure 2.1: Schematic of R.F. Magnetron sputtering system.

In DC, sputtering process discussed above, the secondary electrons have relatively longer mean free path (10's cm) and that's why the processes suffer from inefficient

secondary electron process and thereby low ionization levels. This leads to slow etching of target surface and therefore lower deposition rate at relatively higher pressure. Magnetron sputtering technique, additionally uses a closed magnetic field around the target material so that electrons undergo helical movement near the target, enhancing the efficiency of the ionization process. This allows creation and sustention of plasma at relatively lower pressures which reduces both contamination in the growing film and energy losses of the sputtered atoms through collision with gas molecules. The particular magnetron sputtering system used for the above sample preparation has been described in Chapter-8.

2.2 XAFS measurements and data analysis:

2.2.1 Theoretical Description of XAFS:

As has been mentioned in Chapter-1, X-ray absorption fine structure or XAFS deals with studying small oscillations which appear in the X-ray absorption spectrum of an element present in a material. Interaction of X-rays with matter can be explained by three different processes viz. Thomson scattering, Compton scattering and Photoelectric effect depending on the energy of light and elemental compositions. X-rays are light with energies ranging from 500 eV to 500 keV, or wavelengths from 25\AA to 0.25\AA . In this energy region the photoelectric phenomenon dominates over the others. In the photoelectric process, when X-ray photon interacts with the matter, it gets absorbed by a core shell electron of that particular atom. The atom is then left in an excited state with an empty electronic level (a core hole). The electron ejected from the atom is called the photo electron and this phenomenon is known as photo electric effect. The absorption phenomenon will occur only when the binding energy of the core shell electron is greater than or equal to the energy of the incident X-ray photon. If the binding energy is greater than the energy of the X-rays, the bound electron will not be perturbed from the well-defined quantum state and will not absorb the X-

rays. This process has been well understood for nearly a century. The full implications of this process when applied to molecules, liquids, and solids will give rise to the explanation XAFS oscillations.

In X-ray absorption fine structure spectroscopy, the physically measured quantity is X-ray absorption coefficient $\mu(E)$, which varies with respect to the incident photon energy. According to Beer's law, absorption coefficient, $\mu(E)$ which describes the probability of X-rays being absorbed as a function of incident X-ray energy E :

$$I = I_0 e^{-\mu(E) t} \quad (2.1)$$

where I_0 is the X-ray intensity incident on a sample, t is the sample thickness, and I is the intensity transmitted through the sample.

Initially, $\mu(E)$ decreases as the energy of incident photon increases (approximately as $1/E^3$). At certain energies, the absorption increases drastically and gives rise to an absorption edge. Each such edge occurs when the energy of the incident photons is just sufficient to cause excitation of a core electron of the absorbing atom to a continuum state, i.e. to produce a photoelectron. Beyond the absorption edge the absorption coefficient decreases monotonically with increasing energy, until the next absorption edge is reached.

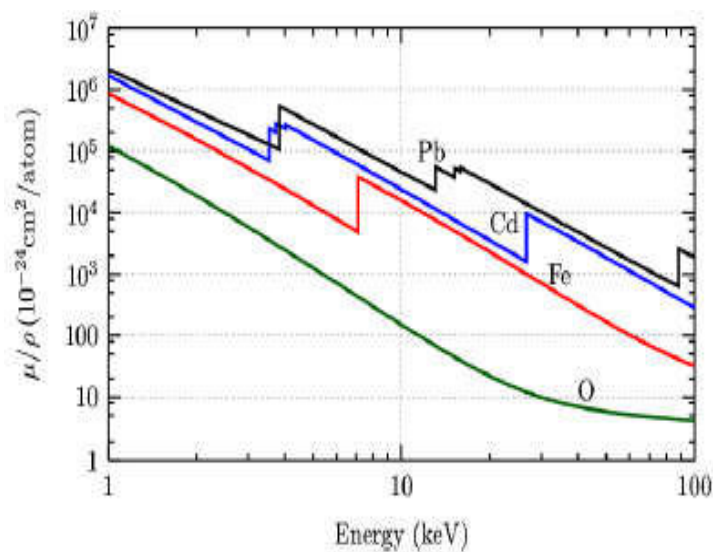


Figure 2.2: Variation of X-ray absorption cross section with incident photon energy[153]

Absorption edges were first measured in 1913 by Maurice De Broglie, the older brother of quantum mechanics pioneer Louis De Broglie. In 1920, using M. Siegbahn's vacuum spectrograph, Hugo Fricke first observed the "fine structure" energy-dependent variations in the $\mu(E)$ – in the vicinity of the X-ray absorption edges of a number of elements. In particular, a controversy existed as to whether a model based on the long-range order (LRO) or short-range order (SRO) in the sample was more appropriate. This confusion was cleared up much later, around 1970 when Stern, Sayers, and Lytle [154-157] synthesized the essential aspects of a viable theory of XAFS, and further demonstrated that XAFS could be a practical tool for structure determination. A detailed historical account of the development of XAFS technique is given in the article by Stumm von Bordwehr [158]. So far, various advancements in the theoretical models have been obtained such as full multiple-scattering (FMS) [159], self-consistent field and fully relativistic calculations [160] especially for a quantitative analysis of the near-edge regime. The EXAFS theory is implemented in various ab-initio codes like EXCURV [161], FEFF [162], GNXAS [163], WIEN2k[164], NSRL-XAFS[165] etc. The principles of X-ray absorption fine structure spectroscopy and data analysis were described by Stern [166], Sayers and Bunker [167] Fendorf and Sparks [168], and Fendorf [169], while more details on the physics of XAFS appear in several books (by Stern and Heald [170], by Koningsberger and Prins [171], by Teo [172] and by Stöhr [173]).

XAFS is an element specific technique which can be applied not only to crystals, but also to materials that possess little or no long-range translational order: amorphous systems, glasses, disordered films, membranes, solutions, liquids, metalloproteinase and also for nanostructured materials and thin films. This versatility allows it to be used in a wide variety of disciplines: physics, chemistry, biology, biophysics, medicine, engineering, environmental science, materials science, and geology.

As has been mentioned in Chapter-1, X-ray absorption fine structure (XAFS) spectrum of an atom around one of its absorption edge consists of two parts: X-ray absorption near-edge spectrum (XANES), ranging from approximately -50 to $+200$ eV relative to the edge energy and the Extended X-ray absorption fine structure (EXAFS) spectrum, above the absorption edge to approximately 1000 eV or higher. X-ray absorption near edge structure (XANES) can be used to determine the valence state and coordination geometry, while EXAFS can be used to determine the local molecular structure of a particular element within a sample. Figure 2.3 represents the typical XAFS spectrum of Fe-foil.

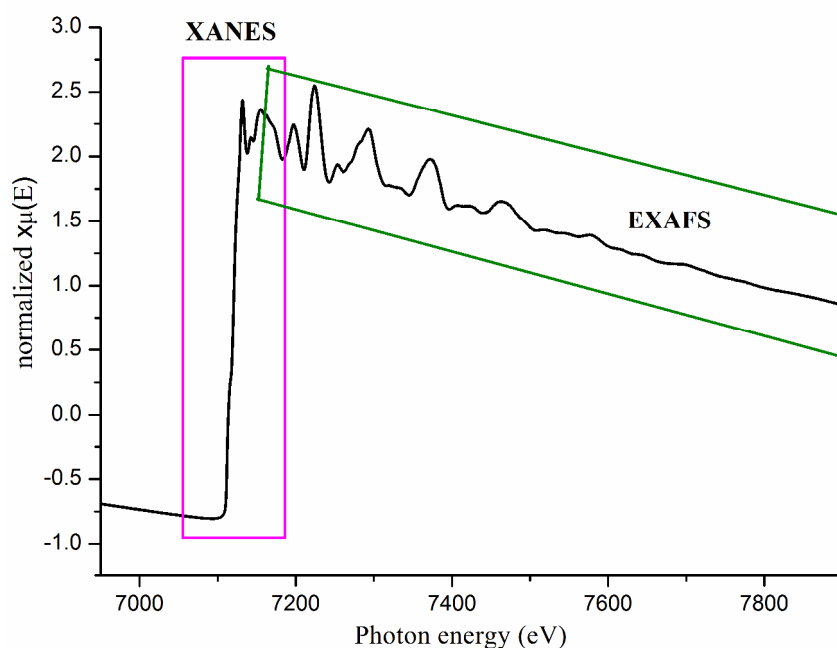


Figure 2.3: A typical X-ray absorption spectrum

EXAFS describes the phenomenon where photoelectron wave scatters from the atoms around the X-ray absorbing atom, creating interferences between the outgoing and scattered parts of the photoelectron wave function. These quantum interference effects cause an energy-dependent variation in the X-ray absorption probability, which is proportional to the

X-ray absorption coefficient. Since the EXAFS oscillations arise due to the presence of neighboring atoms, the photo-electron can scatter from the electrons of this neighboring atom, and the scattered photo-electron can return to the absorbing atom. Since the absorption coefficient depends on whether there is an available electronic state (that is whether there is an electron at the location of the atom and at the appropriate energy and momentum), the presence of the photo-electron scattered back from the neighbouring atom will alter the absorption coefficient.

2.2.2 Theoretical formulation of EXAFS equation:

The EXAFS spectrum can be understood in terms of the EXAFS equation which can be written in terms of a sum of the contributions from all scattering paths of the photoelectron [166-170] the derivation of which has been given in many books and reviews [170-179] .

Since X-ray absorption is a transition between two quantum states, absorption coefficient in this process is proportional to transition probability and can be written using Fermi's Golden rule as: -

$$\mu \propto \left| \langle i | H | f \rangle \right|^2 \quad (2.2)$$

where $\langle i |$ represents the initial state with an X-ray, a core electron, and no photo-electron to a final state and $| f \rangle$ represents the final state with no X-ray, a core hole, and a photo-electron. Initial state of the atom will not be affected by the neighboring atoms since core shell electron is tightly bound, however final state will be altered due to the backscattering of the photoelectron by neighbouring atoms. Now we can span the final state by using two terms, "bare atom" portion $| f_0 \rangle$ and one that is the effect of neighboring atoms $| \Delta f \rangle$, i.e.

$$| f \rangle = | f_0 \rangle + | \Delta f \rangle \quad (2.3)$$

after solving and rearranging eq (2.1) & (2.2) we can write

$$\mu(E) = \mu_0(E)[1 + \chi(E)] \quad (2.4)$$

Where ,
$$\chi(E) = \frac{\mu(E) - \mu_0(E)}{\Delta\mu_0(E)} \quad (2.5)$$

So, EXAFS oscillation can be written as,

$$\chi(E) \propto \langle i | H | \Delta f \rangle \quad (2.6)$$

The interaction term H represents the process of changing between two energy and momentum states. According to quantum theory H is proportional to e^{ikr} . The initial state is a tightly bound core level which can be approximated as a delta function. The change in final state is same as the wave function of scattered photo electron $\Psi_{scatt}(r)$. Putting all these terms, one can write the expression for EXAFS as

$$\chi(E) \propto \int \delta r e^{ikr} \psi_{scatt}(r) dr = \psi_{scatt}(0) \quad (2.7)$$

Thus, we can say, the EXAFS function is proportional to the scatted photoelectron at the absorbing atom. Now if we consider the outgoing photo electron wave function $\psi(k, r)$ as spherical wave, we can write-

$$\psi(k, r) = \frac{e^{ikr}}{kr} \quad (2.8)$$

where k is the photoelectron wave vector, defined as $k = \sqrt{\frac{2m(E - E_0)}{\hbar^2}}$, where E is the incident photon energy and E_0 is the binding energy of the core shell electron. This photoelectron travels a distance R to the neighboring atom, gets scattered from neighboring atoms and then traverses back to the absorbing atom. The amplitude of scattered photo electron at the position of absorbing atom then becomes

$$\psi_{scatt}(k, r = 0) = \frac{e^{ikR}}{kR} \left[2kf(k)e^{i\delta(k)} \right] \frac{e^{ikR}}{kR} + C.C. \quad (2.9)$$

where, $f(k)$ and $\delta(k)$ are back scattering amplitude and scattering phase shift due to the scattering atom. The scattering factors $f(k)$ and $\delta(k)$ depends upon the atomic number, Z of the neighboring atom. These scattering factors make EXAFS sensitive to the presence of neighboring atoms. Combining equation 2.6 and 2.8 we get, after few more simplification

$$\chi(k) = \frac{f(k)}{kR^2} \sin [2kR + \delta(k)] \quad (2.10)$$

This represents the EXAFS equation considering one pair of absorbing atom and scattering atoms. However, in real scenario, often there is large number of scattering atoms are present at approximately same distance, called coordination shells. However, the distance of each atom in coordination shell is not same due to the effect of thermal or static disorder in the bond distances and we need to average over their contributions. As a first approximation i.e., assuming one type of neighboring atoms and Gaussian distributions of neighboring atom's disorder, the EXAFS equation becomes:

$$\chi(k) = \frac{Ne^{-2k^2\sigma^2} f(k)}{kR^2} \sin [2kR + \delta(k)] \quad (2.11)$$

where, N is the coordination number in one coordination shell at a distance of R and σ^2 is the mean-square-displacement in the bond distance R . Summing over the contribution due to different coordination shells, EXAFS equation reduces to

$$\chi(k) = \sum_j \frac{N_j f_j(k)}{kR_j^2} \sin [2kR_j + \delta_j(k)] e^{-2k^2\sigma_j^2} \quad (2.12)$$

where, j stands for the individual coordination shell of identical atoms at approximately the same distance from the central atom. In principle there could be many such

shells, but as shells of similar Z become close enough (i.e., within a 0.05Å of each other), they become difficult to distinguish from one another and they are often represented by a single shell having equivalent multiple degeneracy.

Equation 2.11 needs an important correction before we use it as EXAFS equations. To understand the EXAFS phenomenon, we assume photoelectron as a photoelectron wave. Thus, energy of photoelectrons may change due to inelastic scattering with the conduction electrons; phonons etc. In order to participate in the EXAFS process, the photo-electron has to elastically scatter from the neighboring atom and return back to the absorbing before the excited state decays. To account for both inelastic scattering and the core-hole lifetime one should rather use a damped spherical wave like:

$$\psi(k, r) = \frac{e^{ikr} e^{-2r/\lambda(k)}}{kr} \quad (2.13)$$

where, λ is the mean free path that represents that how far photoelectron can travel without undergoing inelastic scattering and before the core hole is filled. The mean free path typically falls in the range of 5-30 Å and has a fairly universal functional relationship with photo electron wave number, k as shown in fig. 2.4.

EXAFS equation needs further correction by adding passive electron effect also called amplitude reduction factor S_0^2 . It accounts for the slight relaxation of the remaining electrons in the presence of the core hole vacated by the photoelectron. S_0^2 usually has a value between 0.7 and 1.0 and does not depend on k . Hence, the final EXAFS equation becomes

$$\chi(k) = \sum_j \frac{N_j S_0^2 f_j(k)}{k R_j^2} \sin [2k R_j + \delta_j(k)] e^{-2k^2 \sigma_j^2} e^{-2R_j/\lambda(k)} \quad (2.14)$$

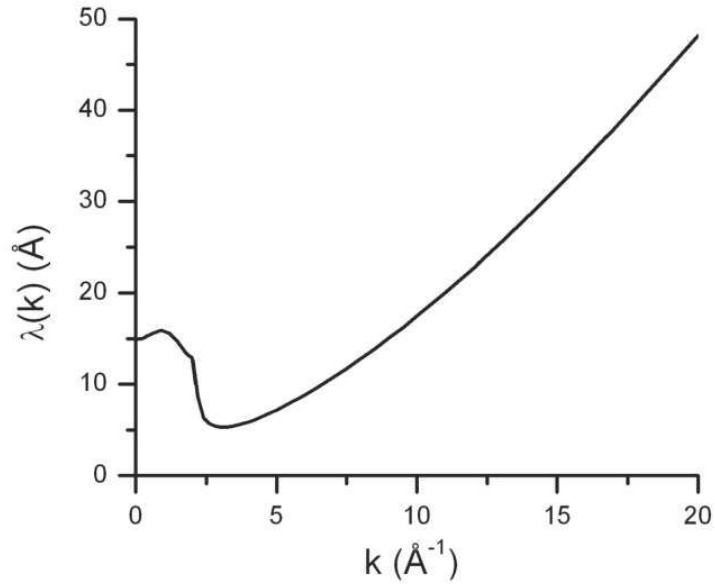


Figure 2.4: Typical characteristic of photoelectron mean free path vs. wave number [179].

In the above equation, N_j and S_0^2 contributes in amplitude of EXAFS signal and does not have k dependence. S_0^2 is different for different elements, but the value is generally transferable between different species from the same element and the same edge. R_j gives the distance between the absorber and a coordinating atom for a single-scattering event. Finally, the term σ^2 has contributions from dynamic (thermal) disorder and static disorder (structural heterogeneity). Since all the coordinating atoms in a shell are not fixed at positions of exactly a distance R_i from the central absorber atom, S_0^2 accounts for the disorder in the interatomic distances. S_0^2 is the mean-square displacement of the bond length between the absorber atom and the coordination atoms in a shell.

From equation (2.13) we can say that because of the $\lambda(k)$ term and the R^{-2} term, XAFS is seen to be an inherently local probe i.e. EXAFS cannot see much further than ~ 5 Å from absorbing atom. It is also clear that XAFS oscillations are sum of the different frequencies that correspond to the different distances for each coordination shell. This will lead us to use

Fourier transforms in the analysis. To process the experimental EXAFS data a prior information about these scattering factors and required, these are basically function of atomic number Z and are usually calculated theoretically with very high accuracy.

2.2.3 XAFS measurements:

X-ray absorption spectroscopy is widely used at synchrotron radiation facilities in all over the world. The first observation of synchrotron radiation came on 24 April 1947, at the General Electric Research Laboratory in Schenectady, New York, however it was not immediately recognised for what it was [180]. Initially, synchrotron radiation was seen as an unwanted but unavoidable loss of energy in accelerators designed (ironically) to produce intense beams of X-rays. The potential advantages of synchrotron radiation for its own end were detailed by Diran Tomboulion and Paul Hartman from Cornell University [181].

Synchrotron radiation (also known as magneto bremsstrahlung radiation) is the electromagnetic radiation emitted when charged particles are accelerated in a circular orbit or storage rings, with the relativistic velocity. On the other hand, if the particle is non-relativistic, then the emission is called cyclotron emission. It is produced, for example, in synchrotrons using bending magnets, undulators and/or wigglers. The radiation produced in this way has wide range of frequencies or wavelengths spanning over almost the entire electromagnetic spectrum. Synchrotron radiation emitted from different points of a storage ring are extracted by a set of mechanical and optical instruments integrated together which are called beamlines and due to its exotic features of self-polarisation, high flux and high collimation, Synchrotron radiation is used in a wide variety of applications concerning material characterisation. Presently, there are over 30 synchrotron sources all over the world having various storage ring energy and catering to a vast research community including material scientists to biologists.

India has also its own Synchrotron radiation facility at Raja Ramanna Centre for Advanced Technology, Indore, Madhya Pradesh. The first Indian synchrotron source Indus-1, a 450 MeV electron storage ring, was commissioned in early 1999 [182]. It provides a broad electromagnetic spectrum extending from far infrared to soft X-ray region. The second synchrotron source Indus-2 was commissioned in 2005 and is presently being operated with 2.5 GeV electron energy at 200 mA beams current and a critical wavelength of about 2\AA , providing a spectrum from Infr-red to hard X-ray regime. Indus -2 lattice is designed to give low beam emittance and high brightness. [183]

The schematic layout of the Indus complex and photograph of a part of the Indus-2 synchrotron source are shown in fig. 2.5.

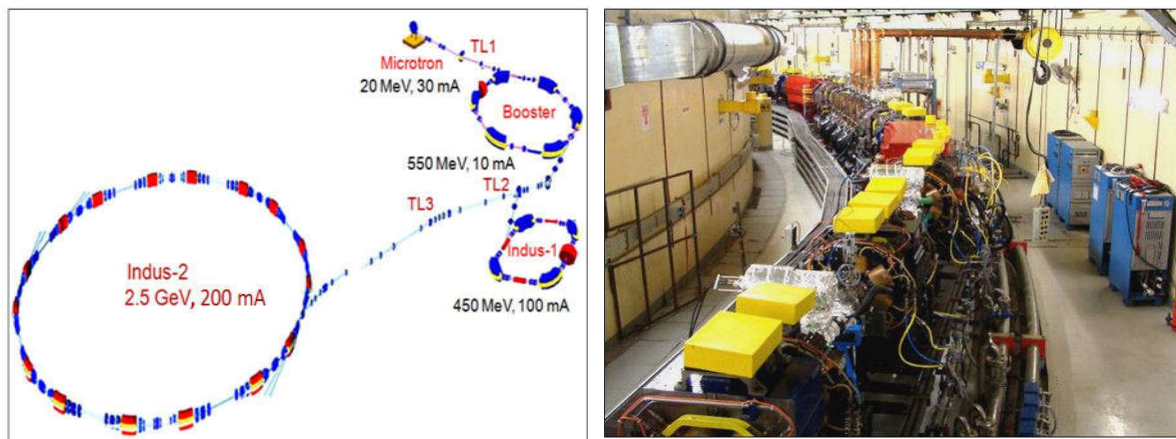


Figure 2.5: Schematic layout of the Indus synchrotron complex (left panel) and photograph of a part of Indus-2 Synchrotron Source (2.5 GeV, 200 mA) at Raja Ramanna Centre for Advanced Technology (RRCAT), Indore, India [182-184]

The storage ring of Indus-2 is 172.4 meter (circumference) consisting of 8 unit cells each providing a 4.5 m long straight section. Each of the eight super periods has two dipole bending magnets (1.502T), four focusing and five defocusing quadrupoles and six sextupoles. Four RF cavities are used for RF voltage of 1.5 MV to achieve 2.5 GeV energy with beam emittance of $X=5.81 \times 10^{-8} \text{m.rad}$ and $Y=5.81 \times 10^{-9} \text{m.rad}$. The insertion devices which are going

to be installed on Indus-2 in near future include two planar undulators, one APPLE type undulator and one super conducting wavelength shifter.

In the present thesis work all the XAFS measurements have been carried out at the Energy Scanning EXAFS beamline (BL-09) at Indus-2 Synchrotron Source [184]. The beamline uses a double crystal monochromator (DCM) which works in the photon energy range of 4–25 KeV with a resolution of 10^4 at 10 KeV. A 1.5 m horizontal pre-mirror with meridional cylindrical curvature is used prior to the DCM for collimation of the beam and higher harmonic rejection. The second crystal of the DCM is a sagittal cylindrical crystal, which is used for horizontal focusing of the beam while another Rh/Pt coated bendable post mirror facing down is used for vertical focusing of the beam at the sample position. EXAFS experiment can be performed in two different mode: transmission and fluorescence mode. Depending on the sample requirement we can choose any of experimental mode mentioned above. For measurements in the transmission mode, the sample is placed between two 30 cm long ionization chamber detectors. The first ionization chamber measures the incident flux (I_0) and the second ionization chamber measures the transmitted intensity (I_t). From these intensities the absorbance of the sample is found as a function of energy. Absorption (μ) is calculated using formula, $\mu = \log(\frac{I_0}{I_t})$. A third ionization chamber is also used after the second ionization chamber where reference metal foils are measured for energy calibration. The selection of appropriate gas pressure and gas mixture have been done to achieve 10-20% absorption in first ionization chamber and 70-90% absorption in second ionization chamber to obtain better signal to noise ratio. However, for measurements in the fluorescence mode, the sample is placed at 45° to the incident X-ray beam and the fluorescence signal (I_f) is detected using a Si drift detector placed at 90° to the incident X-ray beam. An ionization chamber detector is used prior to the sample to measure the incident X ray flux (I_0) and the

absorbance of the sample ($\mu = I_f / I_0$) is obtained as a function of energy by scanning the monochromator over the specified energy range.

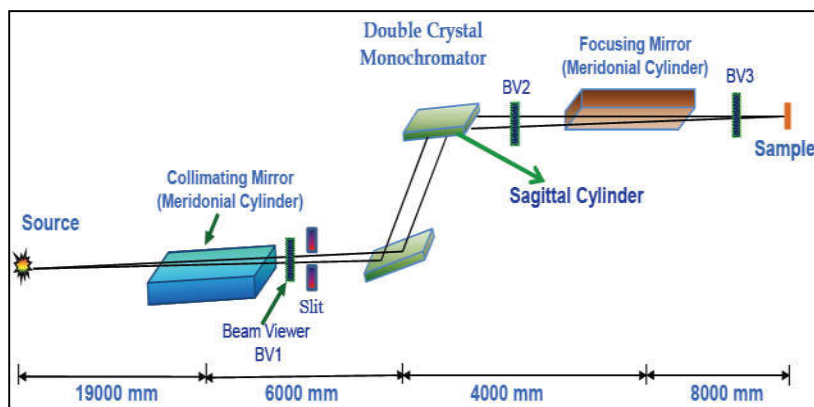


Figure 2.6: Schematic layout of Scanning EXAFS Beamline BL-09.



Figure 2.7: Photograph of (a) optics hutch and (b) experimental station of the Energy Scanning EXAFS Beamline BL-09.

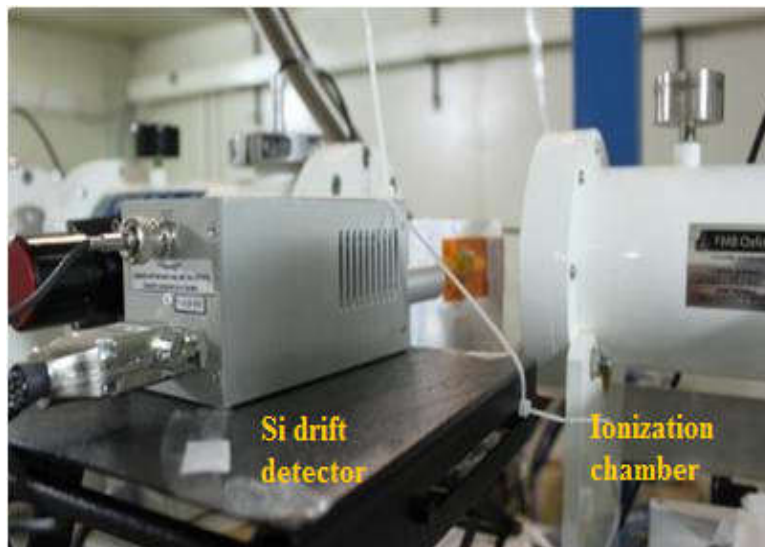


Figure 2.8: Experimental set-up for fluorescence mode of XAFS measurement.

In order to perform the depth dependent XAFS study of magnetic multilayer system a grazing incidence XAFS (GIXAFS) measurement facility has recently been set up at the above beamline. In this GIXAFS experimental setup, a 2-Circle goniometer with a 5-axis sample stage was used to orient the sample, where the sample was kept at the center of the goniometer and two detectors have been used for simultaneous fluorescence and reflectance measurements on the samples. The reflectivity detector which is a 1d line detector has been used for alignment of the sample at a desired grazing angle of incidence w.r.t. the SR beam by measuring its reflectivity while XAFS measurements have been done by collecting the total fluorescence yield from the same surface by a Si drift detector. Fig. 2.9 shows schematic of the GIXAFS setup at energy scanning EXAFS beamline BI-09, while fig. 2.10 shows the actual photograph.

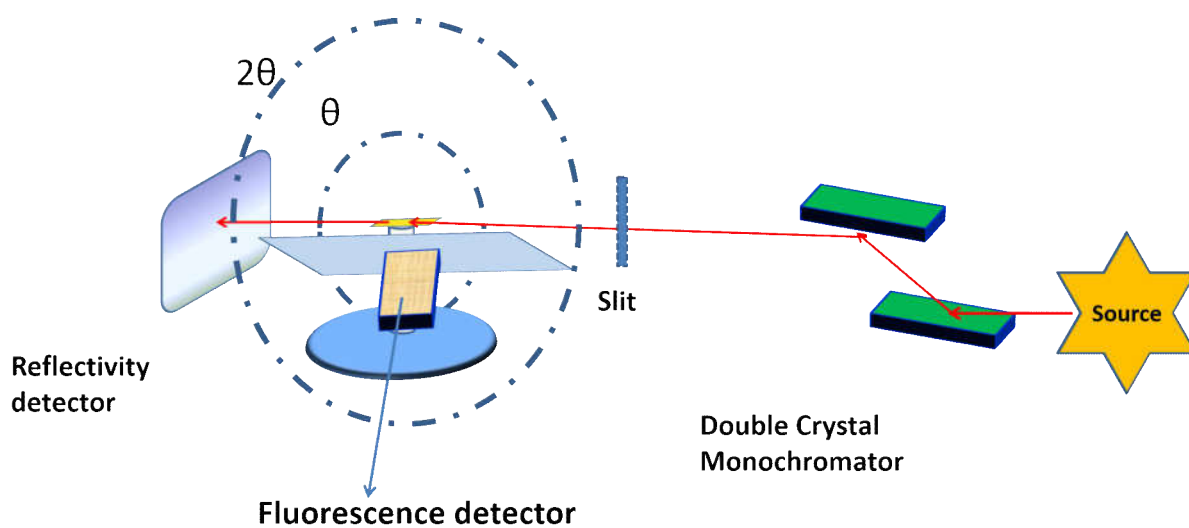


Figure 2.9: Schematic layout of the GIXAFS set up at the Energy Scanning EXAFS Beamline (BL-09).

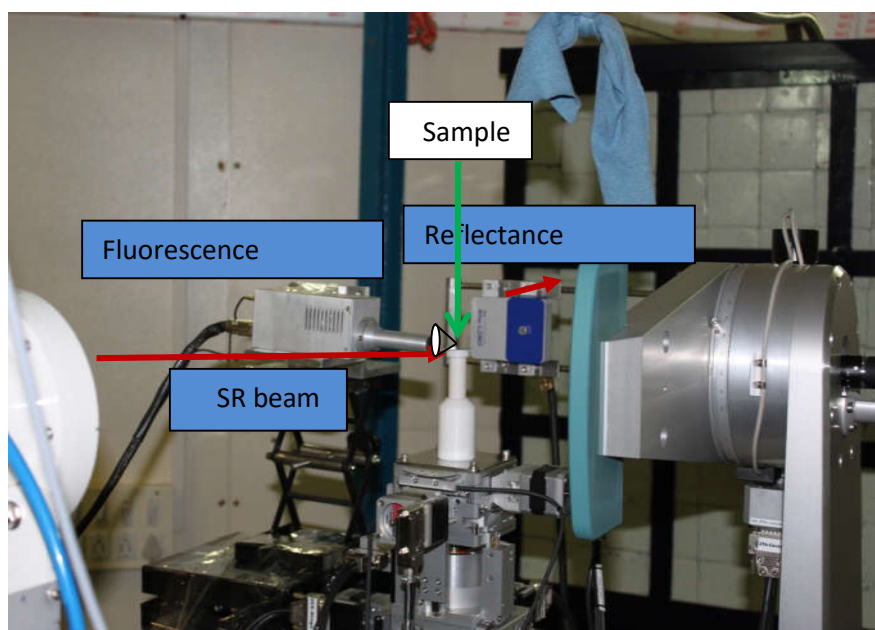


Figure 2.10: Photograph of the GIXAFS set up at the Energy Scanning EXAFS Beamline BL-09.

2.2.4 XANES interpretation:

In the vicinity of the absorption edge, the interaction of the ejected photoelectron with the potential of the neighbouring atoms is still strong so the simplifying single scattering assumption leading to EXAFS is not possible. The EXAFS equation breaks down at low- k , due to the $1/k$ term and the increase in the mean-free-path at very low- k . In the near-edge (XANES) region the muffin-tin approximation is less satisfactory for quantitative analysis and the interpretation of XANES is complicated since there is no simple analytic description of XANES. However, useful information regarding the chemical environment can be obtained from the XANES region. The absorption edge position and shape are sensitive to formal valence state, ligand type, coordination geometry and can be used as a fingerprint to identify phases.

The final states of K and L1 edges are p -states, and the final states in L2 and L3 edges are a mixture of d and s characters. The p final states of K and L1 edges are more diffused than the localized d final state of L2 and L3 edges. All of these edges may show strong peaks at the top of the edge (the “principal maximum”). Historically these were called “white lines,” because that was how they appeared on photographic plates. For K shell absorption, where the core-level is a $1s$ state, the photo-electron has to end up in a p state according to the selection rules of transition. Thus, even if there are available states with the right energy, there might be no $1s$ absorption if there are no available p states. For EXAFS, where the energies are well-above the threshold energy, this is rarely an important concern. For XANES, on the other hand, this can play a very important role. From a molecular orbital point of view, the bound states in the pre-edge region consist of linear combinations of orbitals that have specific symmetry properties. If the Hamiltonian is symmetric under inversion, states of opposite parity cannot mix to make an eigenstate of the Hamiltonian. This implies that p states (odd parity) can only mix with d or s states (located at the central atom)

if the Hamiltonian (and therefore the local environment) is not totally symmetrical under inversion. Since the final state in *K*- and *L*1-edges are of *p* symmetry (by dipole selection rules), any strong transition near the energy of the metal *3d* orbitals indicates a breaking of inversion symmetry. Transition metal oxides, for example, usually have many unfilled *3d* electrons near the Fermi level, and a filled *3p* band. There are empty *2p* electron states from the oxygen, but these are too far away to appreciably over-lap with the metal *1s* band. Therefore, the metal *3d* electrons do not normally participate in the absorption process unless there is a strong hybridization of the O *2p* and metal *3d* levels. The XANES spectra are especially sensitive to such hybridization. For ions with unfilled *d*-electron bands, the *pd* hybridization is dramatically altered depending on the coordination environment, with much stronger hybridization for tetrahedral coordination than for octahedral coordination. Since the photo-electron created due to a *1s* core level (a K-shell) must have *p*-like symmetry, the amount of overlap with the *d*-electron orbitals near the Fermi level can dramatically alter the number of available states to the *p*-electron, causing significant changes in the XANES spectrum. This argument would suggest that the pre-edge transition strength should be identically zero for inversion symmetric sites. However, quadrupole transitions can be weakly present because the transition Hamiltonian contains small terms that are nondipolar. Such terms can be observed in the pre-edge of most transition metal complexes.

Another important and common application of XANES is to use the shift of the edge position to determine the valence state. For example if we record XANES spectra of Fe_2O_3 and Fe_3O_4 , then edge position of Fe^{+3} will be at higher energy as compare to Fe^{+2} . If there is mixing of Fe^{+2} and Fe^{+3} in than with good model spectra, $\text{Fe}^{3+}/\text{Fe}^{2+}$ ratios can be determined with very good precision and reliability. Similar ratios can be made for many other ions. The heights and positions of pre-edge peaks can also be reliably used to empirically determine oxidation states and coordination chemistry. These approaches of

assigning formal valence state based on edge features and as a fingerprinting technique make XANES somewhat easier to crudely interpret than EXAFS, even if a complete physical understanding of all spectral features is not available.

2.2.5 EXAS data analysis:

There are four common techniques for analysing XAFS data. All rely, in one way or another, on making educated guesses as to what is in the material: While fingerprinting, linear combination analysis and Principle component analysis are generally used for interpretation of XANES data a model-based curve fitting technique is generally used to analyse the EXAFS data. In this technique, a theoretical spectrum is generated based on a guess as to the structure of the material, and then the variable parameters of the guessed structure are adjusted so as to match the measured spectrum. This is the only technique which can provide information about structures for which there are no good standards and is the only way of reliably measuring quantitative information such as bond lengths.

Usually in the EXAFS data analysis process after collecting the data in to energy space, first step is to convert it into k space. The data can be fit in k -space (i.e. as a function of k), or they can be Fourier transformed into an r -space (half path length) representation. In this representation the faster oscillations in $\chi(k)$ (which correspond to long path lengths) are represented as r -space peaks that are located at high r . Larger amplitude oscillations in $\chi(k)$ give larger peaks in r -space. Different contributions can be isolated by Fourier filtering and fit in k -space.

Bruce Ravel and co-workers have developed a bunch of computer codes which provides graphical interface to the extensive analytical and numerical capabilities of the IFEFFIT library [185-187]. This software package includes (i) ATHENA, a program for data processing, (ii) ARTEMIS, a program for analysis of extended X-ray absorption fine

structure (EXAFS) data using theoretical standards computed by the FEFF program [188, 191] and (iii) HEPHAESTUS, a collection of beamline utilities based on tables of atomic absorption data.

2.2.6 Data reduction using Athena:

The raw experimental EXAFS data needs some pre-processing before a meaningful data analysis can be carried out to extract relevant information. The data processing includes such steps as conversion of raw data to $\mu(E)$ spectra, background subtraction, energy calibration of spectra, alignment of data, use of reference spectra, deglitching (i.e. the removal of spurious points from spectra), merging of data by calculating the average and standard deviation at each point in a set of spectra and finally Fourier transforming and plotting. The above steps are carried out in the ATHENA subroutine.

ATHENA also supports powerful pre-processing of data as it is imported, including automated deglitching, truncation, alignment and constraint of analysis parameters. Background subtraction is performed using the AUTOBK algorithm [190] which determines an empirical background spline based on a distinction between data and background in terms of Fourier components. Edge-step normalization of the data is determined by a linear pre-edge subtraction and regression of a quadratic polynomial beyond the edge. The difference between these two polynomials extrapolated to the edge energy E_0 is used as the normalization constant in the definition of:

$$\chi(E) = \frac{\mu(E) - \mu(E_0)}{\mu_0(E_0)} \quad (2.15)$$

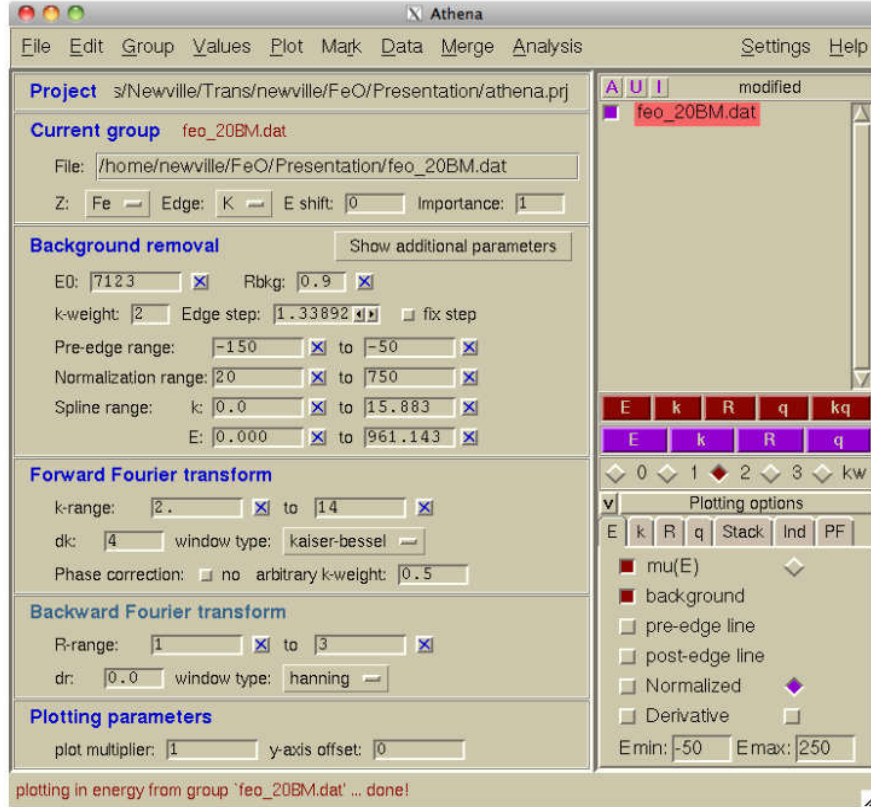


Figure 2.11: Screenshot of the ATHENA software code.

Normalized data are typically presented after subtracting the curvature of the regressed quadratic and the difference in slope between the post- and pre-edge polynomials after the edge.

The absorption edge E_0 is determined automatically as the data is imported by finding the first large peak in the first derivative of the $\mu_0(E)$ spectrum but can also be set interactively. ATHENA also provides utilities for calculation of difference spectra, for fitting line shapes (arctangent, Gaussian, Lorentzian) to spectra, and for fitting linear combinations of standard spectra to unknown spectra. ATHENA can also import and display the results of FEFF8 calculations [162] for comparison with measured data. A significant feature of ATHENA is that processing and displaying many data sets simultaneously is as simple as for

a single data set. The parameters controlling background removal and Fourier transforms can be adjusted for each data set individually or constrained in a flexible manner between data sets. Additional features include principle component analysis and self-absorption corrections for fluorescence data. Once the raw data has been processed appropriately, it is used in ARTEMIS for theoretical modelling and fitting.

2.2.7 Data fitting using Artemis:

ARTEMIS is a graphical interface for EXAFS data analysis and a front-end for FEFF and IFEFFIT built using DEMETER. ARTEMIS includes access to the functionality of the ATOMS program, which generates input file format suitable for FEFF. In EXAFS analysis, a theoretical model of the data is constructed containing unknown parameters and their values are determined by fitting. ARTEMIS can read crystallographic data either in the form of an ATOMS input file or a crystallographic information file (.cif) or can be supplied structure information interactively. These data are then converted into a FEFF input file. ARTEMIS includes access to the functionality of the ATOMS program, which converts crystallographic data into a format suitable for FEFF. FEFF is an *ab initio* multiple scattering code used to generate theoretical fitting standards for EXAFS analysis and simulation of XANES spectra [162] FEFF performs its calculation in real-space on a specified cluster of atoms provided by ATOMS subroutine. $f(k)$ and $\delta(k)$ (the scattering amplitude and phase shift due to the neighbouring backscattering atom respectively) and the photoelectron mean free path $\lambda(k)$ are calculated theoretically. After the FEFF run, ARTEMIS displays a page containing a concise interpretation of the paths computed by FEFF including the path distances, degeneracy, atomic species in the path, whether the path is single or multiple-scattering. Each scattering path has variable parameters such as degeneracy N (the number of equivalent atoms in single scattering paths), an effective distance R (half path-length), and a mean square variation

parameter σ^2 , as mentioned in the canonical EXAFS equation (equation 2.6). Once calculated, each of these paths can be easily modified to give a different N , R , σ^2 , and even E_0 (if that is necessary).

Some of the fitting parameters are correlated, for example, N and σ^2 , however their effect on spectrum is different. The coordination number affects the amplitude parameter uniformly as a function of k and on the other hand σ^2 also affects the amplitude, but it has a greater effect at high k than at low k . A similar correlation is observed between ΔE_0 and the distance R . Both affect the slope of the phase, but in different ways. In case of high

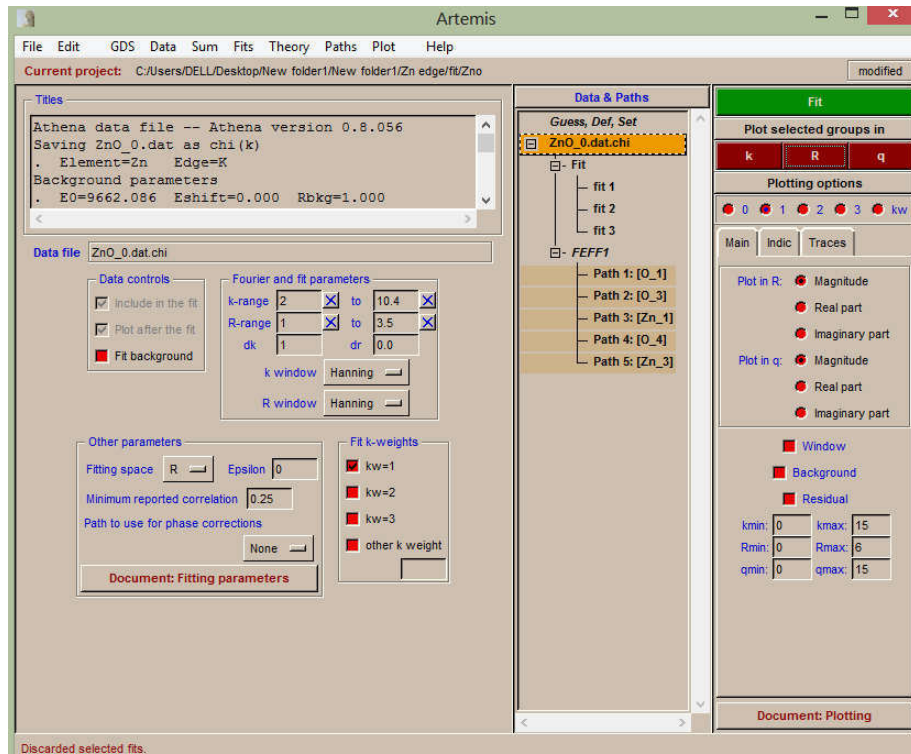


Figure 2.12: Screenshot of the ARTEMIS software code.

correlations, the fitting problem becomes poorly determined and numerically unstable and introduces large error in parameter values. To avoid this problem different strategy can be adopted, such as multiple k weight fit or multiple data sets fit. The number of independent parameters that can be varied during a fitting is limited by information available. Adding

unnecessary parameters may introduce correlations that will cause the error bars to inflate, so the information about the original parameters is masked. EXAFS data exist over a finite range in both k -space and r -space, and therefore they have limited information content. It is known from a Fourier series expansion that only a finite number of coefficients are needed to represent a signal of fixed bandwidth. All of the data in the FT exist on an array of N points in size. If we assume that the k window width is Δk wide, and the r -space data are contained in total width ΔR , the grid spacing's respectively are δk and δr where $\delta r = \pi/(N\delta k)$. The maximum r value in the r space is $(N/2)\delta r = \pi/(2\delta k)$, where the factor of two comes in because half the space is allocated to negative frequencies which offer no new information. The fraction of the total information contained within ΔR is then $2\delta k\Delta R$. The number of k -space data points in the window is (about) $\Delta k/\delta k$. But most of these data points actually carry no information, because the signal can be accurately represented within only a fraction of the total r -space. Therefore, the actual information content in the data is number of k -space points $\Delta k/\delta k$ times the compression factor $2\delta k\Delta R$. This gives a total “independent point” count of $N_{\text{ind}} = 2\Delta k\Delta R/\pi$, also called the Nyquist theorem. Stern [170] has however, argued that a more precise value is $N_{\text{ind}} = 2\Delta k\Delta R/\pi + 2$. ARTEMIS is equally well suited to simple first-shell analysis of single data sets as well as the most challenging fitting models. Among its advanced features are:

- (i) Simultaneous refinement of multiple data sets.
- (ii) Refinement using multiple k -weightings for any data set.
- (iii) Use of multiple FEFF calculations in a single fit.
- (iv) Co-refinement of a background spline to reveal correlations between the spline and the fitting parameters.
- (v) Arbitrary constraints between and restraints on parameters.

Goodness of Fit

The experimental data fitting process based on some theoretical modelling invariably includes some presumably known or determinable experimental uncertainties from random noise and other influences. These can be divided into random noise (such as photon counting) and non-random (systematic) errors. It is important to track and eliminate the systematic errors, but they cannot be completely eliminated. While fitting data we systematically vary the hypothetical values of the “unknown” (i.e. only partially known) parameters to give the best agreement with the experimental data. We will not achieve perfect agreement with the data, because of the noise and other uncertainties (“errors”), however we can determine how far we can vary the parameters around the best-fit values while still getting an acceptable fit to within the experimental (and theoretical) errors. The quality of a fit can be quantified by a comparison between the experimental data and the theoretical fit. The simplest approach is to calculate the squared deviation between the data and theory. The deviation (“residual”) is squared so that both positive and negative deviations contribute positively to the error statistic. If there are many data points the squared deviations are summed:

$$\chi^2 = \sum_{i=\min}^{\max} [(\chi_d(r_i) - \chi_t(r_i))^2]$$

Where, $\chi_d(r_i)$ is the i th measured data point, $\chi_t(r_i)$ represents the theory function, which depends on the independent variable r_i . For EXAFS fitting the goodness of fit can be determined by the following quantities:

- **Chi-square:**

$$\chi^2 = \frac{N_{iap}}{\varepsilon N_{data}} \sum_{i=\min}^{\max} [Re(\chi_d(r_i) - \chi_t(r_i))^2 + Im(\chi_d(r_i) - \chi_t(r_i))^2]$$

where $\chi(r)$ is the Fourier Transformed EXAFS data (which is a complex quantity) and the subscripts d and t denote data and theory respectively and ε = measurement uncertainty

- **Reduced chi-square:**

Chi square scaled by degrees of freedom ν

$$\chi^2_\nu = \frac{\chi^2}{\nu}$$

where

$$\nu = N_{\text{datap}} - N_{\text{var}}$$

The values of $\chi^2_\nu \sim 10$ or higher typically for good quality EXAFS data.

- **R-factor:**

It is the fractional misfit between experimental data and the theoretical fit.

$$R \text{ factor} = \frac{\sum_{i=\text{min}}^{\text{max}} [\text{Re}(\chi_d(r_i) - \chi_t(r_i))^2 + \text{Im}(\chi_d(r_i) - \chi_t(r_i))^2]}{\sum_{i=\text{min}}^{\text{max}} [\text{Re}(\chi_d(r_i))^2 + \text{Im}(\chi_d(r_i))^2]}$$

. In all the EXAFS fittings presented in this thesis, uncertainties in the fitting parameters have been estimated and typical values are $\pm 0.05 \text{ \AA}$ in R , $\pm 10\%$ in coordination number (N) and ± 0.001 in DW factor (σ^2).

2.3 Other characterisation techniques:

As has been mentioned earlier, apart from XAFS, the samples have also been characterised by several other complementary techniques viz., X-ray diffraction (XRD), transmission electron microscopy (TEM), fourier-transform infra-red spectroscopy (FTIR), Raman spectroscopy, Photoluminescence (PL), magnetic measurements etc. which are also discussed below briefly.

2.3.1 X-ray diffraction:

X-ray diffraction techniques are used for the identification of crystalline phases of various materials and the quantitative phase analysis subsequent to the identification. X-ray diffraction techniques are superior in elucidating the three-dimensional atomic structure of crystalline solids. The properties and functions of materials largely depend on the crystal

structures. X-ray diffraction techniques have, therefore, been widely used as an indispensable means in materials research, development and production [191].

The Bragg equation, $n\lambda = 2d\sin\theta$ is one of the keystones in understanding X-ray diffraction. In this equation, n is an integer, λ is the characteristic wavelength of the X-rays impinging on the crystallize sample, d is the interplanar spacing between rows of atoms, and θ is the angle of the X-ray beam with respect to these planes. When this equation is satisfied, X-rays scattered by the atoms residing in the plane of a periodic structure are in phase and diffraction occurs in the direction defined by the angle θ . In the simplest instance, an X-ray diffraction experiment consists of a set of diffracted intensities and the angles at which they are observed. This diffraction pattern can be thought of as a chemical fingerprint, and chemical identification can be performed by comparing this diffraction pattern to a database of known patterns. For all samples used in this thesis a Rigaku, Japan made X-ray diffractometer (model: Miniflex-II) was used.



Figure 2.13: Photograph of X-ray diffractometer (Model: Miniflex-II, Rigaku, Japan)

2.3.2 Transmission Electron Microscopy:

The use of optical microscope limited the ability to resolve an object because of its wavelength. TEM or Transmission Electron Microscopy uses electron beam of much shorter wavelength as a probe and hence details of a specimen can be observed to a much magnification level than the conventional optical microscopes. In TEM a beam of electrons is accelerated up to high energy levels (few hundreds keV) and focused on a material, they can then scatter or backscatter elastically or inelastically, or produce many interactions, source of different signals such as X-rays, Auger electrons or light. Some of them are used in transmission electron microscopy (TEM). An image is formed from the interaction of the electrons transmitted through the specimen; the image is magnified and focused onto an imaging device, such as a fluorescent screen, on a layer of photographic film, or to be detected by a sensor such as a CCD camera [192].

The conventional diffraction mode used in TEM is called selected area diffraction (SAED). The spherical aberrations of the objective lens limit the area of the selected object to few hundred nanometres. SAED patterns of a crystal permit to obtain the symmetry of its lattice and calculate its inter-planar distances using Bragg's law. This is useful to confirm the identification of a phase, after assumptions generally based on the literature of the studied system and on chemical analyses.



Figure 2.14: Photograph of the Transmission Electron Microscope (Technai G2 S-Twin (FEI, Netherlands)) used in this thesis work.

2.3.3 FTIR Spectroscopy:

FTIR is a technique used to obtain an infrared spectrum of absorption or emission of a solid, liquid or gas. An FTIR spectrometer simultaneously collects high-spectral-resolution data over a wide spectral range. This confers a significant advantage over a dispersive spectrometer, which measures intensity over a narrow range of wavelengths at a time. The term Fourier-transform infrared spectroscopy originates from the fact that a Fourier transform (a mathematical process) is required to convert the raw data into the actual spectrum. For other uses of this kind of technique, see Fourier-transform spectroscopy [193].



Figure 2.15: Photograph of Fourier transform infrared (FTIR) spectrometer (NICOLET 6700) used in this thesis work.

2.3.4 Raman spectroscopy:

Raman spectroscopy is a scattering technique, which used to observe vibrational, rotational, and other low-frequency modes in a system. It is based on Raman Effect, i.e., frequency of a small fraction of scattered radiation is different from frequency of monochromatic incident radiation [194]. It relies on inelastic scattering, or Raman scattering, of monochromatic light, usually from a laser in the visible, near infrared, or near ultraviolet range. The laser light interacts with molecular vibrations, phonons or other excitations in the system, resulting in the energy of the laser photons being shifted up or down. The shift in energy gives information regarding the interaction. Raman scattering is one of the effective techniques to investigate lattice disorder and defects created in a host lattice upon incorporation of dopants [195, 196]. Raman spectroscopy has also proven [197] to be a very sensitive technique to detect secondary phases in TM-implanted

ZnO. In this thesis programme Raman spectra were taken with a Reinshaw micro-Raman spectroscope.

2.3.5 Photoluminescence:

Photoluminescence spectroscopy is used to measure the radiative defects present in the sample. Photon on specific energy causes generation of electron-holes within the material and excitation of this electron to higher allowed states. When these electrons return to their equilibrium states, the excess energy is released and electron and holes can either recombine non-radiatively by emitting phonons (or collision transfer to other particles) or radiative by emitting the photons. Photo-luminescence (PL) spectra of the samples were recorded using an Edinburgh FL920 instrument.

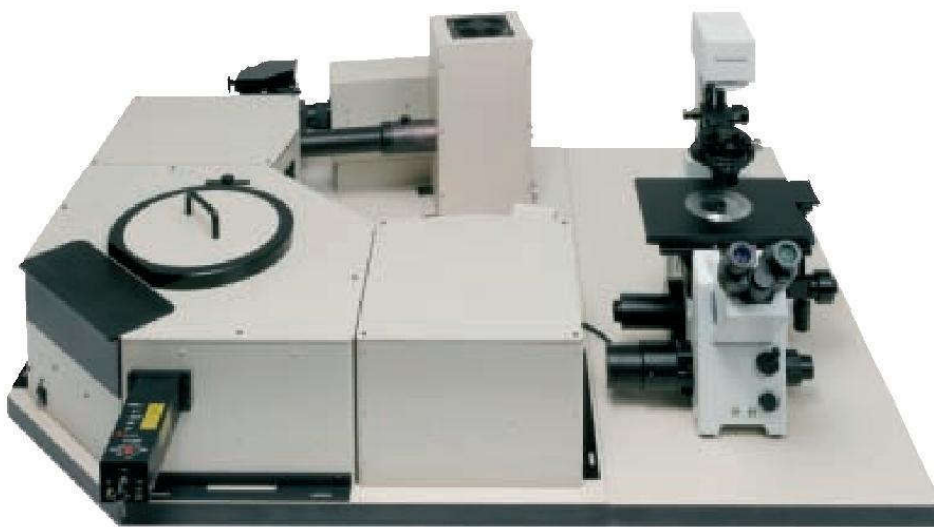


Figure 2.16: Photograph of Edinburgh spectroscopic Photoluminescence instrument.

2.3.6 Magnetic measurements:

For most of the samples discussed in this thesis, the magnetic properties have been measured by a SQUID (for superconducting quantum interference device) magnetometer which is a very sensitive equipment used to measure extremely subtle magnetic fields, based on superconducting loops containing Josephson junctions. SQUID magnetometer measures the magnetic moment of a sample by moving it through superconducting detection coils. The detection coils are connected to the SQUID device through superconducting wires, allowing the current from the detection coils to inductively couple to a SQUID sensor (based on a Josephson junction). As the sample moves through the detection coils, the magnetic moment of the sample induces an electric current in the detection coils. The detection coils, the connecting wires and the SQUID input coil form a closed superconducting loop. Any change in the magnetic flux in the detection coils produces a change in the persistent current in the detection circuit, proportional to the change in magnetic flux. Since the SQUID works as a highly linear current-to-voltage converter, the variations in the current in the detection coils produce corresponding variations in the SQUID output voltage which are proportional to the magnetic moment of the sample.

Fig.2.17 shows the photograph of the commercial SQUID systems, 7-Tesla SQUID-vibrating sample magnetometer (SVSM; Quantum Design Inc., USA) used in this thesis work.



Figure 2.17: Photograph of SQUID-vibrating sample magnetometer.

2.3.6 Theoretical calculations:

In this thesis work Density functional theory (DFT) [198-199] based electronic structure calculations has also been carried out on doped and co-doped ZnO systems to support the experimental findings. For this purpose, we have used Vienna ab-initio simulation package (VASP) within the framework of the projector augmented wave (PAW) method [200-201]. For exchange–correlation (XC) functional, we employ generalized gradient approximation (GGA) given by Perdew–Burke–Ernzerhof (PBE) [202]. The plane waves are expanded with energy cut off of 400 eV. We use Monkhorst–Pack scheme for k-point sampling of Brillouin zone integration with $12 \times 12 \times 6$. The convergence criteria for energy in SCF cycles is chosen to be 10⁻⁶ eV. The geometric structures are optimized by minimizing the forces on individual atoms with the criterion that the total force on each atom is below 10⁻² eV/Å. In order to probe the effect of strong-correlation, we also perform the calculations

using the DFT+U method, where U is the on-site Coulomb interaction between the electrons of D-orbitals of Fe atoms and we have performed the calculations for $U = 1-4$ eV.

Chapter-3

Fe & Cr doped ZnO Nanocrystals (NCs)

In the present section of this chapter, we have presented the results of our investigations by XAS measurements on the origin of room temperature ferromagnetism (RTFM) in Fe, and Cr doped ZnO NCs. The advantage of using XAS techniques in probing the local structure around the host and dopant atoms in these materials and hence in interpretation of their magnetic properties have already been discussed in detail in Chapter-1.

3.1 Fe Doped ZnO:

Several studies have been performed to understand the origin of ferromagnetism in Fe doped ZnO nanocrystals for examples, Tamura et al. [203] got RTFM in Fe-doped ZnO thin film while not for Mn and Co-doped ZnO. Singhal et al. [204] reported weak ferromagnetism at room temperature in colloidal Fe-doped ZnO nanocrystals and described that as an intrinsic property. Kumar et al. [205] also have shown weak ferromagnetism at room temperature in polycrystalline Fe-doped ZnO nanorods. On the other hand, Mishra et al. [206] reported the weak ferromagnetism at room temperature in Fe doped ZnO nanocrystals and Zn-vacancy was taken to be responsible behind the ferromagnetic order. In some recent studies [207] magnetic anisotropy of the dopant cation has been proposed to be a signature of intrinsic ferromagnetism in dilute magnetic oxide materials. Although there is significant progress and exciting experimental data, the origin of ferromagnetic ordering in DMS nanostructures remain poorly understood. In this study to gain more insight into the origin of ferromagnetic ordering, XAS study has been carried out on sol-gel derived Fe doped ZnO NCs.

3.1.1 Experimental Details:

$\text{Zn}_{1-x}\text{Fe}_x\text{O}$ ($0 \leq x \leq 0.06$) samples (named as Fe0, Fe0.5, Fe1, Fe1.5, Fe2, Fe4, and Fe6 for Fe-concentration $x = 0, 0.005, 0.01, 0.015, 0.02, 0.04$, and 0.06 respectively) are synthesized by the sol-gel method mentioned in Chapter 2. Appropriate proportions of analytical grade metal nitrates $\text{Zn}(\text{NO}_3)_2 \cdot 6\text{H}_2\text{O}$ (99.9% purity) and $\text{Fe}(\text{NO}_3)_3 \cdot 9\text{H}_2\text{O}$ (99.9% purity) powders were thoroughly mixed. The mixture was dissolved in aqueous solution of citric acid [$\text{C}_6\text{H}_8\text{O}_7$] (99.6% purity) while stirring to obtain a homogeneous precursor solution. The citric acid serves as a fuel for the reaction. The precursor solution was dried at 80°C for 3h to obtain xerogel and the swelled xerogel was kept at 130°C for 12h to complete. After grinding, the xerogel powders were sintered at 600°C for 10h at air atmosphere to get $\text{Zn}_{1-x}\text{Fe}_x\text{O}$ nanoparticles.

Structural characterization of $\text{Zn}_{1-x}\text{Fe}_x\text{O}$ samples was performed by X-ray diffractometer (Model: Miniflex-II, Rigaku, Japan) with $\text{Cu K}\alpha$ radiation ($\lambda = 1.5406 \text{ \AA}$). The EXAFS measurements were carried out at the dispersive EXAFS beamline (BL-8) at the Indus-2 Synchrotron Source (2.5 GeV, 120 mA) at the Raja Ramanna Centre for Advanced Technology (RRCAT), Indore, India. The details of the beamline have been discussed in Chapter-2. TEM and HRTEM measurements were done with JEOL-2010 (Japan) and Technai G^2 S-Twin (FEI, Netherlands) respectively. Fourier transmission infrared (FT-IR) spectra of the samples (as pellets in KBr) were recorded using FT-IR Spectrometer (Spectrum One, Perkin Elmer Instrument, USA) in the range of $4000\text{--}400 \text{ cm}^{-1}$ with a resolution of 1 cm^{-1} . The powder samples are mixed with KBr to make pellets for the FT-IR measurements. Raman spectra were taken with a Reinshaw micro-Raman spectroscope using 514.5 nm Ar^+ laser as excitation source in the range of $200\text{--}1250 \text{ cm}^{-1}$. The powder samples are made into pellets for the Raman measurements. The photoluminescence (PL) spectra were taken by a Fluorescence Spectrometer (LS-45, Perkin Elmer, USA). The D.C magnetization (M-H)

measurements have been carried out by a Physical Properties Measurement System (PPMS) of Cryogenics Inc, USA and by a Vibrating Sample magnetometer (VSM) from Lakeshore (Model no: 7407). The resistivity measurements were done by the conventional two-probe method fitted with a Closed Cycle Cryo-cooler. Working principles of all the characterization techniques used for this study have been described briefly in Chapter-2.

3.1.2 Results and discussion:

X-ray Diffraction:

Rietveld refinement of the X-ray diffraction (XRD) patterns for $\text{Zn}_{1-x}\text{Fe}_x\text{O}$ ($0 \leq x \leq 0.06$) samples is shown in Fig. 3.1. All peak positions of Fe-doped ZnO correspond to the standard Bragg positions of hexagonal wurtzite ZnO (space group $P6_3mc$) have been shown by the vertical bars and the residue by the line respectively at the bottom of the XRD patterns. Fig. 3.1 shows that the Fe-doping does not lead to the appearance of any extra peaks or disappearance of any peak of the hexagonal wurtzite structure of pure ZnO, confirming the structure of the doped ZnO remains in wurtzite phase belonging to the space group $P6_3mc$. Therefore, the Rietveld analysis shows that the samples are single phase and no trace of other impurities has been found. All the XRD peaks have been indexed using the standard JCPDS file for ZnO. It should be pointed out that the impurities can be detected by XRD only when they form crystalline phases. Hence there is no crystalline impurity within the detection limit of X-rays.

The variation in the lattice parameters (' a ' and ' c ') and the volume of the unit cell have been measured from Rietveld refinement of the X-ray diffraction data and are shown in Fig. 3.2.

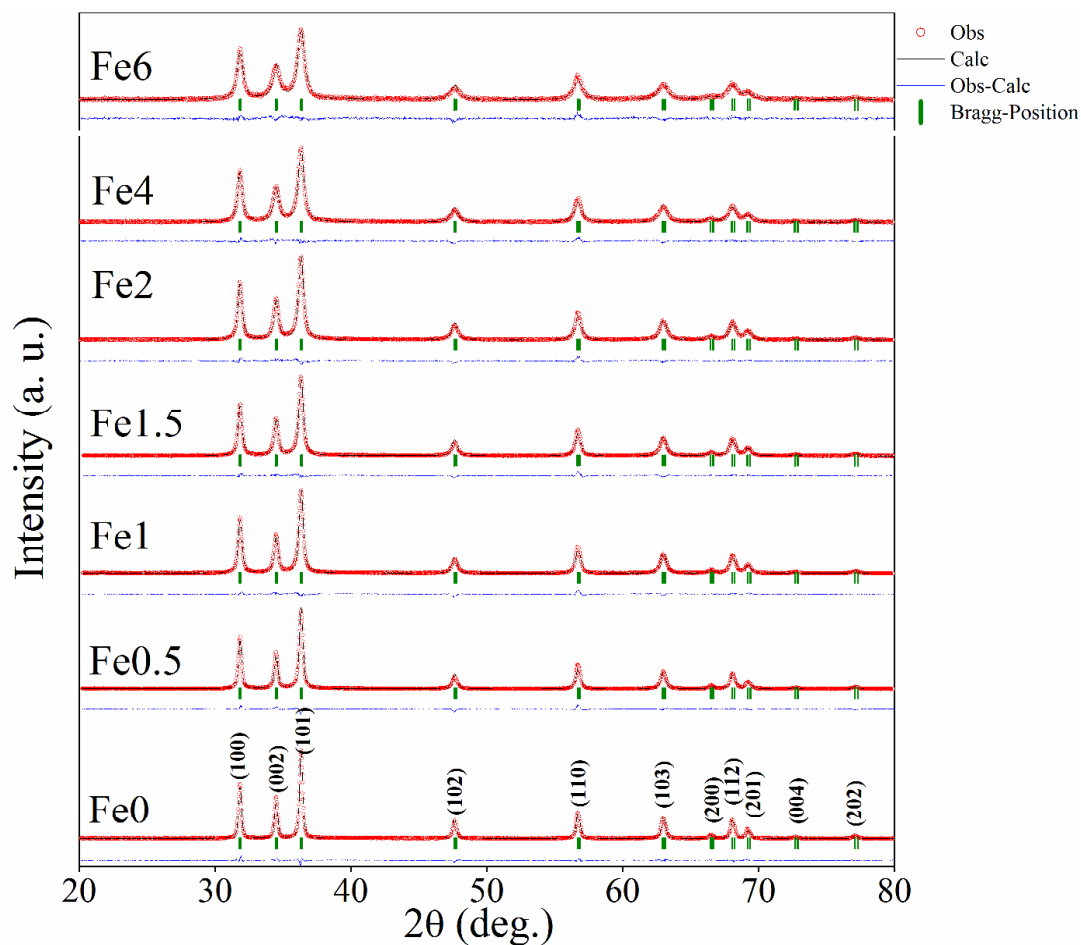


Figure 3.1: Rietveld refinement profiles of X-ray diffraction data of the $\text{Zn}_{1-x}\text{Fe}_x\text{O}$ ($0 \leq x \leq 0.06$) samples. The circle represents the observed data (Obs) while solid line through the circles is the calculated profile (Calc), vertical tics below curves represent allowed Bragg-reflections for the wurtzite phase. The difference pattern of the observed data and calculated profile (Obs–Calc) is given below the vertical tics.

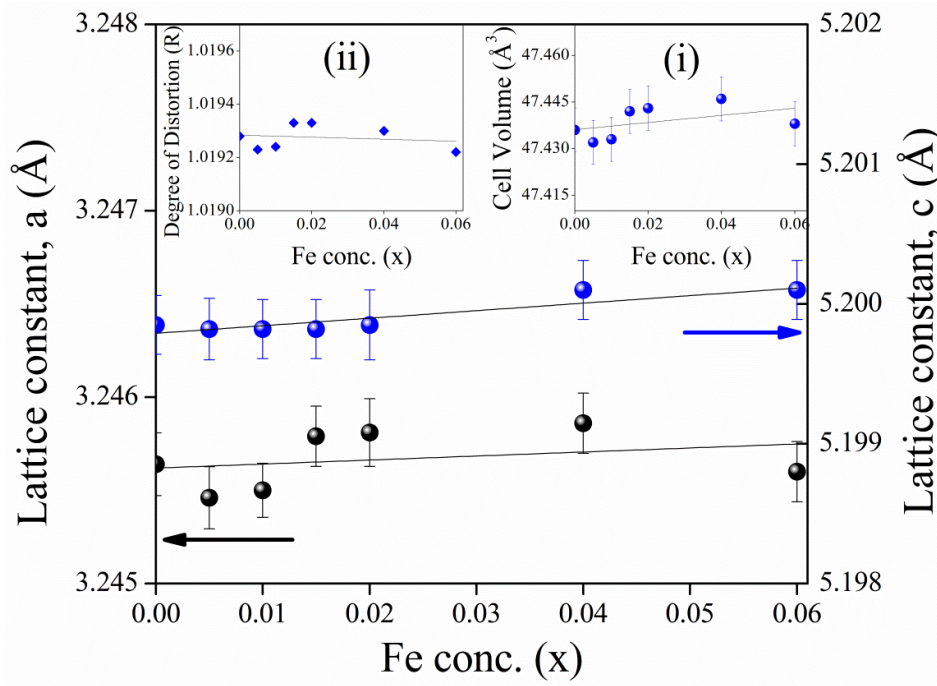


Figure 3.2: Variation of lattice parameter ('a' and 'c') with Fe-concentration (x) calculated from Rietveld refinement. The inset (i) shows the variation of the unit cell volume and inset (ii) shows the variation of the degree of distortion (R).

Fig. 3.2 shows that there is small increase in the lattice parameters 'a' and 'c', and the volume of the unit cell due to increase of Fe ion doping. This result is similar to the previous observations [208-212]. Moreover, FTIR205 studies confirm that Fe-ions did not enter into the octahedral coordination (as discussed letter). To explain small increment of lattice parameters 'a' and 'c' and unit cell volume (V), we have considered the distortion of Zn tetrahedron [213,214] due to Fe-doping. In an ideal wurtzite structure there are two interpenetrating hexagonal-close-packed (*hcp*) sub-lattices with two lattice parameters, *a* and *c*, in the ratio of $c/a = \sqrt{8/3}$. Each of the sub-lattices consists of one type of atom displaced with respect to each other along the three-fold *c*-axis by the amount of 3/8 in an ideal wurtzite structure. Again, *a/c* is the measure of the distortion from its ideal tetrahedron and

the degree of distortion $R = [\sqrt{8/3} (a/c)]$ where $R=1$ gives the ideal wurtzite structure [215] with $c/a = \sqrt{8/3}$. In a real ZnO crystal, the wurtzite structure deviates from the ideal arrangement, by changing the a/c ratio or the R value. The variation of the degree of distortion R is shown in the inset (ii) of Fig. 3.2. In wurtzite ZnO, the Zn- tetrahedron have base in the ab -plane and apex along the c -direction. Different parameters such as a , c , c/a , bond lengths, bond angles, etc. have been calculated from Rietveld refinement and following Morkoc and Özgür [213, 214]. Values of different parameters such as a , c , c/a , bond lengths, bond angles, etc. have been given in Table 3.1 and variations of bond angles and bond lengths with Fe concentration are shown in Figs. 3.3(a) and (b) respectively.

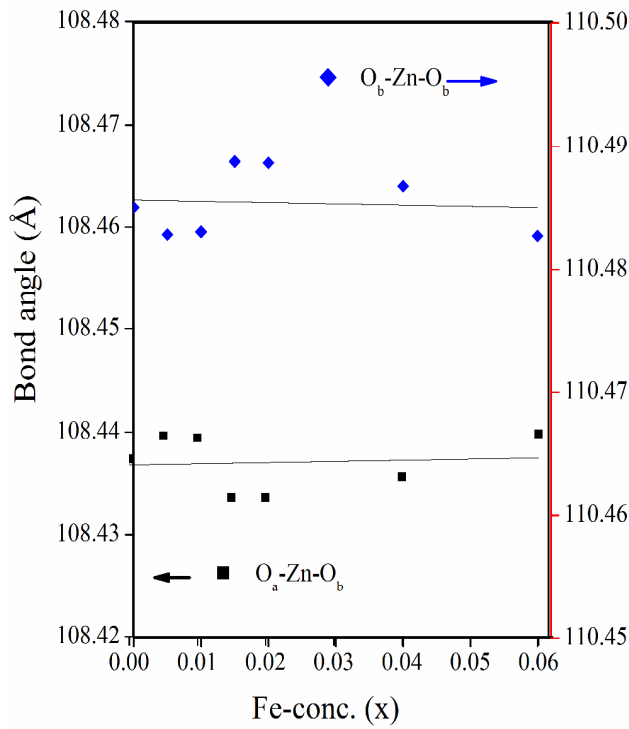


Figure 3.3:(a) Variation of average basal bond angles (O_b-Zn-O_b) and average base-apex angles (O_b-Zn-O_a) with Fe-concentration (x).

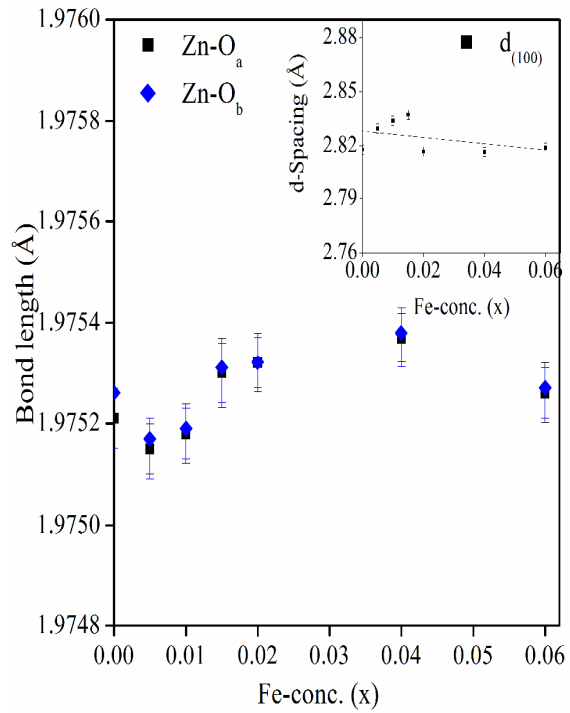


Figure 3.3:(b) Variation of bond length $Zn-O_a$ and $Zn-O_b$ with Fe-concentration (x). Inset of (b) shows the variations of inter planer spacing.

Table-3.1: Values of lattice parameters, bond lengths and bond angles.

Parameter	Fe0	Fe0.5	Fe1	Fe1.5	Fe2	Fe4	Fe6
a (Å)	3.24564	3.24546	3.24550	3.24579	3.24581	3.24586	3.24560
c (Å)	5.19985	5.19982	5.19982	5.19982	5.19985	5.2001	5.20010
c/a	1.60210	1.60218	1.60217	1.60202	1.60202	1.60207	1.60219
U	0.37986	0.37985	0.37985	0.37988	0.37988	0.37987	0.37985
$d_{\text{Zn-O}_a}$ (Å)	1.97521	1.97515	1.97518	1.97530	1.97532	1.97537	1.97526
$d_{\text{Zn-O}_b}$ (Å)	1.97526	1.97517	1.97519	1.97531	1.97532	1.97538	1.97527
$\text{O}_a\text{-Zn-O}_b$ (°)	108.43732	108.43960	108.43939	108.43356	108.43356	108.43556	108.43980
$\text{O}_b\text{-Zn-O}_a$ (°)	110.48503	110.48283	110.48304	110.48874	110.48864	110.48673	110.48271

From Fig. 3.3(a) it is seen that the average basal bond angles ($\text{O}_b\text{-Zn-O}_b$) and average base-apex angles ($\text{O}_b\text{-Zn-O}_a$) [where O_b and O_a are oxygen atoms at the base and at the apex respectively of the tetrahedron] are constant with Fe-doping. However, the bond length Zn-O_a and Zn-O_b both increase slowly [Fig. 3.3 (b)] giving rise to the slow increase of the lattice parameters a and c . This observation is consistent with the result explained on the basis of higher ionic radius. The degree of distortion R [inset (ii) of Fig.3.2] remains constant. It suggests that both the parameters a and c vary with the same manner with increasing Fe-concentration. The linear increase of the unit cell volume (V) is justified by quadratic increase of ' a '. Again, linear variation of lattice constants ' a ' and ' c ' with increasing Fe-concentration confirms that the doping of Fe ions does not change the wurtzite structure (space group $P6_3mc$) of ZnO and Fe-ion has been substituted into the crystal lattice following

the Vegard's law [216]. Variations of inter planer spacing (d -value) of (100) plane with increasing Fe-concentration are plotted in the inset of Fig. 3.3(b) which shows that d -value of (100) plane decreases with increasing Fe-concentration. This observation can be explained with the change of the bond lengths. The variation of bond lengths develops the lattice strain [217]. Lattice strain is defined as the ratio of the incremental change of the lattice parameter to its initial value. Consequently, this lattice strain changes the spacing of crystallographic planes (d -spacing). According to Bragg's Law, the Bragg angles should either decrease or increase when spacing of the crystallographic plane changes. Thus, the uniform tensile strain with increasing the d - spacing shifts a Bragg's peak to lower 2θ angle, whereas uniform compressive strain with decreasing the d - spacing shifts a Bragg's peak to higher 2θ angle in the spectrum. Since, for the (100) plane the d -spacing has decreased with Fe-concentration, [inset of Fig. 3.3(b)] we believe that a uniform compressive strain (hence stress) has been developed in the perpendicular direction of the plane (100). The crystallite size and lattice strain developed in different samples have been estimated from Williamson–Hall (W–H) plot [218] (see Table 3.2). A better estimation of the size and strain parameters can be obtained from ‘size-strain plot’ (SSP) [219] by using the following equation:

$$\left(\frac{d_{hkl}\beta\cos\theta}{\lambda}\right)^2 = \frac{k\lambda}{D}\left(\frac{d_{hkl}^2\beta\cos\theta}{\lambda^2}\right) + \left(\frac{\varepsilon}{2}\right)^2 \quad (3.1)$$

where d_{hkl} the interplaner spacing and ε is the average strain produced in the lattice. β , λ and D are described as earlier, k is the Scherrer constant ($= 0.9$). The plot of $(d_{hkl}\beta\cos\theta/\lambda)^2$ vs. $(d_{hkl}^2\beta\cos\theta/\lambda^2)$ is shown in Fig. 3.4. The crystallite size (D) and average strain (ε) have been estimated from the slope and the intercept of the linear fit of the plot respectively (see Table 3.2).

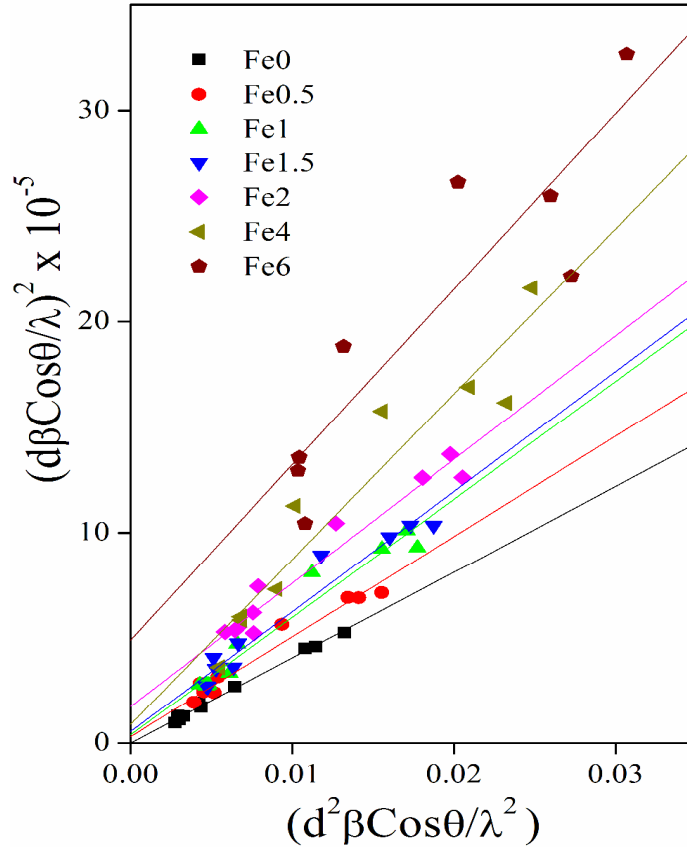


Figure 3.4: $(d_{hkl}\beta\cos\theta/\lambda)^2$ vs. $(d_{hkl}^2\beta\cos\theta/\lambda^2)$ plot of the ZnO: Fe samples to estimate crystallite size (D) and average strain (ϵ).

Fig. 3.5 shows the variation of crystallite size (D) and average strain (ϵ) (inset of Fig. 3.5) with Fe-concentration (x) estimated from size-strain plot. It is observed that the average crystallite size decreases with the increase of Fe-concentration. This result is consistent with the observation of Mishra et al. [220]. However, it reported the qualitative decrement of the grain size where as we have observed an exponential decay which is consistent with our earlier report [212] calculated from Debye–Scherrer’s equation. This is may be because of decrease in growth rate due to higher ionic radius of Fe^{+2} (0.77\AA) cation compared to Zn^{+2} (0.74\AA). Thus, different trends in particle size and lattice constant may be attributed to the intra and inter nucleating forces forming the nanocrystals [221].

Table-3.2: Crystallite size and average strain estimated from Williamson–Hall and Size Strain plot.

Sample	Particle Size (nm)			Strain	
	Scherrer formula	Size-Strain Plot	W-H Plot	Size-Strain Plot	W-H Plot
ZnO	32.71	33.75	33.18	2.89×10^{-4}	4.94×10^{-5}
Zn _{0.995} Fe _{0.005} O	24.99	29.19	30.45	3.52×10^{-3}	3.96×10^{-4}
Zn _{0.99} Fe _{0.01} O	21.82	24.85	25.28	4.01×10^{-3}	3.80×10^{-4}
Zn _{0.985} Fe _{0.015} O	21.24	24.37	26.21	4.71×10^{-3}	6.39×10^{-4}
Zn _{0.98} Fe _{0.02} O	18.68	23.66	25.76	8.36×10^{-3}	1.25×10^{-3}
Zn _{0.96} Fe _{0.04} O	15.68	17.71	20.36	6.01×10^{-3}	1.22×10^{-3}
Zn _{0.94} Fe _{0.06} O	14.50	16.67	20.70	14.01×10^{-3}	2.70×10^{-3}

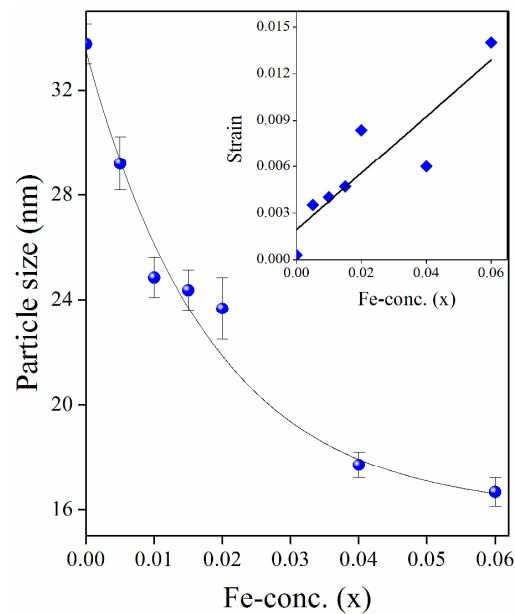


Figure 3.5: Variation of average crystallite size with Fe-concentration (x) estimated from size-strain plot. The inset figure shows the variation of strain estimated from size-strain plot.

Transmission Electron Microscopy:

The morphology and the microstructure of nanoparticles have been examined by transmission electron microscopy (TEM). A typical TEM, HRTEM and SEAD images of Fe₀ (pure ZnO) and Fe₂ nanoparticles are presented in Fig. 3.6. Figures 3.6(a) and 6(d) represent the TEM images of Fe₀ and Fe₂ nanoparticles respectively which show that the nanoparticles tend to coalesce into aggregate which is very common in magnetic nanoparticles. Closer look of TEM images of different parts of the sample tells that most nanoparticles are more or less spherical in shape having smooth surfaces. These nanoparticles contain very developed grain boundaries and free surfaces which may affect the physical properties as observed by Straumal et. al. [222,223]. The average particle size obtained from TEM measurements matches well with the size estimated from the XRD study. High-resolution TEM (HRTEM) gives insight into the detailed atomic structure of the nanoparticles. Figs. 3.6(b) and 3.6(e) show the HRTEM image of a single particle of Fe₀ and Fe₂ nanoparticles respectively. The HRTEM micrograph (Figs. 3.6(b) and 3.6(e)) shows that the interplanar spacing (*d*-value) of fringes is 0.280 nm and 0.274 nm for Fe₀ and Fe₂ respectively and it is in good agreement (slightly increased due to strain as discussed earlier) with the *d*-value of (100) plane (viz. 0.281 nm) of wurtzite ZnO. Moreover, it should be pointed out here that the *d*-value of the Fe-doped sample (e.g. Fe₂) determined from TEM measurements also has been decreased which supports the XRD analysis that the compressive strain has been induced due to Fe-doping in the system. The HRTEM pattern also indicates that all the nanoparticles are single crystalline in nature and are free from major lattice defects. The selected area electron diffraction (SAED) pattern (Figs. 3.6(c) and 3.6(f) for Fe₀ and Fe₂ respectively) also manifests the single crystalline nature of the samples. According to the results of XRD pattern and HRTEM images, we believe that the Fe-ions are well incorporated into the crystal lattice of ZnO.

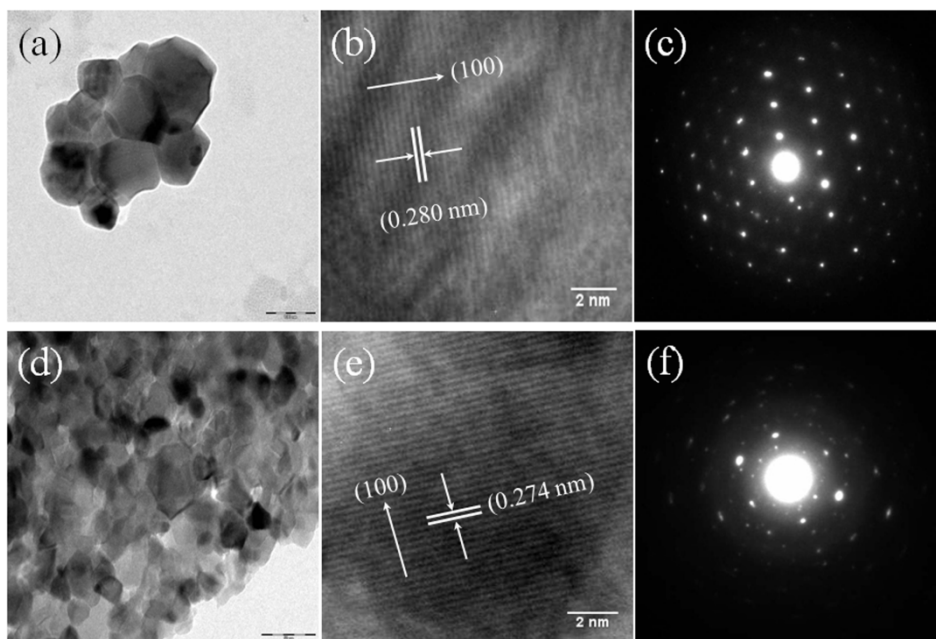


Figure 3.6: Low magnification TEM (a), HRTEM (b), and SAED (c) images of ZnO nanocrystals and low magnification TEM (d), HRTEM (e), and SAED (f) images of $\text{Zn}_{0.99}\text{Fe}_{0.02}\text{O}$ nanocrystals.

EXAFS at Zn K-edge:

The normalized EXAFS spectra of Fe doped ZnO NCs at Zn Kedge is shown in fig. 3.7. The radial structure function or the $\chi(R)$ vs. R (or FOURIER TRANSFORMED EXAFS) spectra in terms of the real distances from the centre of the absorbing atom have been generated from the $\mu(E)$ versus E spectra following the procedure [150] described in Chapter 2 is shown in fig. 3.8 along with the best fit. A set of EXAFS data analysis program (available within the IFEFFIT software package) have been used for reduction and fitting of the experimental EXAFS data.

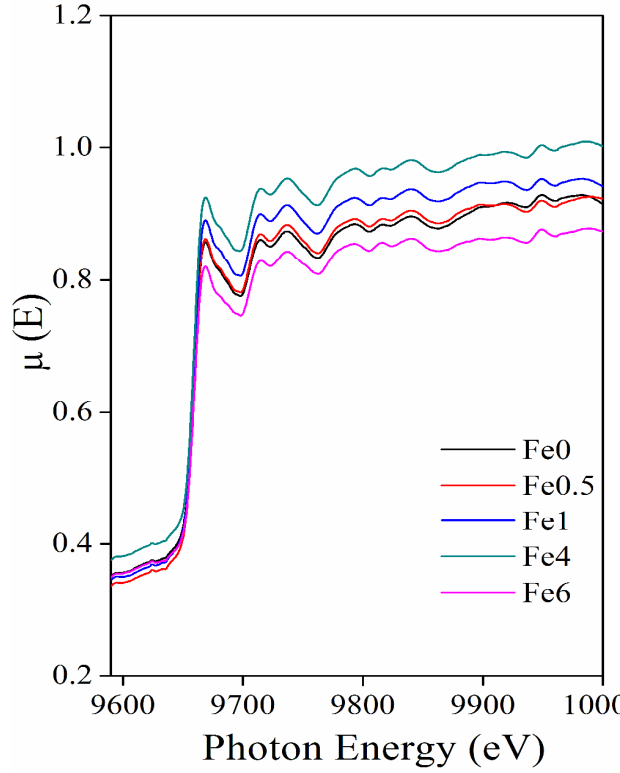


Figure 3.7: Normalized experimental EXAFS ($\mu(E)$ vs E) for undoped and Fe doped ZnO nanocrystals at Zn K-edge.

Fig. 3.8 shows the Fourier transformed EXAFS (Fourier transformed EXAFS) $\chi(R)$ versus R spectra of undoped and Fe doped ZnO samples at the Zn K-edge along with the best fit theoretical spectra. The theoretical Fourier transformed EXAFS spectra have been generated assuming the model described by Kisi et al. [224] namely the first oxygen shell (Zn–O1) at 1.98 Å with coordination number (CN) of 3, second oxygen shell (Zn–O2) at 1.99 Å having a CN of 1 and a Zn shell (Zn–Zn) at 3.21 Å with a CN of 12 in order to fit the first few peaks (in the k range of 3–10 Å⁻¹ and upto 3.5 Å in R space) obtained in the $\chi(R)$ versus R spectra of the samples. The variation in average bond lengths of the first two Zn–O shells and the bond length of the Zn–Zn shell is shown in Fig. 3.9, while total coordination numbers of the two Zn–O shells and coordination number of the Zn–Zn shell is shown in Fig. 3.10 and the average Debye-Waller factors (σ^2) of the first two Zn–O shells and Debye-Waller factor of the Zn–Zn shell is shown in Fig. 3.11 as a function of Fe doping concentration.

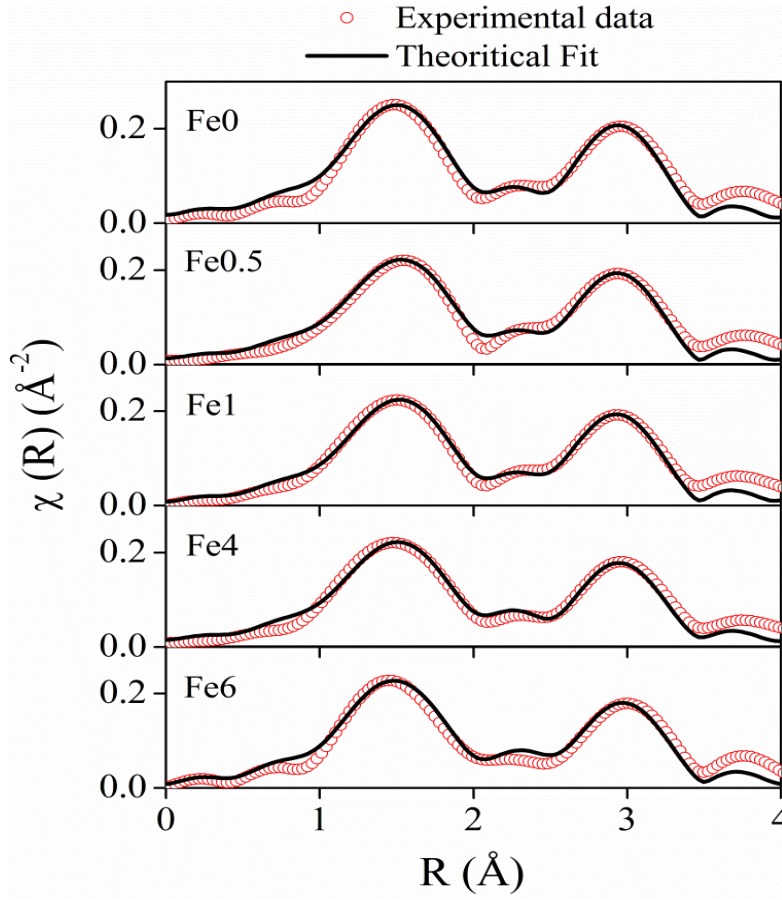


Figure 3.8: Fourier transformed EXAFS($\chi(R)$ vs. R) for undoped and Fe doped ZnO nanocrystals at Zn K-edge.

From Fig. 3.9 it is observed that up to 1% Fe doping, Zn–O bond lengths increase with increase in Fe doping concentration. This corroborates with the Fe K-edge XANES results (given below) which shows that Fe^{3+} substitutes Zn^{2+} in ZnO lattice and since ionic radius of Fe^{3+} (0.49\AA) is less than that of Zn^{2+} (0.60\AA), Fe atoms substituted in Zn sites attract oxygen atoms closer resulting in elongation of Zn–O bond lengths. Similar changes in bond lengths due to doping have been observed in many cases, for example in case Mn doped ZnO by Basu et. al. [225] and in Zr doped TiO_2 samples observed by Lippens et. al. [226] which were explained on the basis of difference in ionic radii. Also substitution of Fe atoms in Fe^{3+} states increases oxygen coordination in the neighborhood of Fe atoms to establish charge

balance. This leads to reduction of oxygen coordination in the neighborhood of Zn atoms manifesting the presence of oxygen vacancies in the sample which increases with increase in Fe doping concentration as shown in Fig. 3.10. It is corroborated with our earlier result that for dopant with lower ionic radius, oxygen vacancies are created near the host site i.e., in the neighborhood of Zn. However, Zn–Zn bonds remain almost unaltered due to low values of doping. It should also be noted that for more than 1% Fe doping, Zn sites get distorted significantly as manifested by the steep increase in Debye–Waller factor at Zn sites as shown in Fig. 3.11. It also corroborates by the fact that for more than 1% Fe doping, Zn–Zn bond length decreases significantly.

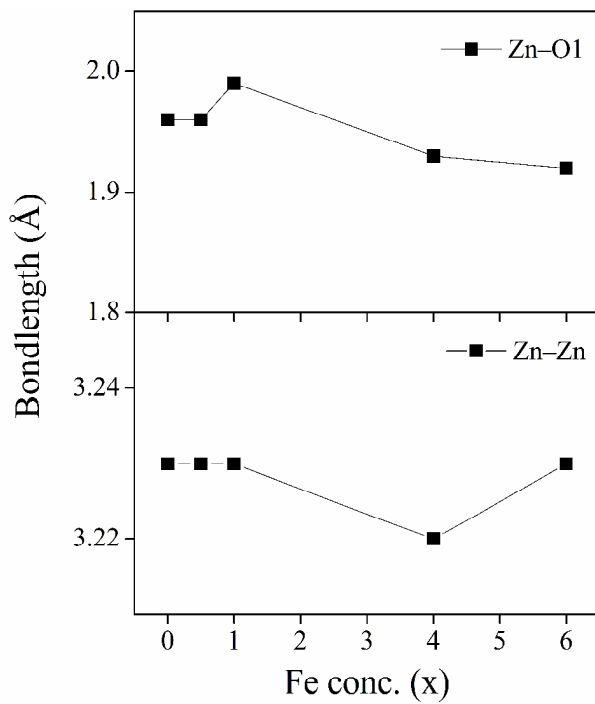


Figure 3.9: Variation of bond lengths of Zn-O shells and Zn-Znshells with change in doping concentration

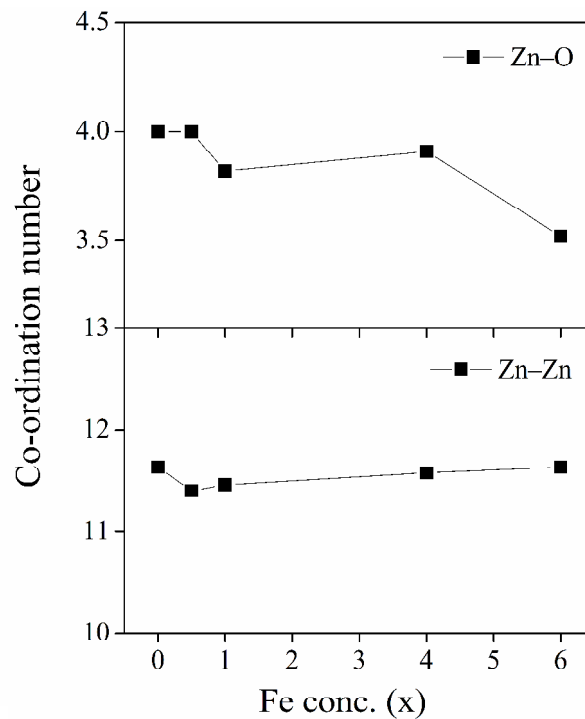


Figure 3.10: Variation of total coordination number of Zn-O shells and Zn-Zn shells with change in doping concentration.

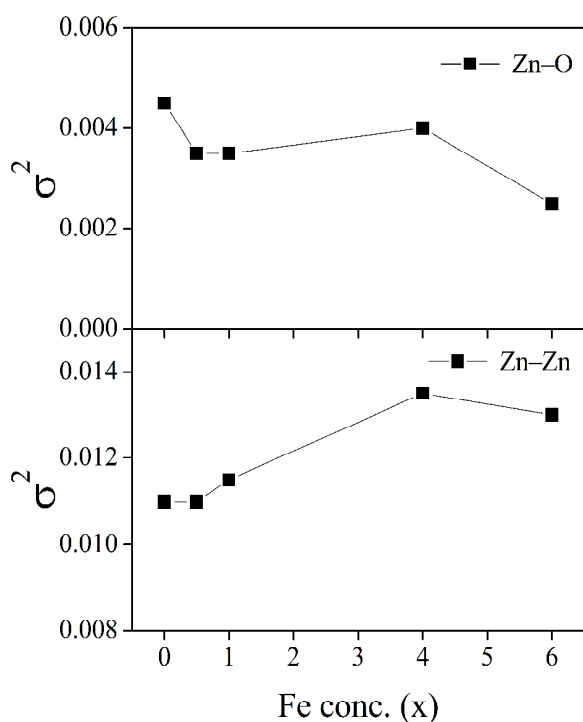


Figure 3.11: Variation of Debye-Waller factor of Zn-O shells and Zn-Zn shells with change in doping concentration.

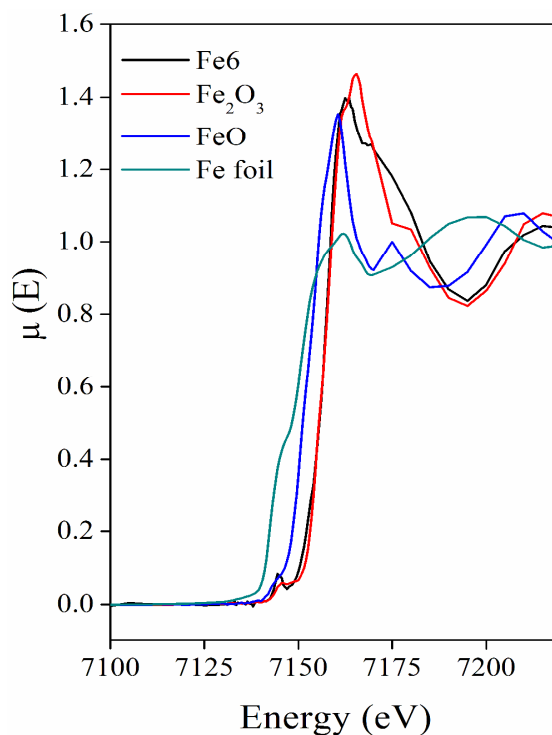


Figure 3.12: XANES spectrum of 6% Fe doped ZnO nanocrystal along with that of Fe metal foil and standard Fe_2O_3 and FeO samples.

XANES at Fe K-edge:

Fig. 3.12 shows the X-ray Absorption Near Edge Structure (XANES) measurements have been carried out at the Fe edge on the samples along with on Fe metal foil and a standard sample of FeO and Fe_2O_3 , where Fe is present in 0 and +2 and +3 oxidation states respectively. The results of the XANES measurements have been shown in for a representative sample with relatively higher Fe doping (viz., 6%, where possibility of clustering is higher) along with that of the standards. It has been observed that for all the samples the absorption edge of Fe appears at significantly higher energy than that in the Fe metal and they are close to the absorption edge of Fe in Fe_2O_3 . The XANES spectra of the samples also clearly resemble that of the Fe_2O_3 standard having characteristic white line. This clearly rules out the presence of metallic Fe clusters, FeO and Fe_2O_3 in the samples.

Raman Spectroscopy

Raman spectroscopy has been employed to confirm the crystalline quality of $\text{Zn}_{1-x}\text{Fe}_x\text{O}$ nanoparticles [227]. Fig. 3.13 represents the room-temperature Raman spectra of $\text{Zn}_{1-x}\text{Fe}_x\text{O}$ ($0 \leq x \leq 0.06$) nanocrystals. The wurtzite ZnO nanoparticles have six Raman-active phonon modes at 101 cm^{-1} (E_2 low), 381 cm^{-1} (A_1 TO), 407 cm^{-1} (E_1 TO), 437 cm^{-1} (E_2 high viz. E_{2H}), 574 cm^{-1} (A_1 LO), and 583 cm^{-1} (E_1 LO) respectively [228,229].

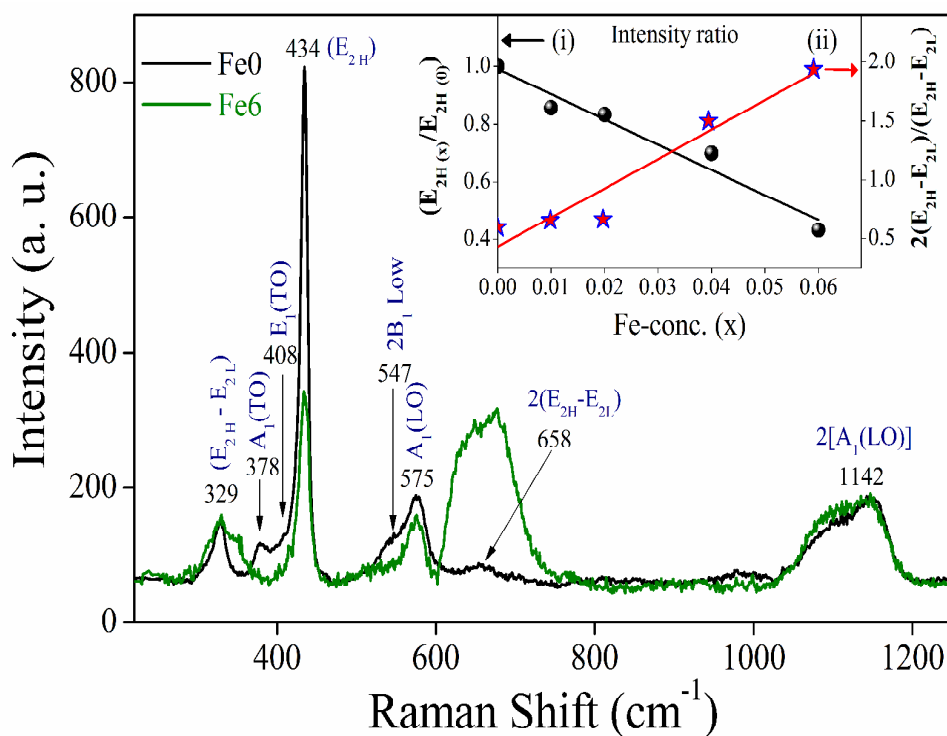


Figure 3.13 Room-temperature Raman spectra of $\text{Zn}_{1-x}\text{Fe}_x\text{O}$ ($0 \leq x \leq 0.06$) nanoparticles. Inset of figure shows the variation of the (E_{2H}) peak with Fe-concentration (x) with respect to its pure ZnO value (curve-I) and the variation of the $2(E_{2H}-E_{2L})$ peak value with x with Respect to its corresponding ($E_{2H}-E_{2L}$) peak value (curve-II).

Though, due to the limitation of the set-up, the phonon mode at 101 cm^{-1} (E_2 low) has not been observed, all other prominent peaks have been observed very clearly for ZnO and Fe-doped ZnO nanocrystals. The assignments of the Raman modes of $\text{Zn}_{1-x}\text{Fe}_x\text{O}$ nanoparticles obtained for different Fe-concentration (x) are summarized in Table 3.3. The

sharpest and strongest peak at about 434 cm^{-1} can be assigned to the nonpolar high-frequency optical phonon branch of E_2 mode (E_{2H}), which involves the motion of oxygen and is the characteristic of wurtzite structure. With increasing Fe-concentration pronounced weakening in peak height of this nonpolar E_{2H} mode for the Fe- doped ZnO samples as compared to undoped ZnO has been observed without any appreciable shifting and broadening in frequency of this mode. To estimate this variation with Fe-concentration, intensity ratio of $(E_{2H})_x/(E_{2H})_0$ [where $(E_{2H})_x$ and $(E_{2H})_0$ are the intensity of E_{2H} modes for Fe-concentration (x) and pure ZnO respectively] has been calculated and plotted in the inset of fig. 3.13. The intensity ratio of $(E_{2H})_x/(E_{2H})_0$ decreases linearly (see inset of Fig. 3.13) with increasing Fe-concentration (x). This result can be attributed to the fact that Fe^{2+} substitution induces the microscopic structural disorder in the periodic zinc atomic sublattice and reduces the translational symmetry giving rise to local distortions in the lattice. This local distortion and disorder disrupt the long-range ordering in ZnO and weakens the electric field associated with the mode [229]. In other words, this observation reveals that the local symmetry in the nanocrystals is different from that of undoped sample (i.e. ZnO), but the crystal structure remains the same. Close observation shows two very weak peaks at 408 cm^{-1} [E_1 (TO) mode] and 585 cm^{-1} [E_1 (LO) mode] in pure ZnO only. The peak at about 329 cm^{-1} and a broad shoulder centered at about 658 cm^{-1} for ZnO (Figure 13) seemed to have originated from a two-phonon process [230]. The peak at about 329 cm^{-1} can be attributed to single crystalline nature of ZnO [228,231] and assigned as a difference mode between the E_2 high and E_2 low frequencies [232,233] viz. $(E_{2H} - E_{2L})$. The peak height and frequency of this peak remains unaffected with Fe-doping concentration (Fig. 3.13). This suggests that the single crystalline nature remains unchanged due to Fe-doping and it supports the TEM observations. The mode at 658 cm^{-1} in pure ZnO nanostructure can be ascribed to the 2nd order mode [viz. $2(E_{2H}-E_{2L})$] of $(E_{2H}-E_{2L})$ arise due to multi-phonon processes [234,235]. Yang et. al. [235] observed this

vibration mode at 660 cm^{-1} and proposed this mode to be related to intrinsic host-lattice defects. For Fe-doped ZnO samples, this peak (at 658 cm^{-1} in pure ZnO) remains constant till $x=0.04$ but shifted to 680 cm^{-1} for $x=0.06$ sample. Comparing Figure 13, it has also been observed that the shoulder centered at about 658 cm^{-1} gradually becomes a peak by increasing its intensity with increasing Fe-concentration. The increment of this peak (2nd order mode) has been quantified by taking the ratio of the intensity of $2(E_{2H}-E_{2L})$ peak to that of $(E_{2H}-E_{2L})$ and the behavior has been plotted in the inset of Figure 13. Other 2nd order mode at around 1142 cm^{-1} [$2A_1(\text{LO})$] for ZnO remains unshifted with increasing Fe-concentration. It should be noted here that we assigned the modes as 2nd order whose frequency is nearly double of any 1st order mode. The weak mode $A_1(\text{TO})$ at 378 cm^{-1} for ZnO remains unchanged in Fe-doped samples up to $x=0.04$ and the mode has been shifted to the lower frequency- 354 cm^{-1} and called as NM for the sample $x=0.06$ (which does not appear in Raman spectrum for Fe0 to Fe4). Ye et. al. [236] considered two possible mechanisms to ascribe the origin of this anomalous mode: disorder-activated Raman scattering (DARS) and local vibrational modes (LVMS). The DARS was said to be induced by the breakdown of the translation symmetry of the lattice caused by defects or impurities due to the nature of the dopant or due to the growth conditions. Therefore, it can be presumed that NM in our samples could arise due to either or both of these two mechanisms. The mode at 547 cm^{-1} can be assigned to the quasi-longitudinal-optical (LO) phonon mode [237], due to the shallow donor defects, such as zinc interstitials and/or oxygen vacancies, bound on the tetrahedral Fe-sites. Hence, in $\text{Zn}_{1-x}\text{Fe}_x\text{O}$ nanocrystals, host Zn ions are partially substituted by Fe-ions, which introduces lattice defects and disorder in host ZnO crystals disturbing the long range ionic ordering in the ZnO.

Table-3.3: Observed Raman peaks of $\text{Zn}_{1-x}\text{Fe}_x\text{O}$ ($0 \leq x \leq 0.06$) nanoparticles and their symmetry assignments.

Vibration frequency (cm^{-1})							Assignments	Process
Fe0	Fe0.5	Fe1	Fe1.5	Fe2	Fe4	Fe6		
329	328	327	327	327	328	329	$\text{E}_{2\text{H}}-\text{E}_{2\text{L}}$	Second order
378	379	378	380	380	398	398	$\text{A}_1(\text{TO})$	First order
408	----	----	----	----	----	----	$\text{E}_1(\text{TO})$	First order
434	435	435	435	434	434	434	$\text{E}_{2\text{H}}$	First order
575	576	579	577	575	574	574	$\text{A}_1(\text{LO})$	First order
585	----	----	----	----	----	----	$\text{E}_1(\text{LO})$	First order
658	658	659	659	659	680	680	$2(\text{E}_{2\text{H}}-\text{E}_{2\text{L}})$	Second order of $(\text{E}_{2\text{H}}-\text{E}_{2\text{L}})$
1142	1124	1150	1144	1147	1120	1120	$2[\text{A}_1(\text{LO})]$	Second order of $\text{A}_1(\text{LO})$

FT-IR spectroscopy.

The study on Fourier transform infrared spectroscopy (FT-IR) of this system has reported earlier [212]. Here we have analyzed those data. The result reveals that the tetrahedral co-ordination (peak at around 480 cm^{-1}) is much stronger than the octahedral co-ordination (peak at around 660 cm^{-1}). Closer observation [212] shows that the (negligibly weak) band at around 660 cm^{-1} due to octahedral co-ordinations remains unaffected for Fe-doping. This result suggests that Fe-ions does not enter in the octahedron but enter in the tetrahedron only.

Magnetic measurements:

We have conducted a detailed study on the RT magnetization of $\text{Zn}_{1-x}\text{Fe}_x\text{O}$. M-H curve of some of the samples are plotted in Fig. 3.14. The magnetization decreases with the

increase in the field for the samples Fe0 and Fe2 whereas it increases with the increase in the magnetic field for the samples Fe4 and Fe6. The observed M-H behavior reveals that the samples Fe0 and Fe2 is a mixture of ferromagnetic (FM) and diamagnetic (DM) phases where DM dominates and the sample Fe4 is in weak ferromagnetic phase. As seen in Figure 15, the sample Fe4 has a well defined hysteresis loop even at room temperature with a coercive field of 0.07 T and a remnant magnetization of 0.005 emu/g. The obtained hysteresis at room temperature supports the fact that the sample is weakly ferromagnetic [237-240, 241] and not superparamagnetic [242,243]. In other words, the magnetization increases with increasing Fe-concentration and weak ferromagnetism arises gradually.

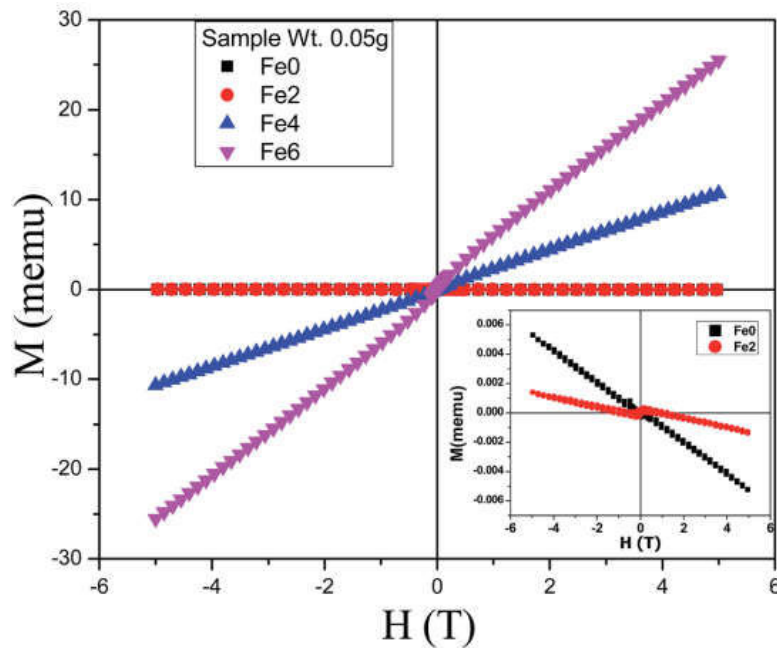


Figure 3.14: Room temperature M-H curves of the Fe doped ZnO samples. Inset shows the enlarged view of Fe0(ZnO) and Fe2 sample

To investigate the origin of RT-ferromagnetism (FM) in Fe-doped ZnO, several mechanisms proposed in the literature have been considered viz. (i) the possibility of spurious ferromagnetism due to magnetic impurities as the intrinsic property of the doped NPs, (ii) extended defects in the NPs, (iii) formation of some Fe-related nanoscale secondary phase,

(iv) metallic iron precipitation, and (v) formation of FeO/Fe₂O₃. However, FeO/Fe₂O₃ phases can be easily ruled out because there is no trace of FeO/Fe₂O₃ in XRD, EXAFS, and TEM measurements. Secondly, metallic Fe and Fe-related secondary phase are also an unlikely source of this FM as XRD, EXAFS, and HRTEM results show. Undoped ZnO prepared under identical conditions as those of Fe-doped ZnO samples, does not exhibit any measurable ferromagnetism but shows diamagnetism. Hence, impurities cannot contribute to the observed magnetic moment in the Fe-doped ZnO NPs. Thus, TMs essentially plays the key role to the observed FM. Moreover, recently Straumal et al. showed that the grain boundary specific area (the ratio of the grain boundary area to the volume) S_{GB} , is the controlling factor for the ferromagnetic behaviour of undoped and TM-doped ZnO [222,223]. For Fe-doped ZnO nanocrystals Straumal et. al. [244]. argued that the samples are FM only if S_{GB} exceeds a certain threshold value $S_{th} = 3 \times 10^4 \text{ m}^2/\text{m}^3$. For our system S_{GB} value is well above the threshold value viz. $S_{GB} = 41 \times 10^6 \text{ m}^2/\text{m}^3$) giving the FM. Hence, FM is expected to arise due to the joint effects of the intrinsic exchange interaction of magnetic moments of TM ions and effects of the grain boundary in doped NPs.

As we have discussed in Chapter-2 that RKKY interaction is based on free electrons and ZnO is not transformed into a metal with such a low doping, RKKY interaction is not valid here. Double-exchange or super exchange are not responsible for the FM because the magnetic cations are dilute (of low concentration) in the present samples. Again, according to donor impurity band exchange model the combination of magnetic cations, carriers, and defects can result in bound magnetic polarons (BMPs) which may also lead to the RTFM [245-248]. Therefore, we can suggest that the joint effects of the intrinsic exchange interactions arising from bound magnetic polarons (BMPs) and the (extrinsic) grain boundary are responsible for the room temperature FM in this system.

Thus to summarise, we have presented the results of extensive study of sol-gel derived Fe-doped ZnO diluted magnetic semiconductors (DMSs) nanoparticles by using different experimental techniques. The XRD with Rietveld refinement, HRTEM, and micro-Raman analysis shows that Fe-doped ZnO nanoparticles have wurtzite structure as that of pure ZnO which indicates that Fe-ions have substituted the Zn ions. The crystallite structure, morphology, and size estimation have been performed by XRD and HRTEM. Crystallite size and lattice strain has also been estimated by Williamson-Hall plot and size-strain plot. The estimated size of the crystallites decreases exponentially with the increase of Fe-concentration which is attributed to the difference of the ionic radii between Zn and Fe atoms. The EXAFS results show that the reduction in oxygen coordination take place. The oxygen coordination remains lower and DW factor remains higher compared to their respective values in undoped ZnO suggests that doping takes place properly throughout the whole composition range. The DW factor for the next near Zn shell shows that Fe-doping affects the O site more than the Zn/Fe site. The substitution of Zn ions by Fe ions does not cause any significant change in the host lattice as manifested in the values of the bond distances. XANES study clearly rules out the presence of metallic Fe clusters, FeO and Fe₂O₃ in the samples. These observations corroborate to those of XRD study. Raman study reveals that the local symmetry in the Fe-doped nanocrystals gradually differ from that of undoped sample, but the crystal structure remains the same as that of the wurtzite structure of pure ZnO, which further supports the incorporation of Fe-ions in the ZnO lattice. The FTIR analysis suggests that Fe-ions does not enter in the octahedron but enter in the tetrahedral sites only. The room temperature PL measurements illustrate weak NBE emission and violet, violet-blue, blue emissions in visible region. The UV emission (NBE) peak originates from the radiative recombination of free excitons. Other emissions may be attributed to the Zn-vacancies for violet emission; interstitial Zn_i levels and radiative defects related to traps existing at grain

boundaries for violet-blue emission; defects related to positively charged Zn vacancies for blue emission. Room temperature (weak) ferromagnetism (RTFM) is observed from M-H measurements and magnetization increases with increasing Fe-concentration. The joint effects of the intrinsic exchange interactions arising from bound magnetic polarons (BMPs) and the extrinsic grain boundary are found to be responsible for the room temperature FM in this system.

3.2 Cr doped ZnO NCs:

Among the TMs, Cr is particularly attractive and has been chosen as the preferred TM dopant by several research groups because of (1) theoretical research by Sato et al. [55] on Cr-based ferromagnetic ordering; (2) Cr^{3+} and Zn^{2+} have close values of ionic radii, which means Cr^{3+} can be easily incorporated into the ZnO crystal lattice; (3) among the impurity phases in ZnO : Cr system, Cr metal, Cr_2O_3 , Cr_3O_4 and ZnCr_2O_4 are anti-ferromagnetic, thus eliminating any role of Cr precipitates in getting spurious FM and (4) the only ferromagnetic oxide of Cr, CrO_2 which has a Curie temperature (TC) of 386 K, is not a stable phase under normal conditions and is easy to be oxidized into Cr_2O_3 when heated at atmospheric pressure. However, compared to the widely studied Fe, Co and Mn-doped ZnO systems, both theoretical and experimental researches on Cr-doped ZnO are relatively less [249-257]. Moreover, quite contradictory experimental results on Cr doped ZnO are available in the literature which have created doubts regarding the origin of ferromagnetism in these materials. For example, Venkatesan et al. [252] and Ueda et al. [253] have not observed any signature of FM in Cr doped ZnO samples, whereas Liu et al. [254] showed that Cr doped ZnO films are ferromagnetic at room temperature. While nanoparticles prepared by sol-gel route are found to be ferromagnetic at room temperature with magnetic moment decreasing with increase in Cr doping concentration from 1–5% [255]. Cr doped ZnO nanoparticles

grown by chemical vapour synthesis technique, shows ferromagnetic ordering only at higher Cr doping concentration [256,257]. In this paper we concentrate on investigating the structural, local structural and optical properties of Cr-doped ZnO (i.e. $\text{Zn}_{1-x}\text{Cr}_x\text{O}$) nanocrystals to get a clear understanding of the behaviour of the Cr dopants in ZnO nanoparticles.

3.2.1 Experimental details:

$\text{Zn}_{1-x}\text{Cr}_x\text{O}$ ($0 \leq x \leq 0.06$) samples (named as Cr0, Cr0.5, Cr1, Cr2, Cr4, and Cr5 for Cr concentration $x = 0, 0.005, 0.01, 0.02, 0.04$, and 0.06 respectively) have been synthesized by the sol-gel method which has been discussed in Chapter 2. The crystallite structure, size, and lattice strain have been estimated by X-ray diffraction (XRD) with Rietveld refinement and high-resolution transmission electron microscopy (HRTEM). The XANES and EXAFS measurements have been carried out at the Energy-Scanning EXAFS beamline (BL-09) at the Indus-2 Synchrotron Source RRCAT, Indore, India. The details of the above beamlines have been described in Chapter-2. TEM and HRTEM measurements were done with Technai G² S-Twin (FEI, Netherlands). Fourier transmission infrared (FT-IR) spectra of the samples (as pellets in KBr) were recorded using FT-IR Spectrometer (Spectrum One, Perkin Elmer Instrument, USA) in the range of $4000\text{--}400\text{ cm}^{-1}$ with a resolution of 1 cm^{-1} . Raman spectra were taken with a Reinshaw micro-Raman spectroscope using 514.5 nm Ar^+ laser as excitation source in the range of $200\text{--}1250\text{ cm}^{-1}$. The powder samples are made into pellets for the Raman measurement. The optical absorption spectra were measured in the range of $300\text{--}800\text{ nm}$ using UV-Vis spectrometer (Perkin Elmer Instrument, Lambda-25, USA). The photoluminescence (PL) spectra were taken by a Fluorescence Spectrometer (LS-45, Perkin Elmer, USA). Synchrotron based Extended X-ray Absorption Fine Structure (EXAFS) measurements of these samples have been carried out in transmission mode while

measurements at the dopant K-edges were carried out at the Scanning EXAFS Beamline (BL-9) at the Indus-2 Synchrotron Source (2.5 GeV, 100 mA) at the Raja Ramanna Centre for Advanced Technology (RRCAT), Indore, India. The EXAFS spectra of the Cr doped ZnO NCs at Cr K-edge were recorded in the energy range of 5984-6635 eV.

3.2.2 Results and discussions:

X-ray Diffraction

Fig. 3.15 shows the X-ray diffraction (XRD) patterns for $\text{Zn}_{1-x}\text{Cr}_x\text{O}$ ($0 \leq x \leq 0.06$) samples. The XRD patterns show that Cr-doping does not lead to the appearance of any extra peak or disappearance of any peak of the hexagonal wurtzite structure of pure ZnO, confirming that structure of the doped ZnO remains wurtzite and belongs to the space group $P6_3mc$. Rietveld analysis tells that the samples are single phase and no trace of other impurities has been found.

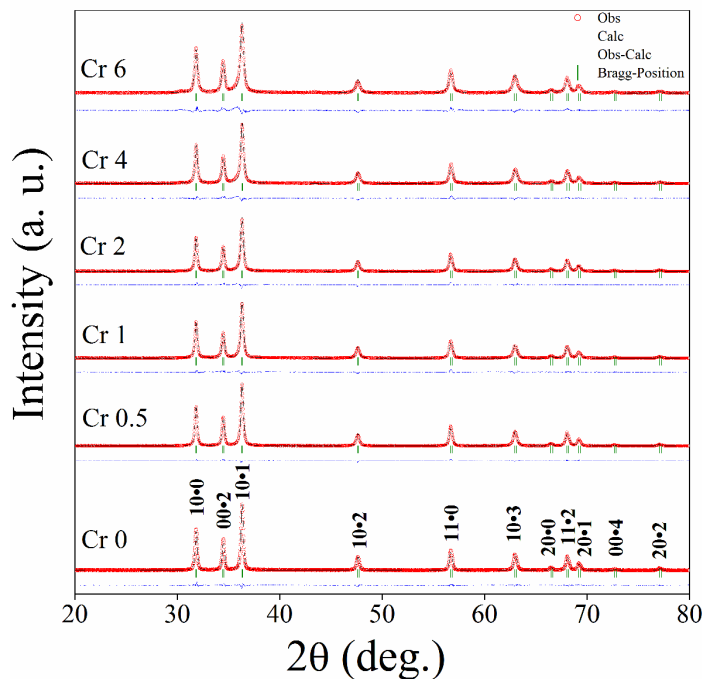


Figure 3.15: Rietveld refinement profiles of X-ray diffraction data of the $\text{Zn}_{1-x}\text{Cr}_x\text{O}$ ($0 \leq x \leq 0.06$) samples. The circle represents the observed data (Obs) while solid line through the circles is the calculated profile (Calc), vertical ticks below curves represent allowed Bragg-reflections for the wurtzite phase. The difference pattern of the observed data and calculated profile (Obs–Calc) is given below the vertical ticks.

Therefore, we believe that the maximum doping concentration (i.e. $x = 0.06$) is well below the maximum solid solubility of Cr ions in ZnO lattice. The secondary phase of ZnCr_2O_4 emerges at $x = 0.08$, which indicates that the doping limit of Cr in ZnO is below 8%. The existence of secondary phase of ZnCr_2O_4 with 8% Cr doped ZnO has also reported in the literature [254].

As we have discussed in the previous section here also we have studied the variation of lattice parameters, crystallite size and average strain present in samples by changing the Cr concentration in host ZnO nanocrystals, by the Rietveld refinement analysis of x-ray diffraction data. The lattice parameters (a and c) have been calculated from Rietveld refinement of the X-ray diffraction data and the volume of the unit cell for a hexagonal system has been calculated and is shown in fig. 3.16. From fig. 3.16, it is seen that there is no appreciable change in the lattice parameters a, c and the volume of the unit cell (V) due to an increase in Cr-ion doping.

The average crystallite size, D , of the samples is estimated using the Scherrer's equation [258,259]. The average crystallite size (D) decreases linearly with the increase of Cr doping concentration which can be attributed to the presence of Cr ion in ZnO lattice. The presence of Cr ion in ZnO lattice prevents the growth of the crystal grains and slows down the motion of grain boundaries. A better estimation of the crystallite size has been achieved from 'size-strain plot' (SSP) [260] by using the following equation:

$$\left(\frac{d_{hkl}\beta\cos\theta}{\lambda}\right)^2 = \frac{k\lambda}{D}\left(\frac{d_{hkl}^2\beta\cos\theta}{\lambda^2}\right) + \left(\frac{\varepsilon}{2}\right)^2 \quad (3)$$

where d_{hkl} is the inter-planar spacing and ε is the average strain produced in the lattice. β , λ and D are described as earlier, k is the Scherrer's constant ($= 0.9$).

The plot of $(d_{hkl}\beta\cos\theta/\lambda)^2$ vs. $(d_{hkl}^2\beta\cos\theta/\lambda^2)$ is shown in fig. 3.17. The crystallite size (D) has been estimated from the slope of the linear fit of the plot. Fig. 3.18 shows the

variation of crystallite size with the Cr-concentration (x) estimated from size-strain plot and from Scherrer's equation. The average crystallite size decreases linearly with the increase in Cr-concentration. This may be due to the decrease in growth rate.

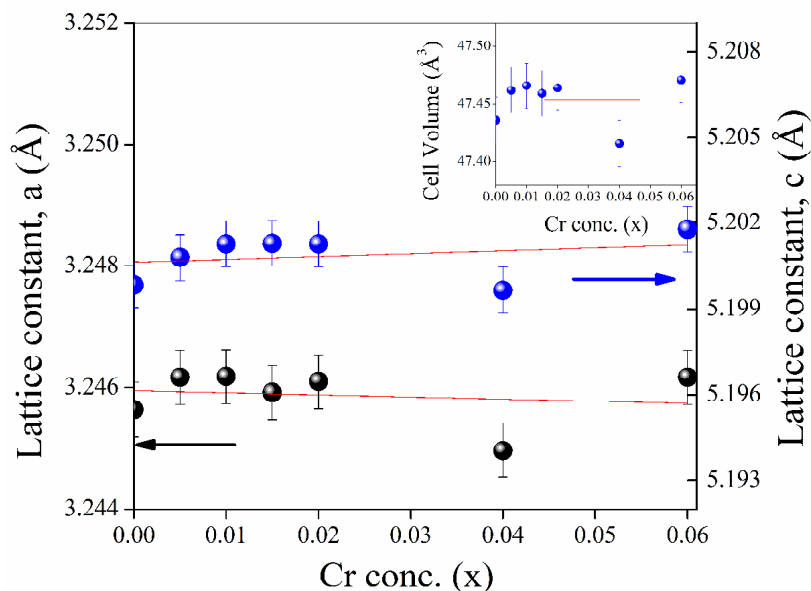


Figure 3.16: Variation of lattice parameter ('a' and 'c') with Cr-concentration (x) calculated from Rietveld refinement. The inset plot shows the variation of the unit cell volume.

The value of lattice parameters (a and c), bond lengths and bond angles calculated from Rietveld refinement for different Cr-concentration are shown in Table 3.4. From fig. 3.16, it is seen that there is no appreciable change in the lattice parameters a , c and volume of the unit cell (V) due to an increase in Cr-ion doping. However, a closer observation shows that the lattice parameter a decrease very slowly with Cr-concentration which can be explained on the basis of the difference in ionic radii of Zn and Cr. On the other hand, the lattice parameters c increases slowly with Cr-doping which can't be explained on the basis of the difference in ionic radii. Some other effect (for example lattice distortion) may be associated which will be studied further elsewhere.

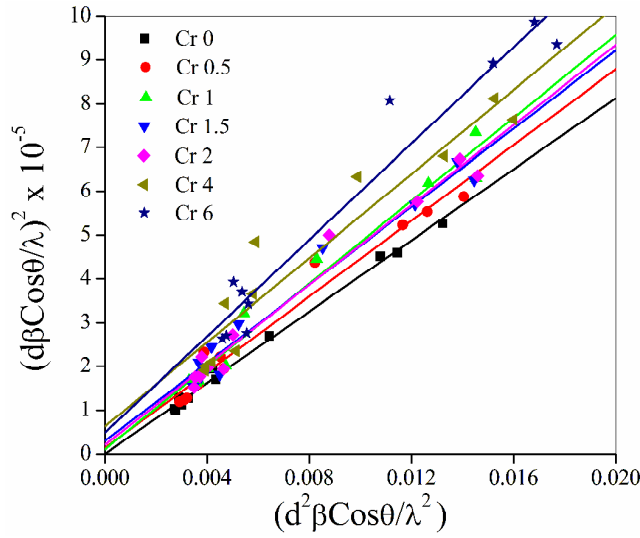


Figure 3.17: $d_{hkl}\beta\cos\theta/\lambda)^2$ vs. $(d_{hkl}^2\beta\cos\theta/\lambda^2)$ plot of the samples to estimate crystallite size(D) and average strain (ϵ).

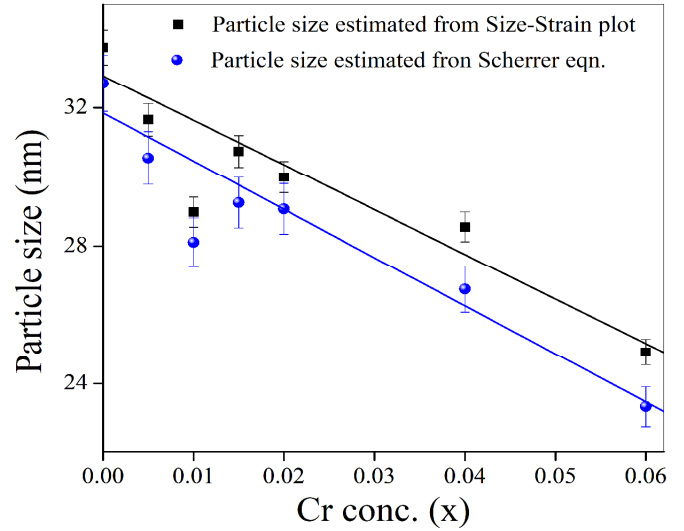


Figure 3.18: Variation of average crystallite size with Cr-concentration (x) estimated from size-strain plot and Scherrer's equation.

Table-3.4: Values of lattice parameters, bond lengths and bond angles calculated following ref. 35

Parameters	Cr 0	Cr 0.5	Cr 1	Cr 1.5	Cr 2	Cr 4	Cr 6
a (Å)	3.24564	3.24617	3.24618	3.24592	3.24610	3.24497	3.24617
c (Å)	5.19985	5.2008	5.20127	5.20129	5.20127	5.19966	5.20178
c/a	1.60210	1.60213	1.60227	1.60240	1.60231	1.60237	1.60243
d_{Zn-O_a} (Å)	1.97521	1.97558	1.97600	1.97554	1.97561	1.97494	1.97570
d_{Zn-O_b} (Å)	1.97526	1.97559	1.97565	1.97555	1.97562	1.97495	1.97571
$angle(O_a-Zn-O_b)$ (°)	108.437 32	108.4376 1	108.4434 0	108.4476 6	108.4438 3	108.4459 1	108.4479 8
$angle(O_b-Zn-O_b)$ (°)	110.485 03	110.4847 6	110.4791 8	110.4750 9	110.4787 6	110.4767 8	110.4747 9

Transmission Electron Microscopy:

The morphology and the microstructure of the nanoparticles have been examined by transmission electron microscopy (TEM). A typical TEM image of several nanoparticles of the sample Cr1 (i.e. $Zn_{0.99}Cr_{0.01}O$) is presented in Fig. 3.19.

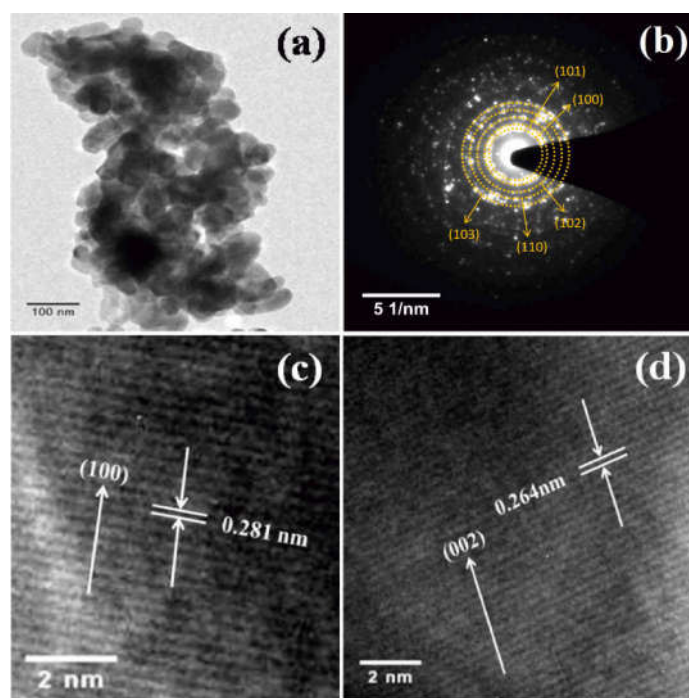


Figure 3.19: Low magnification TEM (a) SAED (b) and HRTEM (c,d), images of $\text{Zn}_{0.99}\text{Cr}_{0.01}\text{O}$ nanocrystals.

As can be seen from fig. 3.19(a), nanoparticles tend to coalesce into aggregate which is a very common phenomenon in magnetic nanoparticles. Closer look of TEM images of different parts of the sample tells that most nanoparticles are more or less spherical in shape and smooth in surface. The TEM micrograph (fig. 3.19) shows that the obtained samples are indeed nano-grained and contain, therefore, very developed grain boundaries and free surfaces which should affect the physical properties as observed by Straumal et al.[222, 223]. The average particle size obtained from TEM measurements matches well with the size estimated from the XRD study. High-resolution TEM (HRTEM) gives insight into the detailed atomic structure of the nanoparticles. Fig. 3.19(c and d) shows the HRTEM image of a single particle of the Cr1 sample. The HRTEM micrograph that the interplanar spacing (d -value) of fringes is 0.264 nm which is in good agreement with the d -value of (002) plane (viz. 0.259 nm) of wurtzite ZnO. Moreover, it should be pointed out here that the d -value of the

Cr-doped sample (e.g. Cr1) determined from TEM measurements also has been increased which corroborates the XRD analysis that the tensile strain has been induced due to Cr-doping in the system. The pattern indicates that all the nanoparticles are single crystalline in nature and are free from major lattice defects. According to the results of XRD pattern and HRTEM images, we believe that the Cr-ions are well incorporated into the crystal lattice of ZnO.

EXAFS measurements:

Fig. 3.20 represents the experimental EXAFS ($\mu(E)$ versus E) spectra of undoped and Cr doped ZnO samples measured at Zn K-edge. The Fourier transform EXAFS spectra or $\chi(R)$ versus R plots have been generated for all the samples from the $\mu(E)$ versus E spectra following the methodology described in Chapter-2. The theoretical Fourier transformed EXAFS spectra of ZnO has been generated assuming the model described by Kisi et. al. [224] and the data has been fitted upto 3.5 Å in R space. The best fit parameters have been shown in Table 3.5.

The normalized experimental EXAFS ($\mu(E)$ versus E) spectra of undoped and Cr doped ZnO samples measured at Cr-K-edge which is shown in fig. 3.21. Fig. 3.22 represents the Fourier transformed EXAFS of Cr doped ZnO NCs at Zn-K-edge spectra along the best fit. The best fit results are given in Table 3.5.

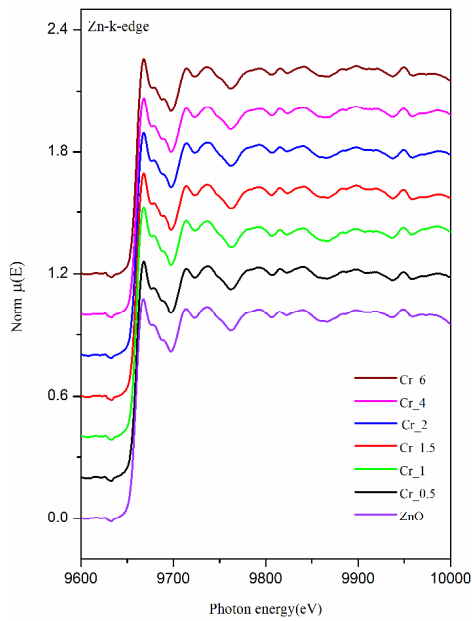


Figure 3.20: Normalized experimental EXAFS ($\mu(E)$ vs E) for undoped and Cr doped ZnO nanocrystals at Zn K-edge.

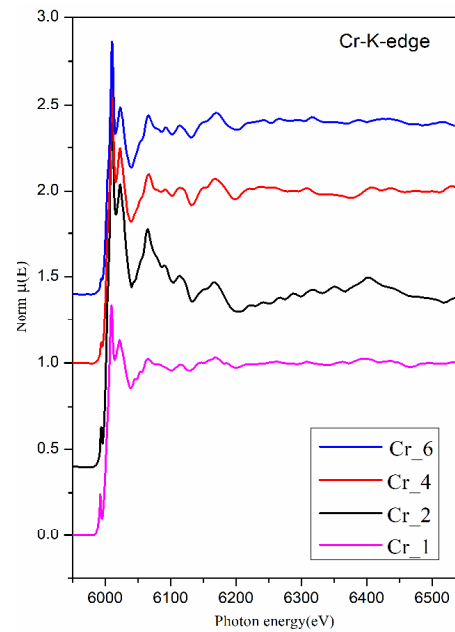


Figure 3.21: Normalized experimental EXAFS ($\mu(E)$ vs E) for undoped and Cr doped ZnO nanocrystals at Cr K-edge.

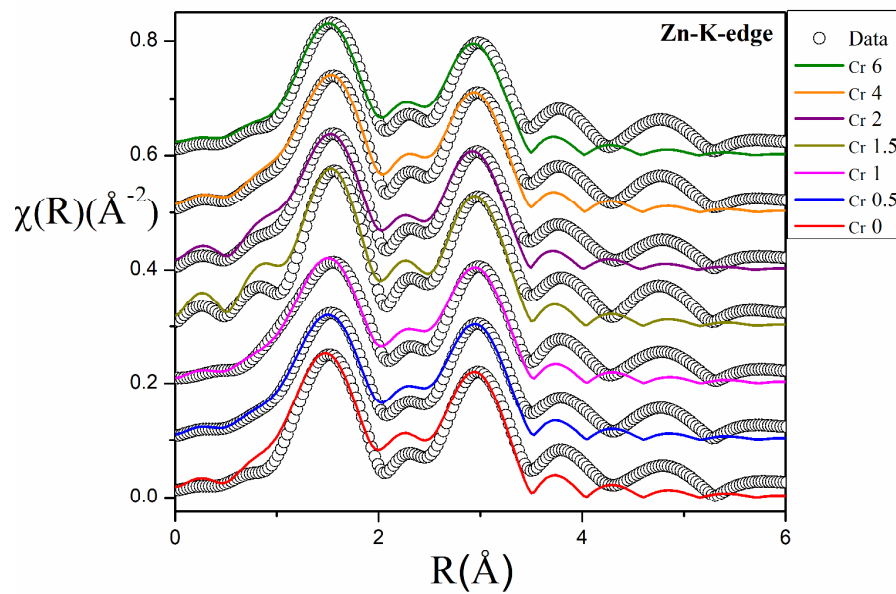


Figure 3.22: The experimental $\chi(R)$ versus R plots and the theoretical fits of undoped and Cr-doped ZnO samples measured at Zn K-edge.

Table-3.5: Best fit results of the EXAFS measurements on Cr doped ZnO samples at Zn K dge:

		Cr 0	Cr 0.5	Cr 1	Cr 1.5	Cr 2	Cr 4	Cr 6
Zn-O	CN	4.16	2.8	2.76	2.84	2.56	2.6	2.48
	R(Å)	1.93	1.95	1.95	1.95	1.95	1.98	1.95
	σ^2	0.008	0.004	0.001	0.002	0.002	0.002	0.002
Zn-Zn	CN	11.8	11.04	10.86	11.52	11.76	11.05	10.82
	R(Å)	3.22	3.23	3.22	3.23	3.22	3.21	3.23
	σ^2	0.008	0.008	0.009	0.008	0.009	0.009	0.009
R-factor		0.002	0.001	0.002	0.002	0.002	0.004	0.001

From Table 3.5 it has been observed that Zn-O bond length for the first coordination shell and Zn-Zn distance of the second coordination shell of the doped samples agree with that of the undoped ZnO. This indicates that Cr is replacing Zn^{+2} as Cr^{+3} since ionic radii of Zn^{+2} (0.60 Å) and Cr^{+3} (0.61 Å) are almost similar while that of Cr^{+2} is significantly higher [261] this will be subsequently supported by Cr K-edge EXAFS measurements as described below. It can also be seen from Table 3.5 that more and more oxygen vacancies are created in the 1st shell and Zn coordination of the 2nd shell is also found to decrease as Cr doping concentration in the samples increase. The decrease in oxygen coordination at Zn sites at higher Cr concentration might be due to the fact that Cr^{+3} preferably takes octahedral coordination instead of tetrahedral coordination of Zn^{+2} in ZnO, depleting the Zn sites of oxygen. This will be more evident from Cr K-edge XANES data discussed later.

Fig. 3.23(a)&(b) represents the Fourier transformed EXAFS spectra of Cr doped ZnO NCs at Cr K- edges along with the best fit. To fit the experimental Fourier transformed EXAFS data at the Cr K-edge two possibilities were explored (a) starting with basic wurtzite

ZnO structure and replacing Zn by Cr as per the concentration and (b) by assuming Cr₂O₃ structure.

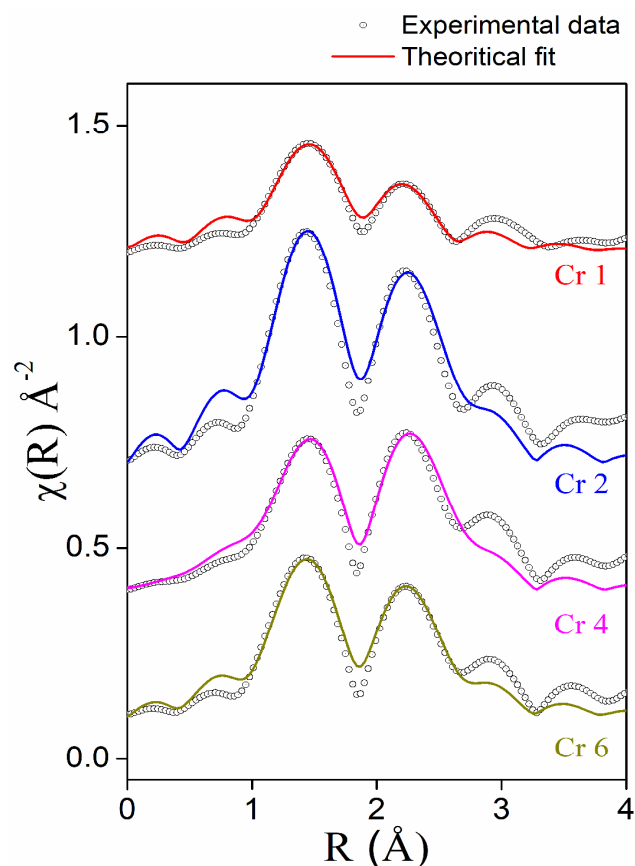


Figure 3.23(a). The experimental $\chi(R)$ versus R plots and the theoretical fits of Cr doped ZnO samples measured at Cr K-edge where the fitting is done assuming ZnO structure with Cr at Zn sites.

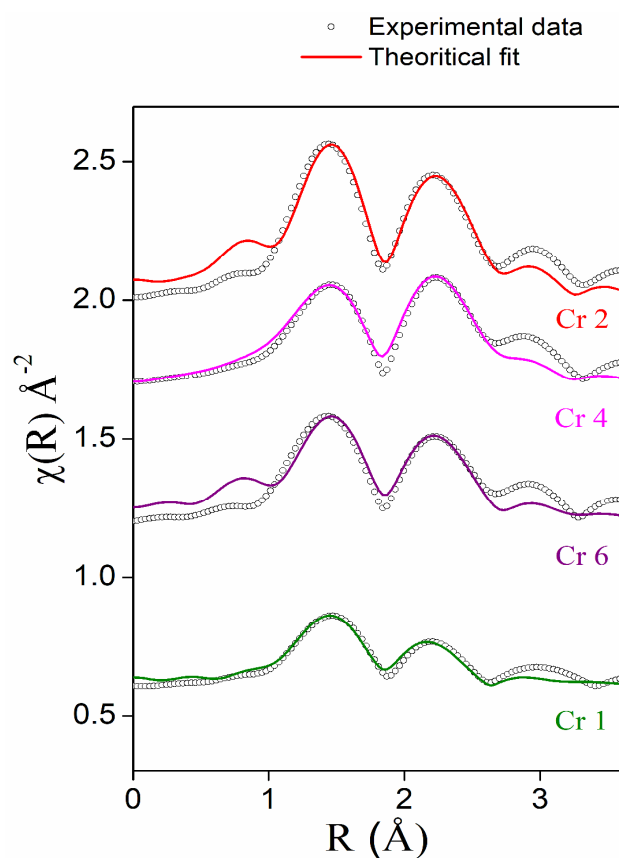


Figure 3.23(b). The experimental $\chi(R)$ versus R plots and the theoretical fits of Cr doped ZnO samples measured at Cr K-edge where fitting has been done assuming Cr₂O₃ structure.

Similar approach has been followed earlier in case of fitting of EXAFS data for Mn and Co doped ZnO nanocrystals [225, 262]. For the second case, structural parameters of Cr has been taken from ICSD database [263] and the data has been fitted assuming the first oxygen shell (Cr-O) at 1.97Å with coordination number (CN) of 5, second Cr shell (Cr-Cr) at 2.58Å having CN of 2 and third Cr shell (Cr-Cr) at 2.88 Å with coordination 2. The best fit parameters have been shown in Tables 3.6 and 3.7.

Table 3.6: Fit parameters by assuming wurtzite ZnO structure with Cr at Zn sites.
(Typical uncertainty for CN $\sim \pm 10\%$; R $\sim \pm 0.02 \text{ \AA}$; $\sigma^2 \sim \pm 0.001 \text{ \AA}^2$).

		Cr 1	Cr 2	Cr 4	Cr 6
Cr-O	CN	2.96	5.2	3.24	3.69
	R(\AA)	1.96	1.96	1.96	1.96
	σ^2	0.005	0.003	0.001	0.002
Cr-Zn	CN	1.54	8.1	6.7	5.04
	R(\AA)	2.94	2.96	2.9	2.95
	σ^2	0.001	0.005	0.005	0.005
R-factor		0.003	0.002	0.003	0.003

Table-3.7: Fit parameters by assuming Cr₂O₃ structure.
(Typical uncertainty for CN $\sim \pm 10\%$; R $\sim \pm 0.02 \text{ \AA}$; $\sigma^2 \sim \pm 0.001 \text{ \AA}^2$).

		Cr 1	Cr 2	Cr 4	Cr 6
Cr-O	CN	5.64	6.48	6.48	6.06
	R(\AA)	2.01	2.00	2.03	2.02
	σ^2	0.018	0.005	0.017	0.014
Cr-Cr/Zn	CN	1.81	1.99	1.96	1.90
	R(\AA)	2.51	2.46	2.51	2.52
	σ^2	0.008	0.004	0.001	0.005
Cr-Cr/Zn	CN	4.16	4.12	4.06	4.0
	R(\AA)	2.94	3.01	3.01	3.00
	σ^2	0.02	0.001	0.007	0.009
R-factor		0.006	0.002	0.002	0.008

It can be seen from Table 3.6 that the Zn-Cr distance and coordination numbers obtained by fitting are much lower than that expected for ZnO structure. However, the parameters obtained by the later approach viz., assuming Cr₂O₃ structure yields more reasonable results as shown in Table 3.7 and it supports our earlier conclusion from Zn K edge EXAFS data that Cr is going to the lattice as Cr⁺³.

Fig.3.24 shows the XANES spectra of the samples measured at Cr K-edge which manifests that the Cr K-edge positions in the samples match with that of Cr_2O_3 standard showing presence of Cr^{+3} in the samples. This clearly rules out the presence of any metallic Cr phase in the samples ensuring proper doping of Cr in ZnO lattice. Furthermore, the Cr K-edge XANES spectra are found to be characterized by the presence of a pre-edge peak at ~ 8041 eV, which is a characteristic of tetrahedral coordination of ZnO lattice. However, it is found that the intensity of the pre-edge peak decreases as Cr concentration in the samples increases. Since pre-edge peaks do not exist in case of pure octahedral coordination, the above observation suggests that Cr is preferentially having octahedral coordination over tetrahedral coordination as Cr concentration increases in the samples. This leads to creation of oxygen vacancies at Zn sites which has also been found from Zn K-edge EXAFS measurements. A similar observation on increase in tetrahedral coordination at Cr sites has also been made by FTIR measurement described later.

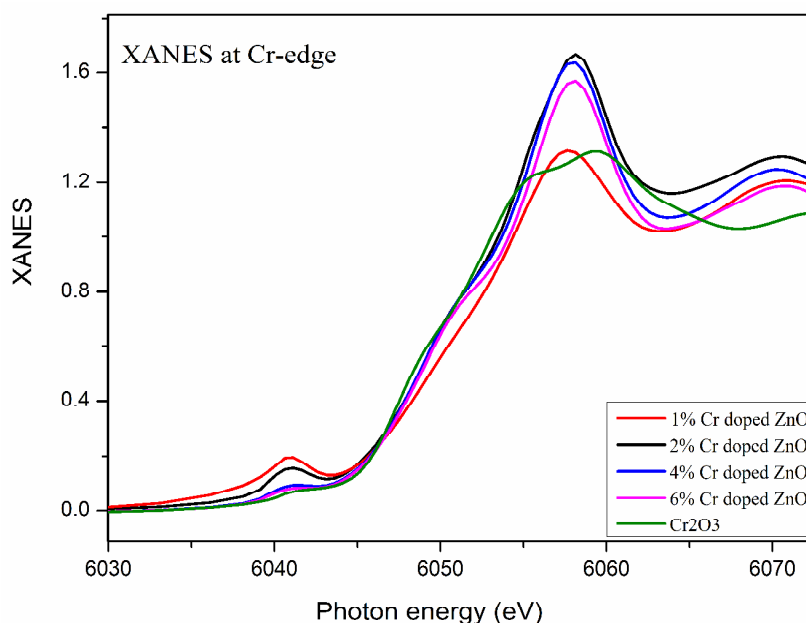


Figure 3.24: XANES spectrum of Cr-doped ZnO nanocrystals measured at Cr K-edge.

Raman Spectroscopy

As has been mentioned earlier, Raman spectroscopy is one of the very sensitive and important techniques to detect local structural changes due to incorporation of TM- ions into the ZnO host lattice [264]. Wurtzite ZnO (number of atoms per unit cell is 4) belongs to the C_{6v}^{4} symmetry group having total number of 12 phonon modes namely, one longitudinal-acoustic (LA), two transverse-acoustic (TA), three longitudinal-optical (LO), and four transverse-optical (TO) branches. At the Γ point of the Brillouin zone, optical phonons have the irreducible representation [265] as: $\Gamma_{\text{opt}} = A_1 + 2B_1 + E_1 + 2E_2$, where both A_1 and E_1 modes are polar and can be split into transverse optical (TO) and longitudinal optical (LO) phonons, with all being the Raman and infrared active. Non-polar E_2 modes are Raman active, while B_1 modes are Raman inactive. For the lattice vibrations with A_1 and E_1 symmetries, the atoms move parallel and perpendicular to the c-axis, respectively. The vibration of heavy Zn sublattice gives rise to the low-frequency E_2 mode while that of oxygen sublattice gives rise to high-frequency E_2 mode [266]. Modes E_1 (TO) and A_1 (TO) reflect the strength of the polar lattice bonds [267]. According to the selection rule, generally E_2 and A_1 (LO) modes can only be observed in the unpolarized Raman spectra of bulk ZnO under backscattering geometry. However, when the crystal is reduced to nanometer size, the selection rule with $k=0$ for the first-order Raman scattering is relaxed and phonon scattering is not being limited to the center of Brillouin zone [265]. In these cases, the phonon dispersion around the zone center should also be considered. Therefore, not only the first-order vibration modes should appear with shift and broadening but also some vibration modes will exist in the symmetry-forbidden geometries. As a result, the wurtzite ZnO nanoparticles have six Raman-active phonon modes at 101 cm^{-1} (E_2 low), 381 cm^{-1} (A_1 TO), 407 cm^{-1} (E_1 TO), 437 cm^{-1} (E_2 high viz. E_{2H}), 574 cm^{-1} (A_1 LO), and 583 cm^{-1} (E_1 LO) respectively [268,269]. Fig. 3.25 represents the room-temperature Raman spectra of $\text{Zn}_{1-x}\text{Cr}_x\text{O}$ ($0 \leq x \leq 0.06$) nanocrystals. It shows that all the

prominent peaks of ZnO are also observed in Cr-doped nanocrystals, but as Cr- content increases, some of the Raman modes become relatively less intense without appreciable shift in frequencies. These observations reveal that the local symmetry in the nanocrystals is different from that of undoped sample (i.e. ZnO), but the crystal structure remains the same. The sharpest and strongest peak at about 434 cm^{-1} can be attributed to the nonpolar high-frequency optical phonon branch of E_2 mode (E_{2H}), which involves the motion of oxygen and is the characteristic of wurtzite structure. With increasing Cr-concentration pronounced weakening in peak height of this nonpolar E_{2H} mode for the Cr-doped ZnO samples, as compared to undoped ZnO, has been observed without any appreciable shifting and broadening in frequency of this mode. This result can be attributed to the fact that Cr^{2+} substitution induces the microscopic structural disorder in the periodic zinc atomic sub-lattice and reduces the translational symmetry giving rise to local distortions in the lattice. This local distortion and disorder disrupt the long-range ordering in ZnO and weakens the electric field associated with a mode [270]. Close observation shows two very weak peaks at 408 cm^{-1} [E_1 (TO) mode] and 585 cm^{-1} [E_1 (LO) mode] in pure ZnO only. The peak at about 329 cm^{-1} and a broad shoulder centered at about 658 cm^{-1} for ZnO seemed to have originated from a two-phonon process [271]. The peak at about 329 cm^{-1} can be attributed to single crystalline nature of ZnO [267, 268] and assigned as a difference mode between the E_2 high and E_2 low frequencies [272, 273]. viz. ($E_{2H}-E_{2L}$). This mode is not affected much for doped samples. The peak height and frequency of this peak remains unaffected with Cr-doping concentration (Fig. 3.25). This suggests that the single crystalline nature of the nanoparticles remains unaffected due to Cr-doping and it corroborates with the TEM results. Comparing Fig. 3.25, it has also been observed that as Cr-concentration increases, the shoulder centered at about 658 cm^{-1} (2nd order mode for ZnO) gradually becomes a peak at around 685 cm^{-1} due to increase in its intensity without any shift in the peak position. The mode at 658 cm^{-1} in pure

ZnO nanostructure can be ascribed to the multi-phonon processes [$2(E_{2H}-E_{2L})$] [274, 275]. For Cr- doped ZnO samples, this peak (at 658 cm^{-1} in pure ZnO) is shifted to 682 cm^{-1} with increase in Cr- concentration. The other 2nd order mode at around 1142 cm^{-1} for ZnO remains unshifted with increasing Cr-concentration. It should be noted here that we have assigned the modes as 2nd order whose frequency is close to the double of any one 1st order mode. Further work should be carried to confirm the 2nd order modes. The weak mode A_1 (TO) at 378 cm^{-1} for ZnO remains unchanged in Cr-doped samples. Besides the first-order and second-order phonon modes of ZnO, two additional new modes mainly NM1 and NM2 centered at about 475 cm^{-1} and 525 cm^{-1} have been observed for samples $x \geq 2$ (fig. 3.25) which do not appear in Raman spectrum of samples with lower Cr concentration. These modes do not have any appreciable shift in frequency with Cr-concentration. Ye et. al. [276] considered two possible mechanisms to ascribe the origin of this anomalous mode: disorder-activated Raman scattering (DARS) and local vibrational modes (LVMs). It was said that the DARS be induced by the breakdown of the translation symmetry of the lattice caused by defects or impurities due to the nature of the dopant or due to the growth conditions. Therefore, it can be presumed that NM1 and NM2 in our samples could arise due to either or both of these two mechanisms. The mode at 547 cm^{-1} can be assigned to the quasi-longitudinal-optical (LO) phonon mode [265], due to the shallow donor defects, such as zinc interstitials and/or oxygen vacancies, bound on the tetrahedral Cr- sites. Ahmed et al. [277] described this mode as $2B_1$ low which contributes to local vibrations of Cr ions in ZnO lattice. In $\text{Zn}_{1-x}\text{Cr}_x\text{O}$ nanocrystals, host Zn ions are partially substituted by Cr ions, which introduces lattice defects and disorder in host ZnO crystals disturbing the long range ionic ordering in ZnO.

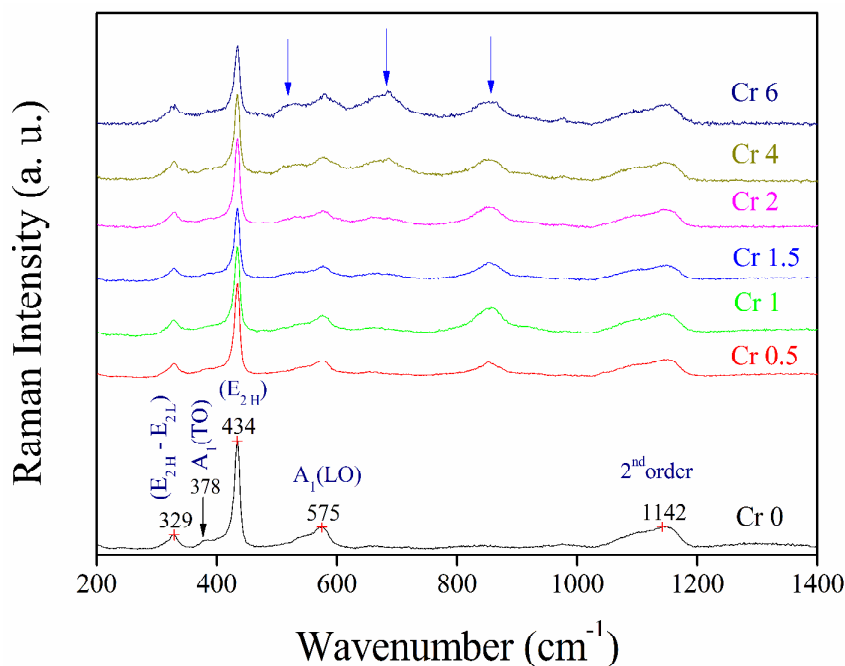


Figure 3.25: Room-temperature Raman spectra of $\text{Zn}_{1-x}\text{Cr}_x\text{O}$ ($0 \leq x \leq 0.06$) respectively.

Fourier transforms infrared spectroscopy:

Since Fourier transform infrared spectroscopy (FTIR) gives information about functional groups present in a compound, the molecular geometry and inter- or intra-molecular interactions, we have employed FTIR to study the vibrational bands of the $\text{Zn}_{1-x}\text{Cr}_x\text{O}$ samples at room temperature. Normally, the band frequencies within 1000 cm^{-1} could be attributed to the bonds between inorganic elements. Fig. 3.26 shows the FTIR spectra of $\text{Zn}_{1-x}\text{Cr}_x\text{O}$ samples. The most prominent band at around 480 cm^{-1} and the negligibly weak band at around 660 cm^{-1} are assigned to stretching vibration of Zn–O bonds [278], in the octahedral and tetrahedral co-ordinations respectively [279]. This observation suggests that the tetrahedral co-ordinations is much stronger than the octahedral co-ordinations in this system which also confirms wurtzite structure formation of the samples [280,281]. It should be pointed out here that the negligibly weak band at around 660 cm^{-1} (octahedral co-ordinations)

gradually becomes stronger due to Cr-doping ($\text{Cr} > 2\%$) which suggests that Cr-ions enter also in the octahedron. The peak around $\sim 2345\text{ cm}^{-1}$ is due to CO_2 molecules present in the acetate and in air. The peaks around 2925 cm^{-1} are due to C–H bond stretching. It should be pointed out here that presence of such band has not been considered as the contamination of the nanoparticles [281,282] rather it suggests the presence of absorbed species on the surface (surface modification) of nanocrystals. The broad absorption peak at $\sim 3465\text{ cm}^{-1}$ is attributed to –OH group of H_2O , indicating the existence of water absorbed on the surface of nanocrystalline powders. Due to the rich surface hydroxyl groups, these Cr-doped ZnO colloids can be easily dispersed into many polar and nonpolar solvents (e.g., water, alcohol, CHCl_3 , etc.), and the dispersions show good stability. In addition, the surface hydroxyl can provide functional groups to react with functional organic molecules with optical or electrical properties (e.g., dyes, cluster compounds), which may generate novel organic-inorganic hybrids [281, 282].

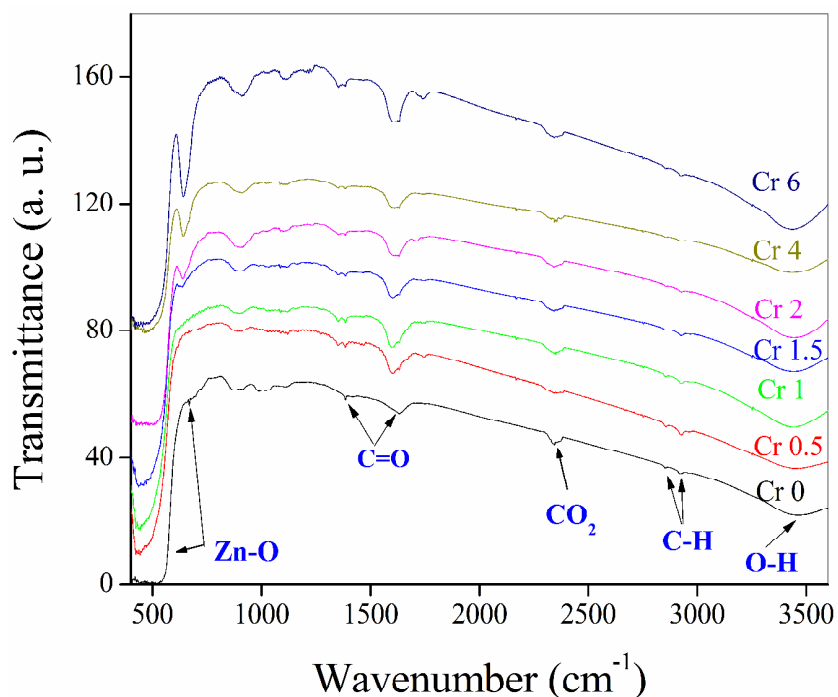


Figure 3.26: FTIR spectra of $\text{Zn}_{1-x}\text{Cr}_x\text{O}$ ($0 \leq x \leq 0.06$) samples showing different modes.

UV-Visible spectroscopy:

The UV–visible spectra of the samples, obtained by dispersing ZnO nanoparticles in distilled water and using distilled water as the reference are shown in Fig. 3.27. An absorption peak centered at around 374 nm is observed and the band gap is estimated from this peak (inset of Fig.3.27). UV-Vis measurements show a blue shift (increase) in the optical band gap up to $\text{Zn}_{0.98}\text{Cr}_{0.02}\text{O}$, while the band gap decreases with increasing Cr-ion concentration for the higher Cr-doping. Since the particle sizes of the present samples are much larger than the sizes for which quantum confinement effect is important, the observed shift cannot be assigned to the size effect. Increase of the band gap can be interpreted mainly with the $4s-3d$ and $2p-3d$ exchange interactions in which the decrease of Zn $3d$ electron density and the increase of Cr $3d$ electron density below the valence band leads to higher binding energy of the valence band-maximum giving rise to the larger band gap [282]. This blue shift behaviour or broadening in the band gap for Cr-doped samples may also be due to the Burstein-Moss band filling effect [283,284]. ZnO is an n-type material. When ZnO is doped with Cr-ions, the Fermi level will shift inside the conduction band (by ξ_n) [284]. Since the states below ξ_n in the conduction band are filled, due to Cr-doping the absorption edge shifts to the higher energy giving the blue shift or widening the band gap [285]. The red shift of the band gap observed for higher Cr doping can be interpreted to be due to the $sp-d$ exchange interactions between the band electrons (in conduction and valence bands) of ZnO and the localized d electrons of the Cr-ions [286]. The $s-d$ and $p-d$ exchange interactions lead to a negative and a positive correction to the conduction-band and the valence-band edges respectively, resulting in a band gap narrowing [287].

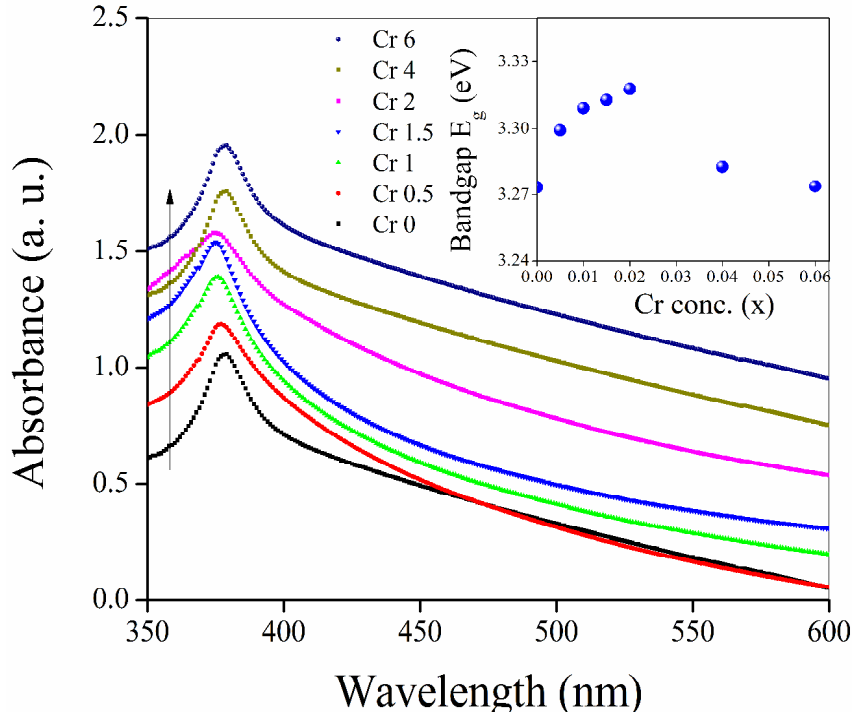


Figure 3.27: Absorption spectra of $\text{Zn}_{1-x}\text{Cr}_x\text{O}$ samples. Inset shows variation of the optical band gap (E_g) with the Cr-concentration (x).

Photoluminescence spectroscopy:

The room temperature PL spectra of Cr-doped ZnO nanocrystalline samples measured by exciting at 320 nm are shown in Fig. 3.28. From the figure it is clear that the PL peaks are broad possibly because of the presence of several recombination sites and defects. The asymmetric nature of the PL spectra is ascribed to the presence of other inherent emission peaks due to distributed defect states on the surface and in the interior of a given nanostructured system. In these asymmetrically broadened PL spectra, the defect-related emissions dominate the band-edge emission of ZnO and hence the band-edge emission (~ 380 nm) is only weakly resolved. The PL spectra (Fig. 3.28) show six peaks occurring around 380 nm, 410 nm, 434 nm, 464 nm, 485 nm and 525 nm. The first peak is in the ultraviolet (UV) region, while other five peaks correspond to violet, violet-blue, blue, blue-green, and green

respectively are in visible region. The peak in the UV region has been assigned to the near band edge excitonic emission (NBE) because the energy corresponding to this peak is almost equal to the band gap energy of ZnO [288] (estimated by UV-Vis measurements). This UV emission (NBE) peak (at 380 nm) originates from the radiative recombination of free excitons through an exciton–exciton collision process [289]. The energy interval between the bottom of the conduction band and the zinc vacancy (V_{Zn}) level (~ 3.06 eV) tells that the violet emission around 410 nm may be related to zinc vacancies. The energy interval between interstitial Zn level (Zn_i) and the valence band is consistent with the energy (~ 2.9 eV) of the violet-blue emission at 434 nm observed in our experiment. Shi et. al. have stated that the violet-blue (423nm) emission might be possibly due to radiative defects related to traps existing at grain boundaries. This emission comes from the radiative transition between this level and the valence band [290]. The weak blue emission around 464 nm may be attributed to the defect related positively charged Zn vacancies [291]. Two new emission bands viz. a blue-green band (~ 485 nm) and a green band (~ 525 nm) have been evolved due to Cr-doping which are absent in pure ZnO. The blue-green band emission (~ 485 nm) is possibly due to surface defects [292]. This green band (~ 525 nm) emission is attributed to the oxygen vacancies (V_o) which results from the recombination of electrons with photo-generated holes trapped in singly ionized oxygen vacancies [293]. Due to the enhancement in the density of singly ionized oxygen vacancies (V_o) with increasing Cr-doping, the density of surface dangling bonds increases. This increase of dangling bonds increases the probability of visible emission, whereas decreases the probability of UV emission. This seems to be the main cause behind the enhanced green emission with increasing Cr-doping.

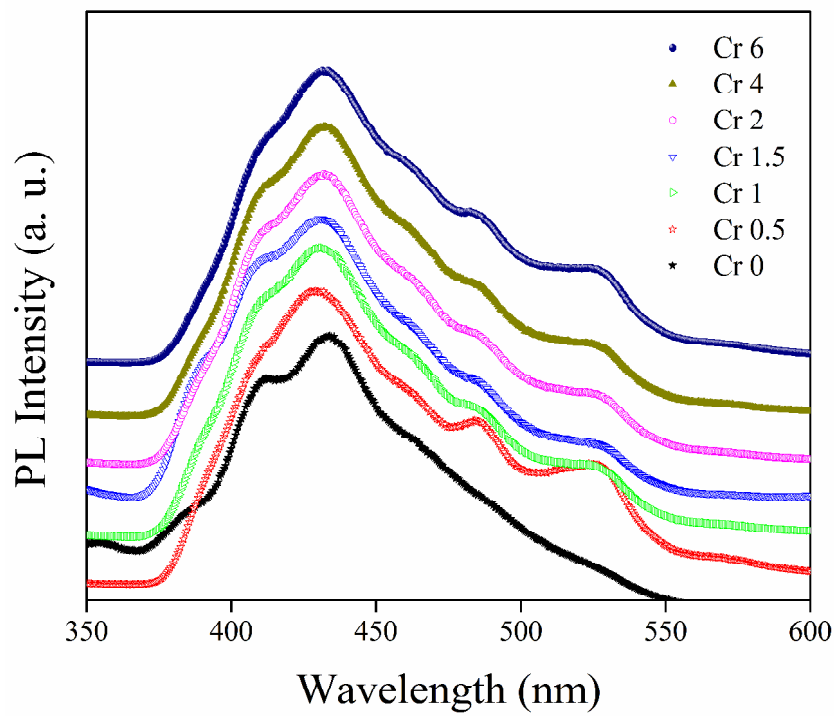


Figure 3.28: Room temperature PL spectra of the $\text{Zn}_{1-x}\text{Cr}_x\text{O}$ ($0 \leq x \leq 0.06$) samples.

Thus in summary XRD, HRTEM and Raman measurements show clear signature of changes in ZnO lattice upon Cr doping though the overall wurtzite structure remains unaffected. XANES measurements show that Cr is present in the samples in Cr^{3+} oxidation state while pre-edge peaks in XANES spectra and FTIR results show that local structure around Cr is increasingly becoming octahedral with increase in Cr doping concentration. EXAFS and PL measurements show that Cr incorporation in ZnO lattice is accompanied by creation of more and more oxygen vacancies.

Chapter 4

(Co,Cu) co-doped ZnO NCs

4.1. Introduction:

As we have discussed in Chapters 1 & 3 after theoretical prediction of room temperature ferromagnetism by Dietl et al. [53], extensive studies have been made on transition metal (TM) ion doped ZnO both in nanocrystalline and thin film form. It has also been theoretically predicted that co-doping of group-I elements alongwith TM ions in ZnO stabilizes its ferromagnetic ordering and increases the Curie temperature due to an increase in carrier concentration [82,83]. The current study primarily deals with examining local structure around the host and dopant atoms in Co doped and (Co,Cu) co-doped ZnO nanocrystals (NC) by Synchrotron based Extended X-ray Absorption Fine Structure (EXAFS) technique to explain the observed difference in magnetic properties of the samples. The NCs have also been characterized by other complementary techniques viz., X-ray diffraction, FTIR, Raman and EPR spectroscopy and their behavior has been predicted by density functional theory (DFT) based electronic structure calculations.

4.2. Experimental details:

Pure, Co doped ZnO and (Co, Cu) co-doped ZnO nanocrystals capped with Poly vinyl pyrrolidone (PVP) were synthesized by wet chemical route at room temperature [294, 295] as described in Chapter 2. For synthesis of pure ZnO, pre-calculated amount of zinc acetate $[\text{Zn}(\text{CH}_3\text{COO})_2]$ was dissolved in distilled isopropyl alcohol (IPA) completely under vigorous stirring. Subsequently, to this solution, PVP dissolved in IPA was added and the

reaction solution was stirred till the mixture became clear. Finally to this solution, NaOH dissolved in distilled IPA was added drop wise to get neutral pH value and the reaction is allowed to proceed for one hour under vigorous stirring. The nanocrystals were obtained in powder form by rotavapourization at 100°C followed by centrifugation and washing with distilled water 2 times and with IPA 1 time. In order to dope the nanocrystals with Co and/or Cu appropriate amount of cobalt (II) acetate tetrahydrate $[\text{Co}(\text{CH}_3\text{COO})_2 \cdot 4\text{H}_2\text{O}]$ and/or copper(II) acetate $[\text{Cu}(\text{CH}_3\text{COO})_2]$ was added with zinc acetate. All other reaction parameters were kept same for the synthesis of doped and co-doped ZnO nanocrystals.

The structural analysis was carried out using a Bruker AXS D8 advance powder X-ray diffractometer with a Cu-K_α radiation source ($\lambda=1.5402 \text{ \AA}$). The samples were functionally characterized by Fourier transform infrared (FTIR) spectroscopy using NICOLET 6700 FT-IR spectrometer at room temperature in the range of $4000\text{--}400 \text{ cm}^{-1}$. Optical absorption spectra have been recorded on Perkin Elmer (Lambda 950) UV-Vis spectrometer at room temperature for band gap measurements and other absorption studies. Electron paramagnetic resonance (EPR) measurements were carried out at 77 K (liquid nitrogen temperature) on JES - FA200 ESR Spectrometer of JEOL, Japan operating at X band (9.154 GHz). Magnetic measurements as a function of temperature and magnetic field were carried out using a commercial 7-Tesla SQUID-vibrating sample magnetometer (SVSM; Quantum Design Inc., USA).

Extended X-ray Fine Structure (EXAFS) measurements on these samples have been carried out at the Scanning EXAFS Beamline (BL-9) at the Indus-2 Synchrotron Source (2.5 GeV, 100 mA) at the Raja Ramanna Centre for Advanced Technology (RRCAT), Indore, India which has been described in Chapter-2. The EXAFS spectra of the samples at Cu K-edge were recorded in the energy range of 5650-6170 eV and at Co K-edge the measurements have been carried out in the range of 7400-8600 eV.

4.3. Results and discussion:

4.3.1 X-ray diffraction:

Figures 4.1(a) and (b) show the X-ray diffraction patterns for pure ZnO, ZnO doped with Co and ZnO co-doped with Co and Cu. X-ray diffraction patterns of the NCs have been analyzed with the help of FullProf program using Rietveld refinement technique [296]. In the above figures, the experimental data are shown with open circle (red), and calculated intensities are shown as solid line (black) while the dotted line represents the difference between the measured and calculated intensities. The allowed Bragg positions for this crystal structure of space group $P6_3mc$ are marked as vertical lines, these are expected peaks for wurtzite phase. The fitting quality of the experimental data is good, as Rietveld refinement R_p , R_B , R_F and χ^2 has been reduced to minimum value in the range of 3.37-0.83, 2.60-0.59, 1.71-0.36 and 1.28-0.23 respectively [297].

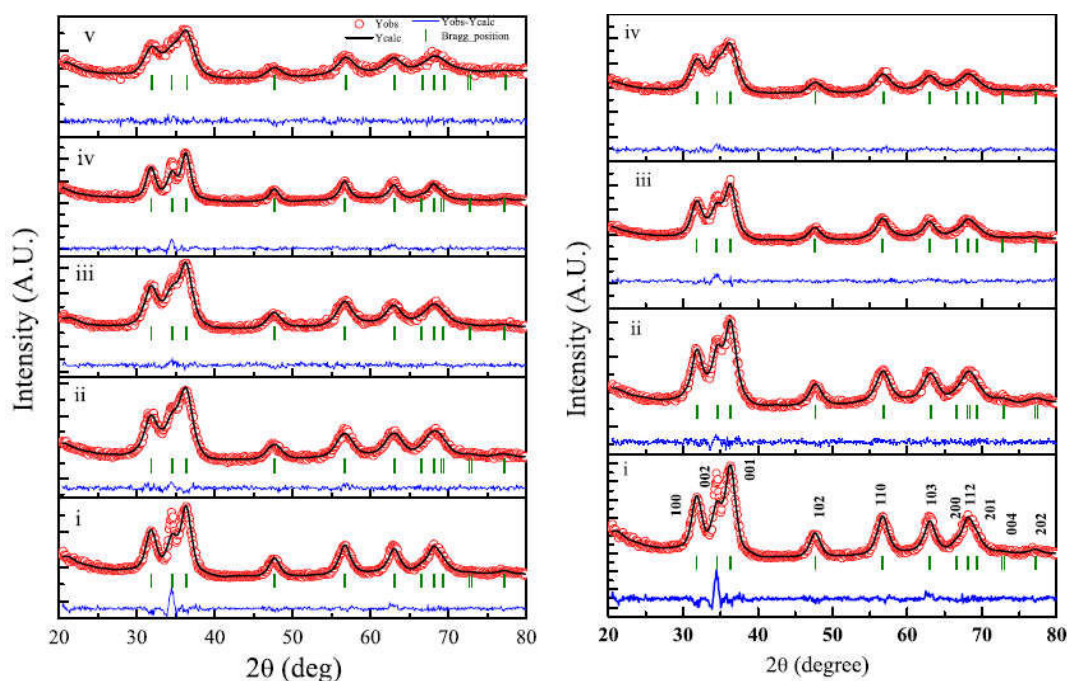


Figure 4.1: X-ray diffraction pattern with Rietveld refinement of (a) Co doped ZnO NCs (i) as-prepared ZnO, (ii) doped with 1% Co, (iii) doped with 2% Co (iv) doped with 3% Co and (v) doped with 5% Co. (b) (Co,Cu) co-doped ZnO NCs (i) as-prepared ZnO, (ii) co-doped with (1%Co, 1%Cu), (iii) co-doped with (1.5% Co, 1.5% Cu) and (iv) co-doped with (2.5% Co, 2.5% Cu).

XRD profile refinement provides convincing proof that NCs are of single phase. The hexagonal a and c cell parameter and cell volume of undoped, doped and co-doped ZnO are given in Table 4.1. It can be seen that the change in cell parameters and cell volume are not significant due to Co and Co:Cu doping in ZnO NCs, except for the 5.0% Co doped in ZnO sample where the lattice is significantly distorted. This is possibly due to the fact that the differences in radii between Co^{2+} in tetrahedral co-ordination (0.58 Å) and Zn^{2+} in tetrahedral co-ordination (0.60 Å) are very small [298].

The line broadening of the X-ray diffraction peaks may be due to the size and micro-strain of NCs. The average particle size and average micro-strain determined from broadening of diffraction peaks using Scherrer's formula, [299,300] have been shown in Table 4.2. The average crystallite size of pure ZnO NCs is calculated as 5.02 (± 0.21) nm, and it in general is found to decrease with the increase in Co and/or Cu concentration. The reduction in size is due to the doping of foreign impurities (Co and/or Cu) in ZnO which affects nucleation and growth [301].

It should be noted here that small portions of the XRD patterns around $2\theta \sim 34^\circ$ in Figs. 4.1(a) and (b), could not be fitted properly, particularly for the as-prepared ZnO NCs. This is possibly due to the fact that structures of the nanocrystals are not exactly bulk-like. Similar observations have also been made by Ganguly et.al. [302] during Rietveld fitting of the XRD pattern of their ZnO nanoparticles synthesized by chemical route, which they have attributed to be due to irregular structures of the nanocrystals or variation in crystallite size. However, the overall fit for the as-deposited samples presented here are reasonably good with low χ^2 values. It should also be noted here that these small disagreement in the fitting does not affect the overall conclusions derived from the XRD measurements. Moreover, we have excluded these particular peaks during estimated of average size and other parameters of the NCs.

Table 4.1: Rietveld refined XRD cell parameters of NCs.

Sample	Cell parameter		Cell volume
Co conc. in ZnO (%)	a (Å)	c (Å)	V (Å ³)
0	3.2464	5.1961	47.4245
1	3.2485	5.1962	47.4888
2	3.2472	5.2015	47.4981
3	3.2486	5.1974	47.5015
5	3.2391	5.2068	47.3097
(Co, Cu) conc. in ZnO (%)			
1.0,1.0	3.2438	5.1914	47.3069
1.5,1.5	3.2460	5.2055	47.4983
2.5,2.5	3.2439	5.1989	47.3796

Table 4.2: Particle size and micro-strains obtained from Rietveld refined XRD of the NCs.

Sample	Particle Size	Micro-strain (*10 ⁻³)
Co conc. in ZnO (%)	(nm)	(lines ⁻² /m ⁴)
0.0	5.02±0.21	6.917±0.35
1.0	3.92±0.21	8.856±0.45
2.0	3.69±0.53	9.611±1.35
3.0	6.08±0.05	5.700±0.06
5.0	3.44±0.13	10.078±0.32
(Co, Cu) conc. in ZnO (%)		
1.0, 1.0	4.26±0.20	8.147±0.37
1.5, 1.5	4.09±0.46	8.584±0.70
2.5, 2.5	3.65±0.11	9.503±0.28

4.3.2 Transmission Electron Microscopy:

To determine the size, shape and crystal structure of NCs, transmission electron microscope (TEM) imaging and electron diffraction were carried out. Figures 4.2(a) and 4.2(d) show the TEM images of 2.5% Co doped and (2.5% Co, 2.5% Cu) co-doped ZnO NCs respectively, which reveal the spherical shape of the NCs. The average size of NCs

(histograms shown in figures 4.2(b) and (e)) found to be 6.0 ± 0.2 nm for 2.5% Co doped and 4.3 ± 0.03 nm for (Co,Cu) co-doped ZnO NCs which are slightly more than that estimated from XRD measurements and shown in Table 4.2. This may be due to the fact that TEM also images organic capping layer at the surface of the NCs. The electron diffraction patterns (figure 4.2(c) and figure 4.2(f)) exhibit diffraction rings corresponding to (1 0 0), (0 0 2) and (1 0 1) lattice planes of wurtzite phase of ZnO. Values of inter-planar distance (d) deduced from electron diffraction and XRD measurements are almost the same and are within the experimental uncertainty. It has been observed that compared to bulk lattice spacing, the 2.5% Co doped ZnO NCs lattice has contracted by ~ 0.58 % and 2.5% (Co:Cu) co-doped ZnO NCs by ~ 0.17 % for (0 0 2) plane.

4.3.3 FTIR Spectroscopy:

FTIR spectra of undoped, Co doped and (Co,Cu) co-doped ZnO NCs are shown in Figs. 4.3(a) and (b). All the samples exhibit absorption bands at 3443, 2350, 2100, 1653, 1507, 1395, 1043, 830, 688, 492 cm^{-1} . The peak found at around ~ 3443 cm^{-1} is assigned to the –OH mode while the peak at 2350 cm^{-1} is due to the existence of CO_2 molecules in air. The peak around ~ 1043 cm^{-1} is due to asymmetric stretching of resonance interaction between vibration modes of oxide ions in NCs [301]. Also, peaks at 525, 576 and 446 cm^{-1} are attributed to ZnO stretching in ZnO lattice [301, 303]. Other peaks are also found in the FTIR spectrum of bare capping agent (PVP) (data is not shown here) and hence they can be attributed to modes related to capping agent. FTIR results thus only show the expected bands for characteristic of ZnO lattice with no extra peak found in the spectra of the doped samples, indicating that Co and Cu are occupying the Zn positions of the host lattice which is in agreement with the XRD results.

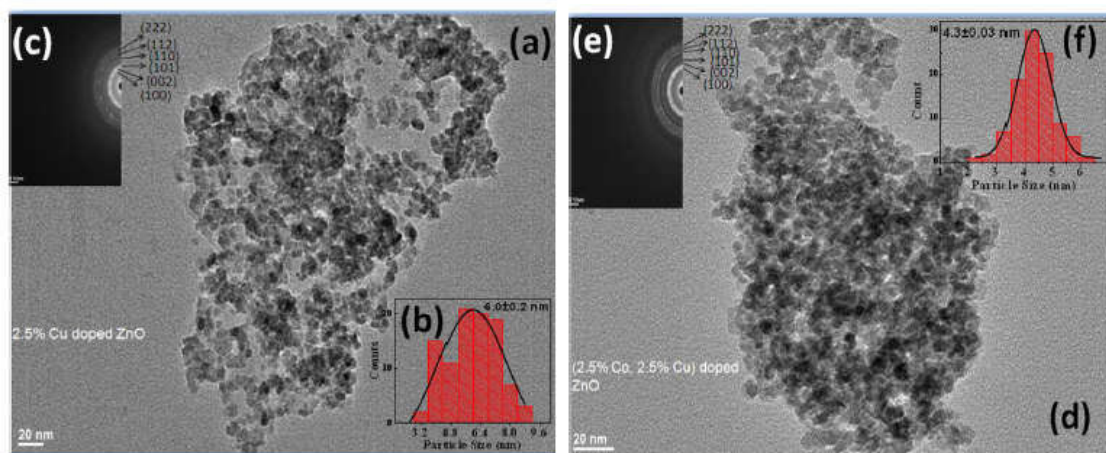


Figure 4.2: (a) TEM micrograph, (b) histograms and (c) diffraction pattern of 2.5% Co doped ZnO NCs, (d) TEM micrograph, (e) histograms and (f) diffraction pattern of (2.5% Co, 2.5% Cu) co-doped ZnO NCs.

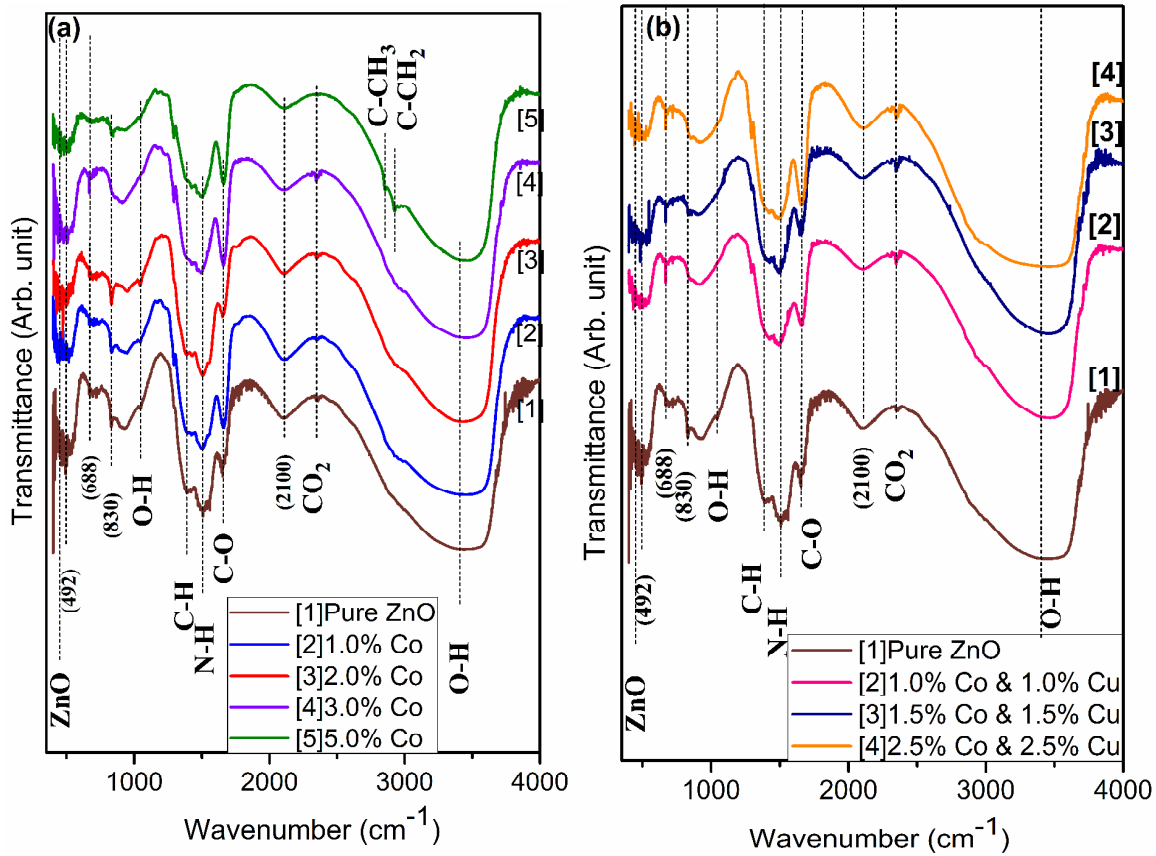


Figure 4.3: FTIR spectra of (a) Co doped ZnO NCs and (b) (Co,Cu) co-doped ZnO NCs.

4.3.4 Raman Spectroscopy:

The room temperature Raman spectra of pure, Co doped and (Co,Cu) co-doped ZnO NCs in the range of 200–800 cm^{-1} are shown in figure 4.4. Usually, the zone centre Raman active optical phonons of ZnO are predicted by group theory analysis to be $\Gamma = A_1 + E_1 + 2E_2$ (Raman active) [304]. Out of these, A_1 and E_1 modes are polar and split into transverse optical (TO) and longitudinal optical (LO) phonons [304] and so six active phonon modes can be seen in case of ZnO [248, 305]. Among the above, in the present case five distinct features respectively at ~ 330 , ~ 413 , ~ 437 , ~ 530 and ~ 575 cm^{-1} are observed for undoped ZnO nanocrystals in the available range of wavelength. The peak at ~ 437 cm^{-1} is assigned [301,306-308] to high frequency branch of E_2 (i.e., E_{2H} : non-polar E_2 optical phonon) mode

and is a characteristic peak for ZnO in wurtzite structure [309], which agrees with XRD results. However, due to the nanocrystalline nature of the samples, the E_{2H} mode is broad and weak, which is similar to the phenomena found in amorphous ZnO [304]. Peak at $\sim 413\text{ cm}^{-1}$ is attributed to $E_1(\text{TO})$ mode [306] of ZnO and this peak is also weak and gets merged into the E_{2H} peak. Peak around 330 cm^{-1} is assigned to E_{2M} mode [310] (second-order Raman processes involving acoustic phonons) which is a signature of a good quality of crystal synthesized [311]. The peak at $\sim 575\text{ cm}^{-1}$ is assigned to $E_1(\text{LO})$ peak [304].

Raman peak about $\sim 530\text{-}540\text{ cm}^{-1}$ which is significant for only (Co,Cu) co-doped and 5% Co doped NCs is attributed to quasi-longitudinal-optical (LO) phonon mode related to dopants bound with the donor defect [301,311-313]. These donor defects are doubly occupied oxygen vacancies, and zinc interstitials [301, 313]. For (Co,Cu) co-doped ZnO NCs, the peak is prominent as compared to others. So, it can be confirmed that, defect density increases for co-doped ZnO NCs. Raman peak around $\sim 675\text{ cm}^{-1}$ which is also observed for only Co doped samples and becomes prominent with increase in Co concentration can be assigned to local vibration mode of Co that is bound with the donor defects [310] which confirms that, substitution of Co^{2+} ions creates new lattice defects or initiates the intrinsic host lattice defects]. It should also be noted that the E_{2H} band at 437 cm^{-1} in case of doped and co-doped ZnO NCs shifts towards lower wave number as Co and/or Cu concentration increases. This shift in position is also accompanied by lowering of intensity and broadening of the peaks which indicates localized distortion in ZnO lattice due to the incorporation of the dopants [310]. Further, no additional Raman modes due to either cobalt and/or copper oxides are observed for doped and/or co-doped ZnO nanocrystals revealing the absence of any impurity phase [301].

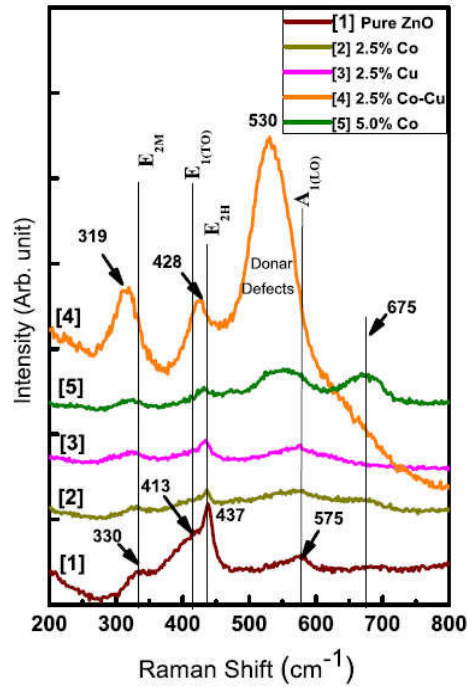


Figure 4.4: Raman spectra of Co doped, Cu doped and (Co,Cu) co-doped ZnO NCs.

4.3.5 Optical Absorption studies:

Figs. 4.5 (a) and (b) show optical absorption spectra of synthesized undoped ZnO, Co doped and (Co,Cu) co-doped NCs. The excitonic feature for undoped ZnO NCs is observed at ~ 350 nm (i.e. $E_g = 3.54$ eV) which is clearly blue-shifted compared to ZnO bulk band gap of ~ 3.37 eV. The Co doped and (Co, Cu) co-doped ZnO NCs reveal a subtle but consistent blue shift of approximately 15 nm and 14 nm respectively.

Optical absorption spectra show additional features at 568, 611, and 653 nm in both Co doped and (Co, Cu) co-doped ZnO nanocrystals with no discernible change in the two cases. The intensity of these features slightly increases with increase in dopant concentration. These sub-forbidden gap features are the ligand field $d-d$ transitions of Co^{2+} in tetrahedral environment and are ascribed as ${}^4A_2(F) \rightarrow {}^2A_1(G)$, ${}^4A_2(F) \rightarrow {}^4T_1(P)$, and ${}^4A_2(F) \rightarrow {}^2E(G)$ ligand field transitions [303]. The appearance of these transitions also implies a high spin

state of Co^{2+} (d^7). These ligand field transitions do not reveal appreciable change with an increase in doping level. The substitutional incorporation of Co^{2+} ions indicated by XRD and FTIR is corroborated by the optical absorption measurements also. Co $d-d$ transition peaks at 611 nm and 653 nm in Co doped ZnO NCs are found to be slightly shifted to 612 nm and 655 nm respectively in (Co,Cu) co-doped ZnO NCs.

4.3.6 EPR Spectroscopy:

Undoped ZnO NCs did not show any EPR signal indicating the absence of significant extent of oxygen vacancies or any transition metal impurity. Figs. 4.6 (a) and (b) show EPR spectra of ZnO NCs co-doped with (Co,Cu) ions with different concentrations which exhibit well-resolved hyperfine splitting, characteristic of isolated Co^{2+} and Cu^{2+} ions [314,315]. The g -values (Lande g -factor) of the various peaks are also indicated in the figures. It has also been observed that for (Co, Cu) co-doped NCs g -values do not change as concentrations of Co and Cu increase from 1% to 2.5%. This suggests that interactions among the dopant ions are rather weak manifesting the fact that they are randomly distributed in the ZnO matrix without clustering. The EPR result thus show that Co^{2+} and Cu^{2+} ions are in a tetrahedral coordination in the ZnO matrix [316] and no secondary or impurity phase is observed in (Cu,Co) co-doped ZnO NCs corroborating the results of XRD and FTIR measurements described above.

Thus the above complementary measurements show that the dopants are uniformly distributed in the ZnO lattice without formation of any secondary phase and thus the magnetic properties of the co-doped ZnO system should be governed by this fact.

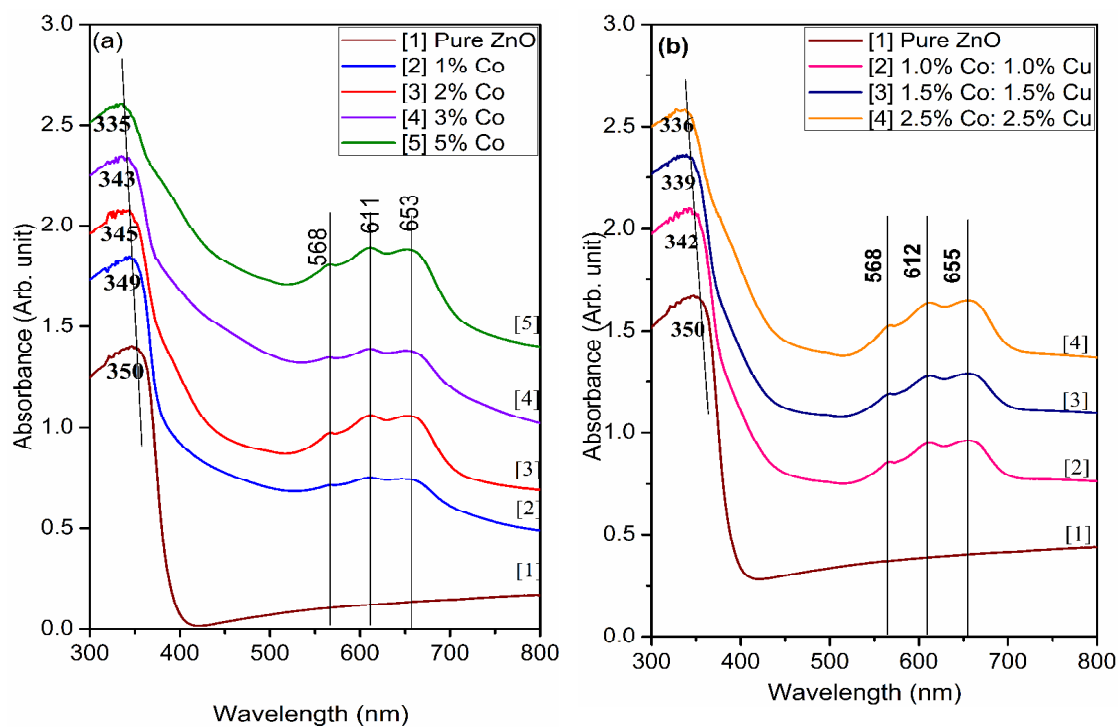


Figure 4.5: Optical absorption spectra of (a) Co doped ZnO NCs and (b) (Co,Cu) co-doped NCs.

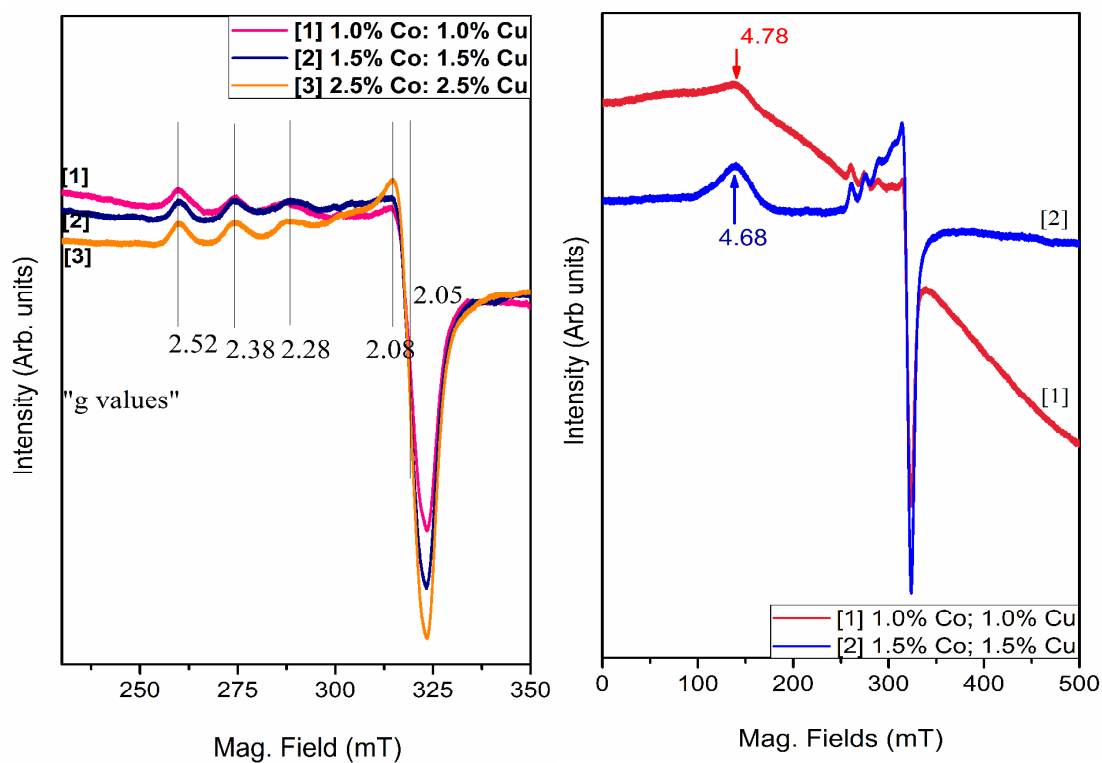


Figure 4.6: EPR spectra of (Co,Cu) co-doped ZnO NCs.

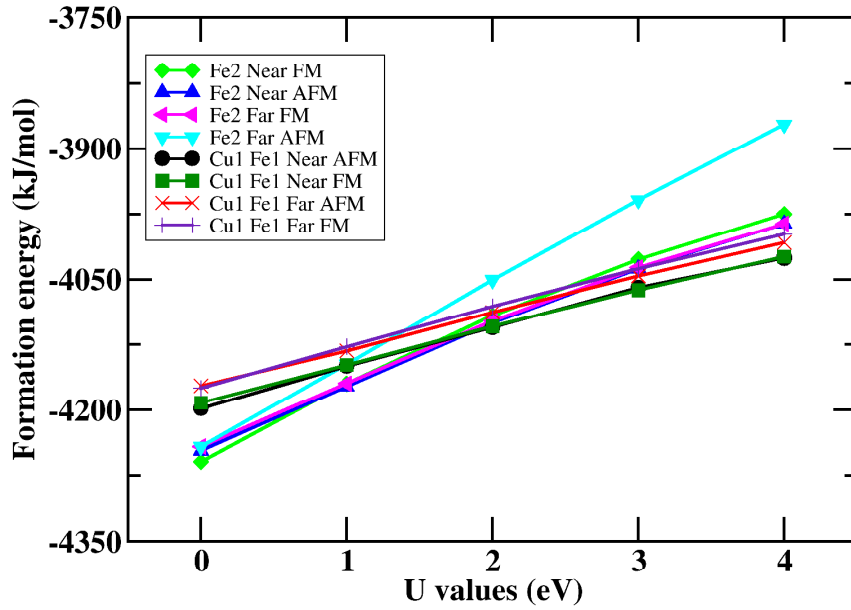


Figure 4.7: Plot of formation energy vs. the on-site Coulomb interaction (U) for both Co doped and (Co, Cu) co-doped ZnO systems

4.3.7 Theoretical calculations:

In order to understand the above experimental observations of the (Co, Cu) co-doped ZnO sample, we have also carried out density functional theory (DFT) [198, 199] based electronic structure calculations for Co and Cu doped ZnO. For this purpose, we have used Vienna ab-initio simulation package (VASP) within the framework of the projector augmented wave (PAW) method [200, 201]. For exchange–correlation (XC) functional, we employ generalized gradient approximation (GGA) given by Perdew–Burke–Ernzerhof (PBE) [202] as mentioned in Chapter 2.

In this case, we choose a (2x2x2) super cell of bulk ZnO containing 16 Zn and 16 O atoms and subsequently two Zn atoms in the super cell are substituted by Co and Cu atoms. Two distinctly different systems have been considered, namely (i) two Co atoms substituted

in the supercell of ZnO ($\text{Co}_2\text{Zn}_{14}\text{O}_{16}$) and (ii) one Co and one Cu atom substituted in the supercell of ZnO ($\text{Cu}_1\text{Co}_1\text{Zn}_{14}\text{O}_{16}$). These correspond to 12.5 % of Co doping in (i) and 6.25 % of Co and 6.25% of Cu dopings in (ii) respectively. In Fig. 4.7, we have probed two relative distances between the substituent atoms ((i) “Near” to and (ii) “Far” from each other and two different magnetic configurations (i) Ferromagnetic (FM) and (ii) Anti-ferromagnetic (AFM). The results of the calculation of formation energy show that both the Co-doped ZnO ($\text{Co}_2\text{Zn}_{14}\text{O}_{16}$) and (Cu, Co) co-doped ZnO ($\text{Cu}_1\text{Co}_1\text{Zn}_{14}\text{O}_{16}$) are energetically stable systems. Furthermore, we observe that when two Zn atoms out of 16 Zn atoms in the ZnO supercell is substituted with two Co atoms, the system is energetically more favorable than the system of ZnO co-doped with Co and Cu atoms i.e., one Co and one Cu replacing the two Zn atoms of the supercell. Further, in each case, the energy differences between “Near” and “Far” locations of the substituent atoms (Co and/or Cu) and also between FM and AFM magnetic configurations are very small. Thus, it appears from the DFT calculations with standard GGA XC functional that co-doping with (Co,Cu) should not significantly modify the magnetic properties of Co doped ZnO system.

However, we wish to mention here that the above DFT calculations with standard GGA XC functional do not take care of any strong on-site electron correlations which may be present in system. In order to probe the effect of strong-correlation, we also perform the calculations using DFT + U method, where U is the on-site Coulomb interaction between the electrons of an atom. First, we perform the calculations with $U = 1\text{--}5$ eV for d-orbitals of Co atoms. We observe from Fig. 4.7 that the energetically most favorable configuration changes from “ $\text{Co}_2\text{Zn}_{14}\text{O}_{16}$ ” to “ $\text{Cu}_1\text{Co}_1\text{Zn}_{14}\text{O}_{16}$ ” at around $U = 2$ eV for d-orbitals of Co atoms. Further, the energy difference between these two doped cases steadily increases with the U value. After $U=5$ eV for d-orbitals of Co atoms, we also introduce the on-site electron correlation (U) for the d-orbitals of both Cu and Zn atoms. However, the results of our

calculations indicate that the trend in most favorable configuration is reversed and “Co₂Zn₁₄O₁₆” becomes more favorable configuration as a result of introduction of U in the d-orbitals of both Cu and Zn atoms. Thus, our calculations indicate that, in the present system, if there is a relatively stronger on-site Coulomb-correlation for the electrons in d-orbitals of Co atoms in comparison to the on-site correlation for the electrons of the Cu and Zn atoms, there is a finite probability that the co-doped sample becomes energetically more favourable and enhanced magnetization may be realized in the sample due to an increase in carrier concentration by Cu doping.

4.3.8 Magnetic Measurements:

Fig. 4.8(a) shows the magnetization (M) vs applied field (H) curves of 2.5% Co doped, 2.5% Cu doped and (2.5% Co, 2.5% Cu) doped ZnO samples measured at 300 K. It can be seen that though the Cu doped sample does not show any magnetic hysteresis behavior, the (Co,Cu) co-doped sample shows weak FM behavior, whereas 2.5% Co doped sample reveals magnetic hysteresis behavior with saturation magnetization (M_s) close to 0.095 emu/gm. It is also found that the (Co,Cu) co-doped sample shows a non-saturation trend, with almost a linear increase in magnetization with magnetic field and its magnetic moment value is less than the Co doped sample. The decrease in magnetization in the (2.5% Co, 2.5% Cu) co-doped sample compared to the 2.5% Co doped sample is similar to that observed by Lin et al. for their (2% Co, 2% Cu) co-doped sample [317].

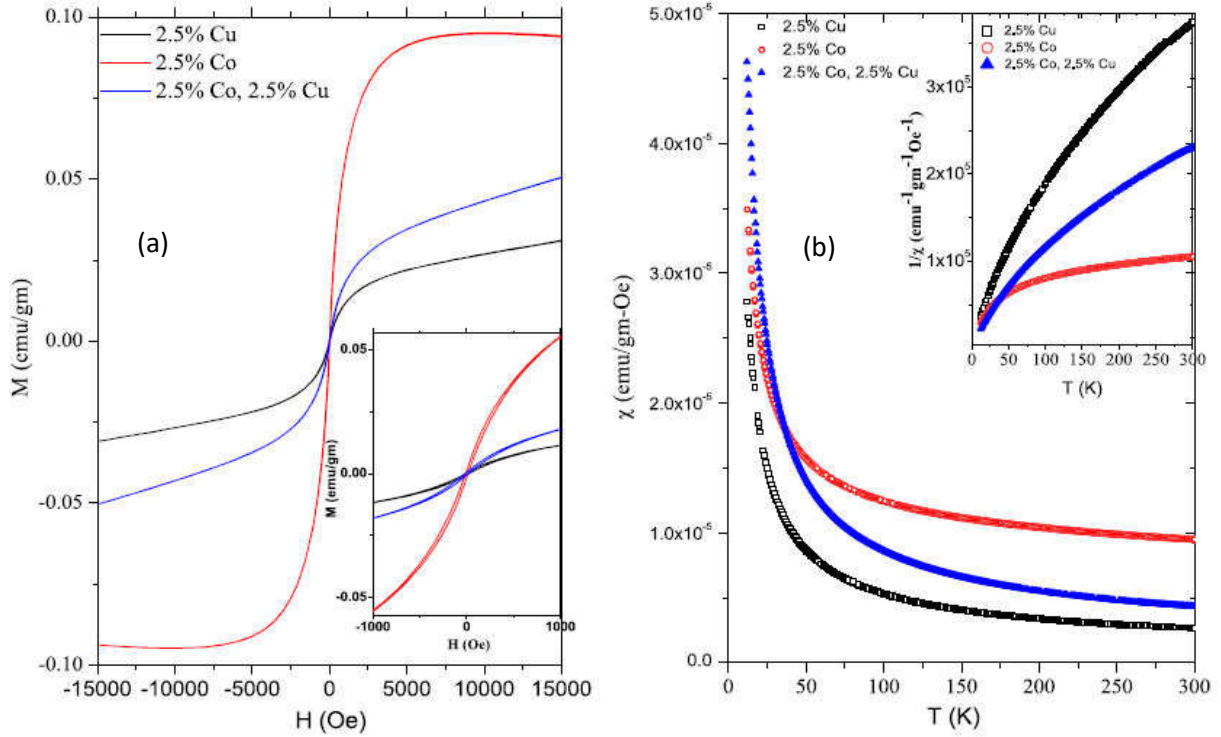


Figure 4.8:(a) M vs. H curve for a 2.5% Codoped, 2.5%Cu doped and (2.5%Co;2.5%Cu) co-doped ZnO NCs. (b) Temperature dependence of magnetic susceptibilities χ and inverse susceptibilities χ^{-1} (inset) measured in a dc field $H=100$ Oe for the above samples.

Temperature dependent susceptibilities $\chi(T)$ of the samples have been recorded in the range 5K to 300 K at a constant magnetic field of 100 Oe and are shown in Fig. 4.8(b). The behavior of magnetic susceptibility follows the paramagnetic like trend for all the samples, interestingly even for Co doped ZnO sample. To understand this behavior better, we plot the inverse susceptibility $\chi^{-1}(T)$ curves for all the samples as, as shown in the inset of Fig. 4.8(b), and attempt to fit the Curie-Weiss behavior as described in Chapter 2. It turns out that the inverse susceptibility behavior does not show linearity with temperature, suggesting that some short range correlation exists between magnetic moments in the studied temperature range. An attempt to fit the linearity at high temperature values point out towards a negative θ value, indicative of anti-ferromagnetic correlation, which could be the reason for a rather low

value of M_s in Co doped sample, even though it reveals magnetic ordering at room temperature.

4.3.9 EXAFS Spectroscopy:

To investigate further the reason for reduction in magnetization in the (2.5% Co, 2.5% Cu) ZnO sample instead of enhancement as has been predicted, we have carried out local structure investigation by synchrotron based EXAFS study at Zn, Co and Cu K edges.

4.3.9.1 Zn K-edge data:

Fig. 4.9(a) represents the experimental EXAFS ($\mu(E)$ versus E) spectra of undoped, Co doped, Cu doped and (Co, Cu) co-doped ZnO NCs measured at Zn K-edge. In order to take care of the oscillations in the absorption spectra, the energy dependent absorption coefficient $\mu(E)$ has been converted to absorption function $\chi(E)$ which is described in Chapter 2. A set of EXAFS data analysis codes available within the IFEFFIT software package have been used for EXAFS data analysis as described in details in Chapter-2.

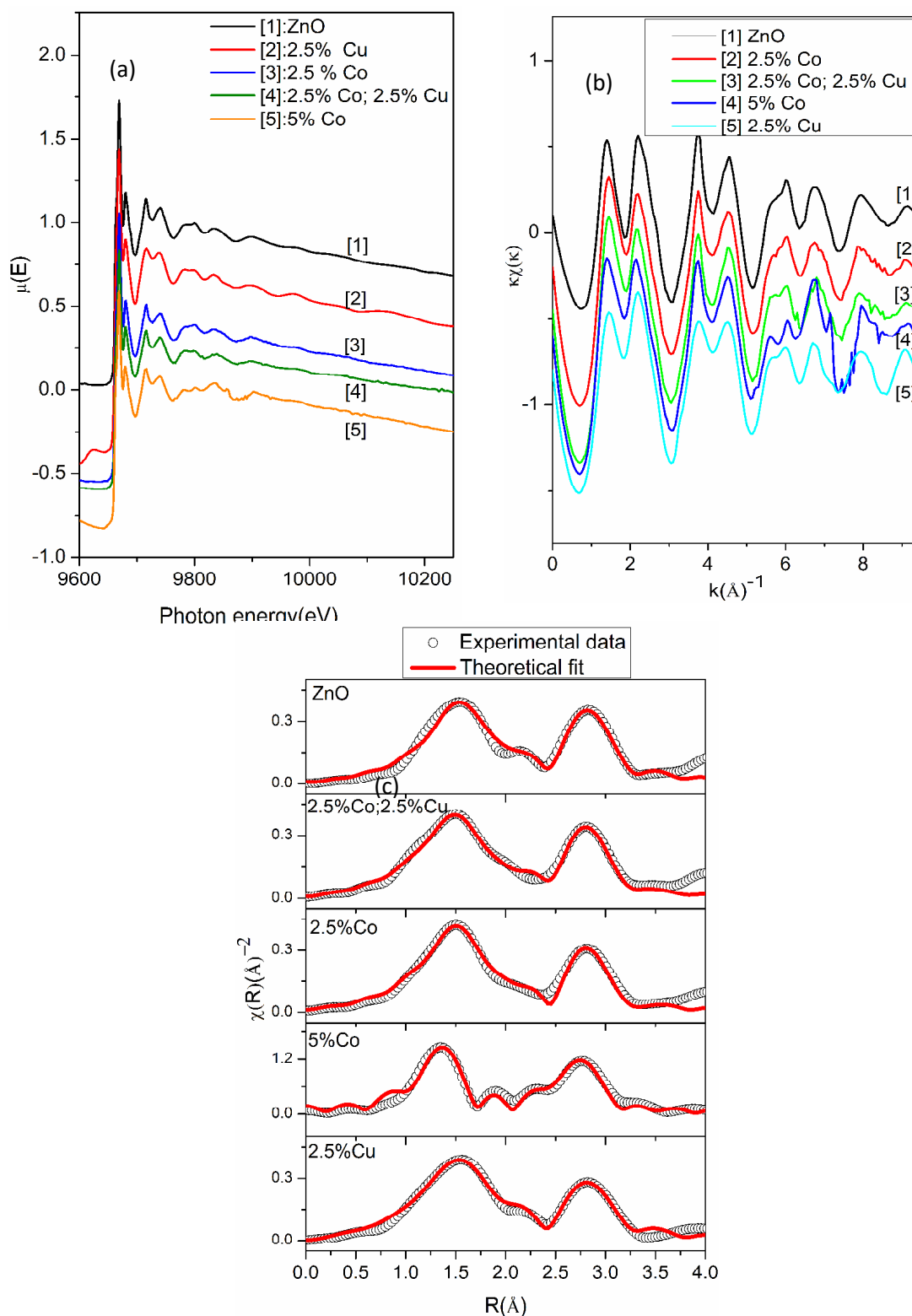


Figure 4.9 (a) Normalized experimental EXAFS ($\mu(E)$ versus E) for 2.5% Co doped, 5% Co doped, 2.5% Cu doped and (2.5% Co; 2.5% Cu) co-doped ZnO NCs measured at Zn K-edge (b) k -weighted $\chi(k)$ function of the Zn K-edge for the undoped and doped samples and (c) the experimental $\chi(R)$ versus R spectra and the theoretical fits of undoped and doped ZnO samples at Zn K-edge.

Table 4.3: Results of fitting of Fourier transformed EXAFS data at Zn K-edge.

	Values in parenthesis are nominal values	ZnO 0%	ZnO: 2.5%Co	ZnO: (2.5% Co, 2.5% Cu)	ZnO: 2.5%Cu	ZnO: 5%Co
Zn-O	CN(4)	3.4±0.6	3.6±0.4	3.67±0.47	4±0.24	1.8±0.1
	σ^2	0.006±0.01	0.003±0.002	0.005±0.004	0.007±0.004	0.005±0.001
	R (Å)	2.00±0.06	1.96±0.03	1.96±0.03	1.98±0.02	1.84±0.005
Zn-Zn	CN(12)	12.0±0.06	11.1±1.0	11.4±1.0	11.4±1.2	5.3±1.2
	σ^2	0.0005±0.001	0.0006±0.0009	0.0004±0.0009	0.0007±0.0001	0.01±0.004
	R (Å)	3.25±0.008	3.25±0.008	3.16±0.01	3.4±0.008	2.71±0.009
Zn-O	CN(1)	1.83±0.64	1	2.4±0.6	0.95±0.54	0
	σ^2	0.001±0.009	0.003±0.004	0.004±0.003	0.001±0.006	0
	R (Å)	3.36±0.04	3.05±0.04	3.06±0.03	3.06±0.07	0
Zn-Co	CN(1)					1.88±0.18
	σ^2					0.011±0.004
	R (Å)					2.89
R_{factor}		0.03	0.028	0.03	0.017	0.017

Fig. 4.9(b) shows the $\chi(k)$ versus k plots for the samples derived from the experimental EXAFS spectra. The structural parameters (atomic coordination and lattice parameters) of ZnO used for simulation of the theoretical Fourier transformed EXAFS spectra

of the samples have been obtained from reference and the best fit $\chi(R)$ versus R plots of the samples have also been shown in figure 4.9(c) along with the experimental data. The bond distances, co-ordination numbers (including scattering amplitudes) and disorder (Debye-Waller) factors (σ^2), which give the mean square fluctuations in the distances, have been used as fitting parameters. The best fit parameters have been shown in Table 4.3. From Table 4.3, it has been observed that no significant changes occur in the local environment of Zn on Cu and Co doping since these dopants have similar ionic radii as Zn in tetragonal coordination and they are most probably getting incorporated in the lattice in +2 oxidation state only. However, it is found that for the 5% Co doped ZnO sample, the oxygen coordination in the 1st shell and the Zn-O bond length decreases drastically and in the Fourier transformed EXAFS data for this sample, an extra peak also appears at $\sim 1.8\text{\AA}$. This is possibly due to elemental Co clustering in the interstitial positions in this sample and an extra Zn-Co path with a bond length of 1.8\AA and CN of 1 has to be added in its theoretical model to account for this contribution. The above result is in contrast with our earlier findings [318] on Co doped ZnO samples which shows no Co clustering upto 10% Co doping and the above difference possibly appears due to difference in preparation process of the two types of samples.

4.3.9.2 Co K-edge data:

Fig. 4.10(a) represents the experimental EXAFS ($\mu(E)$ versus E) spectra of Co doped and (Co, Cu) co-doped ZnO NCs measured at Co K-edge while Fig. 4.10(b) shows the k -weighed $\chi(k)$ versus k plots of the samples derived from the experimental EXAFS spectra. At the Co K-edge we explored the two possibilities of theoretical modeling to fit the experimental data: (a) taking the initial model to be of cubic CoO and (b) starting with the basic wurtzite ZnO structure and replacing the central Zn atom with Co. This approach has

been taken earlier by our group and other workers also in analyzing the EXAFS data of similar systems [318]. Fig. 4.10(c) and 10(d) show the Fourier transformed EXAFS $\chi(R)$ versus R spectra of 2.5% Co, 5%Co, (2.5% Co, 2.5% Cu) doped ZnO samples at the Co K-edge, along with best fit theoretical spectra where the fittings have been carried out by using (i) cubic CoO structure and (ii) wurtzite ZnO structure (where Zn is replaced by Co) respectively and the best fit parameters have been given in Tables 4.4 and 4.5. The theoretical spectrum for CoO is generated assuming the model as described in [319] with the nearest oxygen shell at 2.13 Å and next nearest Co shell at 3.02 Å with CNs 6 and 12 respectively.

It was found from the χ^2 fitting of the data and the R_{factor} 's obtained in the two cases that both the above models fit the experimental data almost similarly. However, for the CoO structure model, as can be seen from Table 4.4, though we have started with the 6 oxygen coordination of the first Co-O shell at a distance of 2.13Å, the final best fit values resemble that of Zn-O bond length of ~1.97 Å and coordination number of 4, which shows that Co goes into the tetrahedral lattice of ZnO. It should also be noted that in both the cases, the first Co-O bond length is significantly less for the 5% Co doped sample compared to the other two samples as has also been observed from the fitting of EXAFS data of the samples at Zn K-edge.

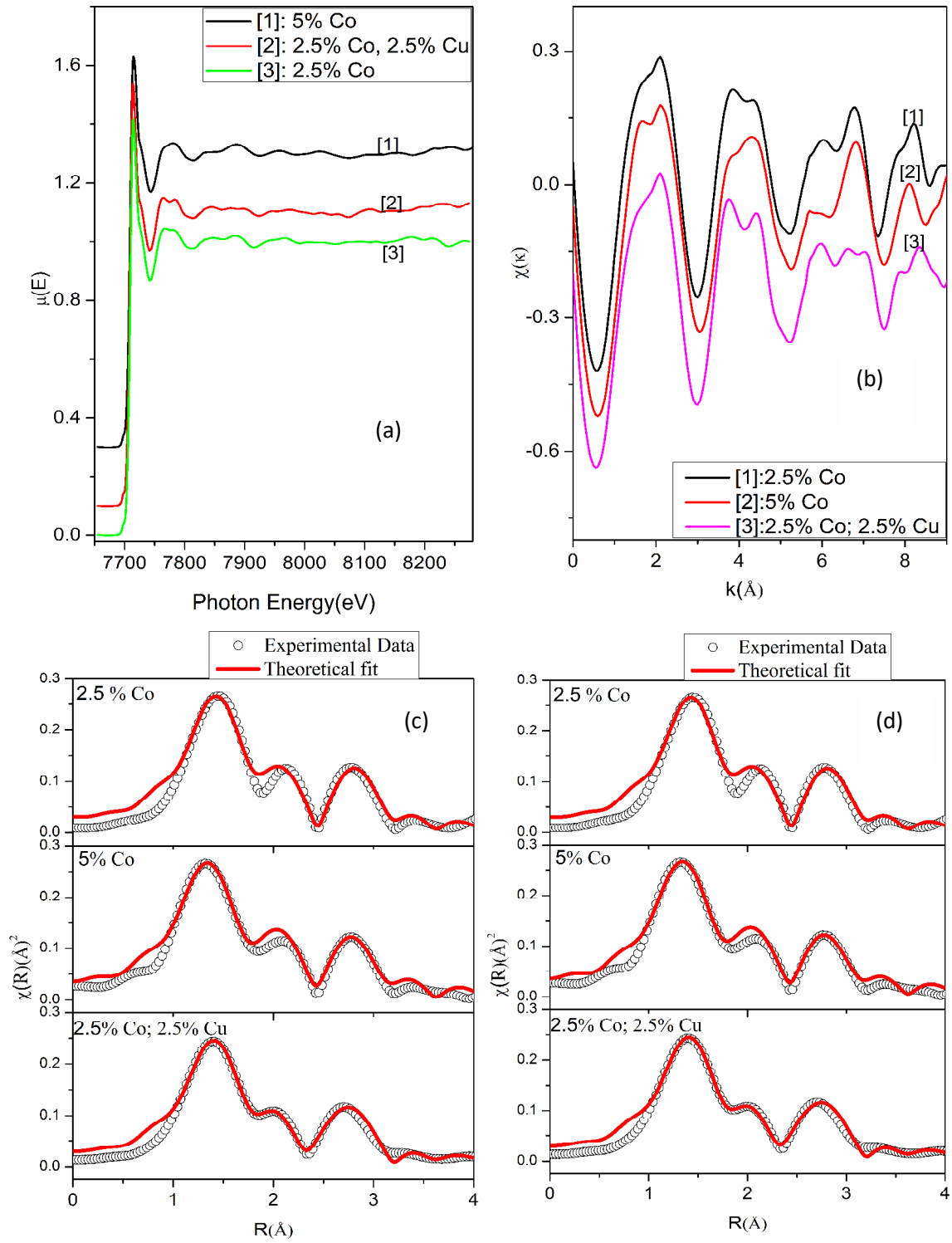


Fig.4.10. (a) Normalized experimental EXAFS ($\mu(E)$ vs. E) for 2.5%Co, 5% Co doped and (2.5%Co;2.5%Cu) co-doped ZnO NCs measured at Co K-edge. **(b)** k -weighed $\chi(k)$ function of the Co K-edge for 2.5% Co, 5% Co doped and (2.5% Co; 2.5% Cu) co-doped ZnO NCs measured at Co K-edge. **(c)** The experimental $\chi(R)$ vs. R spectra and the theoretical fits for the Co doped and (Co, Cu) co-doped ZnO NCs at CoK-edge where the fitting has been carried out with CoO structure. **(d)** The experimental $\chi(R)$ vs. R spectra and the theoretical fits for the Co doped and (Co, Cu) co-doped ZnO NCs at Co K-edge where the fitting has been carried out with ZnO structure with Zn atoms replaced by Co atoms.

4.3.9.3 Cu K-edge data:

Fig. 4.11(a) shows the experimental EXAFS spectra of Co doped and Cu doped ZnO NCs measured at Cu K-edge while Fig. 4.11(b) shows the k -weighed $\chi(k)$ versus k plots of the samples derived from the experimental EXAFS spectra.

Similar to the Co K-edge analysis, in this case also we have explored the two possibilities of theoretical modelling to fit the experimental data: (a) starting with the basic wurtzite ZnO structure and replacing the central Zn atom with Cu and (b) taking the initial model to be of cubic CuO [320]. However, in this case it has been observed that reasonable fitting of the data could only be carried out using the later approach only. Fig. 4.11(c) shows the Fourier Transformed EXAFS $\chi(R)$ versus R spectra of, (2.5% Co, 2.5% Cu) and 2.5% Cu doped ZnO samples at the Cu K-edge along with the best fit theoretical spectra where the fitting has been carried out by using CuO structure. The fits were performed in R -space within 1-3.8 Å range and the best fit parameters are shown in Table 4.6. Thus it shows that local structure of Cu ions resembles that of cubic CuO rather than ZnO tetrahedra, or in other words it proves the presence of CuO phase in the co-doped ZnO NCs. For comparison Fourier transformed EXAFS $\chi(R)$ versus R spectra of 2.5% Cu doped ZnO sample, fitted by assuming wurtzite ZnO structure and replacing the central Zn atom with Cu is shown in Fig. 4.11(d) which shows inferior quality of fitting.

Lin et al. [317] had also observed that though very small amount of Cu doping (~1%), creates additional charge carriers to enhance ferromagnetism in Co doped ZnO samples, a little more Cu doping (~2%) gives rise to a drastic reduction in magnetization. They had also predicted it to be due to the presence of CuO phase but did not furnish any experimental support. Thus the present study undoubtedly establishes the fact that Cu doping ~2.5% indeed gives rise to CuO phase in the co-doped sample which does not allow us to achieve

any significant improvement in magnetization by additional Cu doping in Co doped ZnO NCs. This CuO phase however, is not detectable by any other technique as described above and could only be seen in the local structure probe of EXAFS. The presence of secondary phases in the doped ZnO system which were detected by EXAFS technique but could not be detected by XRD has been reported earlier by us and other groups as well [321,322, 323]. It should also be mentioned here that Kataoka et al. [322] have also observed presence of Cu in a mixed Cu^{+2} and Cu^{+3} state in the bulk of Cu doped ZnO nanowires by Cu L-edge XANES studies, however they have not probed the EXAFS spectra to find out the exact nature of the Cu species in the ZnO matrix.

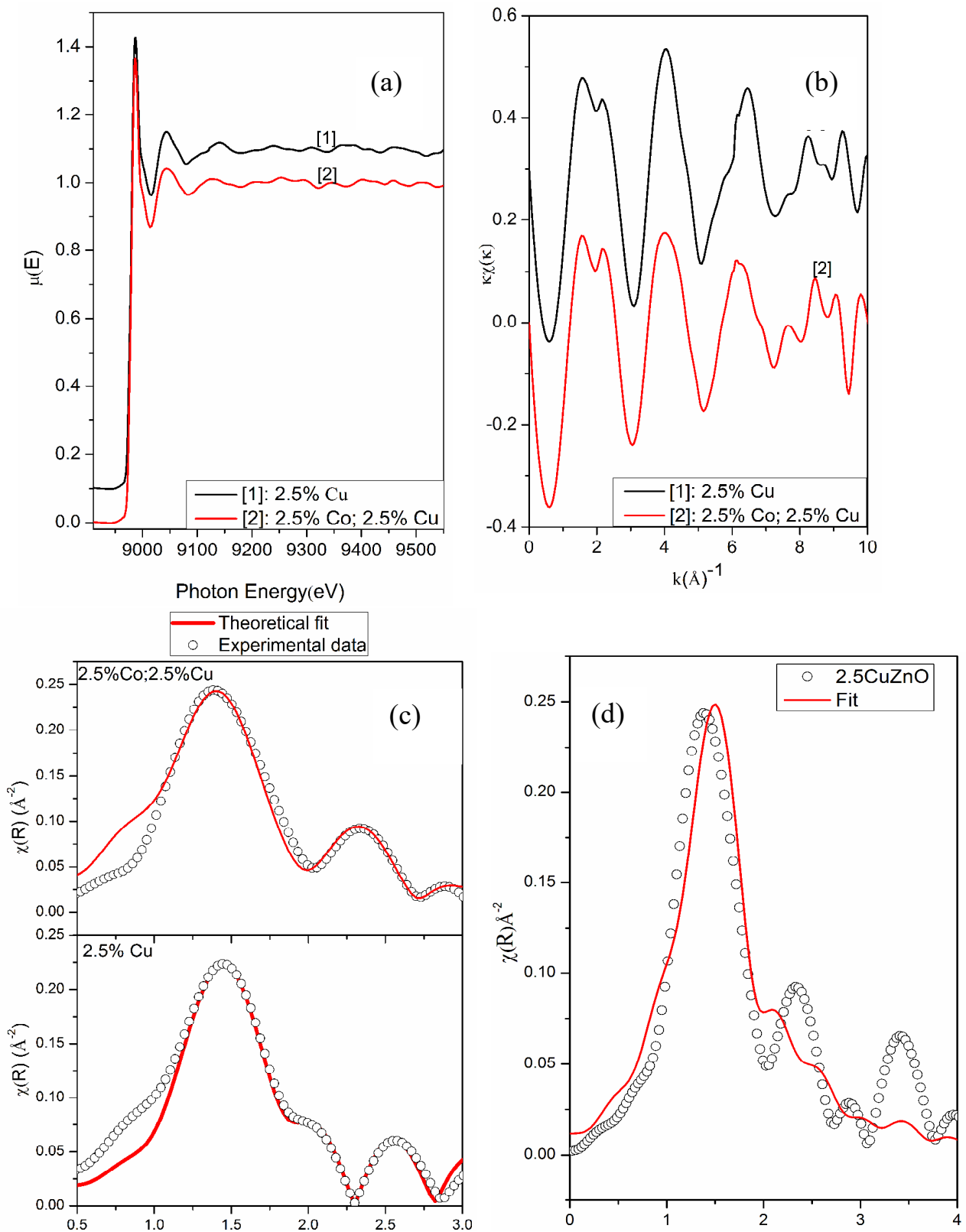


Fig.4.11. (a) Normalized experimental EXAFS ($\mu(E)$ vs. E) for 2.5% Cu doped and (2.5%Co;2.5%Cu) co-doped ZnO NCs measured at Cu K-edge.(b) k -weighed $\chi(k)$ function of the Cu K-edge for the 2.5% Cu and (2.5% Co; 2.5% Cu) co-doped ZnO NCs. (c) The experimental $\chi(R)$ vs. R spectra for the 2.5%Cu and (2.5%Co;2.5%Cu) co-doped ZnO NCs at Cu K-edge where the fitting has been carried out with CuO structure and (d)The experimental $\chi(R)$ vs. R spectra for the 2.5%Cu doped ZnO NCs at Cu-K-edge where the fitting has been carried out with ZnO structure with Zn atoms replaced by Cu atoms.

Raman and EPR measurements do not manifest the presence of a secondary oxide phase in the sample other than wurtzite ZnO with Zn atoms substituted by Cu and Co, EXAFS study clearly establishes that Cu is present as CuO in the samples which is detrimental to its magnetic properties and hence Cu doping in the ZnO samples in addition to Co doping reduces its magnetization.

Table 4.4: EXAFS fitted with CoO structure at Co K-edge.

		ZnO 2.5% Co	ZnO 5% Co	ZnO (2.5% Co, 2.5% Cu)
Co-O	CN(6)	2.76±0.24	2.7±0.12	2.82±0.10
	σ^2	0.006±0.002	0.006±0.001	0.008±0.001
	R (2.13 Å)	1.94±0.01	1.87±0.007	1.91±0.009
Co-Co/Cu/Zn	CN(12)	10.08±1.68	10.56±0.6	11.8±0.12
	σ^2	0.02±0.003	0.02±0.001	0.03±0.003
	R (3.0 Å)	2.93±0.02	2.91±0.02	2.88±0.02
Co-O	CN(8)	6.88±1.04	7.0±0.56	8.56±0.87
	σ^2	0.005±0.005	0.003±0.001	0.01 0.003
	R (3.7 Å)	3.56±0.02	3.58±0.009	3.57±0.02
R_{factor}		0.069	0.038	0.053

Table 4.5: EXAFS data fitted with ZnO structure at Co K-edge.

		ZnO 2.5%Co	ZnO 5%Co	ZnO (2.5% Co, 2.5% Cu)
Co-O	CN(4)	2.2±0.12	2.68±0.16	2.28±0.20
	σ^2	0.0009±0.001	0.004±0.001	0.003±0.003
	R (1.97 Å)	1.96±0.01	1.89±0.01	1.94±0.016
Co- Co/Cu/Z n	CN(6)	7.5±0.42	5.94±0.36	6.0±0.66
	σ^2	0.003±0.003	0.001±0.002	0.008±0.005
	R (3.20 Å)	3.25±0.01	3.25±0.01	3.19±0.02
Co-O	CN(6)	6.8±0.54	5.76±0.47	6.0±1.8
	σ^2	0.004±0.005	0.003±0.003	0.018±0.009
	R (3.25 Å)	3.38±0.006	3.40±0.03	3.30±0.057
R_{factor}		0.02	0.03	0.06

Table 4.6: XAFS fitted with CuO structure at Cu K-edge.

		ZnO 2.5%Cu	ZnO (2.5% Co, 2.5% Cu)
Cu-O	CN(4)	4	2.88±0.12
	σ^2	0.006±0.0006	0.004±0.0006
	R (1.95Å)	1.91±0.009	1.92±0.003
Cu-O	CN(2)	2.46±0.64	2
	σ^2	0.001±0.002	0.03±0.007
	R (2.76Å)	2.83±0.016	2.80±0.06
Cu- Cu/Co/Zn	CN(8)	6.72±0.16	7.12±0.56
	σ^2	0.014±0.003	0.010±0.001
	R (2.90Å)	2.82±0.02	2.94±0.02
Cu- Cu/Co/Zn	CN(2)	1.46±0.32	2.64
	σ^2	0.001±0.002	0.005±0.002
	R (3.17Å)	3.11±0.04	3.18±0.03
R_{factor}		0.013	0.008

Chapter- 5

(Fe, Cu) co-doped ZnO NCs

5.1 Introduction:

In continuation with the work on TM and Cu co-doped ZnO nanocrystals in this chapter we present our work on (Fe,Cu) co-doped ZnO samples. Few studies have already been reported on (Fe, Cu) co-doped ZnO NCs based DMS systems. For example, Viswanatha et. al. [323] have observed an increase in FM ordering in (Fe,Cu) co-doped ZnO nanocrystals (upto 1% Cu doping concentration) and have attributed this to the enhancement in relative concentration of Fe^{+3} ions in the samples due to the presence of Cu^{+2} , the presence of Fe^{+3} and Cu^{+2} being ascertained from X-ray absorption spectroscopy (XAS) and electron paramagnetic resonance (EPR) measurements respectively. Wibowo et. al. [324] have also attributed the observed FM ordering in their chemically synthesized (Fe,Cu) co-doped $\text{Zn}_{0.96}\text{Fe}_{0.01}\text{Cu}_{0.03}\text{O}$ nanoparticles to the presence of small amount of Fe^{+3} and Cu^{+2} ions which are, however, not detectable by other techniques. Shim et. al. [325], on the other hand, have shown that the FM ordering in their $\text{Zn}_{0.95-x}\text{Fe}_{0.05}\text{Cu}_x\text{O}$ polycrystalline bulk samples stems from the presence of the secondary phase of ZnFe_2O_4 . However, none of the above studies have reported satisfactory increase of FM in ZnO due to Cu doping through enhancement of carrier mediated RKKY interaction, as had been predicted theoretically and hence this issue needs further investigations. In the present study (Fe,Cu) co-doped ZnO nanocrystals (NC) have been prepared through chemical synthesis route over a wider concentration range, where Fe doping concentration of 2.5%, 5% and 10% and at each Fe doping concentration three doping concentrations of Cu (viz., 2%, 3% and 5%) are chosen. The samples have been characterized to ascertain their phase purity by X-ray Diffraction (XRD) and Transmission Electron Microscopy (TEM) measurements and the dopant concentrations in the samples

have been verified by Total reflection X-ray fluorescence (TXRF) measurement. Subsequently, the samples have been characterized by Synchrotron based X-ray absorption spectroscopy (XAS) technique which comprises of both X-ray absorption near edge structure (XANES) and Extended X-ray Absorption Fine Structure (EXAFS) measurements and yield element-specific local structure information around the host and dopant cations separately. The magnetic properties of the samples have been investigated by magnetic hysteresis and temperature dependent susceptibility measurements and finally the above results have been corroborated by density functional theory (DFT) based electronic structure calculations on (Fe, Cu) co-doped ZnO nanocrystals using the Vienna ab-initio simulation package (VASP) code.

5.2 Experimental details:

5.2.1 Preparation of samples:

Pure, Fe-doped and (Fe,Cu) co-doped ZnO nanocrystals were synthesized by wet chemical route at room temperature as described in Chapter 2. For synthesis of pure ZnO nanoparticles, zinc acetate dehydrate ($\text{Zn}(\text{CH}_3\text{COO})_2 \cdot 2\text{H}_2\text{O}$) was dissolved in dimethyl sulfoxide (DMSO) solution in appropriate proportion. Subsequently, tetramethylammonium hydroxide (TMHA) dissolved in ethanol was added drop-wise to the solution of zinc acetate in DMSO and left under stirring for 1/2 h. ZnO nanoparticles were obtained in powder form by centrifugation with ethyl acetate and washing for 3 times with heptane. In order to obtain (Fe,Cu) co-doped ZnO nanocrystals, appropriate amounts of iron(II) acetate ($\text{Fe}(\text{CO}_2\text{CH}_3)_2$) and copper(II) acetate ($\text{Cu}(\text{CO}_2\text{CH}_3)_2$) were added with zinc acetate dehydrate. All other reaction parameters were kept same for the synthesis of doped and co-doped ZnO nanocrystals.

5. 2.2 Characterisation of samples:

Elemental compositions of the samples have been verified by Total reflection X-ray fluorescence (TXRF) measurement using an TX-2000 TXRF spectrometer while the structural analysis of the samples was carried out using a Bruker AXS D8 advance powder X-ray diffractometer with a Cu-K α radiation source ($\lambda = 1.5402 \text{ \AA}$). XANES and EXAFS measurements on these samples have been carried out at the Scanning EXAFS Beamline (BL-9) at the Indus-2 Synchrotron Source (2.5 GeV, 100 mA) at the Raja Ramanna Centre for Advanced Technology (RRCAT), Indore, India, the details of which have been described in Chapter-2 [12]. EXAFS spectra of the samples at Zn K-edge were recorded in the energy range of 9550-10350 eV, while that at Fe and Cu K-edges have been obtained in the energy ranges of 7000-7700 eV and 8900-9700 eV respectively.

Magnetization measurements on the samples were carried out using a SQUID magnetometer (Quantum Design MPMS5). Temperature dependences of magnetization were recorded in both Zero-Field-Cooled (ZFC) and Field-Cooled (FC) conditions. Isothermal magnetization measurements were accomplished both at low temperature (5K) and room temperature (300K).

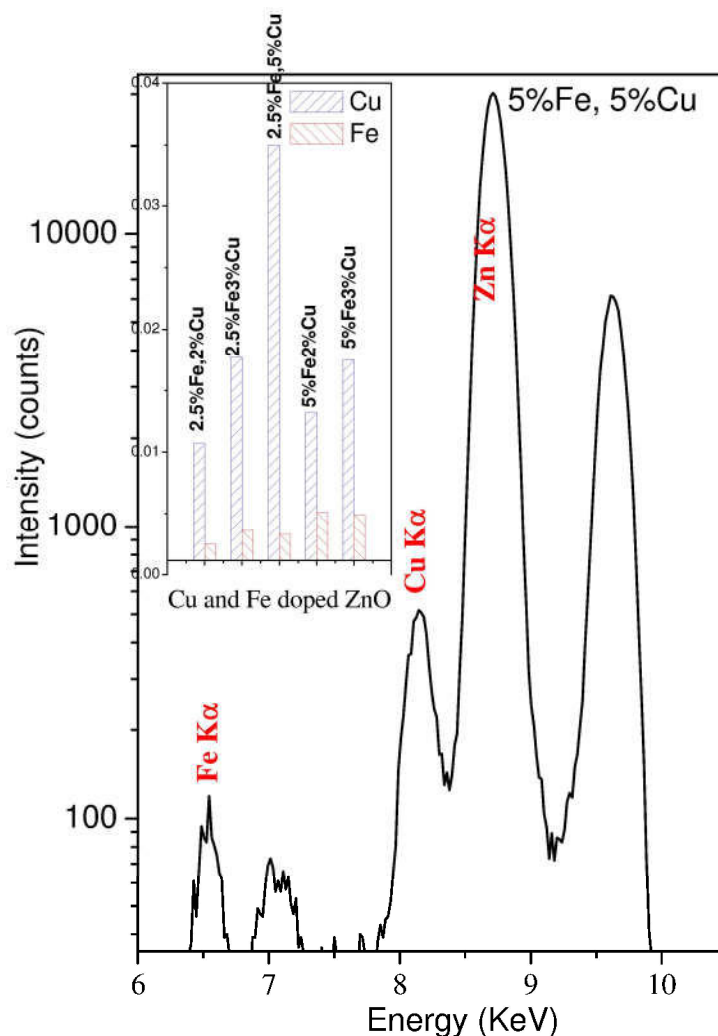


Figure 5.1: TXRF spectrum of a representative (Fe,Cu) co-doped ZnO sample. Inset shows relative concentration of the dopants in few samples

5.3 Results and discussion:

The TXRF spectrum of a representative (5%Fe,5%Cu) co-doped ZnO sample is shown in Fig.5.1. The elemental intensities of Cu, Fe and Zn K_{α} lines were determined by profile fitting of the spectra using a computer program EDXRF 32 provided with the instrument [NLM SAB 2005]. These intensities were normalized with sensitivity values and the relative ratio of the elemental concentrations were determined with these normalized intensity values. The relative concentrations of Fe and Cu in the samples estimated as above

are shown for few samples in the inset of Fig.5.1, which clearly demonstrates the efficient inclusion of the dopants in ZnO as per the intended concentrations.

Phase purity of the (Fe,Cu) co-doped ZnO samples has been checked by XRD measurement (Fig.5.2) which shows that no secondary phase other than wurzite hexagonal ZnO phase is present in the samples even upto 10%Fe and 5%Cu doping concentrations.

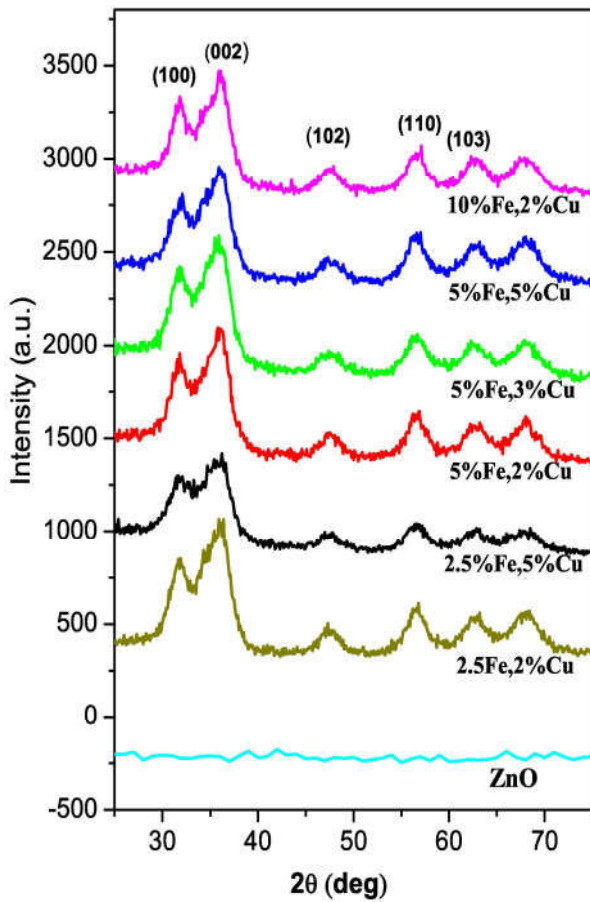


Figure 5.2: X-ray diffraction pattern of few representatives (Fe, Cu) co-doped ZnO samples.

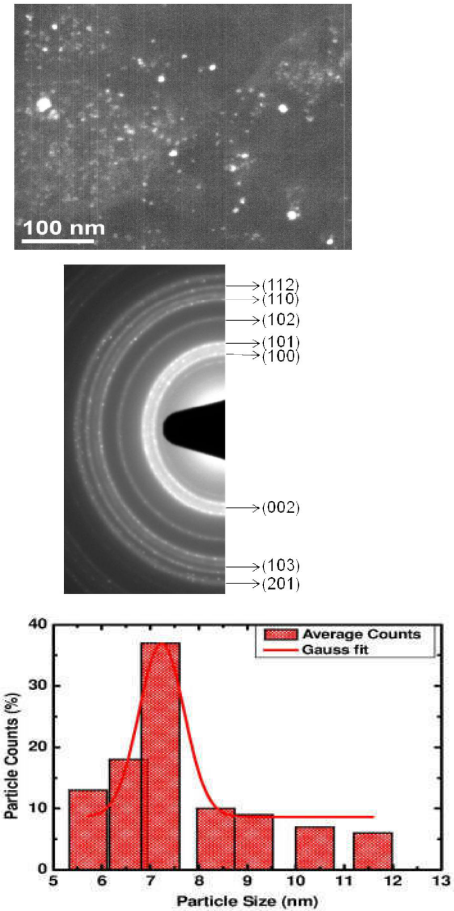


Figure 5.3:(a) Dark field image (b) Diffraction pattern and (c) Particle size histogram of undoped ZnO nanoparticles.

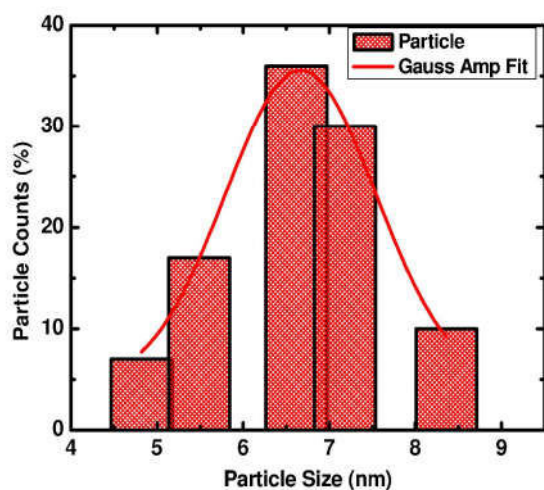
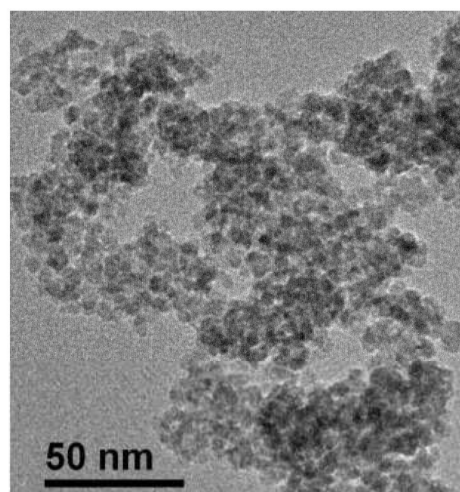
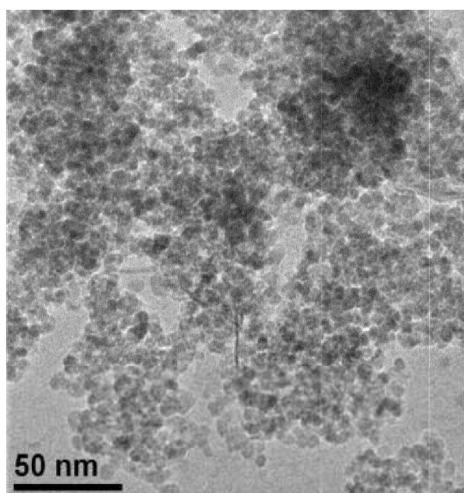


Figure 5.4: (a) Bright field image and (b) Particle size histogram of 2.5% Fe doped ZnO nanoparticles.

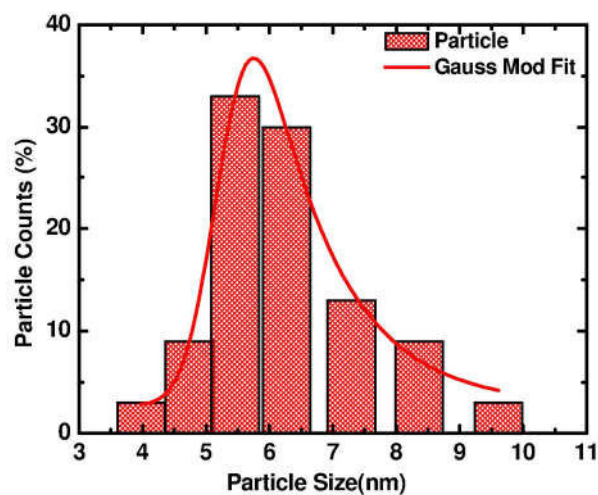


Figure 5.5: (a) Bright field image and (b) Particle size histogram of (2.5%Fe, 3%Cu) co-doped ZnO nanoparticles.

To determine the size, shape and crystal structure of the NCs, transmission electron microscope (TEM) imaging and electron diffraction were carried out. Figs. 5.3(a), (b) and (c) respectively show the dark field image, diffraction pattern and histogram of undoped ZnO nanocrystals. The electron diffraction patterns shown in Fig. 5.3(b) exhibits diffraction rings

corresponding to (1 0 0), (0 0 2) and (1 0 1) lattice planes of wurtzite phase of ZnO. Bright field image and histograms of 2.5% Fe doped and (2.5% Fe, 3% Cu) Fe-doped ZnO NCs are shown in Figs. 5.4 and 5.5 respectively, which reveal that the size of the nanocrystals vary in the range of 6-7 nm.

XANES measurement has been performed to investigate the chemical environment of Fe and Cu in (Fe,Cu) co-doped ZnO NCs at Fe and Cu K-edges. Fig. 5.6(a) represents the Fe K-edge XANES spectra of Fe doped and (Fe, Cu) co-doped ZnO nanoparticles along with that of commercial FeO and Fe₂O₃ standards and Fe foil. It is evident from the above figure that absorption edge energy of Fe of all the samples matches with the Fe absorption edge energy in Fe₂O₃. Thus from the XANES result we can conclude that Fe is present in +3 oxidation state in all the samples, though it should be noted that the Fe K-edge XANES features of the samples do not exactly match with that of Fe₂O₃ standard manifesting that Fe is not present in a separate Fe₂O₃ phase in the samples. Viswanatha et.al. have also observed enhancement of Fe⁺³ species of Fe with Cu doping in their (Fe, Cu) co-doped ZnO nanocrystals prepared by colloidal method [323]. This also agrees with our recent observation of presence of Fe ions in +3 oxidation state in nanocrystalline Fe doped ZnO samples [326], while in case of Fe doped ZnO thin film samples prepared by r.f. sputtering, Fe is found to be present in mixed oxidation states of +2 and +3 with higher probability of +3 state [327]. It can also be found from fig. 5.6(a) that the Fe XANES data of all the doped samples have pre-edge peaks which is mainly due to electric dipole transition of the core shell (1s) electron to the 3d-2p hybridized orbital. The pre-edge transitions are generally allowed for tetrahedral coordination only while these are forbidden in case of pure octahedral geometry. Thus the presence of the pre-edge peaks in the present samples confirms the substitution of Fe atoms in tetrahedral Zn sites in ZnO lattice. Similar pre-edge peaks in the Fe K-edge data have been observed by us in case of Fe doped ZnO thin film samples also [327].

Fig. 5.6(b) shows the XANES spectra of the samples measured at Cu K-edge along with that of a Cu foil and CuO standard. It has been observed that the Cu K-edge energy in the samples match with that of CuO standard showing the presence of Cu in Cu^{+2} oxidation state in the samples. Thus the above XANES results at Fe and Cu K edges show that the dopant atoms do not form separate metallic cluster phases in the samples.

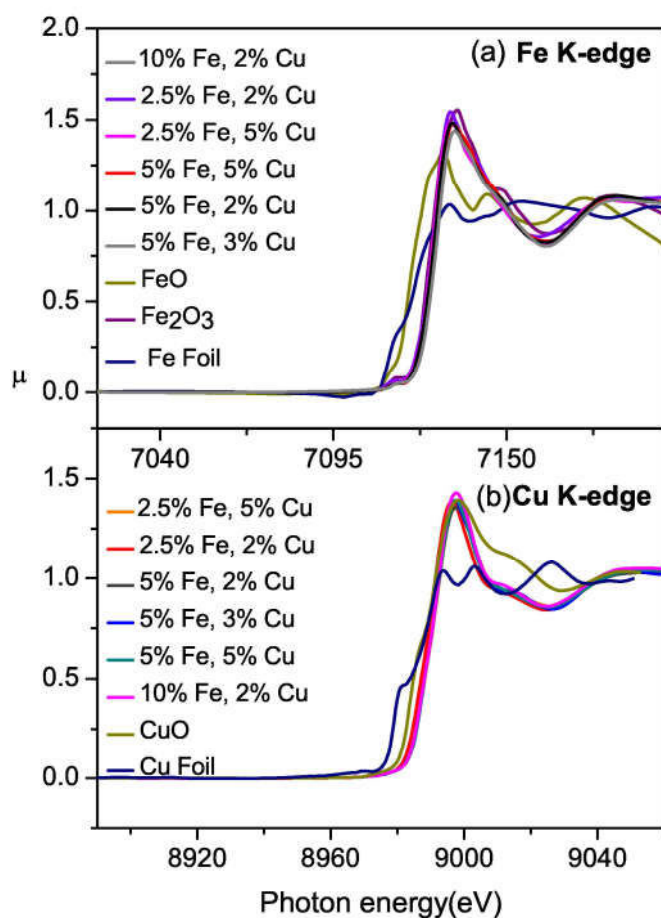


Figure 5.6: Normalized XANES spectra of few representative (Fe,Cu) co-doped ZnO samples measured at (a) Fe K-edge (inset shows the pre-edge portions in expanded scale) and (b) Cu K-edge along with standards.

Subsequently, magnetic properties of the samples have been investigated where temperature dependences of magnetization were recorded in both Zero-Field-Cooled (ZFC) and Field-Cooled (FC) conditions while isothermal magnetization vs. magnetic field (M-H)

measurements were accomplished both at low temperature (5K) and room temperature (300K). Figs. 5.7(a) and (b) show the M-H plots for Fe doped and (Fe,Cu) co-doped samples with various doping concentrations. From the M-H plot at 300K, it can be seen that the sample doped with only 5% Fe shows characteristic behavior of a soft ferromagnet. Weak ferromagnetism is also observed for the co-doped sample with 5% Fe and 2% Cu, however, the ferromagnetic signature changes to paramagnetic type for the samples with higher concentration of Cu i.e., 5% Fe and 5% Cu. From the M-H plot, at 5K, one can see similar behavior i.e., the weak ferromagnetism is retained only up to 2% addition of Cu. Thus one can summarise that addition of Cu beyond 2% quenches the magnetic moment associated with Fe site. This also agrees with the observations of Viswanatha et. al. [323] that an increase in Cu concentration from 1% to 2%, results in a decrease in the magnetic susceptibility of (Fe,Cu) co-doped ZnO samples.

Fig.5.7(c) shows the FC temperature dependence of the susceptibility $\chi(T)$ for all the samples in the temperature range of 5K to 300 K at a magnetic field of 100 Oe. Here too one can see that the sample with 5% Fe is having the highest susceptibility. However, additional substitution of Cu seems to quench the magnetic moment, thereby reducing the susceptibility. To understand this behavior better, we plot the inverse susceptibility $\chi^{-1}(T)$ curves for all the samples as a function of temperature which is shown in the inset of Fig. 5.7(c). Though most of the samples show paramagnetic behavior at high temperature there is a clear deviation from the linear response in the $1/\chi$ vs., T towards the low temperature regime suggesting that some short-range correlation exists between magnetic moments in the studied temperature range. We have fitted the linear portion of the data to the Curie-Weiss behavior which is shortly described in Chapter-2, and is shown in figure 5.7(c).

As can be seen from the inset of Fig. 5.7(c), the above fit yields negative θ values, suggesting the presence of anti-ferromagnetic (AFM) correlation in the samples. It can also

be noted that θ takes higher negative values upon addition of Cu, which indicates that addition of Cu in Fe doped ZnO samples increases anti-ferromagnetic (AFM) correlation.

Thus the above results show that magnetic susceptibility of Fe doped ZnO does not increase rather decreases on Cu co-doping. We have obtained similar result for (Co, Cu) co-doped ZnO nanocrystalline sample also, as described in Chapter 4, [328] where it had been observed that that (2.5% Co, 2.5% Cu) co-doped ZnO sample shows weak FM behavior and its magnetisation is less than that of the only Co doped sample. Further investigations reveal that in the above sample while Co goes into the tetrahedral lattice of ZnO, local environment of Cu resembles that of cubic CuO than tetrahedral ZnO.

To further investigate the change in magnetic behaviour we have performed EXAFS measurement of (Fe,Cu) co-doped ZnO NCs at Zn, Fe and Cu K-edges. The EXAFS measurements have been carried out at Energy scanning EXAFS beamline, Indus-2, RRCAT Indore. Fig. 5.8(a, b and c) represent the experimental EXAFS ($\mu(E)$ versus E) spectra of undoped, Fe doped, Cu doped and (Fe, Cu) Fe-doped ZnO NCs measured at Zn K-edge. The analysis of the EXAFS data have been carried out following the standard procedure using the IFEFFIT software package and as described in detail in Chapter 2. Fig. 5.9 (a) represents the Fourier transformed EXAFS (FOURIER TRANSFORMED EXAFS) $\chi(R)$ versus R spectra of undoped, Fe doped and (Fe,Cu) co-doped ZnO samples at the Zn K-edge along with the best fit theoretical spectra. For undoped and (Fe,Cu) co-doped ZnO samples, in the radial distribution functions, first and

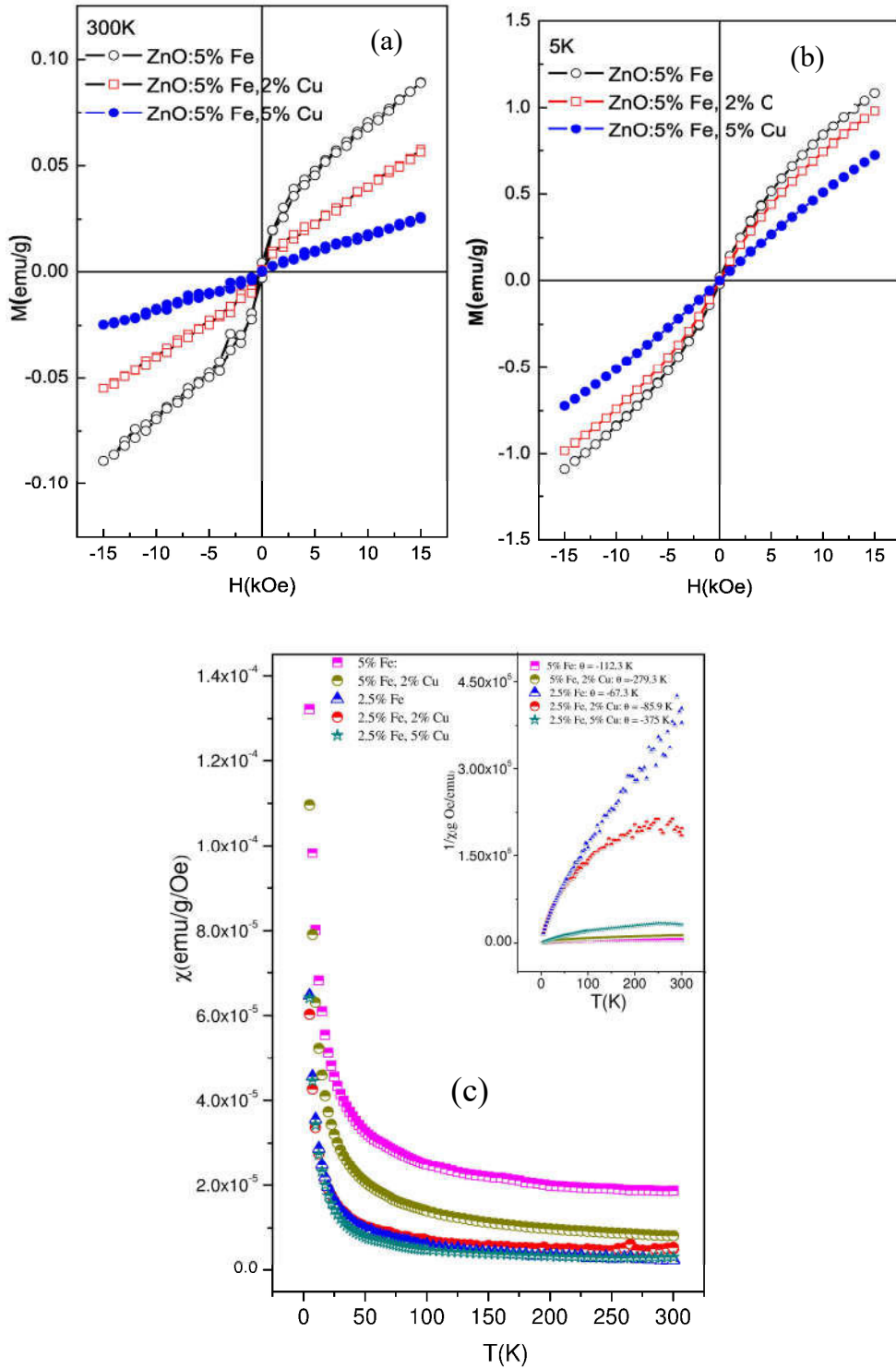


Figure 5.7: (a) M vs H curve for a 5% Fe doped, (5% Fe, 2% Cu) co-doped and (5% Fe; 5% Cu) co-doped ZnO NCs measured at 300 K, (b) measured at 5 K (c) Temperature dependence of magnetic susceptibilities χ and inverse susceptibilities χ^{-1} (inset) for few Fe doped and (Fe, Cu) co-doped samples measured at 100 Oe.

second major peaks correspond to the nearest oxygen and the Zn/Fe/Cu shells respectively from the central Zn atom.

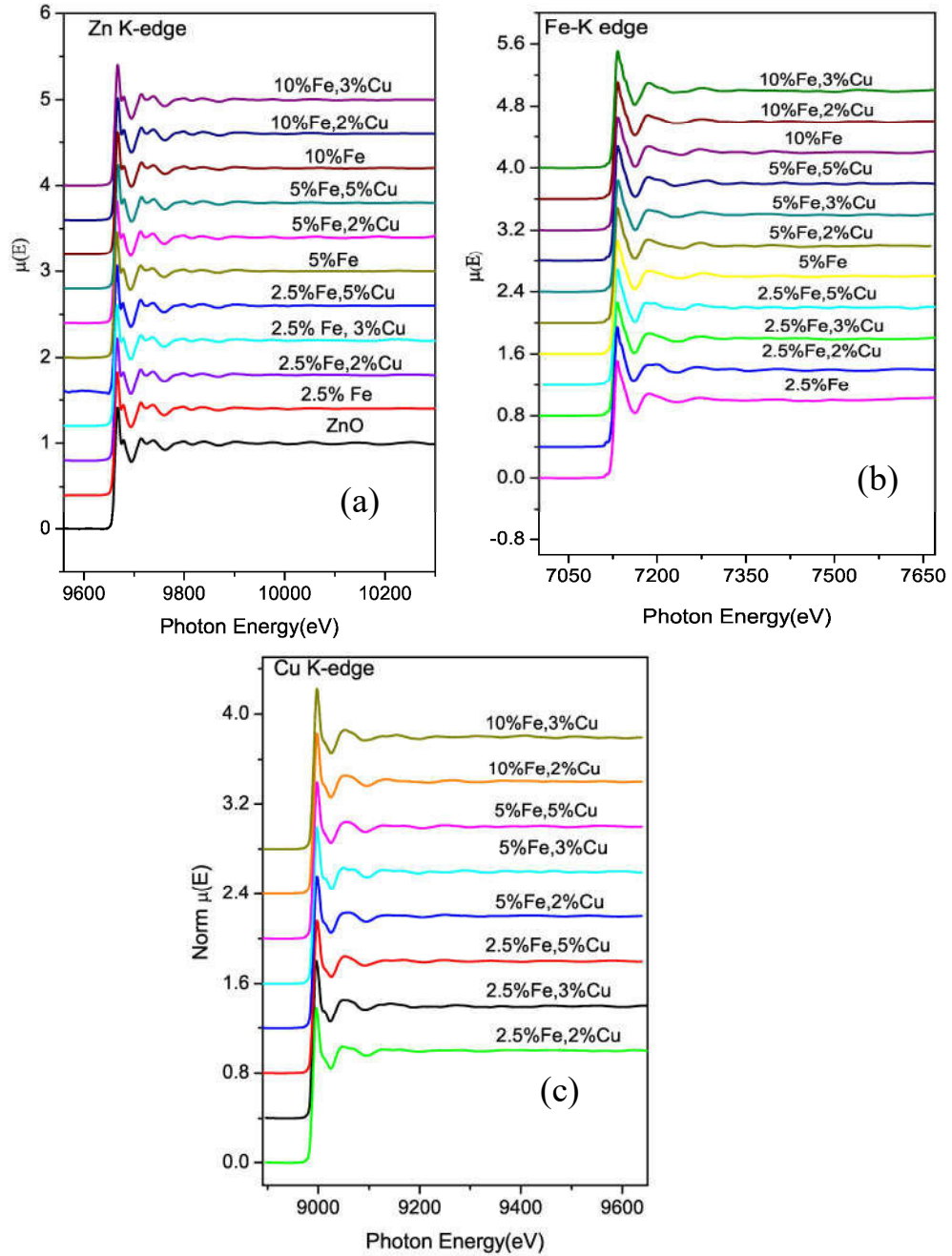


Figure 5.8: Normalized experimental EXAFS ($\mu(E)$ versus E) spectra of undoped, Fe doped and few (Fe,Cu) co-doped ZnO samples measured at (a) Zn K-edge, (b) Fe K-edge and (c) Cu K-edge.

The theoretical Fourier transformed EXAFS spectra have been generated, by assuming the wurtzite ZnO structure which is described by Kisi et. al. [224]. The data has been fitted in the k range of 2-11 Å⁻¹ and in the R range of 1-3.25 Å. It has been found from the best fit data that no significant changes occur with doping of Fe and Cu in the local structure of the ZnO nanocrystals surrounding the Zn sites.

Fig. 5.9(b) represents the $\chi(R)$ versus R plots of (Fe, Cu) co-doped ZnO samples obtained from Cu K-edge EXAFS data. The $\chi(R)$ versus R plots for the undoped ZnO sample obtained from Zn K-edge EXAFS data and that of a CuO standard sample obtained from Cu K-edge data are also shown in Fig. 5.9(b) for comparison. It can be seen from the figure that the peaks in the radial structure function of Cu K-edge data of the co-doped samples match quite well with that of ZnO and not with that of CuO phase and this clearly establishes the fact that the Cu atoms are going to the Zn sites of the ZnO lattice and do not precipitate in any other oxide or metallic phase. This also corroborates with the XANES results, as discussed above, that Cu is present in +2 oxidation state in the samples. To manifest efficient substitution of Fe at Zn sites we have included the Fe K-edge $\chi(R)$ versus R data of the (10%Fe, 3% Cu) co-doped sample in fig. 5.9(b) which also shows similar features as the rest of the plots. It should be noted that the 2nd shell peak ~ 2.8 Å of the Fe K-edge data is significantly reduced due to the large Debye-Waller (disorder) factor associated with this shell because of high Fe doping concentration in the sample.

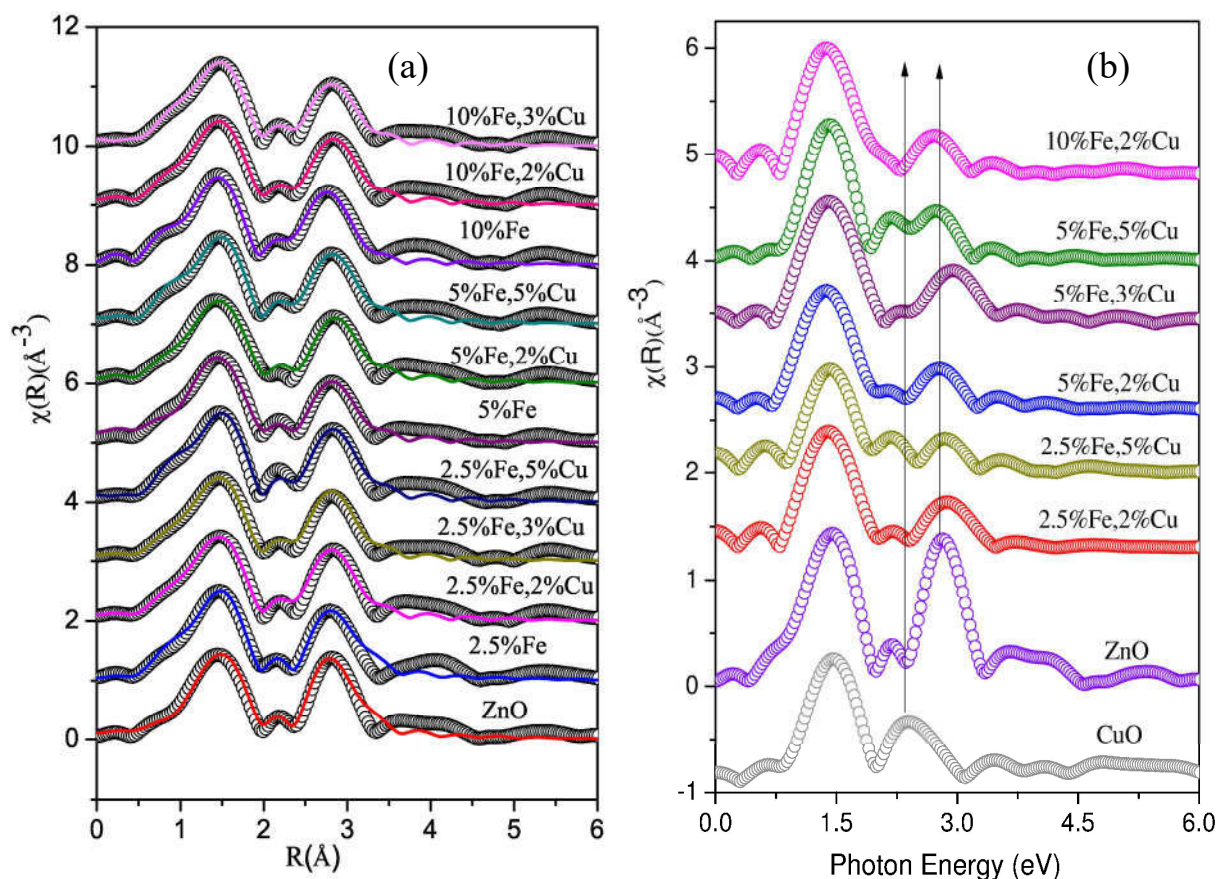


Figure 5.9: (a) Experimental $\chi(R)$ versus R plots alongwith best fit theoretical plots for undoped, Fe doped and few representative (Fe,Cu) co-doped ZnO samples measured at Zn K-edge. (b) Experimental $\chi(R)$ versus R plots of few representative (Fe,Cu) co-doped ZnO samples measured at Cu K-edge alongwith that of CuO standard measured at Cu K-edge, undoped ZnO sample measured at Zn K edge and (10%Fe, 3%Cu) co-doped sample measured at Fe K-edge.

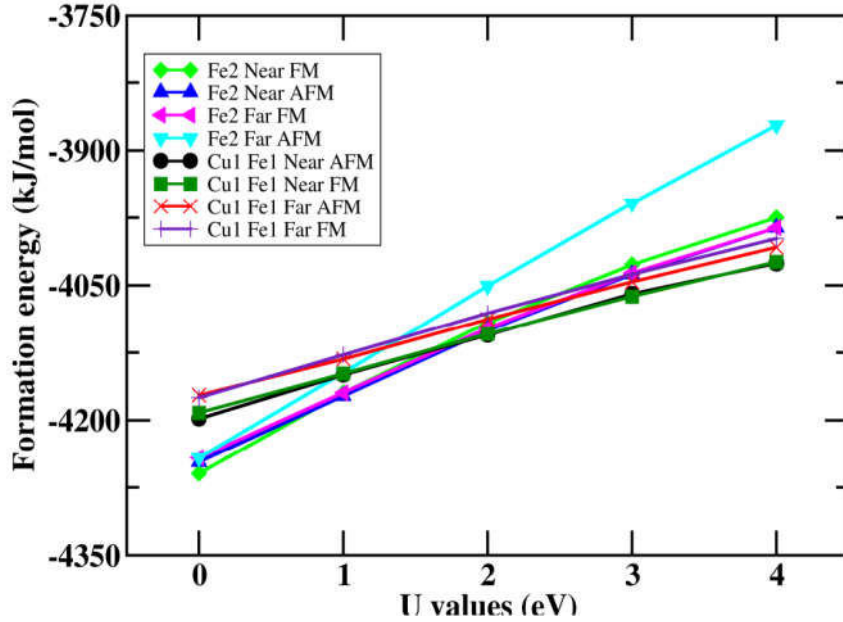


Figure 5.10: Plot of formation energy versus the on-site Coulomb interaction (U) for both Fe doped and (Fe, Cu) co-doped ZnO systems in various configurations.

Thus the above results show that though (Fe,Cu) co-doped samples have been prepared successfully with Fe and Cu ions replacing Zn atoms in wurtzite ZnO lattice, however, magnetic susceptibility of Fe doped ZnO does not increase, rather decreases on Cu co-doping, showing that FM ordering in Fe doped ZnO is not due to carrier mediated interaction between TM ions. To investigate the behaviour of the co-doped samples further, we have also carried out density functional theory (DFT) based electronic structure calculations [198, 199] for (Fe, Cu) co-doped ZnO samples using VASP code [200, 201]. For exchange-correlation functional, we employ generalized gradient approximation (GGA) given by Perdew-Burke-Ernzerhof (PBE) [202]. The plane waves are expanded with energy

cut of 400 eV. We use Monkhorst-Pack scheme for k-point sampling of Brillouin zone integration with the k-spacing less than 0.1 \AA^{-1} .

We start with a $(2 \times 2 \times 2)$ super cell of bulk ZnO containing 16 Zn and 16 O atoms and subsequently substitute two Zn atoms in the super cell by Fe and Cu atoms. Two distinctly different systems have been considered here, namely (i) two Fe atoms substituted in the supercell of ZnO ($\text{Fe}_2\text{Zn}_{14}\text{O}_{16}$) and (ii) one Fe and one Cu substituted in the supercell of ZnO ($\text{Cu}_1\text{Fe}_1\text{Zn}_{14}\text{O}_{16}$). We have probed two relative distances between the substituent atoms (i) “Near” to and (ii) “Far” from each other and two different magnetic configurations (a) Ferromagnetic (FM) and (b) Anti-ferromagnetic (AFM). In order to probe the effect of strong correlation, we have performed the calculations using DFT + U method, where U is the on-site Coulomb interaction between the electrons of d-orbitals of Fe atoms and we have performed the calculations for $U = 1-4 \text{ eV}$. The results of the calculation of formation energy (Fig.5.10) show that for $U=0$, when two Zn atoms out of 16 Zn atoms in the ZnO supercell is substituted with two Fe atoms, the system is energetically more favorable than the system where one Fe and one Cu atom replace the two Zn atoms of the supercell. However, the energetically more favourable configuration changes from “ $\text{Fe}_2\text{Zn}_{14}\text{O}_{16}$ ” (only Fe doped) to “ $\text{Cu}_1\text{Fe}_1\text{Zn}_{14}\text{O}_{16}$ ” (Fe, Cu co-doped) at around $U = 2 \text{ eV}$.

Furthermore, the above results show that though in case of the Fe doped system, energy of the system in “Fe2 Far” case (which is a more likely scenario in case of these dilutely doped samples), is decisively lower in FM configuration than the AFM configuration, upon addition of Cu i.e., in “Cu1 Fe1 Far” case, the energy of the system in both FM and AFM configurations are close to each other making the two configurations equally probable in the co-doped ZnO samples. Thus the reason for quenching of magnetic susceptibility in Fe-doped nanocrystalline ZnO samples upon Cu co-doping might be the enhancement of AFM interaction among the TM ions because of the presence of Cu^{+2} ions. This also

corroborates with our observations from the temperature dependence of magnetic susceptibility (Fig.5.7c) measurement that AFM correlation increases with addition of Cu doping in the samples.

Thus to conclude, XANES measurements show the presence of Cu in the samples in Cu^{+2} and Fe in Fe^{+3} oxidation states. EXAFS measurements confirm that Cu atoms in the (Fe,Cu) co-doped ZnO samples go to Zn sites at ZnO lattice and do not form any other metallic or oxide phase. However, magnetic measurements reveal that 5% Fe-doped sample shows weak ferromagnetic (FM) behavior and its magnetization reduces upon 2% additional Cu doping. DFT calculations show that upon Cu doping in addition to Fe doping, ZnO systems with ferromagnetic (FM) and anti-ferromagnetic (AFM) interactions become energetically comparable compared to the only Fe doped system which is more stable in FM configuration. Thus we can conclude that the decrease in magnetic susceptibility of Fe doped ZnO nanocrystals upon Cu co-doping may be due to the enhancement of AFM interaction among the TM ions in the co-doped samples.

Chapter 6

(Ni, Cu) co-doped ZnO NCs

6.1 Introduction:

After (Co,Cu) and (Fe,Cu) co-doped ZnO samples, in this chapter we present the work on Ni doped and (Ni, Cu) co-doped ZnO nanocrystalline samples prepared through wet chemical route. In this case also the samples have been characterized by X-ray Diffraction (XRD) and Transmission Electron Microscopy (TEM) measurements to look into the phase purity of the doped and co-doped samples. The magnetic properties of the samples have been investigated by magnetic hysteresis and temperature dependent susceptibility measurements. Subsequently, the samples have been characterized by Synchrotron based X-ray absorption spectroscopy (XAS) technique which comprises of both X-ray absorption near edge structure (XANES) and Extended X-ray Absorption Fine Structure (EXAFS) measurements and yields element-specific local structure information around the host and dopant cations separately. Finally the above results have been corroborated by density functional theory (DFT) based electronic structure calculations on (Ni, Cu) co-doped ZnO nanocrystals using the Vienna ab-initio simulation package (VASP) code.

6.2 Experimental Details:

To synthesize (Ni, Cu) co-doped ZnO nanocrystals we follow the wet chemical route method which has been described in Chapter-2. Structural characterization of (Ni,Cu) doped ZnO nanocrystals was performed by X-ray diffractometer (Model: Miniflex-II, Rigaku, Japan) with Cu K α radiation ($\lambda=1.54$ Å). XANES and EXAFS measurements on these samples have been carried out at the Scanning EXAFS Beamline (BL-9) at the Indus-2 Synchrotron Source (2.5GeV,100 mA) at the Raja Ramanna Centre for Advanced

Technology (RRCAT), Indore, India, the details of which have been described in Chapter-2 [148]. For the present set of samples measurements at Zn K-edge has been carried out in transmission mode, while measurements at the dopant (Ni and Cu) K-edges have been carried out in fluorescence mode. The EXAFS spectra of the samples at Zn K-edge were recorded in the energy range of 9550-10200 eV, while that at Ni and Cu K-edges have been obtained in the energy ranges of 8250-9020 eV and 8850-9650 eV respectively.

Magnetization measurements on the samples were carried out using a SQUID magnetometer (Quantum Design MPMS5) described in Chapter-2. Temperature dependences of magnetization were recorded in both Zero-Field-Cooled (ZFC) condition. Isothermal magnetization measurements were accomplished both at low temperature (5K) and room temperature (300K).

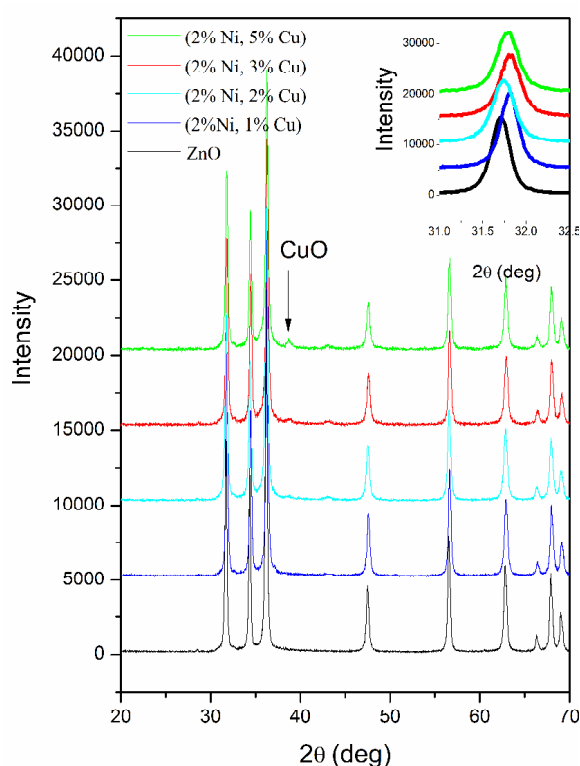


Figure 6.1: X-ray diffraction pattern of (Ni, Cu)

Table-6.1: Particle sizes of the (Ni, Cu) co-doped ZnO nanocrystals determined from XRD patterns.

Samples	FWHM (degree)	Average crystal size (nm)
Zn	0.277	7.12
2% Ni doped ZnO	0.234	7.78
(2% Ni, 1% Cu) co-doped ZnO	0.273	6.66
(2% Ni, 2% Cu) co-doped ZnO	0.311	5.70
(2% Ni, 3% Cu) co-doped ZnO	0.333	5.79
(2% Ni, 3% Ni) co-doped ZnO	0.339	5.39

6.3 Results and discussions:

Fig. 6.1 shows the XRD patterns of undoped and (2%Ni, 1%Cu), (2% Ni, 2% Cu), (2% Ni, 3% Cu) and (2% Ni, 5% Cu) co-doped ZnO nanoparticles at room temperature co-doped ZnO nanocrystals. We have kept Ni doping concentration at 2% since precipitation of secondary Ni phases is observed in the samples at higher doping concentration. It is evident from fig.6.1 that for samples up to 2% Ni and 3% Cu, all the diffraction peaks occurring in the XRD pattern of the samples belong to the hexagonal lattice of wurtzite ZnO, which suggests that Cu and Ni have been incorporated in the substitution sites in ZnO lattice and no other secondary phases are present. With an increase of Cu concentration in Ni doped ZnO, a shift in diffraction peaks has been observed at higher angle side of XRD pattern, which may be because of difference in ionic radii of Cu^{+2} (0.57Å) and Zn^{+2} (0.6 Å) [329]. The average crystallite sizes of the nanoparticles are calculated from the Debye Scherer's formula [330] and are given in Table 6.1. Since it can be seen that the full width half maxima (FWHM) of the diffraction peaks shown in the XRD pattern increases with Cu concentration, a decrease

in average crystallite size has been observed with increase in Cu concentration. It can also be observed from fig.6.1 that with further increase of Cu concentration ($\geq 3\%$) in Ni doped ZnO sample presence of a minor secondary phase of CuO is evident. This suggests that the doping limit of Cu in Ni doped ZnO is around 3%. Ashokkumar and Muthukumaran [330] have also reported similar solubility limit of Cu in their (Ni, Cu) co-doped ZnO nanoparticles prepared by co-precipitation method. Liu et.al. [331] have also observed a 5% upper limit of Cu doping in their sol-gel derived ZnO nanoparticles. They have also observed a decrease of particle size with increase in Cu doping concentration in the samples, though no shift in XRD peak positions was observed.

The size and morphological characteristic of the synthesised powders were investigated by transmission electron microscopy (TEM). Fig. 6.2(a) and (b) show the TEM image and SEAD pattern of (2%Ni,1%Cu) co-doped ZnO nanocrystals. The electron diffraction patterns in Fig. 6.2(b) exhibit diffraction rings corresponding to (1 0 0), (0 0 2) and (1 0 1) lattice planes of wurtzite phase of ZnO.

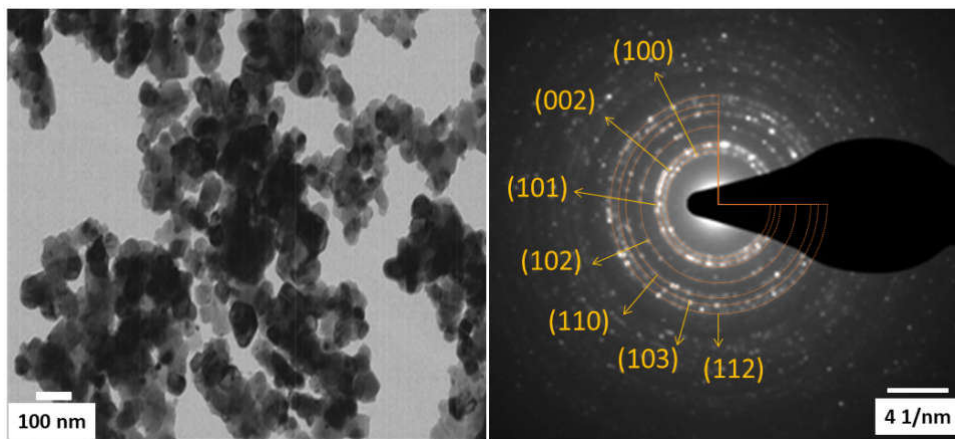


Figure 6.2: (a) TEM micrograph and (b) SAED pattern of (2% Ni, 1%Cu) co-doped ZnO nanocrystals.

Subsequently, magnetic properties of the samples have been investigated where isothermal magnetization vs. magnetic field (M-H) measurements were accomplished both at low temperature (5K) and room temperature (300K). Fig. 6.3(a) shows the M-H plots for Ni doped and (Ni,Cu) co-doped samples with various doping concentrations measured at 5K. From the above plot, it can be seen that the sample doped with 2% Ni shows characteristic behavior of a weak ferromagnet. However, magnetization of the samples is found to be reduced when it is co-doped with Cu and the trend follows upto 3% Cu doping concentration. However, magnetization is found to improve again as the doping concentration increases to 5%. This should be noted that the M-H measurements at room temperature has not shown any ferromagnetism in the samples, rather they are diamagnetic in nature, which is a characteristic of undoped ZnO, nanocrystals, possibly because of low concentration of Ni in the nanocrystals.

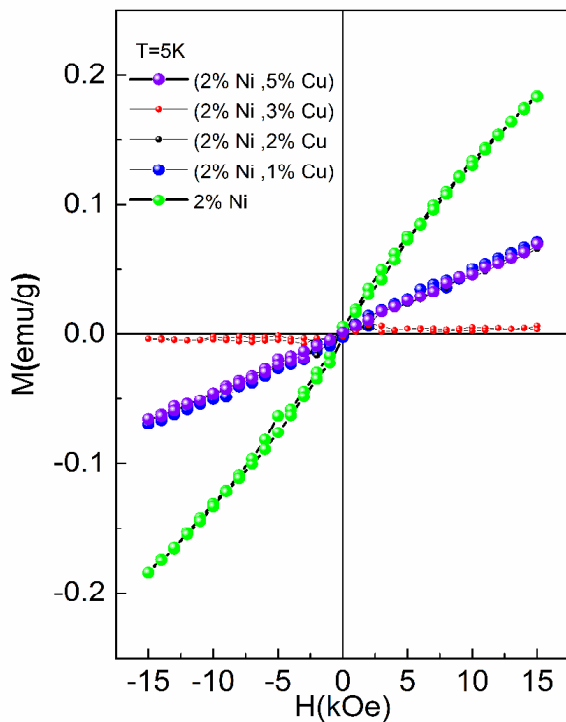


Figure 6.3(a): M-H plots for (Ni,Cu) co-doped ZnO nanocrystals.

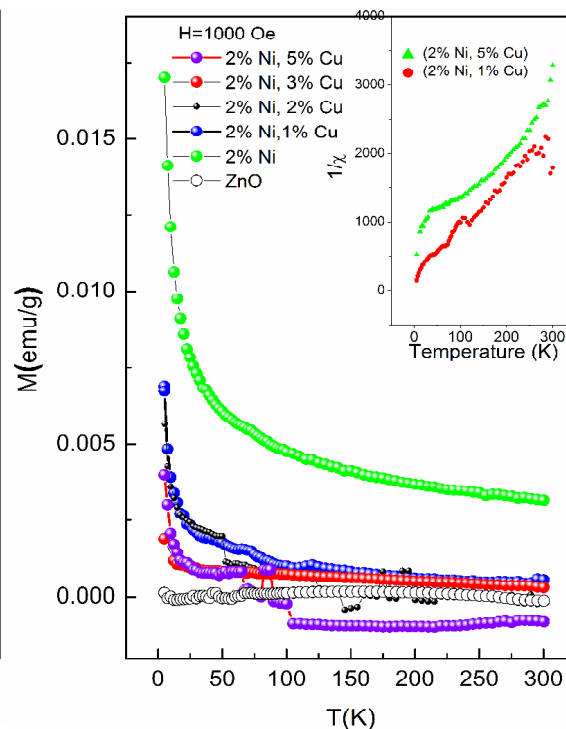


Figure 6.3 (b): M-T plots for (Ni, Cu) co-doped ZnO nanocrystals.

Fig.6.3(b) shows the ZFC temperature dependence of the susceptibility $\chi(T)$ for all the samples in the temperature range of 5K to 300 K at a magnetic field of 1000Oe. Here too one can see that the sample with only 2% Ni is having the highest susceptibility. However, additional substitution of Cu with more than 1% concentration seems to quench the magnetic moment, thereby reducing the susceptibility. However, as has been observed in case of M-H plot, the susceptibility increases again as Cu doping concentration is increased to 5%.

To understand this behavior better, we plot the inverse susceptibility $\chi^{-1}(T)$ curves for the two samples (2%Ni, 1%Cu) and (2%Ni, 3%Cu) co-doped ZnO as a function of temperature which are shown in the inset of Fig. 6.3(b). Though most of the samples show paramagnetic behavior at high temperature there is a clear deviation from the linear response in the $1/\chi$ vs., T towards the low temperature regime suggesting that some short range correlation exists between magnetic moments in the studied temperature range. We have fitted the linear portion of the data to the Curie-Weiss behavior; it has been observed that with increase in Cu content in the samples from 1-3%, the intercept θ in the temperature axis becomes more negative suggesting an increase of anti-ferromagnetic (AFM) correlation in the samples.

Thus the above results show that magnetic susceptibility of Ni doped ZnO does not increase rather decreases on upto 3% Cu co-doping. Tang et. al. [332] have also observed similar decrease in saturation magnetization when Cu doping concentration is increased from 3% to 5% for a constant Ni doping concentration of 2% in their (Ni, Cu) co-doped ZnO nanorods grown by hydrothermal method. We have obtained the similar results in our earlier study of (Co, Cu) [333] co-doped ZnO NCs and (Fe,Cu) [334] co-doped ZnO NCs as described in Chapters 4&5 in this thesis. The reason of decrease in magnetization with the

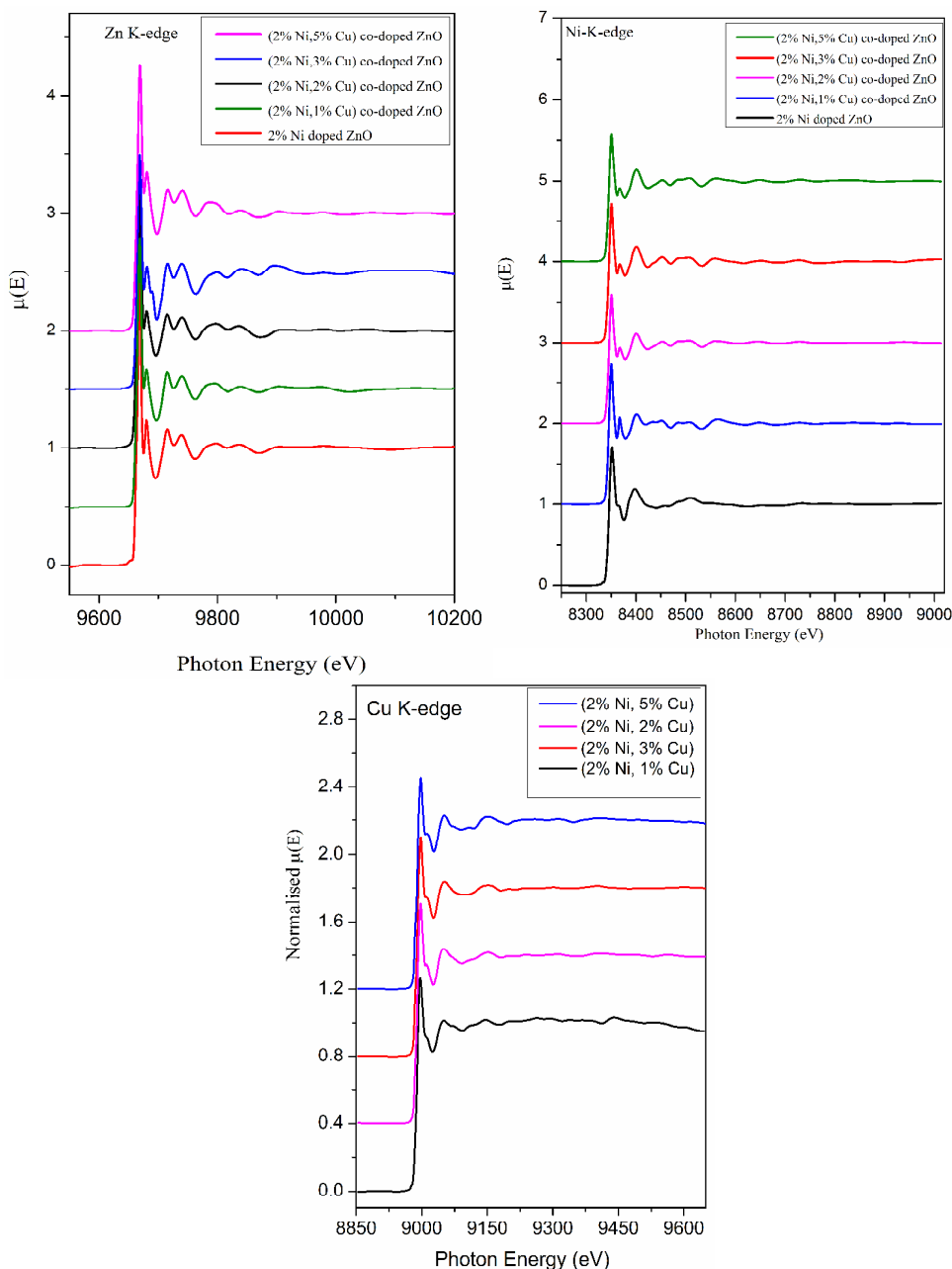
incorporation of Cu in ZnO NCs have been explained in detail by EXAFS analysis and DFT based electronic structure calculations in the earlier Chapters.

Thus the magnetic behavior of the present (Ni, Cu) co-doped system has further been investigated by XAS measurement and DFT based electronic structure calculations. We have probed the system by synchrotron based XAS measurements (comprising of XANES and EXAFS) since XAS probes the local order instead of the long range order and thus can give more accurate information regarding such nanocrystalline systems with large amount of disorders, where single-phase domains are not sufficiently large [335-339]. X-ray diffraction, which acts on the principle of long range order, might not give the correct phase information for such systems.

Figs.6.4, 6.5 &6.6 represent the experimental $\mu(E)$ versus E spectra of (Ni, Cu) co-doped ZnO NCs measured at Zn K-edge. In order to take care of the oscillations in the absorption spectra, the energy dependent absorption coefficient $\mu(E)$ has been converted to absorption function $\chi(E)$ described in Chapter-2 and a set of EXAFS data analysis program available within the IFEFFIT software package have been used for reduction and fitting of the experimental EXAFS data.

Figure 6.7 shows the Fourier transformed EXAFS (FOURIER TRANSFORMED EXAFS) spectra or $\chi(R)$ versus R plots of (Ni, Cu) co-doped ZnO samples at the Zn K-edge along with the best fit theoretical plots. For undoped and co-doped ZnO samples, in the radial distribution functions, first and second major peaks correspond to the nearest oxygen and the Zn shells respectively from the central Zn atom. The theoretical Fourier transformed EXAFS spectra have been generated, assuming the model proposed by Kisi et. al. [224] and described in earlier Chapters, namely the first oxygen shell (Zn-O1) at 1.97Å with

coordination number (CN) of 4 and the second Zn shell (Zn-Zn) at 3.27 Å having CN of 12. The data has been fitted in the range of 1-3.2 Å in R space, while a k range of 2-9 Å⁻¹ has been used for fourier transform. The best fit parameters have been shown in Table 6.2. From fig. 6.7 and Table 6.2, it is clear that no significant changes occur in the local environment of ZnO due to (Ni, Cu) doping.



Figures 6.4, 6.5 & 6.6: Normalized experimental EXAFS ($\mu(E)$) versus E for (Ni, Cu) co-doped ZnO nanocrystals measured at Zn, Ni and Cu K-edges.

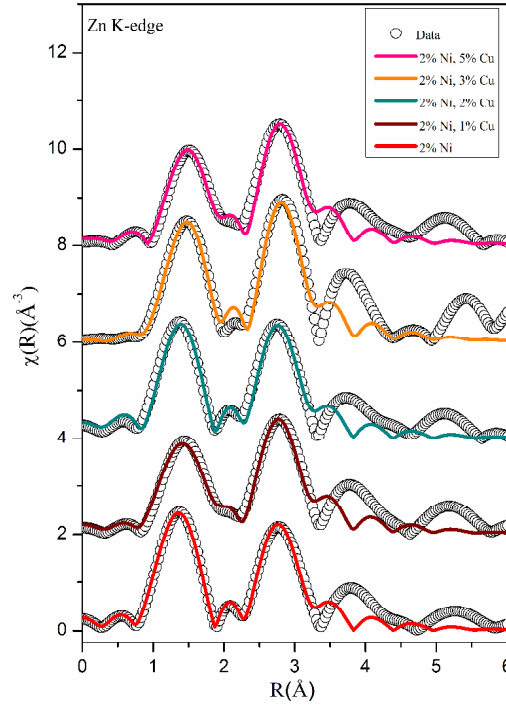


Figure 6.7: Experimental $\chi(R)$ versus R data (scatter points) and best fit theoretical plots (solid line) of 2% Ni doped, (2% Ni, 1% Cu), (2% Ni, 2% Cu), (2% Ni, 3% Cu) & (2% Ni, 5% Cu) co-doped ZnO nanocrystals at Zn K-edge.

Table 6.2: Best-fit parameters of Zn K-edge EXAFS data for (Ni, Cu) co-doped ZnO samples where fitting has been carried out assuming wurtzite ZnO structure.

		ZnO: 2%Ni	(2% Ni, 1% Cu) co-doped ZnO	(2% Ni, 2% Cu) co-doped ZnO	(2% Ni, 3% Cu) co-doped ZnO	(2% Ni, 5% Cu) co-doped ZnO
Zn-O	CN(4)	4.43±0.28	4.48±0.54	4.48±0.42	4.72±0.52	4.72±0.52
	R (1.97Å)	1.91±0.005	1.99±0.014	1.91±0.009	1.96±0.01	2.02±0.014
	σ^2	0.002±0.001	0.003±0.002	0.002±0.001	0.002±0.001	0.006±0.002
Zn-Zn	CN(12)	12.84±1.44	12.24±1.4	12.48±1.16	12.24±1.2	12.12±1.92
	R (3.22Å)	3.24 ±0.01	3.23±0.014	3.24±0.016	3.24±0.01	3.33±0.02
	σ^2	0.007±0.001	0.007±0.001	0.005±0.001	0.003±0.001	0.005±0.002
R_{factor}		0.0037	0.008	0.005	0.01	0.013

Figure 6.8 shows the Ni K-edge XANES spectra of the co-doped samples which shows that though the Ni K-edge positions in the samples match with that in NiO, the absorption peak position (marked by arrow in the figure) of NiO do not match with that of the samples. Moreover the pre-edge observed in case of NiO is also not observed in the samples manifesting that Ni is present in the samples in Ni^{+2} states, however not in NiO structure.

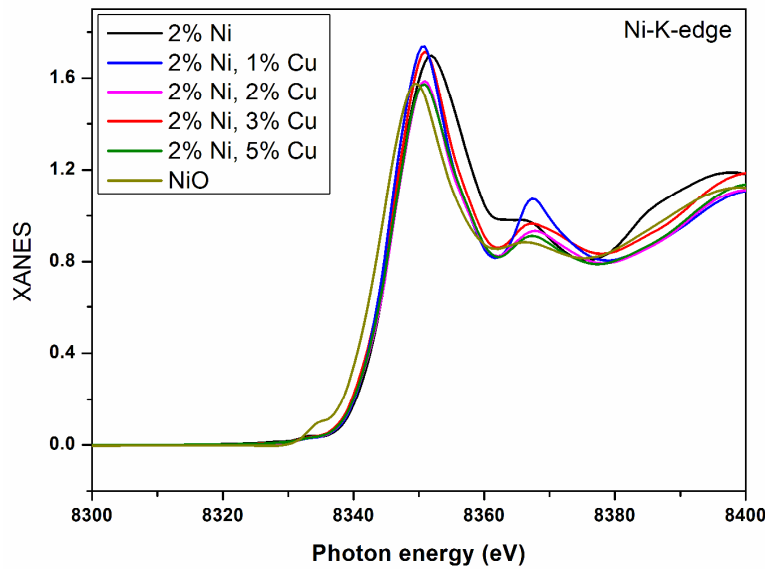


Figure 6.8: XANES plots for Ni doped and (Ni, Cu) co-doped ZnO samples at Ni K-edge.

Figure 6.9 shows the fourier transformed EXAFS $\chi(R)$ versus R plots of the (2%Ni,1%Cu), (2%Ni,2%Cu), (2%Ni,3%Cu) & (2%Ni,5%Cu) co-doped ZnO NCs at the Ni K-edge, along with the best fit theoretical spectra, where the fittings have been carried out by using wurtzite ZnO structure (where Zn is replaced by Ni) and the best fit parameters have been given in Tables 6.3.

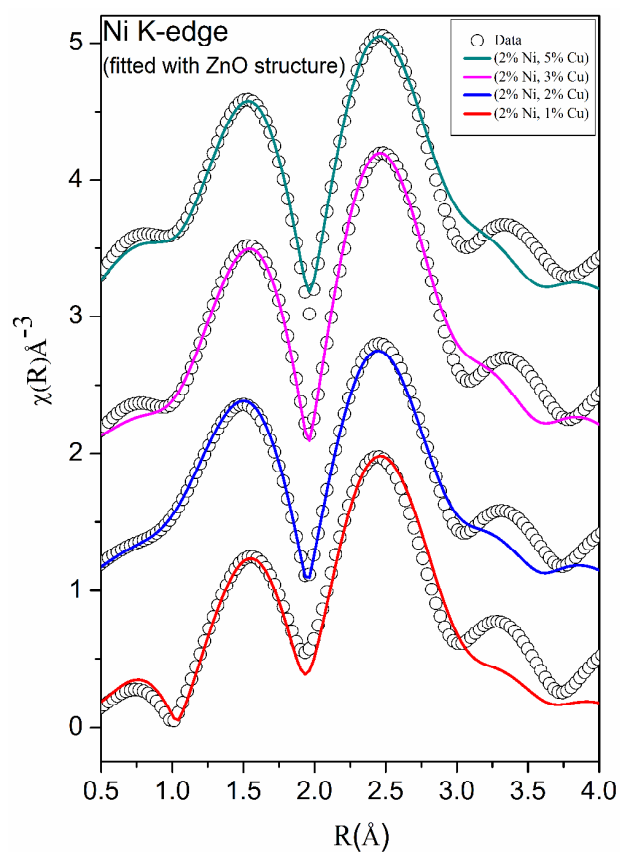


Figure 6.9: Experimental $\chi(R)$ versus R data (scatter points) and best fit theoretical plots (solid line) of (2%Ni, 1%Cu), (2%Ni, 2%Cu) & (2%Ni, 3%Cu) and (2%Ni, 5%Cu) co-doped ZnO nanocrystals at Ni K-edge where fitting has been carried out assuming wurtzite ZnO structure with Zn atoms appropriately replaced by Ni atoms.

Table 6.3: Best-fit parameters of Ni K-edge EXAFS data for (Ni, Cu) co-doped ZnO samples where fitting has been carried out assuming wurtzite ZnO structure with Zn atoms appropriately replaced by Ni atoms.

		(2% Ni, 1% Cu) co-doped ZnO	(2% Ni, 2% Cu) co-doped ZnO	(2% Ni, 3% Cu) co-doped ZnO	(2% Ni, 5% Cu) co-doped ZnO
Ni-O	CN(4)	3.96±0.78	4.46±0.64	4.52±0.72	4.6±0.64
	R (Å)	2.01±0.017	2.01±0.016	2.02±0.018	2.00±0.012
	σ^2	0.005±0.003	0.004±0.002	0.003±0.002	0.003±0.002
Ni-Ni/Zn	CN(12)	12.6±1.38	12.64±1.38	13.8±1.92	13.53±1.16
	R (Å)	2.9±0.01	2.9±0.006	2.9±0.005	2.9±0.003
	σ^2	0.008±0.001	0.009±0.001	0.008±0.001	0.008±0.001
R_{factor}		0.01	0.009	0.01	0.007

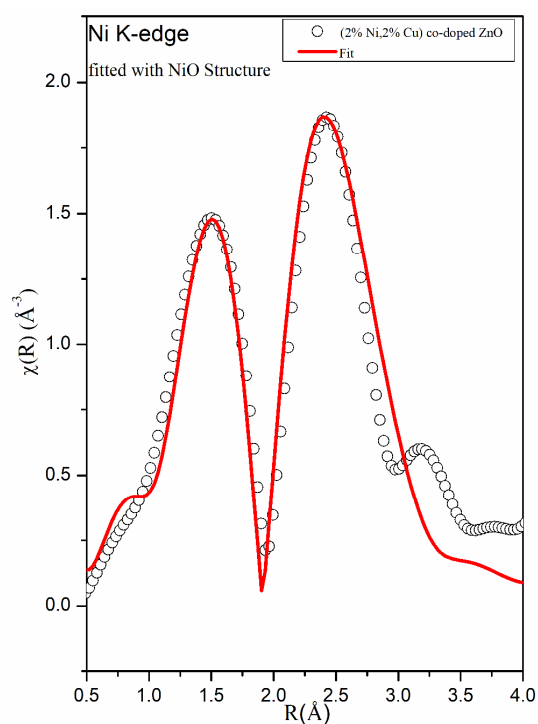


Figure 6.10: Experimental Chi (R) Versus R data and best fit theoretical plots of (2% Ni, 2% Cu) co-doped ZnO nanocrystals at Ni-K-edge where fitting has been carried out by assuming NiO structures at Ni-sites

Table-6.4: Best-fit parameters of Ni K-edge EXAFS data for (Ni,Cu) co-doped ZnO samples where fitting has been carried out assuming NiO structure around Ni sites.

		(2% Ni, 2% Cu) co-doped ZnO
Ni-O	CN(6)	4.2±0.65
	R (2.08 Å)	2.03±0.006
	σ^2	0.005±0.002
Ni-Ni/Zn	CN(12)	13.08±0.84
	R (2.94 Å)	2.94±0.001
	σ^2	0.011±0.006
R_{factor}		0.018

Figure 6.11 represents the Cu K-edge XANES spectra of (2%Ni, 1%Cu) and (2%Ni, 5%Cu) co-doped ZnO NC samples along with that of Cu metal foil and CuO standard for comparison. It can be seen that the absorption edge positions of the co-doped samples match with that of CuO. However, the position of the absorption peak of the (1%Cu, 2%Ni) sample does not match with that of CuO, also the pre-edge hump at 8985 eV (shown by arrow in the figure) observed in case of CuO is also not present in this sample, manifesting that Cu is present in the samples in Cu^{+2} state though not in a separate CuO structure. However, for the (2% Ni, 5% Cu) sample, the position of the absorption peak shifts towards that of CuO and also the pre-edge hump is visible, showing that there is some CuO phase in the sample. The intensity of the hump also increases in 3% and 5% Cu doped samples. Thus from the Cu K-edge XANES spectra we can conclude that at lower doping concentration Cu atoms replace

Zn atoms in ZnO lattice, however at higher doping concentration a separate CuO phase is also formed. In both the samples however, no signature of metallic Cu precipitation observed.

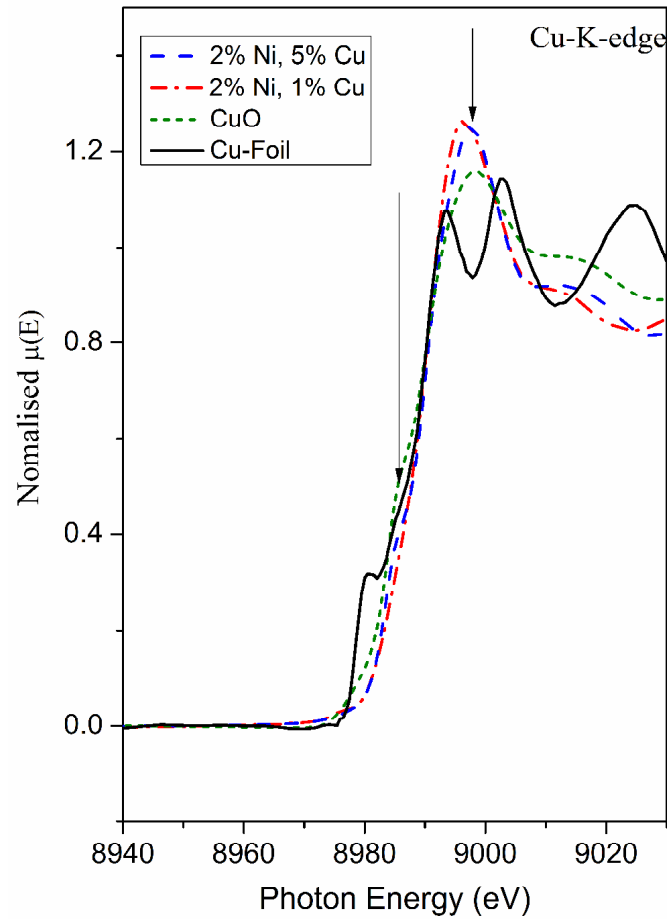


Figure 6.11: XANES plots for (Ni, Cu) co-doped ZnO samples at Cu K-edge along with that of standard CuO and Cu metal foil.

We have further carried out density functional theory (DFT) based electronic structure [198, 199] calculations for Ni and Cu doped ZnO using VASP code [200-201]. For exchange-correlation functional, we employ generalized gradient approximation (GGA) given by Perdew-Burke-Ernzerhof (PBE) [202]. The plane waves are expanded with energy cut off of 400 eV. We use Monkhorst-Pack scheme for k-point sampling of Brillouin zone integration with the k-spacing less than 0.1 \AA^{-1} . In this case, we choose a $(3 \times 3 \times 3)$ super cell of bulk ZnO containing 54 Zn and 54 O atoms. Subsequently we substitute two Zn atoms in the super cell

by Ni and Cu atoms. We consider three distinctly different systems, namely (i) two Ni atoms substituted in the supercell of ZnO ($\text{Ni}_2\text{Zn}_{52}\text{O}_{54}$) corresponding to 3.7% Ni doping, (ii) one Ni and one Cu substituted in the supercell of ZnO ($\text{Cu}_1\text{Ni}_1\text{Zn}_{52}\text{O}_{54}$), corresponding to 1.85% Ni and 1.85% Cu doping and (iii) two Cu atoms substituted in the supercell of ZnO ($\text{Cu}_2\text{Zn}_{52}\text{O}_{54}$), corresponding to 3.7% Cu doping. We have probed two relative distances between the substituted atoms ((i) “Near” to and (ii) “Far” from each other and two different magnetic configurations (i) Ferromagnetic (FM) and (ii) Anti-ferromagnetic (AFM).

It should be noted that our spin-polarized electronic structure calculations reproduce the correct non-magnetic behaviour of bulk ZnO. We find from our calculations that all the doped structures with initial AFM configuration are converged to the structures with FM configurations. Thus, we present the results corresponding to only the FM configuration. The results of the formation energy calculations show that, among the six possible configurations, two structures namely (a) $\text{Ni}_2\text{Zn}_{52}\text{O}_{54}$ with “Near” and (b) $\text{Cu}_1\text{Ni}_1\text{Zn}_{52}\text{O}_{54}$ with “Near” configurations, possess minimum energies. The energy difference between them is very small (~ 0.1 kJ/mol). Our calculations also suggest that the dopant atoms, namely Ni and Cu, carry moments which are similar to that of their atomic magnetic moments. This suggests the magnetic moments are highly localized. We have observed that the magnetic moment ($4.158 \mu_B$) of $\text{Ni}_2\text{Zn}_{52}\text{O}_{54}$ with “Near” configuration is higher than that ($3.032 \mu_B$) of $\text{Cu}_1\text{Ni}_1\text{Zn}_{52}\text{O}_{54}$ with “Near” configuration. Thus, addition of Cu into the system effectively reduces the net magnetic moments of the system. However, we have also observed that if we consider two more configurations viz., $\text{Cu}_2\text{Ni}_1\text{Zn}_{51}\text{O}_{54}$ and $\text{Cu}_3\text{Ni}_1\text{Zn}_{50}\text{O}_{54}$ corresponding respectively to Cu doping concentrations of 3.7% and 5.5%, keeping the Ni concentration fixed at 1.85%, the magnetic moments come out to be $4.111 \mu_B$ and $5.133 \mu_B$ respectively. Thus increase in Cu doping concentration at a fixed Ni concentration eventually increases the magnetic moment of the system.

In order to probe the effect of strong-correlation, if any present in the system, we also perform the calculations using DFT + U method, where U is the on-site Coulomb interaction between the electrons of an atom. First, we perform the calculations with $U = 1 - 5$ eV for d-orbitals of Ni atoms. The variation of formation energy calculated with and without U is summarized in Fig. 6.12.

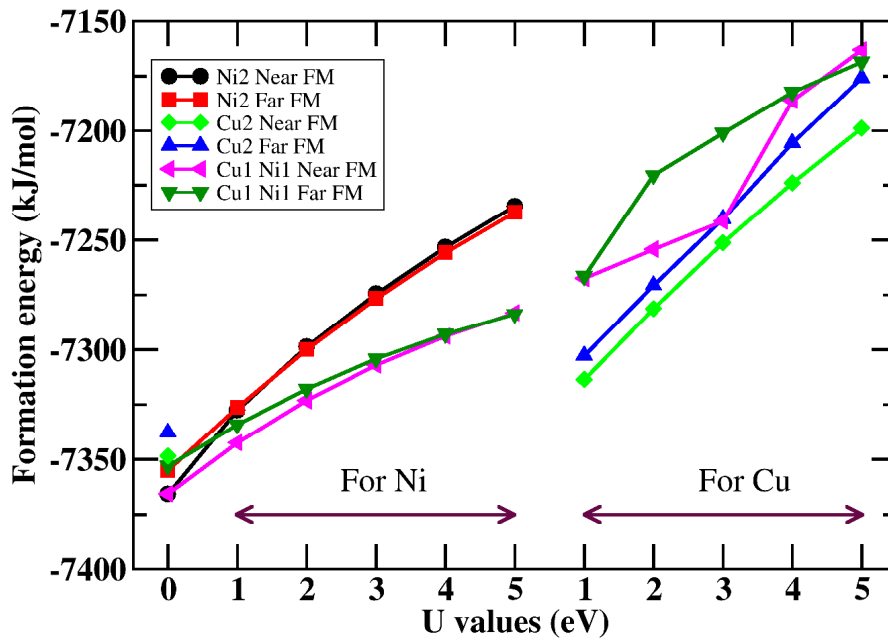


Figure 6.12: Plot of formation energy versus the on-site Coulomb interaction (U) for Ni doped and (Ni, Cu) co-doped ZnO systems in various configurations.

We observe from the figure that the energy difference between the “Near” and “Far” configurations of $\text{Cu}_1\text{Ni}_1\text{Zn}_{52}\text{O}_{54}$ decrease with U value of d-orbitals of Ni atoms. For $U = 5$ eV, the most stable configuration switch from “Near” to “Far” of $\text{Cu}_1\text{Ni}_1\text{Zn}_{52}\text{O}_{54}$. Thus the above theoretical calculations show that both Ni doped and (Ni, Cu) co-doped configurations have equal possibilities of having FM interactions. After $U = 5$ eV for d-orbital of Ni atom, we also introduce the on-site electron correlation (U) for the d-orbitals of both Cu atoms. The results of our calculations indicate that the energetically most stable configuration becomes

$\text{Cu}_2\text{Zn}_{52}\text{O}_{54}$ with “Near” due to inclusion of U for Cu atom, which suggests that the U term for Cu atoms may not be important.

Thus we can summarise the above results as, though our theoretical calculations show that (Ni,Cu) co doped ZnO samples should show FM, magnetic measurements on our samples show reduction of FM in Ni doped ZnO upon inclusion of Cu upto 3% doping concentration. XRD and Ni K-edge XANES results show that at 2% doping concentration Ni goes to the substitutional sites in the ZnO lattice replacing Zn atoms, while Cu K-edge XANES results show that though at lower concentration (~1%) Cu goes to Zn sites, at higher concentration anti-ferromagnetic CuO phase is also formed which reduces the magnetisation in the samples significantly. However, it has also been observed that increasing Cu doping concentration further to 5% again improve magnetization of the samples. This corroborates with our theoretical result that as Cu concentration increases at fixed Ni doping concentration, the magnetic moment of the system increases.

Chapter-7

(Dy, Mn) co-doped ZnO Nanocrystals (NCs)

7.1. Introduction:

As we have discussed in previous chapters that DMS materials are normally formed through the introduction of transition metal (TM) ions, such as Fe, Ni, Mn, Cr or into a host semiconductor like ZnO. In TM, the magnetization arises from partially filled 3d shells and most of the cases since total orbital magnetic moment is zero, the magnetic moment is only due to the spin component and hence total magnetic moment per atom is less. Thus the FM observed in TM doped ZnO samples so far has never been very significant. Rare earth elements doped ZnO nanocrystals are technologically important for industrial applications also in the field of optoelectronics, photo catalysis, fibre amplifier [340] etc. Compared with 3d TMs, 4f rare earth (RE) elements have larger Magnetic moments and likely to enhance the ferromagnetism (FM) in doped semiconductors [339,]. Another advantage of doping with RE ions is that these go into ZnO lattice in +3 oxidation state leading to enhancement of carrier density [339]. Among various rare earth elements, (Er^{3+} & Tb^{3+}) doped ZnO have been reported extensively [340- 344] and doping of ZnO with Dy^{3+} has also been reported [344, 345]. Dy^{3+} ions are also well known for producing visible light by appropriately adjusting yellow and blue emissions [346] and these are also used in thermoelectric devices which directly convert waste heat from the surroundings into electricity [347]. Though there are many reports on the structural as well as magnetic characteristic of TM and RE co-doped ZnO, however the mechanism behind the origin of RTFM is still not clear. Moreover, the results of co-doping of (Mn,Dy) into ZnO have not been reported yet.

In this study we have prepared (Mn,Dy) co-doped ZnO nanocrystals through sol-gel route and characterised them thoroughly by several techniques with an emphasis on synchrotron based Extended X-ray Absorption Fine Structure (EXAFS), which is an element specific technique and can yield important information on local environments of dopants (Mn, Dy) and also host element (Zn) in ZnO nanocrystals.

7.2 Experimentetal details:

7.2.1 Preparation of samples:

To synthesize (Mn, Dy) doped ZnO nanocrystals with Mn-concentrations of 0 and 2% and Dy-concentrations of 0%, 0.5%, 1%, 2%, 4% and 6%, we follow the sol-gel route as has been mentioned in Chapter-2. Appropriate proportions of powders of analytical grade metal nitrates $\text{Zn}(\text{NO}_3)_2 \cdot 6\text{H}_2\text{O}$ from Sigma-Aldrich (99.99%), $\text{Dy}(\text{NO}_3)_3 \cdot 5\text{H}_2\text{O}$ from Alfa Aesar (99.99%), and $\text{Mn}(\text{NO}_3)_2 \cdot 4\text{H}_2\text{O}$ from Merck, Germany (99.98%) were thoroughly mixed and dissolved in equimolar solution of Ethylene glycol and Poly(vinyl alcohol) (PVA) (99+ purity), prepared in double distilled water, while stirring to obtain a homogeneous precursor solution. The obtained solution was slowly heated on a hot plate at 200°C until a highly viscous gel precursor was obtained. The highly viscous gel was kept at 200°C in the oven for 12 hrs. for complete drying. After grinding the powder is calcined at 500°C for 10 hrs.

7.2.2 Characterisation of samples:

Structural characterization of (Mn,Dy) doped ZnO nanocrystals was performed by X-ray diffractometer (Model: Miniflex-II, Rigaku, Japan) with $\text{Cu K}\alpha$ radiation ($\lambda = 1.54 \text{ \AA}$). TEM, HRTEM and Selected Area Electron diffraction (SAED) measurements were done with Technai G² S-Twin (FEI, Netherlands). Fourier transmission infrared (FT-IR) spectra of the samples (as pellets with KBr) were obtained using FT-IR Spectrometer (Spectrum One,

Perkin Elmer Instrument, USA) in the range of 400–4000 cm^{-1} with a resolution of 1 cm^{-1} . The photoluminescence (PL) spectra were taken in a Fluorescence Spectrometer (LS-45, Perkin Elmer, USA) and the magnetic (M-H) measurements were done using Superconducting Quantum Interference Device (SQUID) Magnetometer [Magnetic Property Measurement System (MPMS) XL-7, Quantum Design, Inc.]). XAFS measurements on the samples were carried out at the Energy Scanning EXAFS beamline (BL-9) at the Indus-2 Synchrotron Source (2.5 GeV, 120 mA) at the Raja Ramanna Centre for Advanced Technology (RRCAT), Indore, India described in Chapter-2. The EXAFS spectra of the samples at Mn K-edge were recorded in the energy range of 6470-7250eV and at Dy L₃-edge the measurements have been carried out in the range of 7675-8490eV.

7.3 Results and discussion:

7.3.1 X-ray diffraction:

Phase purity of the (Mn,Dy) co-doped ZnO samples has been checked by XRD measurement (Fig.7.1) which shows that no secondary phase is present in the samples other than wurtzite hexagonal ZnO phase. Thus incorporation of Dy in ZnO:Mn does not change the structure of wurtzite ZnO. However, it can be seen from the Fig.7.1 that there is a shift in the peaks towards lower 2θ values upon Dy doping. Since it has been observed from the XANES studies on the samples at Dy L₃-edge, as discussed later, that Dy goes to ZnO lattice as Dy⁺³, the above shift may be because of expansion of ZnO lattice since the ionic radii of Dy⁺³ (0.91) is higher than the ionic radii of Zn⁺²(0.74), similar results being observed by Khataee et al. also for their Dy doped ZnO nanoparticles [348]. The parameters obtained from the analysis of XRD data of the co-doped samples are shown in Table 7.1.

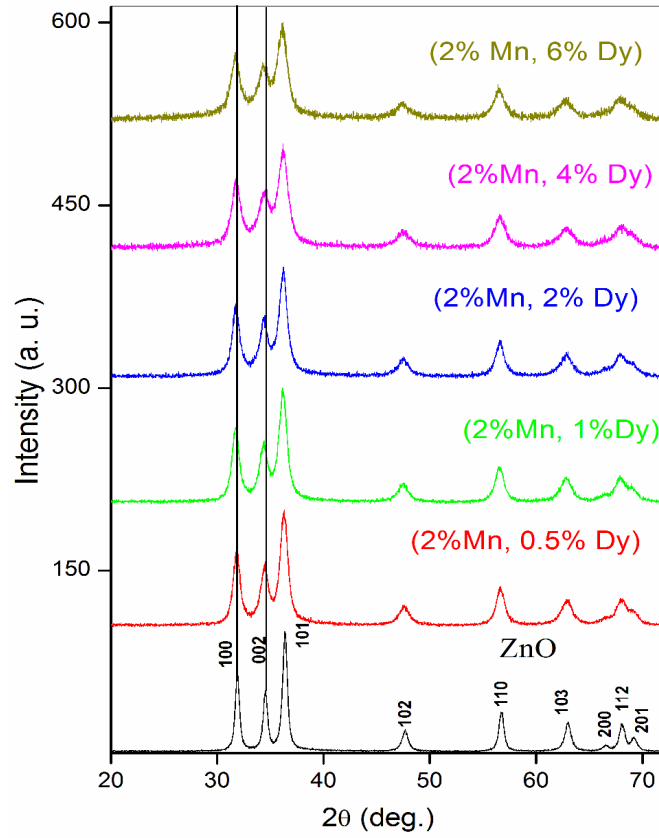


Figure 7.1: X-ray diffraction pattern of (Mn, Dy) co-doped ZnO

Table 7.1: Values of particle size, lattice parameters and interplanar spacing for different plans of the (Mn,Dy) co-doped samples:

Parameters	ZnO	(2% Mn, 0.5% Dy) co-doped ZnO	(2% Mn, 1% Dy) co-doped ZnO	(2% Mn, 2% Dy) co-doped ZnO	(2% Mn, 4% Dy) co-doped ZnO	(2% Mn, 6% Dy) co-doped ZnO
Particle size (nm)	16.5	9.8	9.6	8.9	7.7	7.4
a (Å)	3.239	3.247	3.256	3.249	3.254	3.261
c (Å)	5.191	5.201	5.219	5.226	5.208	5.221
d ₍₁₀₀₎ (Å)	2.805	2.811	2.820	2.813	2.818	2.824
d ₍₀₀₂₎ (Å)	2.595	2.600	2.609	2.613	2.604	2.610
d ₍₁₀₁₎ (Å)	2.469	2.473	2.480	2.483	2.480	2.485

7.3.2 Transmission Electron Microscopy:

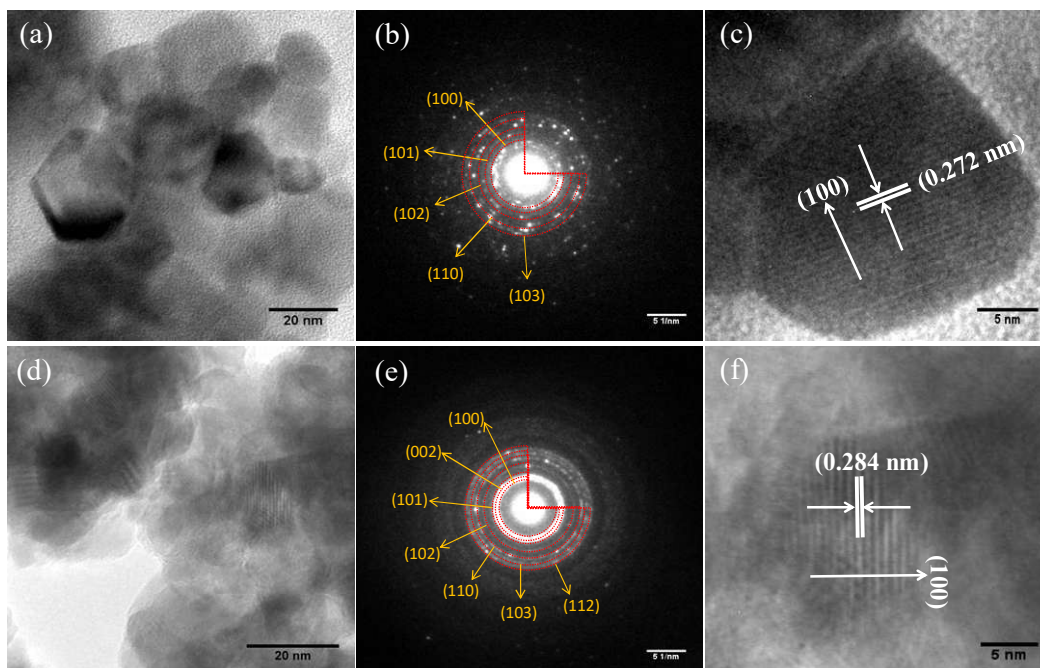


Figure 7.2: Low magnification TEM (a), SAED (b), and HRTEM (c) images of ZnO nanocrystals and low magnification TEM (d), SAED (e), and HRTEM (f) images of (2% Mn, 2% Dy) co-doped ZnO nanocrystals.

The morphology and microstructure of nanoparticles have been examined by transmission electron microscopy (TEM). Figs. 7.2(a)-(b) and 2(d)-(e) represent the TEM images and SAED patterns of pure ZnO and (2%Mn, 2%Dy) co-doped ZnO nanoparticles which show that the sizes of nanocrystals are ~22nm and 12 nm respectively. The HRTEM micrograph of a representative ZnO and (2%Mn,2%Dy) co-doped ZnO sample is shown in Figs. 7.2(c) and 2(f) which show *d*-value of 0.272 and 0.284 nm for (100) plane of wurtzite ZnO. Moreover, it should be pointed out here that *d*-values of the (2%Mn, 2%Dy) co-doped ZnO determined from TEM measurements are found to be higher than that of pristine ZnO, which signifies the

presence of tensile strain in the (Mn, Dy) co-doped samples as observed from XRD measurements. The HRTEM pattern also indicates that all the nanoparticles are single crystalline in nature and are free from major lattice defects. Thus according to the results of XRD pattern and HRTEM images, we can say that the Mn and Dy have been well incorporated into the crystal lattice of ZnO.

7.3.3 FTIR Spectroscopy:

Fig. 7.3 represents FTIR spectra of undoped and (Mn, Dy) co-doped ZnO NCs capped by PVA. It can be seen from fig.7.3 that all the samples exhibited absorption bands at 3444, 2928, 2856, 2360, 1626, 1534, 1387, 842, 440 cm^{-1} . The peak appeared around 440 cm^{-1} can be attributed to the Zn–O stretching mode in the ZnO lattice [349]. The peak found at around $\sim 3444 \text{ cm}^{-1}$ can be assigned to the –OH mode while two other peaks observed around 2928 and 2856 cm^{-1} are due to CO_2 molecule present in the air. The absorption peak observed around 1626, 1534 and 1387 cm^{-1} are due to stretching vibrations of C =H, C = C and C–O group in acetate species which may be present on the surfaces of the undoped and Co doped (Mn,Dy) ZnO nanoparticles. It is clear from the fig.7.3 that with an increase in Dy concentration, the intensity of the ZnO band decreases which manifests successful incorporation of Dy^{+3} ions in ZnO lattice and the disorder produced thereof. Similar results have also been obtained by Soni et al. for their Mn doped ZnO nanoparticles prepared by microwave irradiation [350]. However, it can be seen from Fig.7.3 that in our case there is no significant shift in the Zn-O stretching mode frequency due to Dy incorporation showing that Zn-O bond length does not distort significantly due to Dy incorporation, the result being corroborated from EXAFS measurements as discussed later.

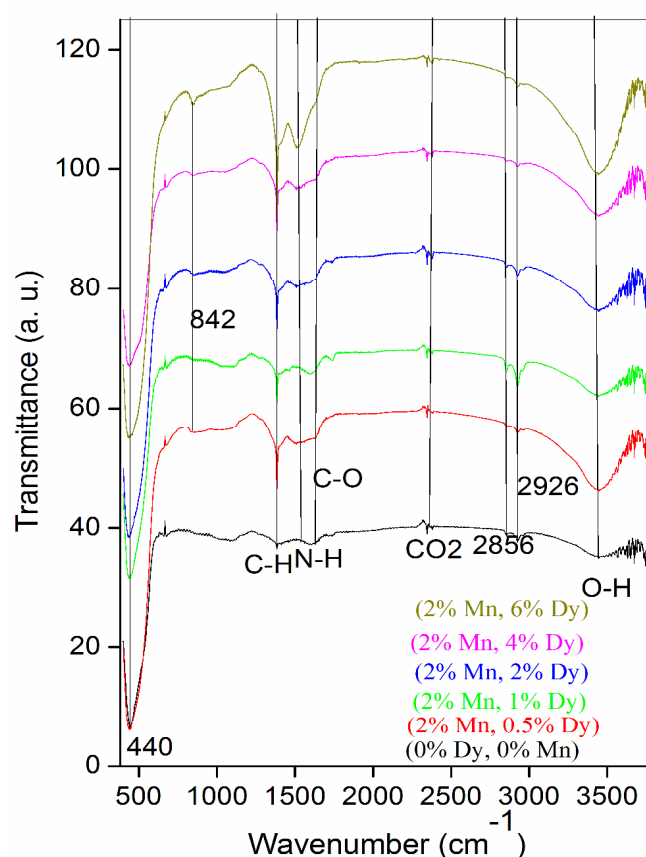


Figure 7.3: FTIR spectra of (Mn,Dy) co-doped ZnO nanocrystals.

7.3.4 Photo luminescence Measurement:

Fig.7.4 shows the room temperature PL spectra of (Mn, Dy) co-doped ZnO samples along with the undoped one recorded between 400nm to 900nm range, at the excitation wavelength of 355 nm. It can be seen from the above figure that pure ZnO sample have four emission bands in the visible range centred at 472.1 nm, 481.6 nm, 588.4 nm and 635.6 nm. It can also be found that PL intensities at the above wavelengths increase with the doping of Dy in ZnO:Mn alongwith the appearance of a green band at 420 nm. Thankgeeswari et. al. have also observed quenching of UV emission and enhancement of green emission which they have attributed to the creation of oxygen vacancies on Dy doping [351] Wu et.al. have observed a PL peak at 575 nm which is due to $^4F_{9/2}$ - $^6H_{13/2}$ transition, characteristic of Dy^{+3}

ions apart from the near band edge transition peak at 384 nm for Dy doped ZnO nanowires [344] Yan et.al. on the other hand observed an additional characteristic peak at 482 nm due to $^4F_{9/2}$ - $^6H_{15/2}$ transition in their Dy complex doped ZnO/polyethelyne glycol hybrid phosphors [352]. We have not observed any of these bands in our samples manifesting that Dy has been successfully incorporated in the ZnO lattice in the samples.

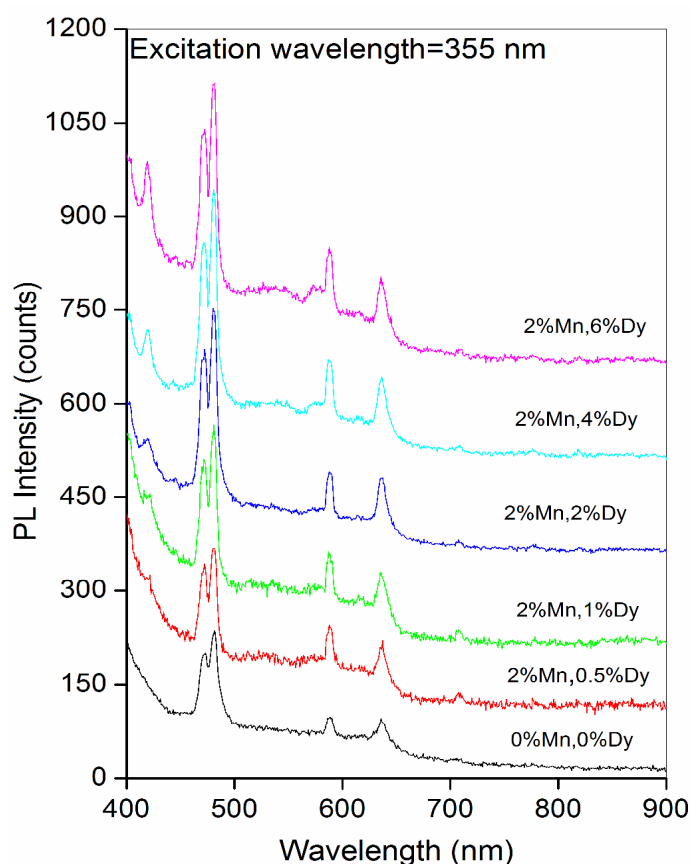


Figure 7.4: Photoluminescence spectra of (Mn,Dy) co-doped ZnO nanocrystals.

7.3.5 Magnetic Measurements:

Fig.7.5 shows the magnetization (M) vs. applied field (H) curve of the M-H plots of 2% Mn doped and (2%Mn,2%Dy), (2%Mn,4%Dy), (2%Mn,6%Dy) co-doped ZnO samples at room temperatures while that of pure ZnO exhibiting diamagnetic behaviour at room temperature is shown in the inset of the figure.

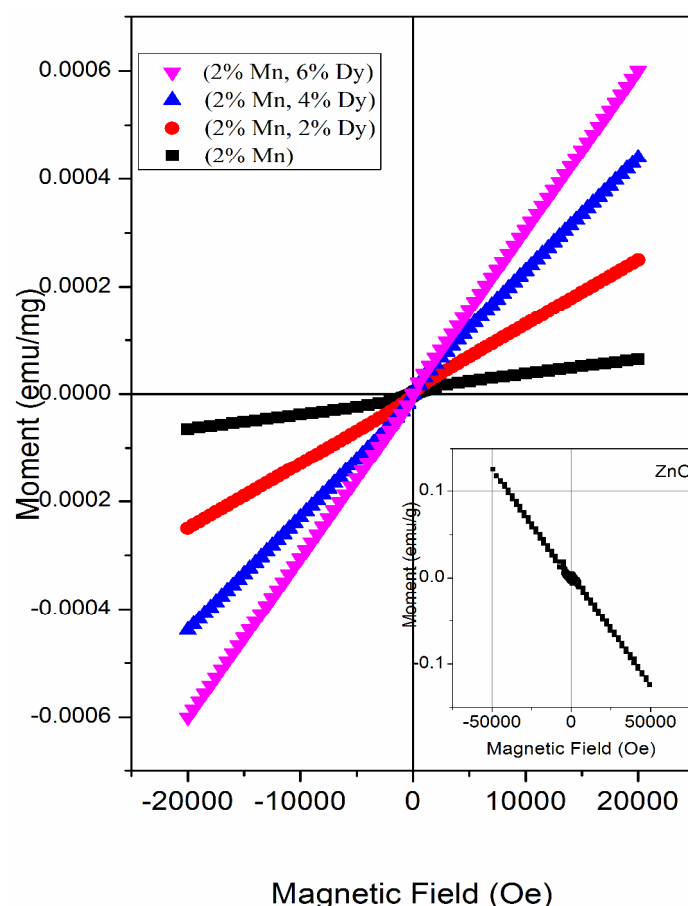
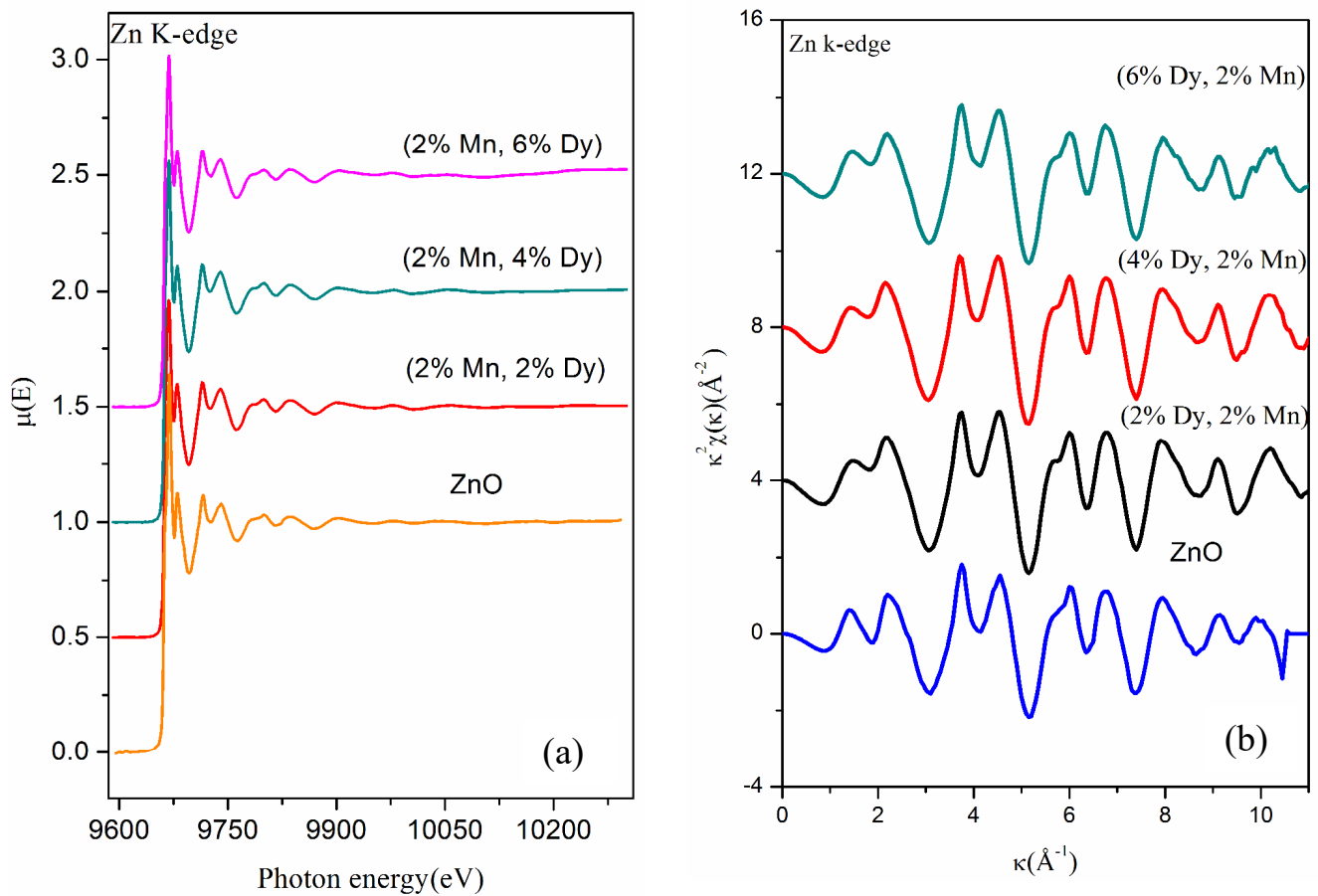


Figure 7.5: M-H plots for (Mn, Dy) co-doped ZnO nanocrystals.

It can be seen that Mn doped and (Mn, Dy) co-doped samples with lower concentration of Dy (2%) exhibit super paramagnetic/weak ferromagnetic behaviour. However, as the concentration of Dy is increased, magnetic behaviour changes from weak ferromagnetic/super paramagnetic to ferromagnetic nature. Thangeeswari et al. [351] however, contrary to our result have observed a decrease in FM in their (Co,Dy) co-doped ZnO samples with an increase in Dy concentration and have attributed it to anti-ferromagnetic (AFM) interaction among the Dy ions. Subramanian et al. [339] and Vijayaprasath et al. [352] have also observed decrease in magnetization with an increase in Gd doping concentration in case of Gd doped ZnO samples possibly due to AFM interaction among Gd atoms.

7.3.6 EXAFS measurement:

To further investigate the origin of RTFM in the above samples XAS measurement have been carried out on Mn doped and (2%Mn, 2%Dy), (2%Mn, 4%Dy) and (2%Mn, 6%Dy) co-doped samples. Fig. 7.6(a &b) represent the normalized EXAFS ($\mu(E)$ versus E) spectra and ($\chi(k)$ versus k) spectra (k range of 3–11 \AA^{-1}) of (Mn, Dy) doped ZnO NCs at Zn K-edges. The $\chi(R)$ versus R plots have been generated for all the samples from the $\mu(E)$ versus E spectra following the methodology described in Chapter-2 and are shown in figure 7. 6(c).



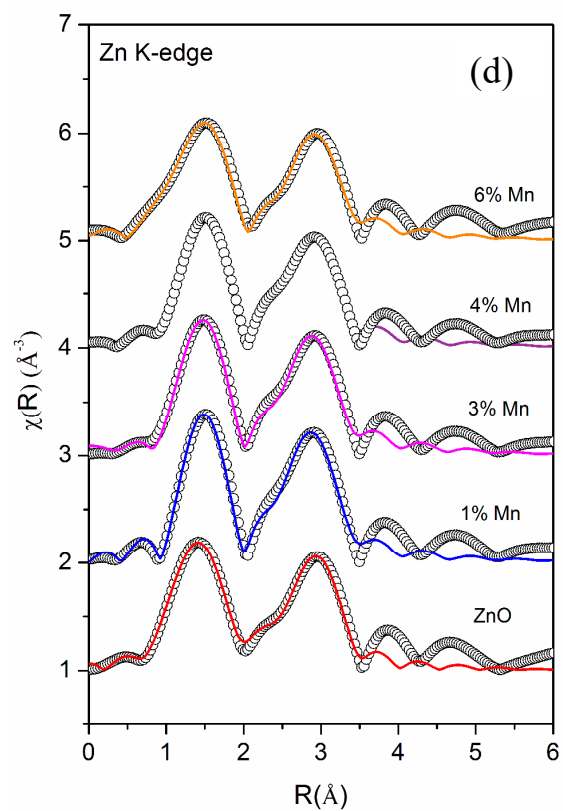
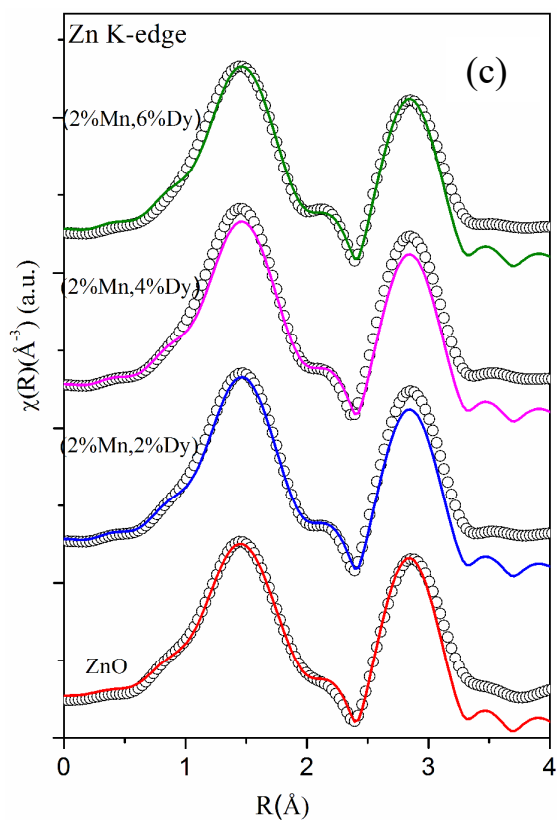


Figure 7.6 (a) Normalized experimental EXAFS ($\mu(E)$ versus E) for (Mn, Dy) co-doped ZnO nanocrystals measured at Zn K-edge. (b) k^2 -weighed $\chi(k)$ function of the Zn K-edge for the (Mn, Dy) co-doped ZnO nanocrystals measured at Zn K-edge. (c) Experimental $\chi(R)$ versus R data (scatter points) and best fit theoretical plots (solid line) of undoped, (2% Mn, 2% Dy), (2% Mn, 4% Dy) & (2% Mn, 6% Dy) co-doped ZnO nanocrystals at Zn Kedge. (d) Experimental $\chi(R)$ versus R data (scatter points) and best fit theoretical plots (solid line) of Mn doped ZnO samples at Zn K-edge.

Table 7.2: Fit parameters at Zn K-edge by assuming wurtzite ZnO structure for (Mn,Dy) co-doped ZnO samples:

		ZnO	(2% Mn, 2% Dy) co-doped ZnO	(2% Mn, 4% Dy) co-doped ZnO	(2% Mn, 6% Dy) co-doped ZnO
Zn-O	N (4)	3.86±0.84	3.86±0.84	3.86±0.84	3.86±0.84
	R (Å)	1.94±0.02	1.93±0.03	1.95±0.02	1.94±0.01
	σ^2	0.005±0.002	0.004±0.002	0.003±0.001	0.004±0.002
Zn-Zn	N (12)	12.48±1.68	12.48±1.68	12.48±1.68	12.48±1.68
	R (Å)	3.20±0.01	3.21±0.01	3.20±0.01	3.21±0.01
	σ^2	0.009±0.001	0.01±0.001	0.008±0.001	0.011±0.001
R_{Factor}		0.02	0.014	0.02	0.011

Table 7.3: Fit parameters at Zn K-edge by assuming wurtzite ZnO structure for Mn doped ZnO samples:

		ZnO	1% Mn doped ZnO	3% Mn doped ZnO	4% Mn doped ZnO	6% Mn doped ZnO
Zn-O	N	4.24±0.43	4.17±0.56	4.17±0.56	4.12±0.64	4.08±0.65
	R	1.91±0.01	1.94±0.03	1.94±0.03	1.94±0.03	1.94±0.03
	σ^2	0.008±0.001	0.008±0.001	0.008±0.001	0.009±0.006	0.009±0.002
Zn-Zn	N	5.16±0.47	5.06±0.61	5.06±0.61	5.04±0.61	4.32±0.34
	R	3.08±0.01	3.08±0.02	3.08±0.02	3.08±0.02	3.07±0.01
	σ^2	0.003±0.001	0.003±0.001	0.003±0.001	0.003±0.001	0.001±0.001
Zn-O	N	1	1	1	1	1
	R	3.61±0.06	3.62±0.034	3.60±0.08	3.62±0.034	3.62±0.034
	σ^2	0.003±0.001	0.003±0.001	0.003±0.001	0.003±0.001	0.003±0.001
Zn-Zn	(6)	7.8±0.24	7.62±0.64	7.62±0.64	7.62±0.64	7.62±0.64
	R	3.25±0.003	3.26±0.004	3.26±0.005	3.26±0.004	3.27±0.004
	σ^2	0.003±0.001	0.001±0.001	0.002±0.001	0.002±0.001	0.002±0.001
R_{Factor}		0.0009	0.0002	0.0007	0.0004	0.0004

In figure 7.6(c) the first and second major peaks correspond to the nearest oxygen and the Zn/Mn/Dy shells respectively from the central Zn atom. The theoretical Fourier transformed EXAFS spectra have been generated, assuming the model described by Kisi et. al. [224] as described in earlier chapters. A set of EXAFS data analysis codes available within the IFEFFIT software package have been used for EXAFS data analysis as described in details in Chapter-2 . The data has been fitted between 1-3.5 Å in R space. The best fit parameters

have been shown in Table 7.2. For comparison in Fig.7.6(d) we have also plotted the Fourier transformed EXAFS (FOURIER TRANSFORMED EXAFS) $\chi(R)$ versus R spectra along with the best fit theoretical spectra for only Mn doped ZnO samples and the best fit parameters have been shown in Table 7.3 from where it can be seen that the results are similar for both Mn doped and (Mn, Dy) co-doped samples. Thus it has been observed that Dy doping has not caused any additional changes around Zn sites.

Fig.7.7(a) shows the experimental EXAFS ($\mu(E)$ versus E) spectra of (Mn,Dy) co-doped ZnO NCs at Mn K-edge while Fig. 7.7(b) shows the k^2 -weighed $\chi(k)$ versus k plots of the samples derived from the experimental EXAFS spectra. At the Mn K-edge we have explored two possibilities of theoretical modelling to fit the experimental data: (a) starting with the basic wurtzite ZnO structure and replacing the central Zn atom with Mn and (b) taking the initial model to be of cubic Mn_2O_3 . Such an approach to modelling has been reported by other authors as well [223] For the second case, structural parameters of Mn_2O_3 has been taken from ICSD database [353] and data has been fitted by assuming the first nearest oxygen at 1.89Å with N of 4 and second nearest oxygen shell at 2.24 Å with N of 2.

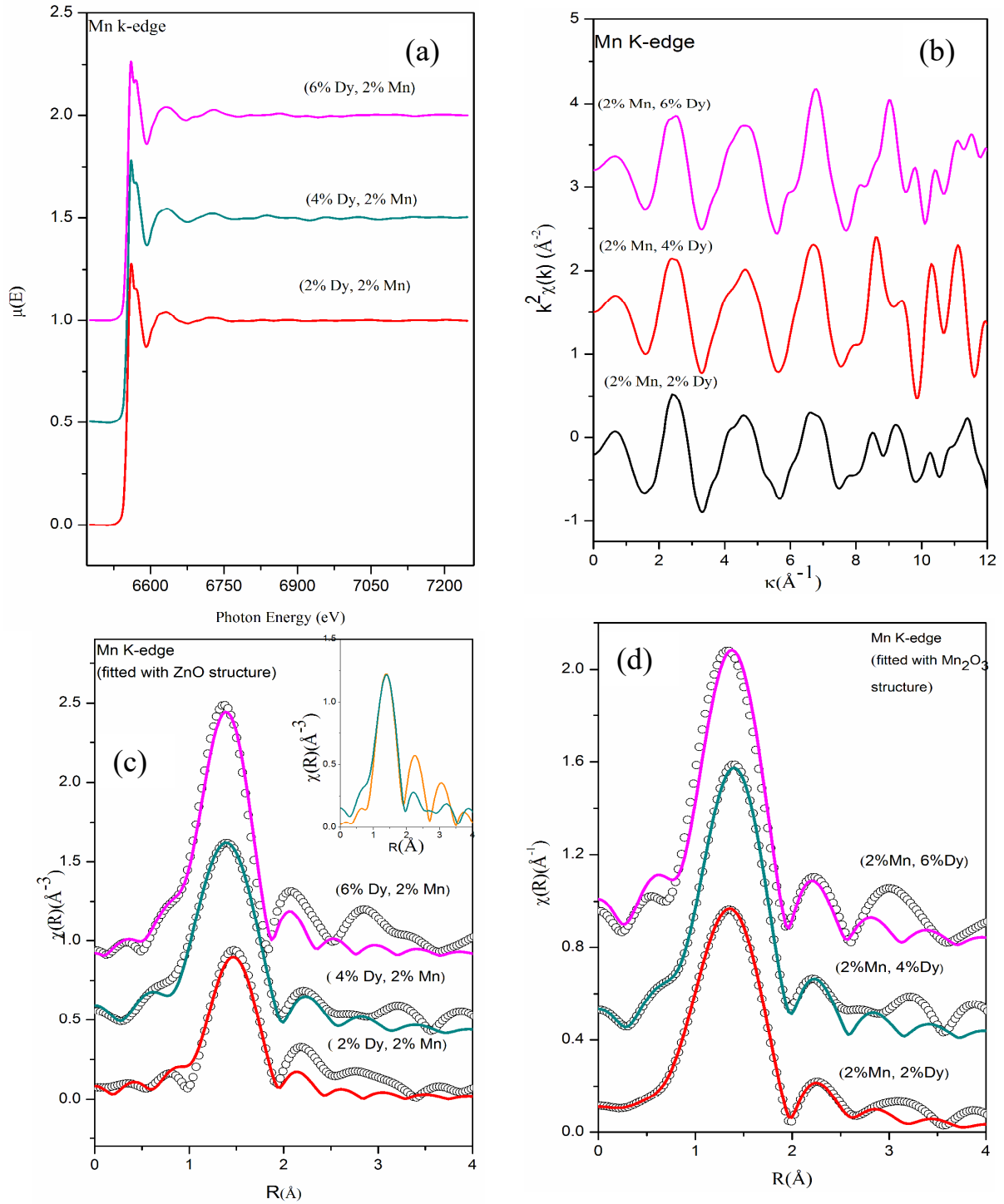


Figure 7.7 (a): Normalized experimental EXAFS ($\mu(E)$ versus E) for (Mn, Dy) co-doped ZnO nanocrystals measured at Mn K-edge. (b) k^2 -weighted $\chi(k)$ function of the Mn K-edge for the (Mn, Dy) co-doped ZnO nanocrystals. (c) Experimental $\chi(R)$ versus R data (scatter points) and best fit theoretical plots (solid line) of (2% Mn, 2% Dy), (2% Mn, 4% Dy) & (2% Mn, 6% Dy) co-doped ZnO samples at Mn K-edge (fitting have been carried out assuming Mn at Zn sites in wurtzite ZnO structure). (d) Experimental $\chi(R)$ versus R data (scatter points) and best fit theoretical plots (solid line) of (2% Mn, 2% Dy), (2% Mn, 4% Dy) & (2% Mn, 6% Dy) co-doped ZnO samples at Mn K-edge (fitting has been carried out by assuming Mn_2O_3 structure around Mn sites).

Table 7.4: Fit parameters at Mn K-edge by assuming Mn at Zn sites in wurtzite ZnO structure for (Mn,Dy) co-doped ZnO samples.

		(2% Mn, 2% Dy) co-doped ZnO	(2% Mn, 4% Dy) co-doped ZnO	(2% Mn, 6% Dy) co-doped ZnO
Mn-O1	$N(4)$	1.468 ± 0.08	2.76 ± 0.23	2.95 ± 0.22
	$R(\text{\AA})$	1.94 ± 0.01	1.9 ± 0.01	1.89 ± 0.01
	σ^2	0.001 ± 0.001	0.002 ± 0.001	0.002 ± 0.001
R_{Factor}		0.01	0.007	0.013

Figs. 7.7(c) and (d) show the Fourier transformed EXAFS spectra or $\chi(R)$ versus R plots of (2%Mn, 2%Dy), (2%Mn, 4%Dy) and (2%Mn, 6%Dy) co-doped ZnO samples at the Mn K-edge, along with the best fit theoretical spectra, where the fittings have been carried out by using (i) wurtzite ZnO structure (where Zn atoms are replaced by Mn atoms according to the doping concentration) and (ii) cubic Mn₂O₃ structure respectively and the best fit parameters have been given in Tables 7.4 and 7.5.

It should be noted here that in the theoretical model, which is generated by assuming Mn₂O₃ structure, the first Mn-Mn path occurs at 3.1 Å, but in FT- spectra of Mn-K edge, no significant peak occurs corresponding to this Mn-Mn path. For comparison the $\chi(R)$ versus R plots of the 2% Mn doped and (2%Mn,2%Dy) doped ZnO nanocrystals measured at Mn K-edge have been plotted in the inset of Fig. 7.7(c), which shows very broad and reduced Mn-Mn peak in case of the later compared to the former sample, manifesting that Dy doping introduces some distortion in and around Mn sites in the lattice. Thus during fitting of the data for (Mn, Dy) co-doped samples only the contribution of nearest oxygen shells have been taken. It has been observed that the parameters obtained by the later approach viz., assuming Mn₂O₃ structure yields more reasonable results as shown in Table-7.5 and it is also

reflected in the better quality of fitting obtained in Fig. 7.7(d) compared to in Fig. 7.7(c). The above results indicate that Mn is going to ZnO lattice as Mn^{+3} .

Table 7.5: Fit parameters at Mn K-edge by assuming Mn_2O_3 structure at Mn site for (Mn, Dy) co-doped ZnO samples.

		(2% Mn, 2% Dy) co-doped ZnO	(2% Mn, 4% Dy) co-doped ZnO	(2% Mn, 6% Dy) co-doped ZnO
Mn-O1	N	4.0 ± 0.39	4.0 ± 0.39	4 ± 0.39
	$R (\text{\AA})$	1.92 ± 0.01	1.92 ± 0.01	1.9 ± 0.01
	σ^2	0.0086 ± 0.001	0.005 ± 0.003	0.005 ± 0.001
Mn-O2	N	1.57 ± 0.38	1.57 ± 0.38	1.57 ± 0.38
	$R (\text{\AA})$	2.26 ± 0.03	2.29 ± 0.01	2.26 ± 0.04
	σ^2	0.01 ± 0.01	0.005 ± 0.003	0.007 ± 0.006
R_{Factor}		0.0008	0.001	0.001

For comparison, Fig.7.8(a) shows the experimental Fourier transformed EXAFS data of the Mn doped samples at the Mn K-edge along with the best fit theoretical plot where the fitting has been carried out assuming Mn at Zn sites in tetrahedral ZnO structure and Fig.7.8(b) shows the corresponding plot for the 1% Mn doped sample where fitting has been carried out using Mn_2O_3 structure at the Mn sites. The best fit parameters of the above two cases have been shown in Tables 7.6 and 7.7. It is clear from the above figures and tables that the fitting quality of the data with the second theoretical model is poor and it yields unreasonable results of very low coordination in the oxygen and Mn shells. Hence we can conclude that in case of Mn doped ZnO samples the EXAFS data is best fitted with the model of Mn replacing Zn atoms in ZnO lattice.

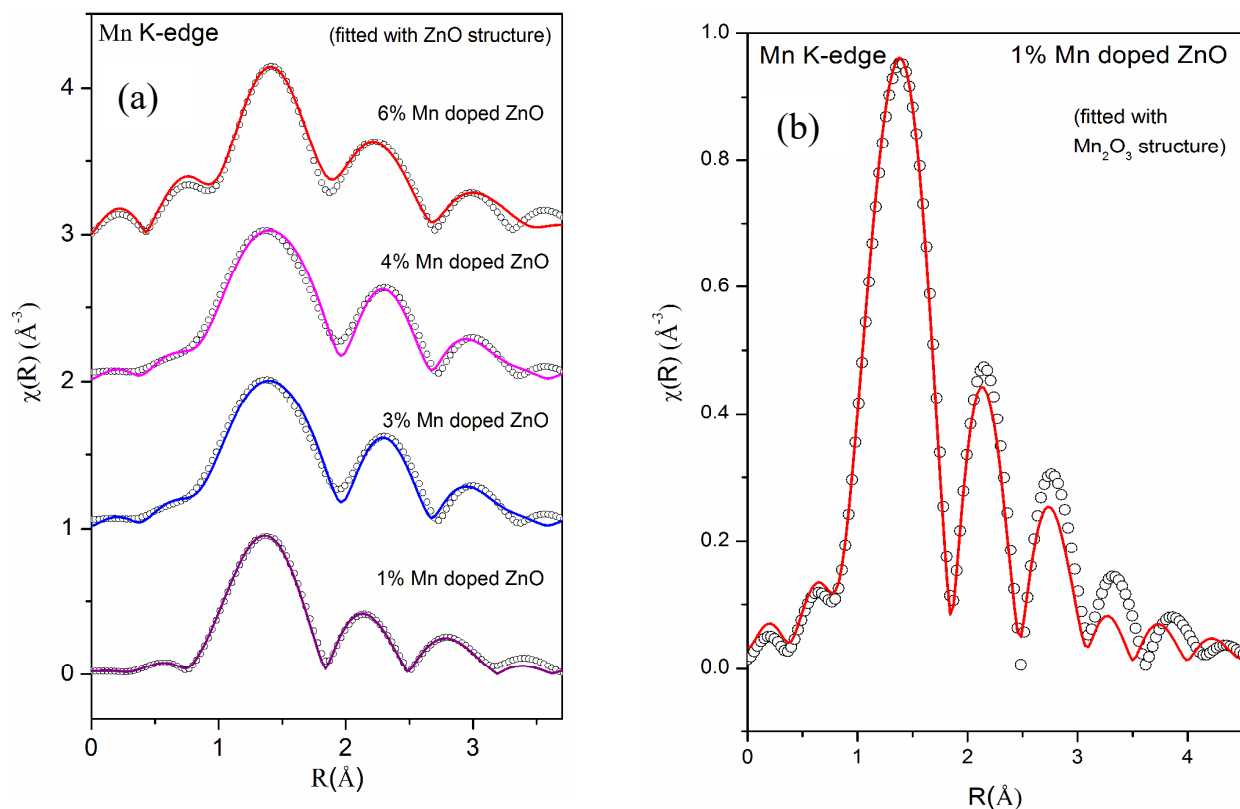


Figure 7.8: (a) Experimental $\chi(R)$ versus R data (scatter points) and best fit theoretical plots (solid line) of Mn doped ZnO samples at Mn K-edge (fitting has been done assuming Mn at Zn sites in wurtzite ZnO structure). (b) Experimental $c(R)$ versus R data (scatter points) and best fit theoretical plots (solid line) of Mn doped ZnO samples at Mn K-edge (fitting has been carried out by assuming Mn_2O_3 structure around Mn sites).

Table 7.6: Fit parameters at Mn sites assuming Mn at Zn sites in wurtzite ZnO structure for Mn doped ZnO sa

Mn-O	N (2)	0.24 ± 0.26
	R (Å)	2.29 ± 0.10
	σ^2	0.03 ± 0.10
Mn-O	N (2)	3.82 ± 0.04
	R (Å)	2.01 ± 0.09
	σ^2	0.015 ± 0.02
Mn-O	N (2)	0.024 ± 0.001
	R (Å)	2.47 ± 0.01
	σ^2	0.04 ± 0.001
Mn-Mn	N (10)	1.6 ± 0.47
	R (Å)	3.28 ± 0.029
	σ^2	0.026 ± 0.005
R_{Factor}		0.0002

Table 7.7: Fit parameters for Mn K-edge data assuming Mn_2O_3 structure at Mn site.

		1% Mn doped ZnO	3% Mn doped ZnO	4% Mn doped ZnO	6% Mn doped ZnO
Mn-O	N (4)	3.12 ± 0.76	2.53 ± 0.44	2.59 ± 2.82	2.56 ± 0.52
	R (1.97Å)	1.95 ± 0.04	1.95 ± 0.01	1.96 ± 0.04	1.95 ± 0.02
	σ^2	0.026 ± 0.034	0.01 ± 0.001	0.01 ± 0.002	0.01 ± 0.004
Mn-Mn	N (6)	5.2 ± 1.08	5.1 ± 0.22	4.98 ± 0.33	4.95 ± 0.30
	R (3.20Å)	2.99 ± 0.03	2.99 ± 0.01	2.98 ± 0.042	2.97 ± 0.01
	σ^2	0.023 ± 0.003	0.012 ± 0.001	0.015 ± 0.001	0.008 ± 0.001
Mn-Mn	N (6)	5.98 ± 1.24	5.95 ± 0.38	5.4 ± 0.81	5.52 ± 0.21
	R (3.25Å)	3.30 ± 0.02	3.31 ± 0.01	3.30 ± 0.01	3.25 ± 0.01
	σ^2	0.021 ± 0.002	0.023 ± 0.001	0.023 ± 0.001	0.012 ± 0.001
R_{Factor}		0.0046	0.0001	0.001	0.003

Thus the above EXAFS measurements on the Mn doped and (Mn,Dy) co-doped samples show two striking dissimilarities, viz, in case of Mn doped samples, the Mn-Mn peak at 3.1 Å is present in the Fourier transformed EXAFS spectra, while in (Mn,Dy) co-doped samples it is significantly reduced due to the disorder introduced by Dy atoms. Secondly, in Mn doped samples Mn is going to the ZnO lattice is Mn^{+2} oxidation state while in case of (Mn,Dy) co-doped samples, Mn is going into the lattice in Mn^{+3} oxidation state. Fig.7.9 shows the XANES spectra of the (Mn, Dy) co-doped ZnO samples along with that of standard MnO_2 and Mn_2O_3 commercial powder and Mn metallic foil. It shows that the Mn absorption edge positions of the samples lie just above that of Mn_2O_3 showing that Mn goes into the samples as Mn^{+3} . However, it is evident from the above figure that the post edge features (shown with arrows in the figure) of Mn_2O_3 do not exactly match with that of the samples. This manifests that though Mn goes into the ZnO lattice in the co-doped samples as Mn^{+3} , however it does not exist as separate Mn_2O_3 phase in the sample manifesting proper Mn doping at Zn sites in the samples

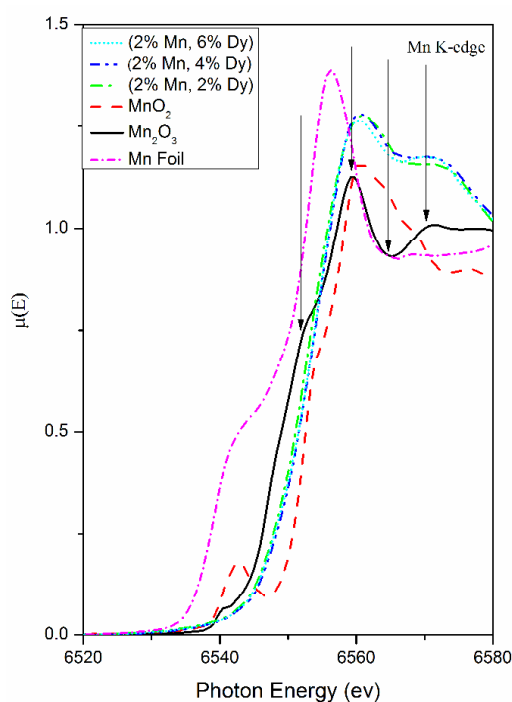


Figure 7.9: XANES plots for (Mn,Dy) co-doped ZnO samples at Mn K-edge alongwith that of standard MnO₂, Mn₂O₃ powders and Mn foil

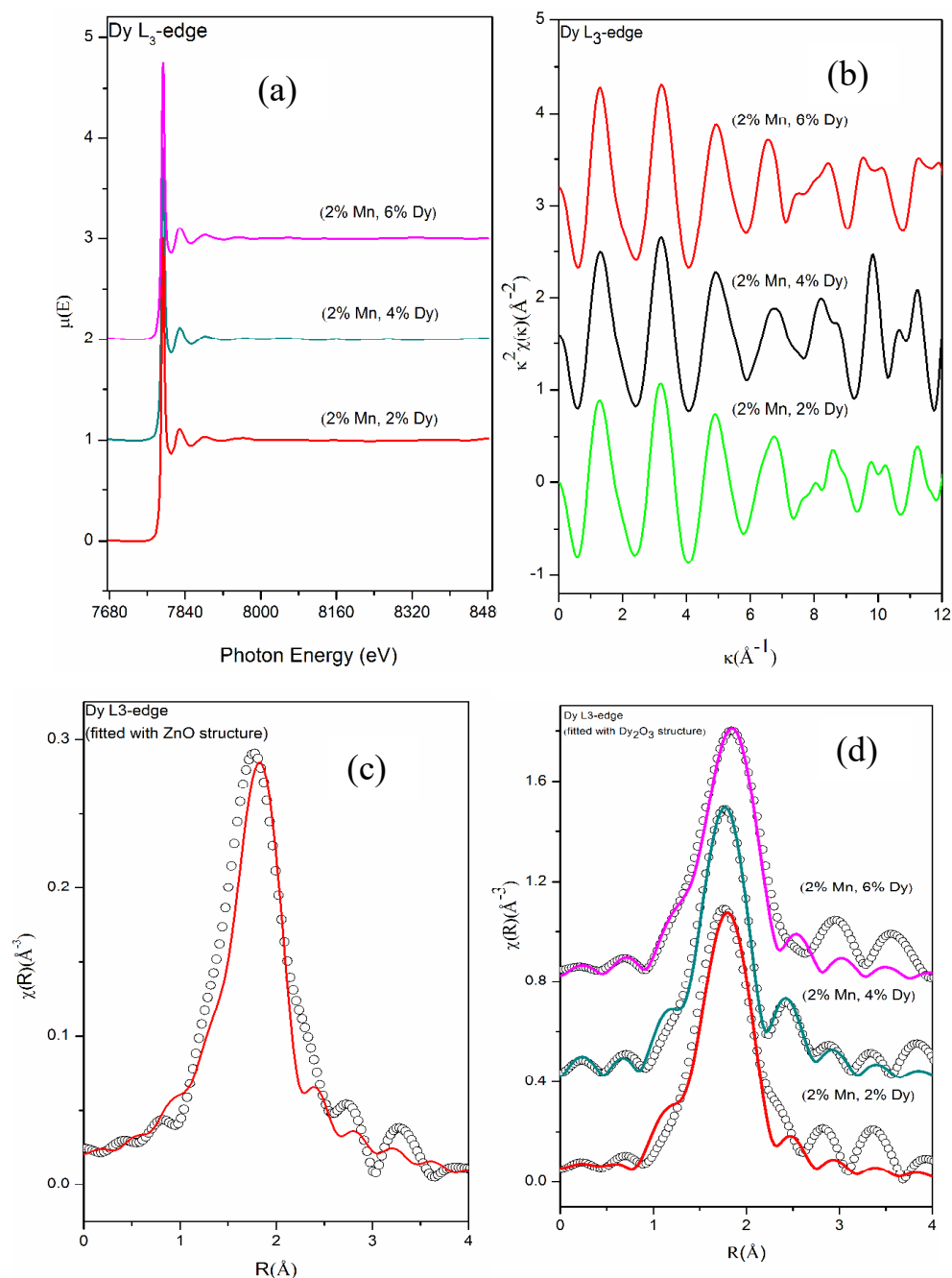


Figure 7.10 (a) Normalized experimental EXAFS ($\mu(E)$ versus E) for (2% Mn, 2% Dy), (2% Mn, 4%Dy) & (2% Mn, 6% Dy) co-doped ZnO samples measured at Dy L₃-edge. (b) k^2 -weighted $\chi(k)$ function of (2% Mn, 2% Dy), (2% Mn, 4% Dy) & (2% Mn, 6% Dy) co-doped ZnO samples measured at the Dy L₃-edge. (c) Experimental $\chi(R)$ versus R data (scatter points) and best fit theoretical plots (solid line) of (2% Mn, 4% Dy) co-doped ZnO samples measured at Dy L₃-edge (fitting has been carried out by assuming Dy at Zn sites in wurtzite ZnO structure). (d) Experimental $\chi(R)$ versus R data (scatter points) and best fit theoretical plots (solid line) of (2% Mn, 2% Dy), (2% Mn, 4% Dy) & (2% Mn, 6% Dy) co-doped ZnO samples measured at Dy L₃-edge (fitting has been carried out by assuming Dy₂O₃ structure around Dy sites).

Table 7.8: Fit parameters for Dy L₃-edge data by assuming Dy₂O₃ structure at Dy site for (Mn, Dy) co-doped ZnO samples

		(2% Mn, 2% Dy)co-doped ZnO	(2% Mn, 4% Dy) co-doped ZnO	(2% Mn, 6% Dy) co-doped ZnO
Dy-O1	$N(4)$	4.92±0.24	4.92±0.34	4.72±0.018
	$R(\text{\AA})$	2.24±0.005	2.28±0.007	2.30±0.003
	σ^2	0.006±0.001	0.006±0.001	0.006±0.007
R_{Factor}		0.009	0.015	0.003

Fig.7.10(a) shows the experimental EXAFS ($\mu(E)$ versus E) spectra of (Mn, Dy) co-doped ZnO nanocrystals while figure 7.10(b) shows $\chi(k)$ versus k plots for the samples derived from the experimental EXAFS spectra. In this case also to fit the experimental Fourier transformed EXAFS data at the Dy L₃-edge two possibilities were examined viz., (a) Dy at Zn sites in tetrahedral ZnO structure and (b) Dy₂O₃ structure at the Dy sites. Fig.7.10(c) shows the Fourier transformed EXAFS or $\chi(R)$ versus R plots of (2%Mn, 4%Dy) co-doped ZnO nanocrystals at the Dy L₃-edge along with the best fit theoretical plots where the fitting has been carried out assuming wurtzite ZnO structure with Zn atoms replaced by Dy atoms according to doping concentration. The theoretical Fourier transformed EXAFS spectra have been generated assuming the wurtzite ZnO structure where Zn is replaced by Dy with the first oxygen shell (Dy-O) at 1.97Å with coordination number (CN) of 4. It has been observed that the fitting quality of the data with this theoretical model is poor and it yields unreasonable results of higher bond distance (2.31 Å) as compared to its theoretical value. Fig.7.10(d) shows the Fourier transformed EXAFS $\chi(R)$ versus R plots of (Dy,Mn) co-doped ZnO nanocrystals at the Dy L₃-edge along with the best fit theoretical plot

where the fitting has been carried out by assuming the 2nd option viz., Dy₂O₃ structure at the Dy sites and the best fit parameters have been shown in Table 7.8. Initially fitting has been carried out assuming the two nearest oxygen shells (Dy-O1) at 2.24Å with coordination number of 2 & (Dy-O2) at 2.35 Å with coordination number of 4 respectively. From the fitting results it has been found that for all the co-doped ZnO samples both oxygens shells are almost at the same distance of 2.25Å and 2.26Å from the central atom Dy. Hence during fitting we have combined the contributions of both oxygen shells at 2.24Å with coordination number of 6 and fitting has been carried out by assuming this single shell of oxygen. It can be seen from Fig. 7.10(d) and Table 7.8 that fitting with this structure has yielded better results with reasonable values of the fitting parameters.

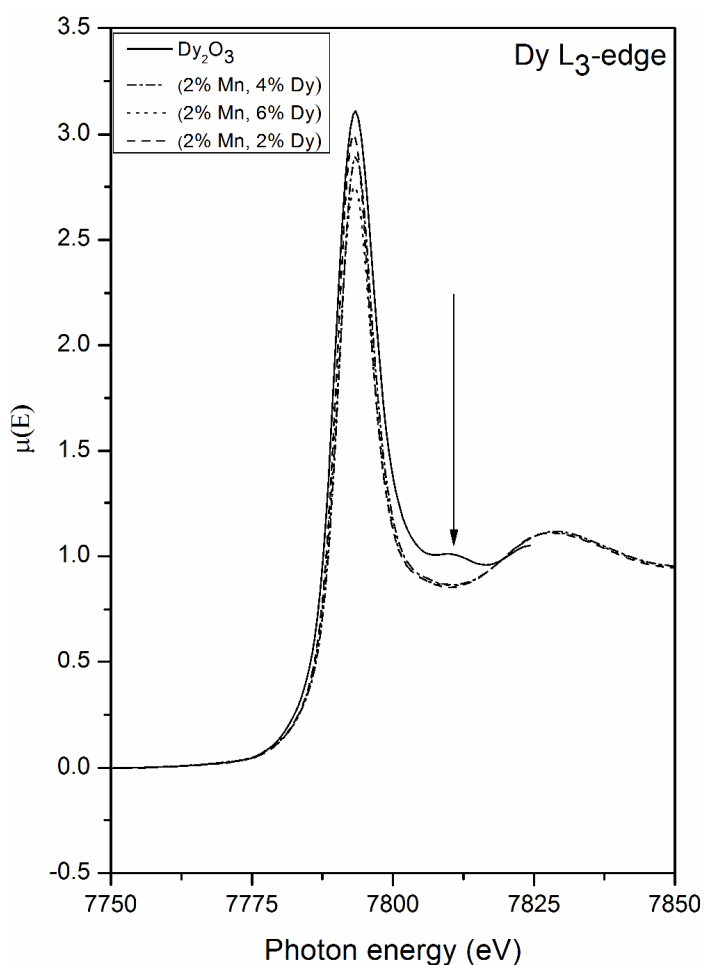


Figure 7.11: XANES plots for (Mn,Dy) co-doped ZnO samples at Dy L₃ edge alongwith that of standard Dy₂O₃ powder.

Fig. 7.11 shows the Dy L₃ edge XANES spectra of the (Mn,Dy) co-doped ZnO samples along with that of standard Dy₂O₃ commercial powder. It shows that the Dy L₃ absorption edge positions of the co-doped samples agree with that of Dy₂O₃ powder. However, the post edge features (like the peak at 7810 eV) of Dy₂O₃ is not exactly matching with that of the co-doped samples showing that though Dy goes as Dy⁺³ in the ZnO lattice, it is not present as a separate Dy₂O₃ phase manifesting successful doping Dy in the ZnO lattice.

However, it can be seen from Table 7.8 that significant oxygen vacancies are present near Dy sites since oxygen coordination is less than that expected which is corroborated by PL measurements also discussed above. Creation of oxygen vacancy at Dy sites takes place possibly to compensate for the charge neutrality at Zn⁺² sites occupied by Dy⁺³ ions. Thus the FM observed in the Dy doped samples can be attributed to the oxygen vacancy mediated exchange interaction between the Dy⁺³ ions or in other words due to the formation of bound magnetic polarons or BMP's. Thangeeswari et.al. have also attributed the FM observed in their (Co,Dy) co-doped nanoparticles to bound magnetic polarons [351]. Oxygen vacancies have been considered to be responsible for FM observed in several RE doped CeO₂ systems also [354]. Oxygen vacancy mediated FM has been observed by us in several other doped TM doped ZnO samples also viz., in Fe doped and Cr doped ZnO nanocrystals and Mn doped ZnO thin film samples [355-357].

Thus from the above study we can conclude that the FM observed in the Dy doped samples can be attributed to the oxygen vacancy mediated exchange interaction between the Dy⁺³ ions or in other words due to formation of bound magnetic polarons or BMP's. It has also been noted from the XANES measurements of the samples at Mn K-edge and Dy L₃

edge alongwith that of standard oxide samples that though Mn and Dy go into ZnO lattice as Mn^{+3} and Dy^{+3} , though no separate Mn_2O_3 or Dy_2O_3 phase exists in the samples.

Chapter- 8

GIXAFS measurement on thin film multilayer structures

8.1. Introduction:

Specular and diffused Grazing incidence X-ray reflectivity is widely used to determine the interfaces of multilayers, however these techniques mostly give information on electron density variation across the depth and not much on atomic level structure. X-ray photo electron spectroscopy, on the other hand can give useful information on the oxidation states of the species, however it has to be employed along with a destructive ion etching process to yield any depth dependent information. X-ray absorption spectroscopy (XAS), which comprises of two techniques viz., X-ray near edge structure (XANES) and Extended X-ray absorption fine structure (EXAFS), is an important technique to investigate element specific local structure in the system. Though it is not really a surface sensitive technique, however, by careful preparation of the samples and careful selection of the grazing angle of incidence, we can probe depth selective XAS in a multilayer structure, by exciting X-ray standing waves with definite positions of nodes and antinodes inside the multilayer [363]. The details of formalism of creation of standing waves in a multilayer structure has been discussed in Chapter-1. In this paper standing-wave effects are used to perform depth selective XAS measurements in a Ni/Ti multilayer structure which is an important magnetic material.

8.2 Experimental details:

Ni/Ti multilayers have been deposited by sputtering technique on c-Si substrates in an indigenously developed d.c. magnetron sputtering unit, where Ti is at the top surface. Thickness of each Ni/Ti bilayer is 120Å with approximately equal layer thickness, the design of the multilayer being carried out using the IMD software code discussed later. The basic principle of dc magnetron sputtering has been discussed in Chapter-2. Grazing incidence XAS (GIEXAFS) measurements of the present sample was carried out at the Energy Scanning EXAFS beamline (BL-9) at the Indus-2 Synchrotron Source (2.5 GeV, 100 mA), Raja Ramanna Centre for Advanced Technology (RRCAT), Indore, India. The procedure of measurement has been described in Chapter-2.

8.2.1 Sample preparation:

We have fabricated the Ni/Ti multilayers in the 9 m long indigenously developed in-line magnetron sputtering system described elsewhere [364]. This system is equipped with three magnetrons on which three sputtering targets, each having dimensions of 125 mm × 200 mm, are fixed. During the deposition process the substrate trolley is scanned below the targets with a stainless steel (SS) pulley rope mechanism, using a motor kept outside the vacuum system and the deposited film thickness is scaled with the inverse velocity of the trolley. During deposition, the online tracking of the exact position of the substrate trolley has been achieved by a laser beam reflection from the back of the trolley tray, the detail description of which has been given in our previous communication [364]. A highly accurate speed control ensured good reproducibility of the films. Just beside each target, one quartz crystal monitor is fixed in the shadow region for in-situ monitoring of the static rate of deposition. Prior to deposition, the system has been evacuated to a base pressure of $\sim 1 \times 10^{-6}$ mbar with the help of two turbo-molecular pumps. High-quality Ti (99.95%) and Ni targets

of specified dimensions are used for all of the depositions. All of the films have been deposited on 30 mm × 20 mm crystalline silicon (111) wafers. Initially single layer Ni and Ti films have been deposited and the thicknesses of the films have been measured by Grazing Incidence X-ray reflectivity (GIXR) technique for calibration of the quartz crystal monitor and using this calibration the multilayers of required thicknesses have finally been deposited with high accuracy of thickness.

8.3 Results and discussion:

To perform GIEXAFS measurement at different regions of multilayer structure, we have theoretically generated electric field distribution of X-ray standing wave inside a 10 bi-layer Ni (60Å)/Ti (60Å) multilayer structure (with Ti as the top most layer) with different grazing angle of incidence at energy of 8.353eV for Ni-K-edge. The theoretical simulation has been carried out using the IMD computer program [365]. IMD is a computer code that can calculate specular and non-specular reflectivity of single layer and multilayer structure of any number of layers and for any material, whose optical constants are known, using Parratt formalism. This program works under XOP (X-ray Oriented Programming) platform and it can also fit the experimentally measured X-ray reflectivity spectrum of a sample and estimate the optical parameters and sample structure. Under the Parratt's formalism the reflectivity of X-rays from a plane boundary between two media can be obtained using Fresnel's boundary conditions of continuity of the tangential components of the electric field vector and its derivative at the interface. Figs. 8.1(a), (b) & (c) represent the electric field profile of standing wave generated in Ni/Ti multilayer structure at energy of 8.353eV. Depending on the positions of node and antinodes in electric distribution pattern of standing wave, we have selected three angles to probe Ni atoms in Ti bulk (region:1), Ti on Ni interface (region:2)

and Ni bulk region (region:3) in the multilayer. The grazing angles of incidences chosen to probe the different parts of the Ni/Ti multilayer structure is given in Table-8.1.

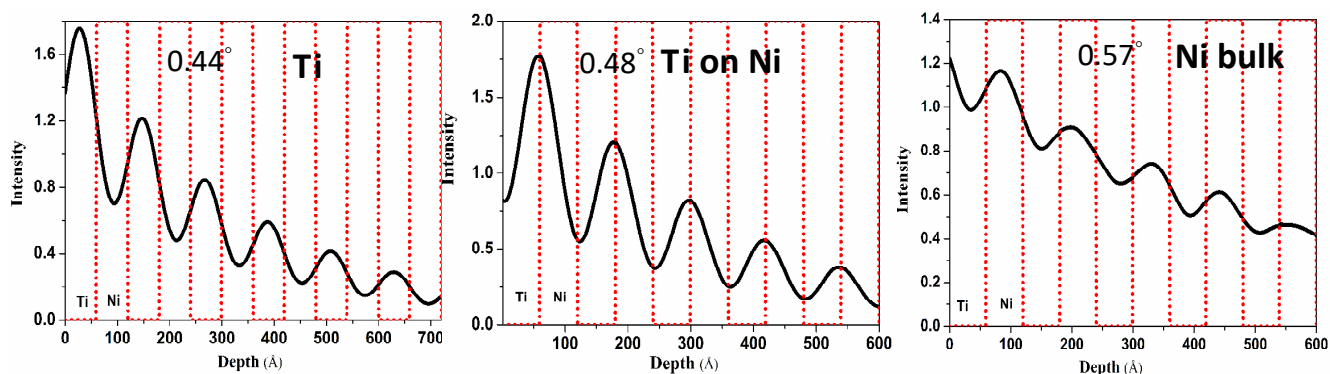


Figure 8.1: Variation of electric field intensity inside multilayer structure with grazing angle of incidences.

Table 8.1: Grazing angle of incidences used for probing different portions of the 10 bi-layer Ni (60Å)/Ti(60Å) multilayer.

Sample name	Grazing angle (degree)
Ti- Bulk	0.44°
Ti on Ni	0.48 °
Ni Bulk	0.57 °

Subsequently the multilayer has been deposited in the indigenously developed magnetron sputtering system described above. To probe various regions of multilayer we have recorded Grazing Incidence XAFS (GIXAFS) spectra of Ni/Ti multilayer samples at three different grazing angles of incidence which viz., 0.44°, 0.46° and 0.57° at Ni-Kedge, along with a standard Ni metal foil for comparison. During the measurement using the GIEXAFS set up of

the Energy Scanning EXAFS beamline (BL-09) at Indus-2 SRS, described in detail in Chapter-2, a reflectivity detector and a fluorescence detector have been used simultaneously in perpendicular geometry to ascertain the correct grazing angle of incidence of the SR beam on the sample and to measure the XAFS signal respectively. It should be noted that the XAFS measurement on Ni foil has been done in a conventional way in transmission mode. It is clear from XANES spectra, shown in fig. 8.2(a), that the absorption edge of Ni in Ni/Ti ML sample coincide with that of Ni metal foil in each cases manifesting that in all the three regions Ni is in metallic state, ruling out any other compound formation particularly at the interfaces.

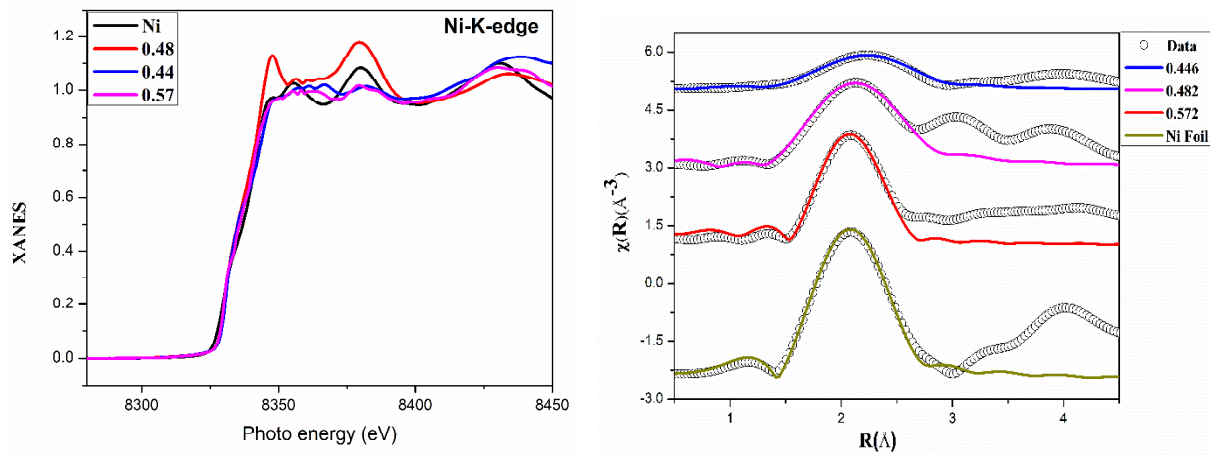


Figure 8.2. (a) Normalised XANES spectra of Ni-Ti multilayer at 0.44, 0.48 and 0.57° grazing angles of incidence along with that of pure Ni foil measured at Ni K edge. **(b)** Fourier transformed GIEXAFS spectra (scatter points) of Ni/Ti multilayer at the three different grazing angles of incidence along with the Ni-foil at Ni-k-edge and corresponding theoretical fits (solid lines).

Fig. 8.2(b) shows the $\chi(R)$ versus R plots for Ni/Ti multilayer at three different angles of incidence at Ni-K-edge, along with best fit theoretical curves. The above figure shows the appearance of a major peak around 2\AA in the phase uncorrected radial structure function of Ni/Ti multilayer sample in all three cases. Position of this peak is matching exactly with the

major peak present in bulk Ni foil which corresponds to the 1st coordination shell of Ni atoms surrounding the absorbing atom. It is clear from the spectra that amplitude of the 1st major peak increases as we increase the angle of incidence. Taking into consideration the XANES results, all three EXAFS data of Ni/Ti multilayer sample were fitted by metallic Ni (face-centered cubic (fcc)) structure. It should be mentioned here that a set of EXAFS data analysis program available within the IFEFFIT software package [217] have been used for reduction and fitting of the experimental EXAFS data, as discussed in details in earlier Chapters. The Ni-Ni distance (R), coordination number of the 1st coordination shell (CN) and the disorder parameter σ^2 have been used as fitting parameters in the above exercise and the best fit results are given in Table-8.2. Since σ^2 and CN are correlated with each other, thus to have better idea about the variation in CN, value of σ^2 is kept constant during the fitting. It should be noted here that the value of σ^2 has been taken from the reference Ni metal foil.

Table 8.2: Best fit parameters obtained by fitting the FT- EXAFS

		Ni Foil	Ni/Ti_0.57	Ni/Ti_0.48	Ni/Ti_0.44
Ni-Ni	CN(12)	11.72±0.36	7.44±0.72	7.08±0.19	3.36±0.33
	$\Delta R(2.4)$	2.45±0.01	2.44±0.01	2.45±0.11	2.53±0.02
	σ^2	0.007±0.001	0.007±0.001	0.007±0.001	0.007±0.001
<i>R-Factor</i>		0.003	0.013	0.012	0.012

It can be seen from the Table-8.2 that Ni-Ni coordination is very less compared to bulk Ni in case of the measurement at the lowest grazing angle of incidence of 0.44°, where we are probing Ni atoms inside the top surface of Ti. This is possibly due to the fact the full coordination shell of fcc Ni structure is not getting formed in this case since very few Ni atoms are able to diffuse inside the bulk of the Ti layers. However as we are increasing the grazing angle of incidence and moving towards Ni bulk, Ni CN approaches that of bulk Ni,

though inside the bulk Ni layer also it is low compared to the bulk value possibly due to very small grain sizes of these amorphous-like layers.

Thus three regions, viz., Ni bulk layer, in the Ti-on-Ni interface and Ti bulk of a 10 bi-layer Ni/Ti magnetic multilayer structure have been probed by Grazing incidence X-ray absorption spectroscopy measurement in a newly developed set-up at the Energy Scanning EXAFS beamline at Indus-2 SRS. By comparing the XANES results of the sample at the three grazing angles of incidence with that of a standard Ni metal foil, the metallic character of Ni atoms in all the three regions could be established. While the EXAFS measurements have shown the depth dependent variation of local environment of Ni inside the multilayer. Thus it has been demonstrated that depth dependent XAS studies of thin films and multilayers can be carried out successfully in the above set up.

Chapter 9

Summary & Conclusion

The brief summery and conclusion for the individual chapters are given below.

Fe and Cr doped ZnO:

In Chapter 3 we have presented the results of the studies on sol–gel derived Fe- and Cr doped ZnO diluted magnetic semiconductors (DMSs) nanoparticles. The X-ray diffraction data with Rietveld refinement, HRTEM, and micro-Raman analysis show that Fe-doped ZnO nanoparticles have wurtzite structure as that of pure ZnO. Furthermore, these results indicate that Fe-ions have entered in Zn-sites by substituting the Zn ions. Crystallite structure, morphology, and size of the nanocrystals have been estimated by XRD and HRTEM. The estimated size of the crystallites decreases exponentially with the increase of Fe concentration which is due to the difference of the ionic radii between Zn and Fe atoms. The EXAFS results show that the reduction in oxygen coordination has taken place which manifests generation of oxygen vacancies in the samples due to Fe doping. The oxygen coordination remains lower and DW factor remains higher compared to their respective values in undoped ZnO suggests that doping takes place properly throughout the whole composition range. The DW factor for the next near Zn shell shows that Fe-doping affects the O site more than the Zn/Fe site. The substitution of Zn ions by Fe ions does not cause any significant change in the host lattice as manifested in the values of the bond distances. XANES study clearly rules out the presence of metallic Fe clusters, FeO and Fe₂O₃ phases in the samples. However, it indicates that Fe gets incorporated in the ZnO lattice as Fe³⁺ causing creation of oxygen vacancies. These observations corroborate to those of EXAFS study.

Raman spectroscopy study reveals that the local symmetry in the Fe-doped nanocrystals gradually differ from that of undoped sample, but the crystal structure remains the same as that of the wurtzite structure of pure ZnO; which further supports the incorporation of Fe-ions in the ZnO lattice. Room temperature (weak) ferromagnetism (RTFM) is observed from M–H measurements and magnetization increases with increasing Fe-concentration. The joint effects of the intrinsic exchange interactions arising from oxygen vacancy assisted bound magnetic polarons (BMPs) and the extrinsic grain boundary are responsible for the room temperature FM in this system.

For Cr doped ZnO NCs XRD and HRTEM results show that estimated size of the crystallites decreases linearly with the increase of Cr doping concentration while there is an increase in tensile strain in the ZnO lattice due to Cr incorporation. The above results clearly indicate that Cr-ions have substituted Zn ions in the ZnO lattice of the nanocrystals. EXAFS results show that there is a reduction in oxygen coordination and increase in oxygen vacancies with increase in Cr doping concentration in the samples, however the substitution of Zn ions by Cr ions of almost similar size does not cause any significant change in the host lattice as manifested in the values of the bond distances. XANES study clearly rules out the presence of metallic Cr clusters in the samples. These observations corroborate to those of XRD study. Raman spectroscopy measurement reveals that the local symmetry in the Cr doped nanocrystals is different from that of undoped sample, though the crystal structure remains the same as that of the wurtzite structure of pure ZnO, which further supports the incorporation of Cr-ions in the ZnO lattice. Wurtzite structure has been confirmed by FTIR analysis which also indicates the increase in octahedral coordination around Cr site with increase in Cr doping concentration in the samples and thus corroborates the results obtained from pre-edge structures of XANES measurements at Cr K-edge.

UV-Vis measurements show blue shift (increase) in the optical band gap occurs up to $x = 0.02$ (viz. $\text{Zn}_{0.98}\text{Cr}_{0.02}\text{O}$) after that for higher Cr-doping ($x > 0.02$) the band gap decreases with increasing Cr concentration. This increase (blue shift) of the band gap can be interpreted mainly with the 4s–3d and 2p–3d exchange interactions and the Moss–Burstein effect while the decrease (red shift) of the band gap can be interpreted to be due to the sp–d exchange interactions between the band electrons of ZnO and the localized d electrons of the Cr-ions. The room temperature PL measurements illustrate NBE emission and violet, violet-blue, blue, blue-green, and green emissions are in visible region. The UV emission (NBE) peak originates from the radiative recombination of carriers bound within excitons while the other emissions may be attributed to the Zn-vacancies, interstitial Zn levels, radiative defects related to traps existing at grain boundaries, defects related to positively charged Zn vacancies, surface defects and singly ionized oxygen vacancies (V_o) respectively. It has also been observed that increasing Cr doping increases the density of singly ionized oxygen vacancies (V_o) enhancing the green emission. Thus in summary XRD, HRTEM and Raman measurements show clear signature of changes in ZnO lattice upon Cr doping though the overall wurtzite structure remains unaffected. XANES measurements show that Cr is present in the samples in Cr^{3+} oxidation state while pre-edge peaks in XANES spectra and FTIR results show that local structure around Cr is increasingly becoming octahedral with increase in Cr doping concentration. EXAFS and PL measurements show that Cr incorporation in ZnO lattice is accompanied by creation of more and more oxygen vacancies.

(Co, Cu) co-doped ZnO NCs :

In Chapter-4 Pure, Co doped and (2.5%Co, 2.5%Cu) co-doped ZnO nanocrystals have been prepared by wet chemical route at room temperature to study the possible enhancement

in magnetization of Co doped ZnO system due to an increase in carrier concentration by Cu doping. X-ray diffraction analysis reveals the characteristic hexagonal wurtzite structure of ZnO NCs with no secondary phase appearing for Co doped and (Co,Cu) co-doped ZnO NCs. TEM measurements have also corroborated with XRD results. FTIR results also indicate that Co and Cu dopants are occupying the Zn positions in the ZnO matrix as there is no peak found in the spectra that corresponds to Co and Cu. Raman spectroscopy measurements however shows that in the co-doped samples the major optical phonon mode of ZnO shift to lower frequencies and there is a decrease in intensity and broadening of peaks manifesting distortion of long-range order of ZnO nanocrystals to some extent by doping. The peaks due to dopant atoms with defects become significant in doped samples and it increases significantly for the (2.5% Co, 2.5% Cu) co-doped sample. Optical absorption spectra show that the excitonic feature for undoped ZnO NCs is clearly blue-shifted compared to bulk ZnO. The Co doped and (Co,Cu) co-doped ZnO NCs show sub-forbidden gap features characteristics of ligand field d-d transitions of Co^{2+} in tetrahedral environment. EPR results also suggest that Co^{2+} and Cu^{2+} ions are in a tetrahedral coordination in the ZnO matrix with no secondary or impurity phase observed in (Co,Cu) co-doped ZnO NCs. DFT based electronic structure calculations show that if we consider a strong on-site Coulomb interaction among the electrons of Co atom, a ZnO supercell substituted with co-doped with one Co and one Cu atoms can be energetically more favorable than two Co atoms substituted in the ZnO supercell. However, magnetic measurements reveal that (2.5% Co, 2.5% Cu) co-doped sample shows weak FM behavior and its magnetisation is less than that of the Co doped sample. Further investigations by EXAFS measurements at Co and Cu K edges reveal that while Co goes into the tetrahedral lattice of ZnO, local environment of Cu resembles that of cubic CuO than tetrahedral ZnO. The presence of CuO phase is detrimental

to the magnetic properties of the sample which causes the reduction in the magnetization of the (Co,Cu) co-doped sample compared to the Co doped sample. Thus the above study clearly shows that though characterization by XRD, FTIR, Raman and EPR measurements do not manifest the presence of a secondary oxide phase in the sample other than wurtzite ZnO with Zn atoms substituted by Cu and Co, EXAFS study clearly establishes that Cu is present as CuO in the samples which is detrimental to its magnetic properties and hence Cu doping in the ZnO samples in addition to Co doping reduces its magnetization.

(Fe, Cu) co-doped ZnO NCs:

Undoped, Fe doped and (Fe,Cu) co-doped ZnO nanocrystals have been prepared by wet chemical route at room temperature to study the possible enhancement in magnetization of Fe doped ZnO system due to an increase in carrier concentration by Cu co-doping, which have been described in Chapter-5. TXRF measurements show satisfactory inclusion of the dopant ions in the ZnO matrix, while XRD measurement reveals the characteristic hexagonal wurtzite structure of ZnO NCs with no secondary phase appearing for Fe doped and (Fe,Cu) co-doped ZnO NCs. TEM measurements have also corroborated the XRD results and reveal 6–7 nm sizes of the nanocrystals. XANES measurements show the presence of Cu in the samples in Cu^{+2} and Fe in Fe^{+3} oxidation states. EXAFS measurements show that the peaks in the Cu K-edge Fourier transformed EXAFS spectra match with that of Zn K-edge Fourier transformed EXAFS spectra of the samples and do not match with that of any other oxide phases of copper. The above results manifest that Cu atoms in the (Fe,Cu) co-doped ZnO samples go to Zn sites at ZnO lattice and do not form any other metallic or oxide phase. However, magnetic measurements reveal that 5% Fe-doped sample shows weak ferromagnetic (FM) behavior and its magnetization reduces upon 2% additional Cu doping. DFT based electronic structure calculations show that upon Cu doping in addition to Fe

doping, ZnO systems with ferromagnetic (FM) and anti-ferromagnetic (AFM) interactions become energetically comparable compared to the only Fe doped system which is more stable in FM configuration. Thus we can conclude that the decrease in magnetic susceptibility of Fe doped ZnO nanocrystals upon Cu co-doping may be due to the enhancement of AFM interaction among the TM ions in the co-doped samples.

(Ni, Cu) co-doped ZnO NCs:

In Chapter-6 we have discussed the results of several complementary characterizations carried out on (Ni, Cu) co-doped ZnO nanocrystals prepared through wet chemical route. and have been subjected to. XRD measurements show that though phase purity of the ZnO samples is retained by Ni doping at 2%, Cu doping beyond 3% creates a separate CuO phase in the samples. It has also been observed that (Ni,Cu) co-doping does not introduce much deformation in the lattice though there is a shift in lower d values due to Cu inclusion followed by a decrease in crystallite size. EXAFS measurements at Zn K-edge also supports that the ZnO lattice is not too much deformed due to inclusion of Cu and Ni. Ni Kedge XANES measurements confirm that Ni is present in the ZnO lattice is Ni^{+2} oxidation state and it does not form any separate NiO phase. Cu K-edge XANES measurements however show that there is a shift in the XANES pattern from substitutional Cu phase to a separate CuO phase as Cu doping concentration is increased from 1% to 5%. This manifests in the decrease in magnetization in the samples due to increase in Cu doping upto 3% as have been observed from magnetic hysteresis measurements. Magnetic susceptibility measurement as a function of temperature also indicates an enhancement of AFM interaction in the samples with increase in Cu doping concentration upto 3%, possibly due to appearance of the CuO phase. However, it has been observed that magnetization in the sample again increases as the

Cu doping concentration increases upto 5%. Theoretical electronic structure calculations however predict that FM phase in phase pure (Ni, Cu) co-doped ZnO sample is equally probable as in Ni doped ZnO sample and also that the magnetic moment of the system increases with increase in Cu doping concentration at a fixed Ni doping concentration. Thus magnetization of (Ni,Cu) co-doped ZnO system is found to be governed by two competing processes viz., decrease in magnetization due to presence of CuO phase and increase in magnetization due to interaction between the TM ions mediated by Cu doping induced free charge carriers.

(Mn, Dy) Co-doped ZnO NCs:

Sol gel derived (Mn, Dy) doped ZnO nanocrystals with Mn concentrations of 0 and 2% and Dy-concentrations of 0.5%, 1%, 2%, 4% and 6% have been subjected to various complementary characterisation techniques which have been discussed in Chapter-7. XRD measurements show that incorporation of Dy in Mn doped ZnO does not change the structure of wurtzite ZnO though there is slight expansion of ZnO lattice to accommodate relatively larger Dy^{3+} (0.91Å) ions which is also confirmed by HRTEM measurement. TEM measurements show (100) oriented wurtzite structure and 22 nm and 12 nm sizes respectively for the undoped and co-doped nanocrystals. FTIR study also corroborates the above results that upon rare earth doping ZnO lattice is not distorted significantly. PL measurements however indicate creation of oxygen vacancies on Dy doping. Magnetic measurement shows that as doping concentration of Dy is increased, magnetic behaviour changes from weak ferromagnetic/super paramagnetic to ferromagnetic nature. EXAFS data analysis at Zn K-edge shows that the results are similar for both Mn doped and (Mn,Dy) co-doped samples corroborating the above results that Dy doping has not caused any additional changes around Zn sites. However, EXAFS results at Mn K-edge on the Mn doped and (Mn, Dy) co-doped

samples show two striking dissimilarities, viz., in case of co-doped samples, the second shell Mn–Mn peak is significantly reduced due to the disorder introduced by doping of Dy atoms and in only Mn doped samples Mn is going to the ZnO lattice is Mn^{2+} oxidation state while in case of (Mn, Dy) co-doped samples, Mn is going into the lattice in Mn^{3+} oxidation state. Dy L3-edge results also show that Dy is going to the ZnO lattice as Dy^{3+} and significant oxygen vacancies are created near Dy sites to compensate for the charge neutrality at Zn^{2+} sites, a result also corroborated by PL measurements. Thus, the FM observed in the Dy doped samples can be attributed to the oxygen vacancy mediated exchange interaction between the Dy^{3+} ions or in other words due to formation of bound magnetic polarons or BMP's. It has also been noted from the XANES measurements of the samples at Mn K-edge and Dy L3 edge along with that of standard oxide samples that though Mn and Dy go into ZnO lattice as Mn^{3+} and Dy^{3+} , no separate Mn_2O_3 or Dy_2O_3 phase exists in the samples.

GIEXAFS study of thin film and multilayers:

In Chapter-8, we have described the setting up of facility for grazing incidence XAFS (GIXAFS) measurements at the Energy Scanning EXAFS beamline (BL-09) at Indus-2 SRS using simultaneous measurements of X-ray reflectivity and XAFS using two detectors. To test the above set-up a good quality 10 bi-layer Ni (60Å)/Ti (60Å) multilayer was deposited by magnetron sputtering technique in an indigenously developed d.c. sputtering system with Ti layer on top. By studying the variation of nodes and antinodes in the electric field distribution pattern of standing wave generated inside the multilayer theoretically we have found three different grazing angles of incidence to probe Ni atoms in three regions of the sample, viz., Ni bulk layer, in the Ti-on-Ni interface and Ti bulk. The grazing incidence XAS (XANES and EXAFS) measurements of the sample at the above three grazing angles of incidence has been carried out at the Energy Scanning EXAFS beamline at Indus-2 SRS. By

comparing the XANES results of the sample at the three grazing angles of incidence with that of a standard Ni metal foil, the metallic character of Ni atoms in all the three regions could be established. EXAFS measurements show that Ni-Ni coordination is very less compared to bulk Ni in case of the measurement at the lowest grazing angle of incidence of 0.44° , where we are probing Ni atoms inside the top surface of Ti. However, as we are increasing the grazing angle of incidence and moving towards Ni bulk, Ni CN approaches that of bulk Ni, though inside the bulk Ni layer also it is low compared to the bulk value possibly due to very small grain sizes of these amorphous-like layers.

Thus, from the above study it has been demonstrated that depth dependent XAS studies of thin films and multilayers can be carried out successfully in the above set up.

Reference:

1. R. P. Feynman, *Found. Phys.* **16**, 507 (1986).
2. S. Datta and B. Das, *Appl. Phys. Lett.* **56**, 665 (1990).
3. G. A. Prinz, *Science*. **282**, 1660 (1998).
4. H. Ohno, N. Akiba, F. Matsukura, A. Shen, K. Ohtani, and Y. Ohno, *Appl. Phys. Lett.* **73**, 363 (1998).
5. M. Oestreich, *Nature (London)*. **402**, 735 (1999).
6. Y. Ohno, D. K. Young, B. Beschoten, F. Matsukura, H. Ohno, and D. D. Awschalom, *Nature*. **402**, 790 (1999).
7. S. A. Wolf, D. D. Awschalom, R. A. Buhrman, J. Daughton, S. von Molnar, M. L. Roukes, A. Y. Chtchelkanova and D. M. Treger, *Science*. **294**, 1488 (2001).
8. S. D. Sarma, *Am. Sci.* **89**, 516 (2001).
9. B. T. Jonker, A. T. Hanbicki, Y. D. Park, G. Itskos, M. Furis, G. Kioseoglou, and A. Petrou, *Appl. Phys. Lett.* **79**, 3098 (2001).
10. M. N. Baibich, J. M. Broto, A. Fert, F. N. Van Dau, F. Petroff, P. Etienne, G. Creuzet, A. Friederich and J. Chazelas, *Phys. Rev. Lett.* **61**, 2472 (1988).
11. G. Binasch, P. Grünberg, F. Saurenbach and W. Zinn, *Physical Review B*, 1989, **39**, 4828-4830.
12. C. Chappert, A. Fert and F. N. van Dau, “The emergence of spin electronics in datastorage”, *Nature Mat.* **6**, 813-823, (2007) and references therein.
13. T. Bland, K. Lee and S. Steinmuller, “The spintronics challenge”, *Physics World*. 2124, 28 (2008) and references therein.
14. D. D. Awschalom and M. E. Flatté, “Challenges for semiconductor spintronics”, *Nature Phys.* **3**, 153 (2007).
15. S. A. Wolf, D. D. Awschalom, R. A. Buhrman, J. M. Daughton, S. von Molnár, M. L. Roukes, A. Y. Chtchelkanova and D. M. Treger, “Spintronics: a spin-based electronics vision for the future”, *Science*. 294, 1488-1495 (2001).
16. S. J. Peaton, C. R. Abernathy, D. P. Norton, A. F. Hebard, Y. D. Park, L. A. Boatner, and J. D. Budai, “*Materials Science and Engineering R*”, **40**, 137 (2003).
17. H. Munekata, H. Ohno, S. von Molnar, A. Segmuller, L. L. Chang, and L. Esaki, *Phys. Rev. Lett.* **63**, 1849 (1989).
18. H. Ohno, A. Shen, F. Matsukura, A. Oiwa, A. Endo, S. Katsumoto, and Y. Iye, *Appl. Phys. Lett.* **69**, 363 (1996).
19. A. V. Esch, L. V. Bockstal, J. de Boeck, G. Verbanck, A. S. van Steenbergen, R. J. Wellman, G. Grietens, R. Bogaerts, F. Herlach, and G. Borghs, *Phys. Rev. B*. **56**, 13103, (1997).
20. T. Hayashi, M. Tanaka, K. Seto, T. Nishinaga, and K. Ando, *Appl. Phys. Lett.* **71**, 1825 (1997).
21. T. Hayashi, M. Tanaka, T. Nishinaga, and H. Shimada, *J. Appl. Phys.* **81**, 4865 (1997).
22. T. Hayashi, M. Tanaka, T. Nishinaga, H. Shimoda, H. Tsuchiya, and Y. Otsuka, *J. Cryst. Growth*. **175**, 1063 (1997).
23. Y. Satoh, N. Inoue, Y. Nishikawa, and J. Yoshino, “Proceedings of the third symposium on physics and applications of spin-related phenomena in semiconductors,” 23, 1997.
24. K. Ando, T. Hayashi, M. Tanaka, and A. Twardowski, *J. Appl. Phys.* **83**, 65481 (1998).
25. F. Matsukura, H. Ohno, A. Shen, and Y. Sugawara, *Phys. Rev. B*. **57**, 2037 (1998).

26. R. Shioda, K. Ando, T. Hayashi, and M. Tanaka, *Phys. Rev. B.* **58**, 1100 (1998).
27. M. Tanaka, *J. Vac. Sci. Technol. B.* **16**, 2267 (1998).
28. B. Beschoten, P. A. Crowell, I. Malajovich, D. D. Awschalom, F. Matsukura, A. Shen, and H. Ohno, *Phys. Rev. Lett.* **83**, 3073 (1999).
29. H. Ohno, F. Matsukura, T. Owiya, and N. Akiba, *J. Appl. Phys.* **85**, 4277 (1999).
30. H. Shimizu, T. Hayashi, T. Nishinaga, and M. Tanaka, *Appl. Phys. Lett.* **74**, 398, (1999).
31. A. Shen, F. Matsukura, S. P. Guo, Y. Sugawara, H. Ohno, M. Tani, A. Abe, and H. C.Liu *J. Cryst. Growth.* **201202**, 379 (1999).
32. A. Twardowski *Mater. Sci. Eng. B.* **63**, 96 (1999).
33. B. Grandidier, J. P. Hys, C. Delerue, D. Stievenard, Y. Higo, and M. Tanaka *Appl. Phys. Lett.* **77**, 4001 (2000).
34. R. K. Kawakami, E. Johnson-Halperin, L. F. Chen, M. Hanson, N. Guebels, J. S. Speck, A. C. Gossard, and D. D. Awschalom, *Appl. Phys. Lett.* **77**, 2379 (2000).
35. D. Chiba, N. Akiba, F. Matsukura, Y. Ohno, and H. Ohno, *Appl. Phys. Lett.* **77**, 1873 (2000).
36. T. Hayashi, M. Tanaka, and A. Asamitsu, *J. Appl. Phys.* **87**, 4673 (2000).
37. N. Akiba, D. Chiba, K. Natata, F. Matsukura, Y. Ohno, and H. Ohno, *J. Appl. Phys.* **87**, 6436 (2000).
38. Y. Nagai, T. Kurimoto, K. Nagasaka, H. Nojiri, M. Motokawa, F. Matsukura, T. Dietl, and H. Ohno, *Jpn. J. Appl. Phys.* **40**, 6231 (2001).
39. J. Sadowski, R. Mathieu, P. Svedlindh, J. Z. Domagala, J. Bak-Misiuk, J. Swiatek, M. Karlsteen, J. Kanski, L. Ilver, H. Asklund, and V. Sodervall, *Appl. Phys. Lett.* **78**, 3271 (2001).
40. S. J. Potashnik, K. C. Ku, S. H. Chun, J. J. Berry, N. Samarth, and P. Schiffer, *Appl. Phys. Lett.* **79**, 1495 (2001).
41. G. M. Schott, W. Faschinger, and L. W. Molenkamp, *Appl. Phys. Lett.* **79**, 1807 (2001).
42. H. Ohno, H. Munekata, T. Penney, S. von Molnar, and L. L. Chang, *Phys. Rev. Lett.* **68**, 2864 (1992).
43. H. Munekata, A. Zaslevsky, P. Fumagalli, and R. J. Gambino, *Appl. Phys. Lett.* **63**, 2929 (1993).
44. Y. L. Soo, S. W. Huang, Z. H. Ming, Y. H. Kao, and H. Munekata, *Phys. Rev. B.* **53**, 4905 (1996).
45. Y. Nishikawa, A. Tackeuchi, M. Yamaguchi, S. Muto, and O. Wada, *IEEE J. Sel. Top. Quant. Electron.* **2**, 661 (1996).
46. S. Koshihara, A. Oiwa, M. Hirasawa, S. Katsumoto, Y. Iye, C. Urano, H. Takagi, and H. Munekata, *Phys. Rev. Lett.* **78**, 4617 (1997).
47. K. J. Akai, *Phys. Rev. Lett.* **81**, 3002 (1998).
48. A. Oiwa, T. Slupinski, and H. Munekata, *Appl. Phys. Lett.* **78**, 518 (2001).
49. H. Ohno, *Science*. **281**, 951 (1998).
50. H. Ohno, *J. Magn. Magn. Mater.* **200**, 110 (1999).
51. H. Ohno, *J. Vac. Sci. Technol. B.* **18**, 2039 (2000).
52. H. Ohno, F. Matsukura, and Y. Ohno, *Jap. Soc. Appl. Phys. Int.* **5**, 4 (2002).
53. T. Dietl, H. Ohno, F. Matsukura, J. Cibert, and D. Ferrand, *Science*, **287**, 1019 (2000).
54. K. Sato and H. Katayama-Yoshida, *Jpn. J. Appl. Phys.* **39**, L555 (2000).
55. K. Sato and H. Katayama-Yoshida, *Jpn. J. Appl. Phys.* **40**, L334 (2001).
56. K. Ueda, H. Tabada, and T. Kawai, *Appl. Phys. Lett.* **79**, 988 (2001).

57. S. J. Pearton, C. R. Abernathy, D. P. Norton, A. F. Hebart, Y. D. Park, L. A. Boatner, and J. D. Budai, *Mater. Sci. and Engineering*, **R 40**, 137 (2003).
58. W. Prellier, A. Fouchet, and B. Mercey, *J. Phys.: Condens. Matter*, **15**, R1583 (2003).
59. A. C. Tuan, J. D. Bryan, A. B. Pakhomov, V. Shutthanandan, S. Thevuthasan, D. E. McCready, D. Gaspar, M. H. Engelhard, J. W. Rogers, K. Krishnan, D. R. Gamelin, and S. A. Chambers, *Phys. Rev. B*, **70**, 054424 (2004).
60. S. J. Pearton, W. H. Heo, M. Ivill, D. P. Norton, and T. Steiner, *Semicond. Sci. Technol.*, **19**, R59, (2004).
61. S. J. Pearton, D. P. Norton, K. Ip, Y. W. Heo, and T. Steiner, *J. Vac. Sci. Technol. B*, **22**, 932 (2004).
62. C. Liu, F. Yun, and H. Morkoc, *J. Mater. Sci.: Mater. in Electronics*, **16**, 555 (2005).
63. R. Janisch, P. Gopal, and N. A. Spaldin, *J. Phys.: Condens. Matter*, **17**, R657 (2005).
64. J. J. Liu, M. H. Yu, and W. L. Zhou, *J. Appl. Phys.*, **99**, 08M119 (2006).
65. W. Pacuski, D. Ferrand, J. Cibert, C. Deparis, J. A. Gaj, P. Kossacki, and C. Morhain, *Phys. Rev. B*, **73**, 035214 (2006).
66. J. Zhang, X. Z. Li, Y. F. Lu, and D. J. Sellmyer, *J. Phys.: Condens. Matter*, **19**, 036210 (2007).
67. N. Akdogan, A. Nefedov, H. W. Becker, C. Somsen, R. I. Khaibullin, L. R. Tagirov, and H. Zabel *Submitted*.
68. J. M. Wesselinowa and A. T. Aposto, *J. Appl. Phys.*, **107**, 5 (2010).
69. P. K. Sharma, R. K. Dutta, A. C. Pandey, S. Layek and H. C. Verma, *J. Magn. Magn. Mater.*, **32**, 2587 (2009).
70. B. Martinez, F. Sandiumenge, L. Balcells, J. Arbiol, F. Sibiude and C. Monty, *Phys. Rev. B*, **72**, 16 (2005).
71. Z. X. Cheng, X. L. Wang, S. X. Dou, K. Otawa, H. Kimura and P. Munroe, *J. Phys. D: Appl. Phys.*, **40**, 21 (2007).
72. J. B. Wang, G. J. Huang, X. L. Zhong, L. Z. Sun, Y. C. Zhou and E. H. Liu, *Appl. Phys. Lett.*, **88**, 252502 (2006).
73. H. L. Liu, J. H. Yang, Y. J. Zhang, Y. X. Wang, M. B. Wei, D. D. Wang, L. Y. Zhao, J. H. Lang and M. Gao, *J. Mater. Sci.: Mater. Electron*, **20**, 2009, 628–631.
74. S. Khatoon, I. A. Wani, J. Ahmed, T. Magdaleno, Omar A. Al-Hartomy and T. Ahmad, *Mater. Chem. Phys.*, **138**, 519 (2013).
75. T. Ahmad, S. Khatoon, K. Coolahan and Bull. *Mater. Sci.*, **36**, 997 (2013).
76. S. Khatoon and T. Ahmad, *J. Mater. Sci. Engg. B*, **2(6)**, 325 (2012).
77. Y. Matsumoto, M. Murakami, T. Shono, T. Hasegawa, T. Fukumura, M. Kawasaki, P. Ahmet, T. Chikyow, S.-y. Koshihara and H. Koinuma, *Science*, **291**, 854 (2001).
78. T. Dietl, H. Ohno and F. Matsukura, *Physical Review B*, **63**, 195205 (2001).
79. T. Fukumura, Z. Jin, A. Ohtomo, H. Koinuma and M. Kawasaki, *Applied Physics Letters*, **75**, 3366 (1999).
80. J. A. Wibowo, N. F. Djaja and R. Saleh, *Adv. Mater. Phys. Chem.*, **3**, 48 (2013).
81. X. F. Liu and R. H. Yu, *J. Appl. Phys.*, **102**, 8 (2007).
82. L. Petit, T. C. Schulthess, A. Svane, Z. Szotek, W. M. Temmemman, A. Janotti, *Phys. Rev. B*, **73**, 045107, (2006).

83. G. Q. Pei, C. T. Xia, B. Wu, T. Wang, L. L. Zhang, Y. J. Dong and J. Xu, *Comput. Mater. Sci.* **43**, 489, (2008).
84. X. C. Liu, E. W. Shi, Z. Z. Chen, H. W. Zhang, B. Xiao and L. X. Song, *Appl. Phys. Lett.* **88**, 252503 (2006).
85. Hua-Wei Zhang, Zhi-Ren Wei, Zhi-Qiang Li and Guo-Yi Dong, *Mater. Lett.* **61**, 3605 (2007).
86. S. J. Han, J. W. Song, C. H. Yang, S. H. Park, J. H. Park and Y. H. Jeong, *Appl. Phys. Lett.* **81**, 4212 (2002).
87. J. Shim, T. Hwang, J. Park, S. J. Han and Y. Jeong, *Appl. Phys. Lett.* **86**, 8 (2005).
88. M. H. N. Assadi, Y. B. Zhang, P. Photongkam and S. Lib, *J. Appl. Phys.* **109**, 013909 (2011).
89. H. Huang, Y. Ou, S. Xu, G. Fang, M. Li and X. Z. Zhao, *Appl. Surf. Sci.* **254**, 2013 (2008).
90. S. Ji, L. Yin, G. Liu, Y. Zhang and C. Ye, *J. Phys. Chem. C* **113**, 16439 (2009).
91. G. S. Wu, Y. L. Zhuang, Z. Q. Lin, X. Y. Yuan, T. Xie and L. D. Zhang, *Phys. E* **31**, 5 (2006).
92. M. Subramanian, P. Thakur, M. Tanemura, T. Hihara, V. Ganesan, T. Soga, K. H. Chae, R. Jayavel and T. Jimbo, *J. Appl. Phys.* **108**, 053904 (2010).
93. G. Vijayaprasath, R. Murugan, Y. Hayakawa and G. Ravi, *J. Lumin.* **178**, 375 (2016).
94. T. Thangeeswari, P. Murugasen and J. Velmurugan, *J. Supercond. Novel Magn.* **28**, 2505 (2015).
95. S. Dhar, O. Brandt, M. Ramsteiner, V. F. Sapega and K. H. Ploog, *Phys. Rev. Lett.*, **94**, 037205 (2005).
96. T. Fukumura, H. Toyosaki, and Y. Yamada, *Semicond. Sci. Technol.* **20**, S103 (2005).
97. Liu, C., F. Yun, and H. Morko, *J. Mat. Sci: Materials in Elect* **16**, 555 (2005).
98. K. Sato and H. Katayama-Yoshida, *Physica E: Low-dimensional Systems and Nanostructures*, **10**, 251 (2001).
99. F. Pan, C. Song, X. J. Liu, Y. C. Yang and F. Zeng, *Materials Science and Engineering: R: Reports*, **62**, 1 (2008).
100. T. Fukumura, Y. Yamada, H. Toyosaki, T. Hasegawa, H. Koinuma and M. Kawasaki, *Applied Surface Science*, **223**, 62 (2004).
101. K. Ueda, H. Tabata and T. Kawai, *Applied Physics Letters*, **79**, 988 (2001).
102. M. Berciu and R. N. Bhat, *Phys. Rev. Lett.* **87**, 108203 (2001).
103. R. N. Bhat, M. Berciu, M. D. Kennett, and X. X. Wan, *J. Supercond.: Inc. Novel Magn.* **15**, 71 (2002).
104. T. Dietl, F. Matsukura, and H. Ohno, *Phys. Rev. B* **66**, 033203 (2002).
105. S. D. Sarma, E. H. Hwang, and A. Kaminski, *Phys. Rev. B* **67**, 155201 (2003).
106. P. A. Cox, *Transition Metal Oxides*, Clarendon Press, Oxford, (1992).
107. J. M. D. Coey, M. Venkatesan, and C. B. Fitzgerald *Nature Materials*, vol. **4**, p. 173 (2005).
108. M. V. Schilfkaarde and O. N. Mryasov, *Physical Review B* **63**, 233205 (2001).
109. S. J. Pearton, W. H. Heo, M. Ivill, D. P. Norton and T. Steiner, *Semiconductor Science and Technology*, **19**, R59 (2004).
110. M. Diaconu, H. Schmidt, A. Pöppel, R. Böttcher, J. Hoentsch, A. Rahm, H. Hochmuth, M. Lorenz and M. Grundmann, *Superlattices and Microstructures*, **38**, 413 (2005).

111. Y. Belghazi, G. Schmerber, S. Colis, J. L. Rehspringer, A. Dinia and A. Berrada, *Applied Physics Letters*, **89**, 122504 (2006).
112. D. C. Kundaliya, S. B. Ogale, S. E. Lofland, S. Dhar, C. J. Metting, S. R. Shinde, Z. Ma, B. Varughese, K. V. Ramanujachary, L. Salamanca-Riba and T. Venkatesan, *Nature Materials*, **3**, 709 (2004).
113. X. Z. Li, J. Zhang and D. J. Sellmyer, *Solid State Communications*, **141**, 398 (2007).
114. D. Wang, Z. Q. Chen, D. D. Wang, J. Gong, C. Y. Cao, Z. Tang and L. R. Huang, *Journal of Magnetism and Magnetic Materials*, **322**, 3642 (2010).
115. Y. M. Cho, W. K. Choo, H. Kim, D. Kim and Y. Ihm, *Applied Physics Letters*, **80**, 3358 (2002).
116. H.-J. Lee, S.-Y. Jeong, C. R. Cho and C. H. Park, *Applied Physics Letters*, **81**, 4020 (2002).
117. X. X. Wei, C. Song, K. W. Geng, F. Zeng, B. He and F. Pan, *Journal of Physics: Condensed Matter*, **18**, 7471 (2006).
118. M.von Laue, *Roentgenstrahl-Interferenzen* (AkademischeVerlagsge-sellschaft, Frankfurt, 1960).
119. B. W. Batterman and H. Cole, *Rev. Mod. Phys.* **36**, 681 (1964).
120. B. W. Batterman, *Phys. Rev.* **133**, A759 (1964).
121. J. A. Golovochenko, B. W. Batterman and W. L. Brown, *Phys. Rev. B.* **10**, 4239 (1974).
122. S. K. Andersen, J. A. Golovochenko and M. F. Robbins, *Phys. Rev. Lett.* **37**, 1141 (1976).
123. M. J. Bedzyk, G. Materlik and M. V. Kovalchuk, *Phys. Rev. B.* **30**, 2453 (1984).
124. Th. Gog, T. Harasimowicz, B. N. Dev and G. Materlik, *Europhys. Lett.* **25**, 253 (1994).
125. P. L. Cowan, J. A. Golovochenko and M. F. Robbins, *Phys. Rev. Lett.* **44**, 1680 (1980).
126. E. Vlieg, A. E. M. J. Fischer, J. F. van der Veen, B. N. Dev and G. Materlik, *Surf. Sci.* **178**, 36 (1986).
127. M. J. Bedzyk and G. Materlik, *Phys. Rev. B.* **31**, 4110 (1985).
128. B. N. Dev, F. Grey, R. L. Johnson and G. Materlik, *Europhys. Lett.* **6**, 311 (1988); B. N. Dev, *Phys. Rev. Lett.* **64**, 1182 (1990).
129. J. Zegenhagen, *Surf. Sci. Rep.* **18**, 199 (1993).
130. B. N. Dev, in *X-ray and Inner-Shell Processes*, (Eds.), R. L. Johnson, H. Schmidt-Boecking and B. F. Sonntag, *AIP Conference Proceedings*, **389**, 249 (1997).
131. T. W. Barbee and W. K. Warburton, *Mater. Lett.* **3**, 17(1984).
132. B. Lai, G. M. Wells, R. Readaeli, F. Cerrina, K. Tan, J. H. Underwood and J. Kortright, *Nucl. Instrum. Methods, A.* **266**, 684 (1988).
133. M. J. Bedzyk, D. H. Bilderback, G. M. Bommarito, M. Caffrey and J. S. Schildkraut, *Science*, **241**, 1788 (1988).
134. A. Iida, T. Matsushita and T. Isikawa, *Jpn. J. Appl. Phys.* **24**, L675 (1985).
135. J. B. Kortright and A. Fischer-Colbrie, *J. Appl. Phys.* **61**, 1130 (1987).
136. T. Kawamura and H. Takenaka, *J. Appl. Phys.* **75**, 3860 (1994).
137. S. I. Zheludeva, M. V. Kovalchuk, N. N. Novikova, and I. V. Bashelhanov, *Rev. Sci. Instrum.* **63**, 1519 (1992).
138. S. M. Heald and J. M. Tranquada *J. Appl. Phys.* **65**, 290 (1989).
139. B. N. Dev, A. K. Das, S. Dev, D. W. Schubert, M. Stamm and G. Materlik, *Phys. Rev. B* **61**, 8462 (2000).

140. L. G. Parratt, *Phys. Rev.* **95**, 359 (1954)
141. B. W. Batterman, *Phys. Rev.* **133**, A759 (1964)
142. J. Zegenhagen, *Surf. Sci. Rep.*, **18**, 199 (1993)
143. L. Properzi, A. Di Cicco, L. Nataf, F. Baudelet and T. Irifune, *Scientific Reports*, **5**, 10188 (2015).
144. N. C. Das, N. K. Sahoo, D. Bhattacharyya, S. Thakur, N. M. Kamble, D. Nanda, S. Hazra, J. K. Bal, J. F. Lee, Y. L. Tai and C. A. Hsieh, *Journal of Applied Physics*, **108**, 023515 (2010).
145. N. C. Das, N. K. Sahoo, D. Bhattacharyya, S. Thakur, D. Nanda, S. Hazra, J. K. Bal, J. F. Lee, Y. L. Tai and C. A. Hsieh, *Journal of Applied Physics*, **110**, 063527 (2011).
146. A. Biswas, A. Porwal, Debarati Bhattacharya, C.L. Prajapat, Arnab Ghosh, Mangla Nand, C. Nayak, S. Rai, S.N. Jha, M.R. Singh, D. Bhattacharyya, S. Basu, N.K. Sahoo. *Applied Surface Science* **416** (2017) 168–177.
147. Maidul Haque, A. biswas, Debarati Bhattacharyya, R.B. Tokas, D. Bhattacharyya and N.K. Shaoo, *J. Appl. Phys.* **114** (2013) 103508.
148. S Basu, C Nayak, A K Yadav, A Agrawal, A K Poswal, D Bhattacharyya, S N Jha and N K Sahoo, *Journal of Physics: Conference Series* **493** (2014) 012032.
149. D. Bhattacharyya, A.K. Poswal, S.N. Jha, Sangeeta and S.C. Sabharwal, *Nuclear Instruments Method. in Phys. Res. A* **609** (2009) 286.
150. M. Newville, B.Ravel, D. Haskel, J.J. Rehr, E.A. Stern and Y. Yacoby, *Physica B* **154**, 208 (1995).
151. Wright, J. D., & Sommerdijk, N. A. J. M. (2001). *Sol-gel materials: chemistry and applications*. (Advanced chemistry texts; Vol. 4).
152. <http://eng.thesaurus.rusnano.com/wiki/article1209>.
153. Matthew Newville Consortium for Advanced Radiation Sources University of Chicago, “*Fundamentals of XAFS*” (2004).
154. Sayers, D. E., Stern, E. A., and Lytle, F. W., *Phys. Rev. Lett.*, **27**, 1204 (1971).
155. Stern, E. A. *Phys. Rev.*, *B10*, **8**, 3027 (1974).
156. Lytle, F. W., Sayers, D. E., and Stern, E. A. *Phys. Rev. B11*, **12**, 4825 (1975).
157. Stern, E. A., Sayers, D. E., and Lytle, F. W. *Phys. Rev. B11*, **12**, 4836 (1975).
158. Stumm von Bordwehr, R. *Ann. Phys. Fr.* **14**, 377 (1989).
159. T. Fujikawa and N. Yiwata, *Surface Science*, , **357-358**, 60-64 (1996).
160. A. L. Ankudinov, B. Ravel, J. J. Rehr and S. D. Conradson, *Physical Review B*, **58**, 7565 (1998).
161. N. Binsted, *EXCURV98: CCLRC Daresbury Laboratory computer program*; <http://srs.dl.ac.uk/XRS/Computing/Programs/excurv97/intro.html>, 1998.
162. J. J. Rehr, J. J. Kas, F. D. Vila, M. P. Prange and K. Jorissen, *Physical Chemistry Chemical Physics*, **12**, 5503 (2010).
163. A. Filipponi, A. Di Cicco and C. R. Natoli, *Physical Review B*, **52**, 15122 (1995).
164. K. S. P. Blaha, GKH Madsen, D. Kvasnicka, J. Luitz, *Wien2k An Augmented Plane Wave Plus Local Orbital Program for Calculating the Crystal Properties*, Vienna University of Technology, Austria, 2001.
165. W. Zhong, B. He, Z. Li and S. Wei, *Journal of China University of Science and Technology*, **31**, 328 (2001).
166. Stern, E.A. *Contemp. Phys.* **19**, 239 (1978).
167. Sayers, D.E., and B. Bunker. *Data analysis*. 211 (1988).

168. Fendorf, S.E., and D.L. Sparks. 1996, "X-ray absorption fine structure spectroscopy" p. 357–375. In D.L. Sparks (ed.) *Methods of soil analysis. Part 3.* SSSA Book Ser. 5. SSSA, Madison, WI.
169. Fendorf, S.E. "Fundamental aspects and applications of x-ray absorption spectroscopy in clay and soil science" p. 19–67 In D.G. Schulze et al. (ed.) *Synchrotron methods in clay science.* CMS Workshop Lectures, **9**, 1999.
170. Stern, E.A., and S.M. Heald. "Basic principles and applications of EXAFS" **10**, 995–1014, 1983, In E.E. Koch (ed.) *Handbook of synchrotron radiation.* Vol. 10. North-Holland, Amsterdam.
171. Koningsberger, D.C., and R. Prins (ed.) 1988. "X-ray absorption: Principles, applications, techniques of EXAFS, SEXAFS and XANES". John Wiley & Sons, New York.
172. Teo, B.K. 1986. "EXAFS spectroscopy: Basic principles and data analysis". Springer-Verlag, New York.
173. Stöhr, J. 1992. "NEXAFS Spectroscopy", Springer-Verlag, New York.
174. G. Bunker, "Introduction to XAFS A Practical Guide to X-ray Absorption Fine Structure Spectroscopy", Cambridge University Press, New York, 2010.
175. D. C. K. R. Prince, X-Ray Absorption: Principles Applications Techniques of EXAFS SEXAFS and XANES Wiley, New York 1988.
176. Jeroen A. van Bokhoven and C. Lamberti, "X-Ray Absorption and X-Ray Emission Spectroscopy: Theory and Applications", John Wiley & Sons, Ltd, West Sussex, 2016.
177. P. Willmott, "An Introduction to Synchrotron Radiation: Techniques and Applications", John Wiley & Sons, Ltd, West Sussex, 2011.
178. Z. Sun, W. Yan, T. Yao, Q. Liu, Y. Xie and S. Wei, *Dalton Transactions*, **42**, 13779 (2013).
179. S. Kelly, D. Hesterberg and B. Ravel, *Methods of soil analysis. Part*, **5**, 387 (2008).
180. F. R. Elder, R. V. Langmuir, and H. C. Pollock, *Phys. Rev.* **74**, 52 (1948).
181. D. H. Tomboulion and P. L. Hartman, *Phys. Rev.* **102**, pp.
182. <http://www.rrcat.gov.in/technology/accel/indus/index.html>
183. <http://www.rrcat.gov.in/technology/accel/indus2.html>.
184. A. K. Poswal, A. Agrawal, A. K. Yadav, C. Nayak, S. Basu, S. R. Kane, C. K. Garg, D. Bhattacharyya, S. N. Jha and N. K. Sahoo, *AIP Conference Proceedings*, **1591**, 649 (2014).
185. B. Ravel and M. Newville, *J. Synchrotron Radiat.* **12**, 537 (2005).
186. B. Ravel, *J. Synchrotron Radiat.* **8(2)**, 314 (2001).
187. M. Newville, *J. Synchrotron Radiat.* **8(2)**, 322 (2001).
188. S. I. Zabinsky, J. J. Rehr, A. Ankudinov, R. C. Albers, and M. J. Eller. *Phys. Rev. B*, **52**, 4 (1995).
189. A. L. Ankudinov, B. Ravel, J. J. Rehr, and S. D. Conradson, *Phys. Rev. B*, **58**, 7565 (1998).
190. M. Newville, P. Līviņš, Y. Yacoby, J. J. Rehr, and E.A. Stern, *Phys. Rev. B*, **47**, 14126 (1993).
191. <https://www.rigaku.com/en/techniques/xrd>]
192. http://www.mecheng.iisc.ernet.in/~bobji/mspc/assign_2012/PROJECT%20TEM.pd.
193. [https://en.wikipedia.org/wiki/Fourier-transform_infrared_spectroscopy].

194. Settle FA, “*Handbook of instrumental techniques for analytical chemistry*”; 1997.
195. H. Zhu, J. Iqbal, H. Xu, D. Yu, *J. Chem. Phys.* **129**, 12 (2008).
196. A. Singhal, S.N. Achary, J. Manjanna, S. Chatterjee, P. Ayyub, A.K. Tyagi, *J. Phys. Chem. C*, **114**, 3422 (2010).
197. M. Schumm, M. Koerdel, S. Müller, C. Ronning, E. Dynowska, Z. Gołacki, W. Szuszkiewicz, J. Geurts, *J. Appl. Phys.* **105**, 2009 (2009).
198. P. Hohenberg, W. Kohn, *Phys. Rev.* **136**, B864 (1964).
199. W. Kohn, L.J. Sham, *Phys. Rev.* **140**, A1133 (1965),
200. G. Kresse, J. Furthmuller, *Phys. Rev. B*, **54**, 11169 (1996).
201. G. Kresse, D. Joubert, *Phys. Rev. B*, **59**, 1758 (1999);
202. J.P. Perdew, K. Burke, M. Ernzerhof, *Phys. Rev. Lett.* **77**, 3865 (1996).
203. T. Tamura and H. Ozaki, *J. Phys.: Condens. Matter*, **21**, 026009 (2009).
204. A. Singhal, S. N. Achary, A. K. Tyagi, P. K. Manna and S. M. Yusuf, *Mater. Sci. Eng. B*, **47**, 153 (2008).
205. S. Kumar, Y. J. Kim, B. H. Koo, S. K. Sharma, J. M. Vargas, M. Knobel, S. Gautam, K. H. Chae, D. K. Kim, Y. K. Kim and C. G. Lee, *J. Appl. Phys.* **105**, 07C520 (2009).
206. A. K. Mishra and D. Das, *Mater. Sci. Eng., B*, **171**, 5 (2010).
207. M. Venkatesan, C. B. Fitzgerald, J. G. Lunney and J. M. D. Coey, *Phys. Rev. Lett.* **93**, 177206 (2004).
208. S. J. Han, J. W. Song, C. H. Yang, S. H. Park, J. H. Park, Y. H. Jeong and K. W. Rhie, *Appl. Phys. Lett.* **81**, 4212 (2002).
209. D. Karmakar, S. K. Mandal, R. M. Kadam, P. L. Paulose, A. K. Rajarajan, T. K. Nath, A. K. Das, I. Dasgupta and G. P. Das, *Phys. Rev. B: Condens. Matter Mater. Phys.* **75**, 144404 (2007).
210. J. Anghel, A. Thurber, D. A. Tenne, C. B. Hanna and A. Punnoose, *J. Appl. Phys.* **107**, 09E314 (2010).
211. R. Saleh, S. P. Prakoso and A. Fishli, *J. Magn. Magn. Mater.* **324**, 665 (2012).
212. S. Kumar, S. Mukherjee, R. K. Singh, S. Chatterjee and A. K. Ghosh, *J. Appl. Phys.* **110**, 103508 (2011).
213. H. Morkoç and U. “Ozg” ur, “Zinc Oxide-Fundamentals, Materials and Device Technology”, WILEY-VCH Verlag GmbH, Germany, 2009.
214. U. “Ozg” ur, Y. I. Alivov, C. Liu, A. Teke, M. A. Reshchikov, “S. Doğan, V. Avrutin, S.-J. Cho and H. Morkoç, *J. Appl. Phys.* **98**, 041301 (2005).
215. M. Gaudon, O. Toulemonde and A. Demourgues, *Inorg. Chem.* **46**, 10996 (2007).
216. J. Luo, J. K. Liang, Q. L. Liu, F. S. Liu, Y. Zhang, B. J. Sun and G. H. Rao, *J. Appl. Phys.* **97**, 086106 (2005).
217. A. K. Zak, W. H. A. Majid, M. E. Abrishami and R. Yousefi, *Solid State Sci.* **13**, 251 (2011).
218. G. K. Williamson and W. H. Hall, *Acta Metall.*, **1**, 22–31 (1953)
219. E. Prince and J. K. Stalick, “*Accuracy in Powder Diffraction II, NIST Special Publication*”, vol. **597** (1992).
220. A. K. Mishra and D. Das, *Mater. Sci. Eng., B*, **171**, 5–10 (2010).
221. J. A. Sans, J. F. S’anchez-Royo, A. Segura, G. Tobias and E. Canadell, *Phys. Rev. B: Condens. Matter Mater. Phys.*, **79**, 195105 (2009)
222. B. B. Straumal, A. A. Mazilkin, S. G. Protasova, P. B. Straumal, A. A. Myatiev, G. Schutz, E. J. Goering, T. Tietze and B. Baretzky, *Philos. Mag.*, **93**, 1371–1383 (2013).

223. B. B. Straumal, S. G. Protasova, A. A. Mazilkin, G. Schutz, E. Goering, B. Baretzky and P. B. Straumal, *JETP Lett.*, **97**, 367–377 (2013)
224. E. H. Kisi and M. M. Elcombe, *Acta Crystallogr., Sect. C: Cryst. Struct. Commun.*, **45**, 1867–1870 (1989).
225. S. Basu, D. Y. Inamdar, S. Mahamuni, A. Chakrabarti, C. Kamal, G. R. Kumar, S. N. Jha and D. Bhattacharyya, *J. Phys. Chem. C*, **118(17)**, 9154–9164 (2014).
226. P. E. Lippens, A. V. Chadwick, A. Weibel, R. Bouchet and P. Knauth, *J. Phys. Chem. C*, **112**, 43–47 (2008).
227. J. B. Wang, G. J. Huang, X. L. Zhong, L. Z. Sun, Y. C. Zhou and E. H. Liu, *Appl. Phys. Lett.*, **88**, 252502 (2006).
228. J. M. Calleja and M. Cardona, *Phys. Rev. B: Condens. Matter Mater. Phys.*, **16**, 3753 (1977).
229. X. Wang, J. Xu, X. Yu, K. Xue, J. Yu and X. Zhao, *Appl. Phys. Lett.*, **91**, 031908 (2007).
230. T. C. Damen, S. P. S. Porto and B. Tell, *Phys. Rev.*, **142**, 570–574 (1966).
231. S. Singh and M. S. Ramachandra Rao, *Phys. Rev. B: Condens. Matter Mater. Phys.*, **80**, 045210 (2009).
232. J. Serrano, A. H. Romero, F. J. Manjo'n, R. Lauck, M. Cardona and A. Rubio, *Phys. Rev. B: Condens. Matter Mater. Phys.*, **69**, 094306 (2004).
233. R. Cuscó, E. A. Lladó, J. Ibáñez, L. Artís, J. Jiménez, B. Wang and M. J. Callahan, *Phys. Rev. B: Condens. Matter Mater. Phys.*, **75**, 165202, (2007).
234. S. Chen, Y. Liu, C. Shao, R. Mu, Y. Lu, J. Zhang, D. Shen and X. Fan, *Adv. Mater.*, **17**, 586–590 (2005).
235. Y. J. Xing, Z. H. Xi, Z. Q. Xue, X. D. Zhang, J. H. Song, R. M. Wang, J. Xu, Y. Song, S. L. Zhang and D. P. Yu, *Appl. Phys. Lett.*, **83**, 1689–1691, (2003).
236. J. D. Ye, S. L. Gu, S. M. Zhu, S. M. Liu, Y. D. Zheng, R. Zhang, Y. Shi, Q. Chen, H. Q. Yu and Y. D. Ye, *Appl. Phys. Lett.*, **88**, 101905 (2006).
237. L. W. Yang, X. L. Wu, G. S. Huang, T. Qiu and Y. M. Yang, *J. Appl. Phys.*, **97**, 014308 (2005).
238. A. Singhal, S. N. Achary, A. K. Tyagi, P. K. Manna and S. M. Yusuf, *Mater. Sci. Eng., B*, **47**, 153 (2008).
239. S. Kumar, Y. J. Kim, B. H. Koo, S. K. Sharma, J. M. Vargas, M. Knobel, S. Gautam, K. H. Chae, D. K. Kim, Y. K. Kim and C. G. Lee, *J. Appl. Phys.*, **105**, 07C520 (2009).
240. A. K. Mishra and D. Das, *Mater. Sci. Eng., B*, **171**, 5–10, (2010).
241. D. Karmakar, S. K. Mandal, R. M. Kadam, P. L. Paulose, A. K. Rajarajan, T. K. Nath, A. K. Das, I. Dasgupta and G. P. Das, *Phys. Rev. B: Condens. Matter Mater. Phys.*, **75**, 144404 (2007).
242. B. Martínez, F. Sandiumenge, Ll. Balcells, J. Arbiol, F. Sibiude and C. Monty, “*Phys. Rev. B: Condens. Matter Mater. Phys.*”, **72**, 165202 (2003).
243. O. D. Jayakumar, H. G. Salunke, R. M. Kadam, M. Mahapatra, G. Yashwant and S. K. Kulshreshtha, *Nanotechnology*, **17**, 1278–1285 (2006).
244. B. B. Straumal, A. A. Mazilkin, S. G. Protasova, A. A. Myatiev, P. B. Straumal, G. Schutz, P. A. V. Aken, E. Goering and B. Baretzky, *Phys. Rev. B: Condens. Matter Mater. Phys.*, **79**, 205206, (2009).

245. A. Kaminski and S. D. Sarma, *Phys. Rev. Lett.*, **88**, 247202 (2002).
246. J. M. D. Coey, M. Venkatesan and C. B. Fitzgerald, *Nat. Mater.*, **4**, 173–179 (2005).
247. S. D. Sarma, E. H. Hwang and A. Kaminski, *Phys. Rev. B: Condens. Matter Mater. Phys.*, **67**, 155201, (2003).
248. B. Pal and P. K. Giri, *J. Appl. Phys.*, **108**, 084322 (2010).
249. Y. Liu, J. Yang, Q. Guan, L. Yang, H. Liu, Y. Zhang, Y. Wang, D. Wang, J. Lang, Y. Yang, L. Fei and M. Wei, *Appl. Surf. Sci.*, **256**, 3559–3562 (2010).
250. K. Jayanthi, S. Chawla, A. G. Joshi, Z. H. Khan and R. K. Kotnala, *J. Phys. Chem. C*, **114**, 18429–18434 (2010).
251. B.-Z. Lin, L. Zhou, S. U. Yuldashev, D.-J. Fu and T.-W. Kang, *Appl. Surf. Sci.*, **315**, 124–130 (2014).
252. M. Venkatesan, C. Fitzgerald, J. Lunney and J. Coey, *Phys. Rev. Lett.*, **93**, 177206 (2004).
253. K. Ueda, H. Tabata and T. Kawai, *Appl. Phys. Lett.*, **79**, 988 (2001).
254. H. Liu, X. Zhang, L. Li, Y. Wang, K. Gao, Z. Li, R. Zheng, S. Ringer, B. Zhang and X. Zhang, *Appl. Phys. Lett.*, **91**, 072511 (2007).
255. Y. Liu, Y. Yang, J. Yang, Q. Guan, H. Liu, L. Yang, Y. Zhang, Y. Wang, M. Wei, X. Liu, L. Fei and X. Cheng, *J. Solid State Chem.*, **184**, 1273–1278 (2011).
256. W. Jin, I. Lee, A. Kompch, U. Dorfer and M. Winterer, *J. Eur. Ceram. Soc.*, **27**, 4333–4337 (2007).
257. L. Schneider, S. V. Xaitsev, W. Jin, A. Kompch, M. Winterer, M. Acet and G. Bacher, *Nanotechnology*, **20**, 135604 (2009).
258. B. D. Cullity, *Elements of X-ray diffraction*, Addison-Wesley Inc., USA, 1959.
259. A. Patterson, *Phys. Rev.*, 1939, 56, 978.
260. E. Prince and J. Stalick, *Accuracy in Powder Diffraction II*, 1992.
261. <http://abulafia.mt.ic.ac.uk/shannon/ptable.php>.
262. N. Tiwari, S. Doke, A. Lohar, S. Mahamuni, C. Kamal, A. Chakrabarti, R. Choudhary, P. Mondal, S. Jha and D. Bhattacharyya, *J. Phys. Chem. Solids*, **90**, 100–113 (2016).
263. I. Brown and D. Altermatt, *Acta Crystallogr., Sect. B: Struct. Sci.*, **41**, 244–247 (1985).
264. A. Singhal, S. Achary, J. Manjanna, S. Chatterjee, P. Ayyub and A. Tyagi, *J. Phys. Chem. C*, **114**, 3422–3430, (2010).
265. L. Yang, X. Wu, G. Huang, T. Qiu and Y. Yang, *J. Appl. Phys.*, **97**, 014308 (2005).
266. D. Mead and G. Wilkinson, *J. Raman Spectrosc.*, **6**, 123–129, (1977).
267. S. Singh and M. R. Rao, *Phys. Rev. B: Condens. Matter Mater. Phys.*, **80**, 045210 (2009).
268. J. Calleja and M. Cardona, *Phys. Rev. B: Condens. Matter Phys.*, **16**, 3753 (1977).
269. X. Wang, J. Xu, X. Yu, K. Xue, J. Yu and X. Zhao, *Appl. Phys. Lett.*, **91**, 031908 (2007).
270. J. Wang, G. Huang, X. Zhong, L. Sun, Y. Zhou and E. Liu, *Appl. Phys. Lett.*, **88**, 252502 (2006).
271. T. C. Damen, S. Porto and B. Tell, *Phys. Rev.*, **142**, 570 (1966).

272. J. Serrano, A. Romero, F. Manjon, R. Lauck, M. Cardona and A. Rubio, *Phys. Rev. B: Condens. Matter Mater. Phys.*, **69**, 094306 (2004).
273. R. Cuscó, E. Alarcón-Lladó, J. Ibáñez, L. Artís, J. Jiménez, B. Wang and M. J. Callahan, *Phys. Rev. B: Condens. Matter Mater. Phys.*, **75**, 165202, (2007).
274. S. Chen, Y. Liu, C. Shao, R. Mu, Y. Lu, J. Zhang, D. Shen and X. Fan, *Adv. Mater.*, **17**, 586–590 (2005).
275. Y. Xing, Z. Xi, Z. Xue, X. Zhang, J. Song, R. Wang, J. Xu, Y. Song, S. Zhang and D. Yu, *Appl. Phys. Lett.*, **83**, 1689–1691, (2003).
276. J. Ye, S. Gu, S. Zhu, S. Liu, Y. Zheng, R. Zhang, Y. Shi, Q. Chen, H. Yu and Y. Ye, *Appl. Phys. Lett.*, **88**, 101905, (2006).
277. F. Ahmed, S. Kumar, N. Arshi, M. Anwar, B. H. Koo and C. G. Lee, *Microelectron. Eng.*, **89**, 129–132 (2012).
278. M. M. Hassan, W. Khan, A. Azam and A. H. Naqvi, *J. Ind. Eng. Chem.*, **21**, 283–291 (2015).
279. S. Kumar, S. Basu, B. Rana, A. Barman, S. Chatterjee, S. Jha, D. Bhattacharyya, N. Sahoo and A. K. Ghosh, *J. Mater. Chem. C*, **2**, 481–495 (2014).
280. S. Kumar, S. Chatterjee, K. Chattopadhyay and A. K. Ghosh, *J. Phys. Chem. C*, **116**, 16700–16708 (2012).
281. Y. Guo, X. Cao, X. Lan, C. Zhao, X. Xue and Y. Song, *J. Phys. Chem. C*, **112**, 8832–8838 (2008).
282. P. D. Cozzoli, M. L. Curri, A. Agostiano, G. Leo and M. Lomascolo, *J. Phys. Chem. B*, **107**, 4756–4762 (2003).
283. S. Gilliland, J. Sans, J. Sánchez-Royo, G. Almonacid, B. García-Domene, A. Segura, G. Tobias and E. Canadell, *Phys. Rev. B: Condens. Matter Mater. Phys.*, **86**, 155203 (2012).
284. E. Burstein, *Phys. Rev.*, **93**, 632 (1954).
285. F. Shan and Y. Yu, *J. Eur. Ceram. Soc.*, **24**, 1869–1872 (2004).
286. R. Bylsma, W. Becker, J. Kossut, U. Debska and D. Yoder Short, *Phys. Rev. B: Condens. Matter Mater. Phys.*, **33**, 8207 (1986).
287. P. Koidl, *Phys. Rev. B: Condens. Matter Mater. Phys.*, **15**, 2493 (1977).
288. Y. Wang, S. Lau, H. Lee, S. Yu, B. Tay, X. Zhang and H. Hng, *J. Appl. Phys.*, **94**, 354–358 (2003).
289. V. A. Fonoberov, K. A. Alim, A. A. Balandin, F. Xiu and J. Liu, *Phys. Rev. B: Condens. Matter Mater. Phys.*, **73**, 165317 (2006).
290. L. Shi, H. Shen, L. Jiang and X. Li, *Mater. Lett.*, **61**, 4735–4737 (2007).
291. T. Kataoka, Y. Yamazaki, Y. Sakamoto, A. Fujimori, F.-H. Chang, H.-J. Lin, D. Huang, C. Chen, A. Tanaka and S. Mandal, *Appl. Phys. Lett.*, **96**, 252502 (2010).
292. E. Gur, S. Tüzemen, K. Meral and Y. Onganer, *Appl. Phys. A*, **94**, 549–554 (2009).
293. K. Vanheusden, C. Seager, W. T. Warren, D. Tallant and J. Voigt, *Appl. Phys. Lett.*, **68**, 403–405 (1996).
294. P. Kadam, C. Agashe, S. Mahamuni, *J. Appl. Phys.* **104**, 103501 (2008).
295. L. Guo, S. Yang, C. Yang, P. Yu, J. Wang, W. Ge, G.K. L. Wong, *Chem. Mater.* **12**, 2268 (2000).
296. J. Rodríguez-Carvajal, *Physica B* **192** (1993) 55.
297. L. Kumar, P. Kumar, A. Narayan, M. Karl, *Int. Nano Lett.* **3**, 1 (2013).
298. <http://abulafia.mt.ic.ac.uk/shannon/ptable.php>.

299. B.D. Cullity, Elements of X-Ray Diffraction, 3rd ed., Prentice Hall.
300. S. Singhal, J. Kaur, T. Namgyal, R. Sharma, *Physica B* **407**, 1223 (2012).
301. V. Gandhi, R. Ganesan, H.H.A. Syedahamed, M. Thaiyan, *J. Phys. Chem. C* **118**, 9715 (2014).
302. B. Nandi Ganguly, S. Dutta, S. Roy, J. Röder, K. Johnston, M. Martin, *Nucl. Instrum. Methods Phys. Res. B* **362**, 103 (2015).
303. D.Y. Inamdar, A.D. Lad, A.K. Pathak, I. Dubenko, N. Ali, S. Mahamuni, *Phys. Chem. C* **114**, 1451(2010).
304. Y. Jin, Q. Cui, G. Wen, Q. Wang, J. Hao, S. Wang, J. Zhang, *J. Phys. D Appl. Phys.* **42**, 215007 (2009).
305. Y.Q. Chang, P.W. Wang, S.L. Ni, Y. Long, X.D. Li, *J. Mater. Sci. Technol.* **28**, 313 (2012).
306. H. Zhu, J. Iqbal, H. Xu, D. Yu, *J. Chem. Phys.* **129** 12 (2008).
307. W. Szuszkiewicz, J.F. Morhange, Z. Golacki, *Acta Phys. Pol. A* **112**, 363 (2007).
308. K. Samanta, P. Bhattacharya, R. Katiyar, W. Iwamoto, P. Pagliuso, C. Rettori, *Phys. Rev. B* **73**, 245213 (2006).
309. A. Singhal, S.N. Achary, J. Manjanna, S. Chatterjee, P. Ayyub, A.K. Tyagi, *J. Phys. Chem. C* **114**, 3422 (2010).
310. Y.Q. Chang, P.W. Wang, S.L. Ni, Y. Long, X.D. Li, *J. Mater. Sci. Technol.* **28**, 313 (2012).
311. M.F. Cerqueira, M.I. Vasilevskiy, F. Oliveira, A.G. Rolo, T. Viseu, J. Ayres de Campos, E. Alves, R. Correia, *J. Phys. Condens. Matter* **23**, 334205, (2011).
312. C. Bundesmann, N. Ashkenov, M. Schubert, D. Spemann, T. Butz, E. M. Kaidashev, M. Lorenz, C. Bundesmann, N. Ashkenov, M. Schubert, D. Spemann, T. Butz, E.M. Kaidashev, *Appl. Phys. Lett.* **10**, 1974 (2011)
313. T.L.Phan, R. Vincent, D. Cherns, N.X. Nghia, V.V. Ursaki, *Nanotechnology* **19**, 475702 (2008).
314. S.K. Misra, C. Wang, *Phys. Rev. B* **41**,1 (1990).
315. G. Thennarasu, A. Sivasamy, *Powder Technol.* **1**, 250 (2013).
316. B.D. Yuhas, D.O. Zitoun, P.J. Pauzauskie, R. He, P.Y. Angew, *Chem. Int. Ed.* **45**, 420 (2006).
317. H.T. Lin, T.S. Chin, J. Shih, *Appl. Phys. Lett.* **85**, 621 (2004).
318. Shiv Kumar, S. Basu, B. Rana, A. Barman, S. Chatterjee, S.N. Jha, D. Bhattacharyya, N.K. Sahoo, Anup K. Ghosh, *J. Mater. Chem. C* **2**, 481 (2014).
319. <http://cars9.uchicago.edu/atomsdb/CoO.inp>.
320. <http://cars9.uchicago.edu/atomsdb/CuO.inp>.
321. R. Knut, J.M. Wikberg, K. Lashgari, V.A. Coleman, G. Westin, P. Svedlindh, O. Karis, *Phys. Rev. B* **82** 094438 (2010).
322. T. Kataoka, Y. Yamazaki, V.R. Singh, A. Fujimori, F.-H. Chang, H.-J. Lin, D. J. Huang, C.T. Chen, G.Z. Xing, J.W. Seo, C. Panagopoulos, T. Wu, *Phys. Rev. B* **84**, 153203 (2011).
323. R. Viswanatha, D. Naveh, J.R. Chelikowsky, L. Kronik, D.D. Sarma, *J. Phys. Chem. Lett.* **3**, 2009 (2012).
324. J.A. Wibowo, N.F. Djaja, R. Saleh, *Adv. Mater. Phys. Chem.* **3**, 48 (2013).
325. J.H. Shim, T. Hwang, S. Lee, *Appl. Phys. Lett.* **86**, 082503 (2005).
326. Shiv Kumar, N. Tiwari, S.N. Jha, S. Chatterjee, D. Bhattacharyya, N.K. Sahoo, Anup K. Ghosh, *RSC Adv.* **5**, 94658 (2015).

327. Ashok Kumar Yadav, Sk. Maidul Haque, Shilpa Tripathi, Dinesh Shukla, Md.A. Ahmed, D.M. Phase, S. Bandyopadhyay, S.N. Jha, D. Bhattacharyya, *RSC Adv.* **6**, 74982 (2016).
328. N. Tiwari, S. Doke, A. Lohar, Shailaja Mahamuni, C. Kamal, Aparna Chakrabarti, R.J. Choudhary, P. Mondal, S.N. Jha, D. Bhattacharyya, *J. Phys. Chem. Sol.* **90**, 100 (2016).
329. H. Liua, J. Yanga, Z. Huaa, Y. Liua, L. Yanga, Y. Zhanga, J. Cao, *Mater. Chem. Phys.* **125**, 656–659. (2011)
330. S. Muthukumaran, R. Gopalakrishnan, *Phys. B*, **407**, 3448–3456 (2012)
331. H. Liu, J. Yang, Z. Hua, Y. Zhang, L. Yang, L. Xiao, Z. Xie, *Appl. Surf. Sci.* **256**, 4162–4165 (2010).
332. G. Tang, X. Shi, C. Huo, Z. Wang, *Ceram. Int.* **2013**, **39**, 4825–4829.
333. N. Tiwari, S. Doke, A. Lohar, S. Mahamuni, C. Kamal, A. Chakrabarti, R. J. Choudhary, P. Mondal, S. N. Jha, D. Bhattacharyya, *J. Phys. Chem. Solids* **90**, 100–113 (2016)
334. N. Tiwari, A. Lohar, C. Kamal, A. Chakrabarti, C. L. Prajapat, P. K. Mishra, P. Mondal, B. Karnar, N. L. Misra, S. N. Jha, D. Bhattacharyya, *J. Phys. Chem. Solids* **104**, 198–206. (2017)
335. G. Q. Pei, C. T. Xia, B. Wu, T. Wang, L. L. Zhang, Y. J. Dongand, J. Xu, *Comput. Mater. Sci.*, **43**, 489 (2008).
336. X. C. Liu, E. W. Shi, Z. Z. Chen, H. W. Zhang, B. Xiao, L. X. Song, *Appl. Phys. Lett.* **88**, 252503 (2006).
337. Hua-Wei Zhang, Zhi-Ren Wei, Zhi-Qiang Li, Guo-Yi Dong, *Mater. Lett.* **61**, 3605–3607 (2007).
338. S. J. Peartn and D. P. Norton, *IEEE Trans. Electron Devices*, **54**, 1040–1048 (2007).
339. M. Subramanian, P. Thakur, M. Tanemura, T. Hihara, V. Ganesan, T. Soga, K. H. Chae, R. Jayavel and T. Jimbo, *J. Appl. Phys.*, **108**, 053904 (2010).
340. M. Kohls, T. Schmidt, H. Katschorek, L. Spanhel, G. Muller, N. Mais, A. Wolf and A. Forchel, *Adv. Mater.*, **11**, 288 (1999).
341. M. Kohls, M. Bonanni and L. Spanhel, *Appl. Phys. Lett.*, **81**, 3858 (2002).
342. X. Wang, G. Kong, G. Y. Shan, Y. Yu, Y. J. Sun, L. Y. Feng, K. F. Chao, S. Z. Lv and Y. J. Li, *J. Phys. Chem. B*, **108**, 18408 (2004).
343. T. Monteiro, M. J. Soares, A. Neves, S. Pereira, M. R. Correia, M. Peres, E. Alves, D. Rogers, F. Teherani, V. Munoz-SanJose, T. Trindade and A. Pereira, *J. Non-Cryst. Solids*, **352**, 1453 (2006).
344. B. Yan, X. Chen and J. H. Wu, *Appl. Surf. Sci.*, **253**, 8575 (2007).
345. S. Ji, L. Yin, G. Liu, Y. Zhang and C. Ye, *J. Phys. Chem. C*, **113**, 16439–16444 (2009).
346. G. S. Wu, Y. L. Zhuang, Z. Q. Lin, X. Y. Yuan, T. Xie and L. D. Zhang, *Phys. E*, **31**, 5 (2006).
347. K. Ark, H. K. Hwang, J. W. Seo and W. S. Seo, *Energy*, **54**, 139 (2013)
348. A. Khataee, R. D. C. Soltani, Y. Hanifehpour, M. Safarpour, H. G. Ranjbar and S. W. Joo, *Ind. Eng. Chem. Res.*, **53**, 1924 (2014).
349. J. Singh, P. Kumar, K. S. Hui, K. N. Hui, K. Ramam, R. S. Tiwari and O. N. Srivastava, *Cryst Eng Comm*, **14**, 5898 (2012).
350. B. H. Soni, M. P. Deshpande, S. Bhatt, N. Garg, N. N. Pandya and S. H. Chaki, *J. Opt.*, **42**, 328 (2013).

351. T. Thangeeswari, P. Murugasen and J. Velmurugan, *J. Supercond. Novel Magn.*, **28**, 2505 (2015).
352. G. Vijayaprasath, R. Murugan, Y. Hayakawa and G. Ravi, *J. Lumin.*, **178**, 375, (2016)
353. <https://icsd.FIZ-karlsruhe.de>.
354. M. C. Dimri, H. Khanduri, H. Kooskora, J. Subbi, I. Heinmaa, A. Mere, J. Krustok and R. Stern, *Phys. Status Solidi A*, **209**, 353 (2012).
355. S. Kumar, N. Tiwari, S. N. Jha, S. Chatterjee, D. Bhattacharyya, N. K. Sahoo and A. K. Ghosh, *RSC Adv.*, **5**, 94658 (2015).
356. S. Kumar, N. Tiwari, S. N. Jha, S. Chatterjee, D. Bhattacharyya, N. K. Sahoo and A. K. Ghosh, *RSC Adv.*, **6**, 107816, (2016).
357. A. K. Yadav, S. Maidul Haque, D. Shukla, R. J. Choudhary, S. N. Jha and D. Bhattacharyya, *AIP Adv.*, **5**, 117138 (2015).
358. Y. P. Feng, S. K. Sinha, H. W. Deckman, J. B. Hastings, and D. P. Siddons, *Phys. Rev. Lett.* **71**, 537 1993.
359. A. Biswas, Sk. Maidul Haque, J. Misal, K.D. Lagoo, R. D.Veerapur, M. Padmanabhan, R.K. Puri, R. Sampathkumar, Ajaykumar, Debarati Bhattacharya, D. Bhattacharyya and N.K. Sahoo. *AIP Conference Proceedings*, **1591**, 985 (2014).
360. D. L. Windt, "IMD Version 4.1.1," 2000,
361. L. G. Parratt, "Surface studies of solids by total reflection of X-rays," *Phys. Rev.* **95**, 359–369 (1954).

